Measurement of the Flux of Ultra High Energy Cosmic Rays using very inclined Extensive Air Showers measured at the Pierre Auger Observatory

Zur Erlangung des akademischen Grades eines
DOKTORS DER NATURWISSENSCHAFTEN
von der Fakultät für Physik
des Karlsruher Institut für Technologie (KIT)

genehmigte
DISSERTATION

von Talianna Christina Schmidt

aus Heilbronn

Tag der mündlichen Prüfung: 23.04.2010
Referent: Prof. J. Blümer
Korreferent: Prof. G. Quast

In Loving Memory of Martina Schmidt

Measurement of the Flux of Ultra High Energy Cosmic Rays using very inclined Extensive Air Showers

The Pierre Auger Observatory is an indirect cosmic ray detector combining the detection techniques of an array of water Cherenkov detectors and fluorescence telescopes on an area of $3000\,\mathrm{km}^2$ near Malargüe/Mendoza/Argentina. Both detector components are optimised for measuring extensive air showers caused by ultra high energetic cosmic rays with primary energies larger than $10^{18}\,\mathrm{eV}$.

The surface detector measures particles of extensive air showers with zenith angles up to almost 90°. Depending on the zenith angle, the atmospheric depth traversed by the shower varies from one atmosphere at vertical showers to 36 atmospheres at very inclined showers. Thus the signature of very inclined showers at ground differs a lot from the signature of vertical showers. The most important effects are attenuation of the electromagnetic component, geometrical effects and geomagnetic deflection of the muonic component of the shower. These effects become important at zenith angles above 60°. The zenith angle interval from 60° to 80° contributes $25\,\%$ of the aperture of the surface detector. Two reconstruction algorithms are available for this zenith angle interval.

The standard reconstruction used by the Pierre Auger Collaboration for showers up to 60° can be applied to showers at higher zenith angles too. The method is based on a radially symmetric prediction of the signal in the water Cherenkov detectors. An empirical fine tuning of the parameters of the signal prediction function is introduced. A reduction of biases in this reconstruction algorithm from $8\,\%$ to less than $4\,\%$ is achieved in the whole zenith angle range from 0° to 68°. For highest zenith angles the radial symmetry of the shower footprint is broken. A Monte Carlo based model of the muon distribution at ground and a model for the contribution of the electromagnetic component have been established. A reconstruction algorithm based on the two-dimensional signal profiles has been implemented.

Both reconstruction algorithms provide only an energy estimator. The conversion of the energy estimator into an energy estimate has been performed in a calibration procedure. As reference energy the measurement of the fluorescence detector was used. Two calibration methods were applied. The resulting energy determinations with both reconstruction and both calibration methods were compared. The radially symmetric reconstruction was found to be equal in resolution and bias with respect to the two dimensional reconstruction up to zenith angles 68°. At higher zenith angles only the method based on muon profiles is valid.

The flux of ultra-high energetic cosmic rays was inferred using extensive air showers of zenith angles from 60° to 80° for the two-dimensional reconstruction method and from 60° to 68° for the radially symmetric method respectively. The result supports the measurement of the flux suppression using less inclined showers of the Pierre Auger Observatory. In an end-to-end comparison of the two methods a good agreement of the results was found in the overlap region of zenith angles from 60° to 68°.

Messung des Flusses ultrahochenergetischer kosmischer Strahlung mittels stark geneigter ausgedehnter Luftschauer

Im Pierre Auger Observatorium sind zwei indirekte Detektionsmethoden für kosmische Strahlung vereint: Ein Oberflächendetektorfeld aus Wasser-Cherenkov-Detektoren und Fluoreszenzteleskope. Das Detektorfeld ist $3000\,\mathrm{km}^2$ groß und befindet sich nahe Malargüe in der argentinischen Provinz Mendoza. Beide Detektorkomponenten sind für die Messung ultrahochenergetischer kosmischer Strahlung mit Energien größer als $10^{18}\,\mathrm{eV}$ mittels ausgedehnter Luftschauer optimiert.

Der Oberflächendetektor misst Luftschauerteilchen aus Schauern mit bis zu 90° Neigung gegen den Zenit. Abhängig vom Zenitwinkel durchqueren der Schauer zwischen einer Atmosphäre Materiesäule bei vertikalem Einfall und der Dicke von 36 Atmosphären bei sehr stark geneigten Schauern. Die Signatur stark geneigter Schauer unterscheidet sich daher stark von der Signatur senkrechter Schauer. Die bedeutendsten Unterschiede werden von der Abschwächung der elektromagnetischen Komponente in der Atmosphäre, geometrischen Effekten und der Ablenkung von Myonen durch das Erdmagnetfeld verursacht. Diese Effekte werden für Zenitwinkel größer 60° bedeutend. Der Bereich zwischen 60° und 80° macht $25\,\%$ der Apertur des Oberflächendetektors aus. Zwei Rekonstruktionsmethoden stehen für diesen Zenitwinkelbereich zur Verfügung.

Die Standardrekonstruktion, welche innerhalb der Pierre Auger Kollaboration für Zenitwinkel bis 60° benutzt wird, kann auch auf Schauer größerer Zenitwinkel angewendet werden. Die Methode basiert auf einem radialsymmetrischen Modell des Signals in den Wassercherenkovdetektoren. Eine empirische Bestimmung der Parameter des Modells wurde vorgenommen, mit welcher Verzerrungen der rekonstruierten Größen im gesamten Zenitwinkelbereich von 0° bis 68° von $8\,\%$ auf weniger als $4\,\%$ reduziert werden konnten. Im Bereich der höchsten Zenitwinkel ist die radiale Symmetrie des Energieeintrages des Schauers am Boden nicht erhalten. Basierend auf Monte-Carlo-Simulationen wurden Modelle der Myonenverteilung am Boden und des Beitrages der elektromagnetischen Komponente erstellt. Eine Rekonstruktion auf der Basis dieser zweidimensionalen Signalprofile wurde implementiert.

Beide Rekonstruktionsalgorithmen liefern einen Energieschätzer. Mit einer Kalibrationsprozedur wurde die Konversionsfunktion zwischen dem Energieschätzer und der Energie des Primärteilchens bestimmt. Als Referenzenergie diente hierbei die Messung der Primärteilchenenergie mit dem Fluoreszenzdetektor. Zwei verschiedene Kalibrationsmethoden wurden benutzt. Ein Vergleich der Energiebestimmungen mit beiden Rekonstruktionsmethoden und Kalibrationsmethoden wurde durchgeführt. Für Zenitwinkel von 60° bis 68° sind beide Rekonstruktionsmethoden in Energieauflösung und Abweichungen miteinander verträglich. Bei höheren Zenitwinkeln ist nur noch die Methode der zweidimensionalen Myonenprofile anwendbar.

Der Fluss ultrahochenergetischer kosmischer Strahlung wurde mit den jeweilig anwendbaren Methoden im Bereich von 60° bis 80° mittels der zweidimensionalen Rekonstruktion und von 60° bis 68° mit der radialsymmetrischen Rekonstruktion bestimmt. Die Flussunterdrückung bei höchsten Energien, welche mit Schauern geringeren Zenitwinkels am Pierre Auger Observatorium gemessen wurde, konnte bestätigt werden. Im Überlappbereich der beiden Methoden bei Zenitwinkeln von 60° bis 68° stimmen die mit den beiden Methoden gewonnen Spektren sehr gut überein.

Contents

Introduction **1**

1 Ultra High Energy Cosmic Rays **3**

1.1 Cosmic Ray Flux 3

1.2 Extensive Air Showers 10

2 The Pierre Auger Observatory **15**

2.1 The Fluorescence Detector 16

2.2 The Surface Detector 19

3 Event Reconstruction **25**

3.1 Surface Detector Reconstruction 25

3.2 Shower Size Determination For Low And Moderate Zenith Angles 34

3.3 Fine Tuning of the LDF parameterisation 36

3.4 Shower Size Determination For Moderate And High Zenith Angles 51

3.5 Fluorescence Detector Reconstruction 61

4 Comparison of the Surface Detector Energy Determination **69**

4.1 Event Selection and Data Sets 69

4.2 Validating the Energy Estimator 73

4.3 Calibration 81

4.4 Results and Comparison 95

5 Comparison of Reconstruction Methods **101**

5.1 Geometry 101

5.2 Energy Resolution 105

6 Energy Spectrum **117**

6.1 Acceptance Calculation 117

6.2 The cosmic ray spectrum with inclined shower data 122

Summary and Conclusion **129**

Acknowledgement **147**

A Monte Carlo set **v**

B Calibration **vii**

Introduction

Humanity's curiosity has always been attracted by the borders of what humans could reach at their time. There are two fundamental symbols of both the limit of our scope and the way beyond this boundary: On the one hand the clear sky in the night unveiling more and more stars when the eyes adapt. Stars that are visible but out of reach for our hands. On the other hand there ist the horizon: Much more likely to be blurred by fog and clouds or inaccessible because of obstacles for our exploration but still easier to reach.

In the tradition of science the different fields of scientific research have been dominated by the one or the other symbol of the limits of accessibility. Geography for example has reached for the horizon where astronomy took the view to the skies. Very strikingly astronomy showed that human senses can be extended by tools. Telescopes gave access to fainter objects farther away. Fotography, spectroscopy and electronic sensors revealed the world of invisible frequencies from the giant wavelengths of radio up to the giant frequencies of gamma radiation. But still astronomy and astrophysics had new frontiers: Other particles like neutrinos and hadrons reach the earth from space and give complementary information to what light can tell. Again the way of exploring those other messengers was the view up to the sky. The first approaches of detection of other messengers than light lacked the fundamental feature of astronomy: information about the incoming direction. Different from the detection of light neutrinos and highly energetic hadrons are detected using their interactions with matter of the earth in case of neutrinos or its atmosphere in case of hadrons and nuclei respectively. Here again especially for hadrons and nuclei detection techniques and methods of reconstruction worked optimally for only a part of the sky centered at the zenith. Within this restricted field of view the features of cosmic rays have been explored giving hints on their yet unclear origin. Together with other messengers of astronomy the investigation of cosmic rays gives hints not only on their sources but also on other phenomena between the sources and the observers on Earth. Over the course of the last four decades new techniques extending the field of view closer to the horizon have been developed. A more detailed view on hadronic cosmic rays and their detection is given in chapter 1. The largest experiment in that field is the Pierre Auger Observatory combining successful detection techniques that feature detection of hadronic cosmic rays in a very large range of zenith angles. The experimental setup is described in chapter 2.

But as obstacles, clouds and fog can hide the horizon from the human eye a much thicker layer of atmosphere rises the complication in interpreting the signature of hadronic cosmic rays coming from close to the horizon. Hence not only different detector types require different methods to reconstruct the physics data. Also the view close to the horizon has to be treated differently than the view up to the sky. The reconstruction methods accounting for all this are introduced in chapter 3. Also improvements to the reconstruction methods in the context of this work are shown there. The determination of relevant physics data from those methods is performed in chapter 4. Sticking with

the picture of the horizon and the view to the clear sky of course it has to be made sure that what is seen in both ranges can be compared. Chapter 5 deals with comparisons of different methods in order to ensure the possibility to combine the two parts of the field of view. Finally the flux of hadronic cosmic rays using very inclined events of the Pierre Auger Observatory is presented and compared to other results in chapter 6.

Chapter 1

Ultra High Energy Cosmic Rays

Only a few years after the discovery of radioactivity, non-terrestrial radiation was detected by Victor Hess in 1912. In almost one century cosmic rays have been investigated both as probes for particle physics and as messengers from space. Enormous progress has been made in both measuring the interactions of high energetic charged particles with the atmosphere and the characteristics of the particles arriving at the top of the atmosphere. Some measurements of the cosmic ray flux as a function of energy referred as the energy spectrum of cosmic rays are compiled in figure 1.1. An overview of the current knowledge of high energy cosmic rays is given in section 1.1 including models that describe the flux over the whole energy range above $10^{15}\,\mathrm{eV}$ as it has been measured by various experiments.

The products of high energetic interaction of cosmic rays with nuclei of the atmosphere have been measured on ground and led to the discovery new particles for example the positron in 1931 [15]. The mechanism of cascades of interaction producing a large number of secondary particles has been verified by coincident measurement of radiation in seperate and distant detectors at varying distance by Pierre Auger in 1938. The observation of such extensive air showers gives an indirect measure of the arrival direction, the energy and other characteristics of the primary particle without actually measuring the primary in space above the top of the atmosphere. In section 1.2 the characteristics of extensive air showers are described. Especially for the rare particles of high and highest energies measurements using extensive air showers are the only way to establish a detection area large enough to collect enough statistics for analyses of the properties of these highest energetic particles ever measured.

With the experiments of AGASA [182] and HiRes Fly's Eye [49] two successful techniques for the detection of ultra high energetic cosmic rays gave different results in both the shape of the energy spectrum and first anisotropy studies of the arrival direction of cosmic rays of extreme energies. Both results pointed on different features of ultra high energy cosmic rays but did not confirm each other.

1.1 Cosmic Ray Flux

The energy spectrum as shown in figure 1.1 of cosmic rays can be described by a steeply falling power law spanning over ten decades in energy and thirty decades in flux. Few changes of the power law index are the only features of the spectrum. Those features occur at high energies and therefore low

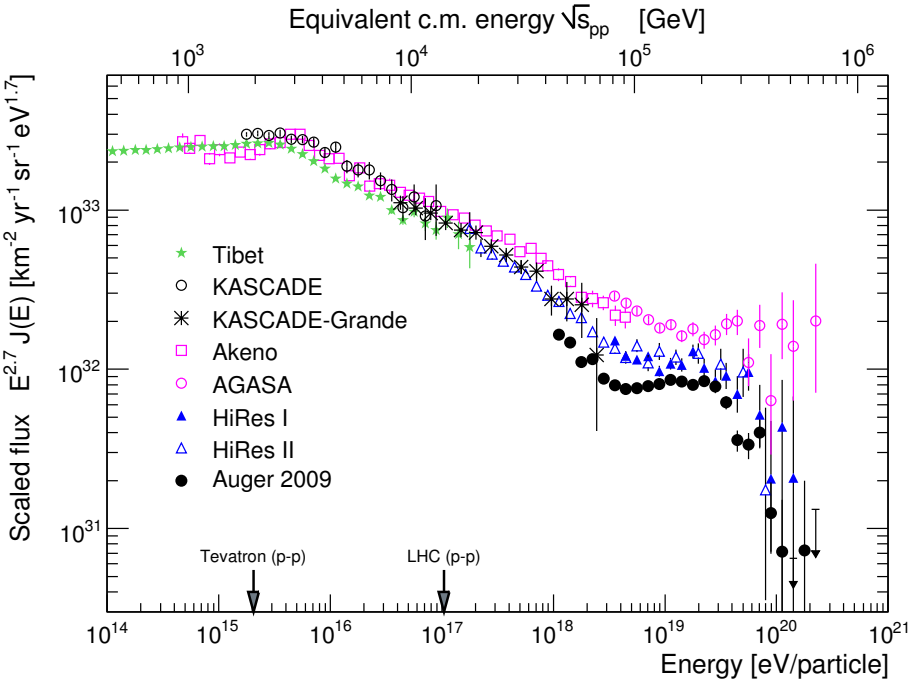

Figure 1.1: The cosmic ray flux versus the particle energy. In the steeply falling power law spectrum only a few features are observed [3, 4, 17, 49, 79, 107, 155, 182].

fluxes so that for a precise measurement of the features only indirect observation via detection of extensive air showers is possible.

From the power law shape of the spectrum the candidate for an acceleration mechanism is Fermi acceleration [98]. The engine of the mechanism are shock fronts propagating through the medium faster than the speed of sound within a magnetic field. In this environment particles cross the shock several times as they are deflected by the magnetic field gaining energy at every time they cross the shock. The probability to escape the magnetic containment rises with energy giving a power law spectrum. A superposition of the fluxes accelerated by multiple sources of Fermi acceleration with different maximum energies can explain the cosmic rays spectrum qualitatively [122].

The remaining question are the sites of acceleration. In the Hillas diagram [121] as shown in figure 1.2. The maximum energy is given by the size and the magnetic field of the acceleration region

$$E_{max} \sim L \cdot B \cdot Z \cdot \Gamma \tag{1.1.1}$$

with a characteristic length of the acceleration region L, the magnetic field B and the charge of the accelerated particles Z. For shocks fronts moving at relativistic speed the relativistic factor Γ plays a role. Within the galaxy possible sitesof acceleration are pulsars and supernova remnants. For the highest energies radio galaxies, galaxy clusters, gamma ray bursts and active galactic nuclei have enough acceleration potential according to equation 1.1.1.

Active galactic nuclei are one of the candidate sites for Fermi acceleration to highest energies. An AGN is a supermassive black hole in the centers of galaxie. Permanent accretion of mass from the vicinity creates relativistic jets of matter ejected at the poles of the black hole. Shock fronts

are created near the black hole as well as in *hot spots* where the jet hits a cloud of intergalactic matter. Through observations of the maximum energy in the emission spectra of electrons in AGN the expected maximum energy for hadron acceleration is estimated to be $E = 1000\,\mathrm{EeV}$. So besides other astrophysical objects AGN are candidates for acceleration of extragalactic cosmic rays up to the highest energies. As AGN are tracers of the matter distribution in the universe other astrophysical objects remain candidates for cosmic ray acceleration.

High Energy Cosmic Rays

The region of high energy cosmic rays extends from $10^{15}\,\mathrm{eV}$ until about $10^{18}\,\mathrm{eV}$. The prominent feature in this region is the *knee* of the spectrum that is clearly visible in the measurements shown in figure 1.1. This steepening from a spectral index of $\gamma \approx 2.7$ to $\gamma \approx 3.1$ happens at $E \approx 3 \cdot 10^{15}\,\mathrm{eV}$ [130]. Measurements indicate the knee to be not only a kink in the power law spectrum but also a phenomenon visible in mass composition [188]: Above $3 \cdot 10^{15}\,\mathrm{eV}$ the contribution of protons to the total flux is dropping and subsequently the contribution of Helium and other lighter nuclei falls off. The energy threshold for the drop of the flux contribution rises with the nuclei getting heavier and having larger electric charges. Several mechanisms are suggested for this behaviour:

- Fermi acceleration in the sources of high energy cosmic rays is charge dependent as shown in equation 1.1.1. A heavier composition together with a softer spectrum indicate the maximum energy E_{max} to be comparable to the position of the knee for protons. In this case the cut-off energies for nuclei are proportional to their charge Z [85].
- A change in hadronic interactions above some PeV is possible, producing new invisible particles. According to this assumption the fall-off of different nuclei scales with the nuclear mass A [86, 150]. As LHC [90] cuts into this regions of interaction energy, a conclusion on this model can be expected soon.
- High energy cosmic rays are contained in the galaxy magnetically. Due to diffusion effects in the complex structure of the galactic magnetic field a mechanism has been suggested [58, 188] how protons of PeV energies could escape the magnetic confinement with larger probability than lower energy protons. The effect scales with E/Z, so the fall-off energy of other elements is $E^Z_{falloff} = Z \cdot E^p_{falloff}$.

The scaling of the fall-off energies of the components heavier than protons has not yet been identified to be clearly proportional to atomic mass A or charge Z. Above the knee the composition of cosmic rays grows heavier with increasing energy up to $E \approx 100\,\mathrm{PeV}$. Observations also indicate another steepening of the spectrum at these energies [3, 49, 81] that is called the *second knee*. Experiments like KASCADE-Grande [113], IceTop [100], the Telescope Array Low Energy extension TALE [187] and the low energy extensions of the Pierre Auger Observatory HEAT [129] and AMIGA [88, 89] will clarify the experimental situation. Depending on the model for highest energy cosmic rays the transition from galactic to extragalactic cosmic rays happens at $100\,\mathrm{PeV}$ or a few EeV.

For energies up to $10^{15}\,\mathrm{eV}$ the non-relativistic shock fronts caused by supernovae are a strong candidate for the acceleration region for protons [102]. Heavier nuclei might even be accelerated to much higher energies and explain the cosmic ray flux up to the energies of the second knee. Observations of high energy gamma rays [6] proved acceleration of electrons in supernova remnants

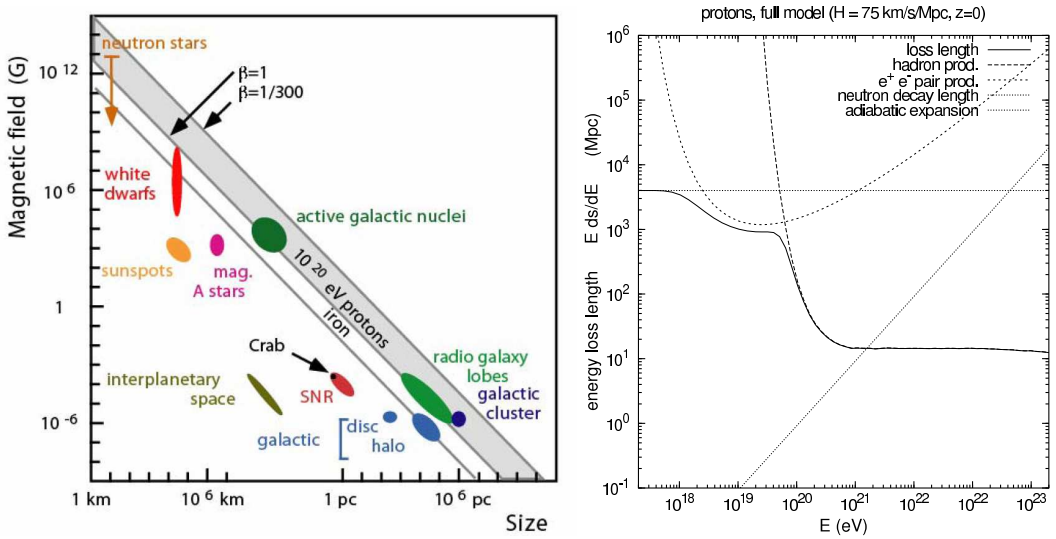

Figure 1.2: Left panel: The Hillas diagram [121] relates the size and the magnetic field of potential accelerators with their acceleration power e.g. the maximum energy the source can accelerate particles to. Right panel: The average path length of cosmic ray particles before energy loss in the intergalactic medium due to different processes [177].

but acceleration of hadrons has not been proven so far. For the energies above the second knee an extragalactic origin is discussed in the following section. Also a reacceleration of galactic cosmic rays has been suggested [40]. Backtracing high energy cosmic rays to their sources by detecting their incoming direction is not possible. The particles are confined to the galaxy by the galactic magnetic field up to energies of $E \approx 10^{15}\,\mathrm{eV}$ depending on their mass or charge [174]. The particles propagate for more than $10^6\,\mathrm{yr}$ through the inhomogeneous galactic magnetic field. Therefore the arrival direction of high energy cosmic rays does not point back to the source.

Ultrahigh Energy Cosmic Rays

At the highest energies the cosmic ray flux as shown in figure 1.3 has the two dominant features of a flattening of the spectrum called the ankle and of the flux suppression at the high energetic end of the spectrum. According to present models extragalactic cosmic rays dominate at these energies and the flux suppression at the end of the spectrum is a feature of extragalactic cosmic rays [41, 42, 69, 122, 202]. The models for the second knee and the ankle differ in the transition energy from galactic to extragalactic energies. Either model to explain the features of the flux suppression and the ankle respectively are connected with predictions of the evolution of the mass composition of highest energy cosmic rays and in case of the flux suppression predictions about anisotropies in the arrival direction.

The transition model suggests the transition from galactic to extragalactic cosmic rays at the ankle. The flux at the energy of the ankle requires a relatively hard spectrum with $\gamma = 2.6$ for extragalactic cosmic rays. The steeply falling spectrum of the galactic cosmic rays and the extragalacitc component having equal contributions to the flux defines the position of the ankle. The steeply falling spectra of galactic cosmic rays are not sufficient to explain the position of the ankle. Another component is necessary to explain the spectrum between the second knee and the

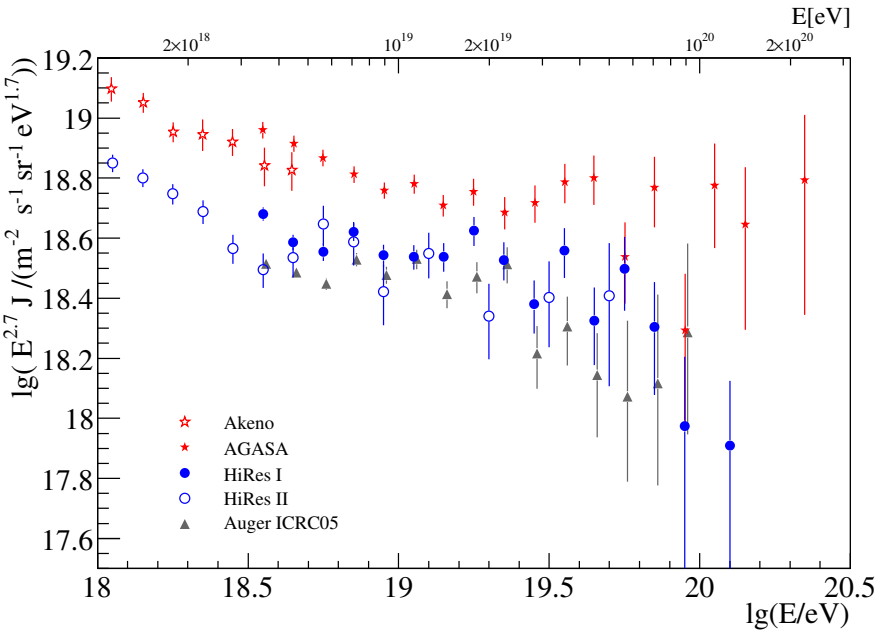

Figure 1.3: The cosmic ray flux versus the particle energy at highest energies. The kink at $E \approx 5\,\mathrm{EeV}$ is called the ankle. It is visible in all measurements. Above $E = 40\,\mathrm{EeV}$ a flux suppression is observed by the HiRes and Auger experiments [4, 49, 178, 182].

ankle [40]. Scenarios assuming the ankle at the transition point with pure protonic extragalactic component [69, 122, 202] and mixed composition of the extragalactic component [9, 10] as in figure 1.4, left panel are possible. Photodisintegration of nuclei heavier than protons is assumed to happen above $10\,\mathrm{EeV}$ in case of a mixed extragalactic component leaving basically only protons and an iron contribution depending on the composition at the acceleration site [7].

The dip model assumes an extragalactic component of only protons [41, 42]. These protons start to dominate the flux above $0.5\,\mathrm{EeV}$. The very steeply falling galactic cosmic ray flux above the fall off of the galactic iron is compensated for by the extragalactic protons with a much harder spectrum. In this model the shape of the extragalactic flux is a pure propagation effect in this model resulting in a hardening of the spectrum at the plateau of the energy loss through pair production as illustrated by the mean free path lengths as a function of energy in figure 1.2, left panel. This hardening of the spectrum is the ankle as demonstrated in figure 1.4, right panel.

In the current knowledge the flux suppression above $5 \cdot 10^{19}\,\mathrm{eV}$ marks the end of the cosmic ray spectrum. Basically two processes are discussed to cause the flux suppression. The experimental situation is characterised by low statistics and large systematic uncertainties as the expected flux is as low as $1\,[\mathrm{km^2\ sr\ yr}]^{-1}$ at $100\,\mathrm{EeV}$. Despite of the results of the AGASA experiment [182] that do not indicate a flux suppression the results of the HiRes experiment [4, 49] hints on the presence of a flux suppression. This feature has been verified with more than 5σ by the Pierre Auger Observatory [2]. Two possible explanations for this feature are a maximum energy of the sources of ultra high energy cosmic rays at about the energy of the feature or the Greisen-Zatsepin-Kuz'min (GZK) process [106, 203]. The latter is an energy loss process due to the interaction of ultra high energy cosmic rays with the photons of the cosmic microwave background. Due to the extreme energy of the cosmic ray

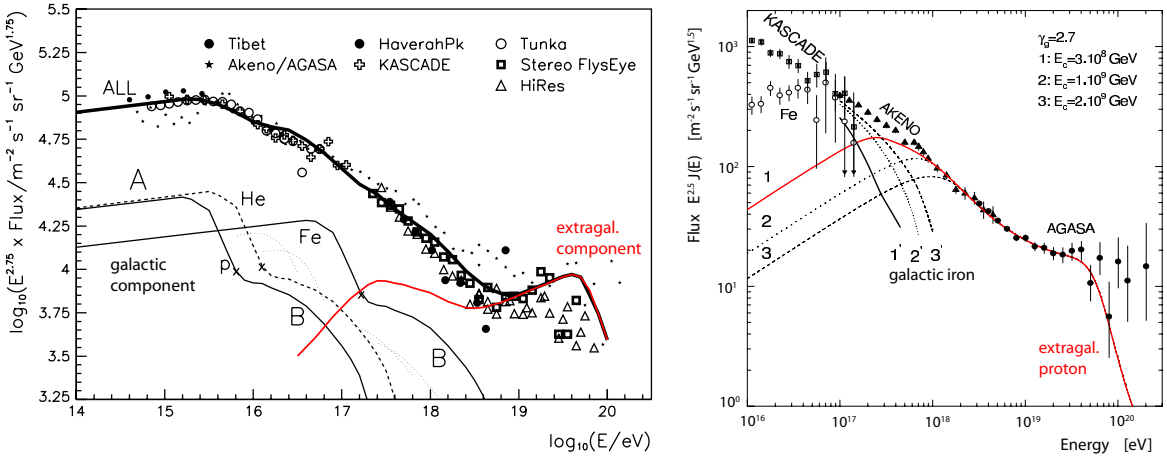

Figure 1.4: Two models that can explain the structure of the spectrum of the highest energy cosmic rays. Left panel: The ankle model with a transition from galactic to extragalactic cosmic rays at the ankle [122]. Right panel: The dip model with a transition from galactic cosmic rays to extragalactic protons at energies slightly above the second knee [41].

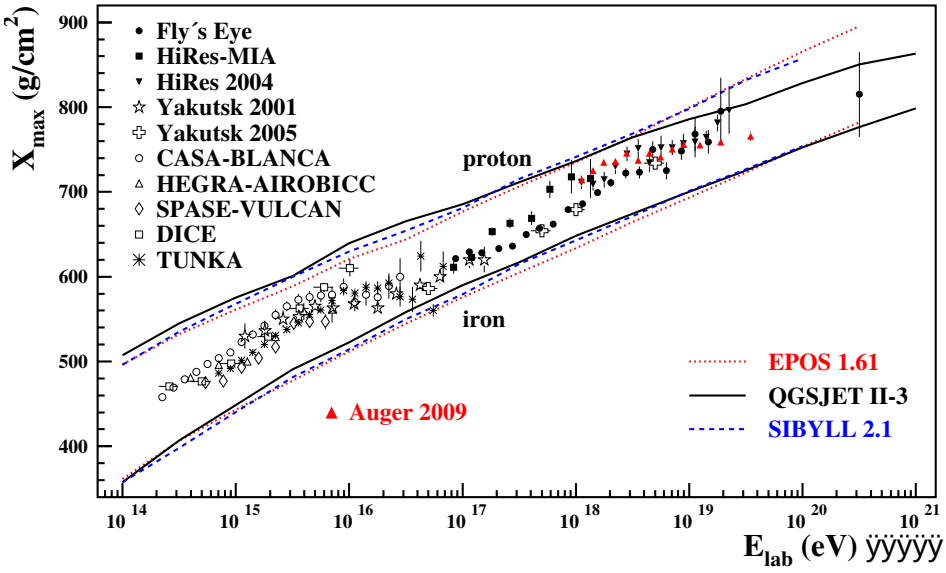

Figure 1.5: The atmospheric depth of the shower maximum as a measure of the primary mass. The lines show the expectations for protons or iron. The experimental situation is not conclusive yet as the measurements differ significantly for different experiments [38].

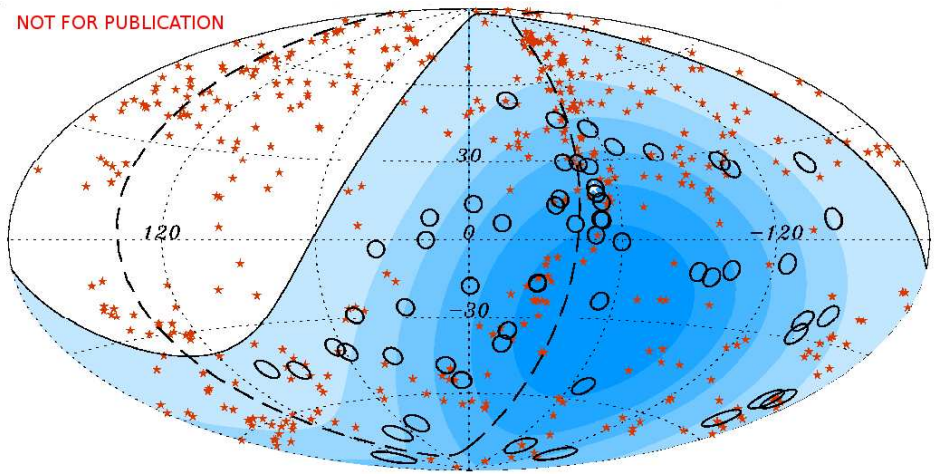

Figure 1.6: An update of the high energy events measured by the Pierre Auger Observatory [1, 110] with energies above $E > 56\,\mathrm{EeV}$ superimposed with nearby active galactic nuclei from the Veron-Cetty catalogue. The circles show an angular distance of 3.1° between the source and the incoming direction of the partcle, containing angular resolution and estimated deflection of the particle.

particles the background photons are blueshifted in the rest frame of the proton. Hence for energies above $E \approx 50\,\mathrm{EeV}$ a Δ resonance can be produced through $N + \gamma_{CMB} \rightarrow \Delta \rightarrow N + \pi$. The mean distance until the particles loses a significant fraction of its energy drops rapidly above the threshold for the GZK process as shown in figure 1.2, left panel and so the volume in that sources can contribute to the flux decreases dramatically.

Both the models explaining flux suppression and the ankle predict not only the shape of the flux suppression but also the mass composition of ultra high energy cosmic rays as a function of energy. Up to now the shape of the spectrum and the analysis of the shower maximum as a parameter sensitive to the shower maximum [193] do not clearly prefer one of the models despite the latter indicates a heavier composition at highest energy as shown figure 1.5. As the dip model predicts protons at highest energies the transition model is preferred by this data as it allows for heavy nuclei in highest energy cosmic rays.

Cosmic rays of highest energies propagate through the intergalactic and galactic magnetic field. At highest energies the dominant deflection in the galactic magnetic field of $\approx 3\,\mu\mathrm{G}$ becomes relatively low. The intergalactic magnetic field is assumed to be two to three orders of magnitude lower than the galactic magnetic field. The deflection of ultra high energy cosmic rays in the intergalactic field also depends on the propagation distance so that the deflection outside the galaxy can be comparable to the deflection in th galactic magnetic field. So at $40\,\mathrm{EeV}$ the deflection of protons from nearby sources is in the order of 5° or less [62, 132, 148]. Combined with the free path length for these particles of a few Mpc due to the GZK effect a visible asymmetry of the arrival directions of the highest energetic cosmic rays is expected under the assumption of non-diffuse sources. As shown in figure 1.6 the arrival directions of the highest energetic events measured by the Pierre Auger Observatory have been found to be correlated to close-by active galactic nuclei [1].

The correlation of events measured by the Pierre Observatory with AGN closer than $75\,\mathrm{Mpc}$ within 3.1° has been found only for events with more than $E = 56\,\mathrm{EeV}$. At lower energies no small scale anisotropy has been observed.

1.2 Extensive Air Showers

To cosmic rays Earth's atmosphere acts like a beam dump or a calorimeter. The particles interact with the molecules of the air and the collisions produce secondary particles. If the secondary particles carry enough energy theis interactions result in further particle multiplication. At primary energies of $E > 10^{15}\,\mathrm{eV}$ many generations of secondaries are produced building up a cascade. At energies $E = 10^{19}\,\mathrm{eV}$ the number of produced particles in the first interaction is of the order of 100 [83]. Non-central collisions and Fermi motion of quarks in nucleons result in transversal momentum and so the secondaries drift away from the original incoming direction of the primary particle. As the particles travel with a speed close to the speed of light an extended, $1\,\mathrm{m}$ thick disc of secondaries propagates through the atmosphere forming an *extensive air shower*. Both the particles as well as their trace of exited molecules the atmosphere can be measured at ground. This allows to detect cosmic rays at ground and with detectors that cover only a small fraction of the full detection area.

The first interaction of a cosmic ray particle is a collision with an atmospheric nucleus. In this collision baryons, mesons and nuclear fragments are produced. Pions make up the largest fraction of the secondaries. Secondary hadrons either reinteract or decay. Decay of these secondary hadrons fuels the electromagnetic component via almost immediate decay of neutral pions π^0 and the muonic component via decay of charged pions $\pi^\pm$ at the end of the hadronic cascade respectively. Further collisions of the produced hadrons with air nuclei carry on the hadronic cascade.

The hadronic component is produced by collisions of shower hadrons and air molecules. The most particles that are produced are pions ($\pi^\pm$, π^0) as they are the lightest hadrons. Also neutrons, protons and kaons ($K^\pm$, K^0) contribute to the particle content of the hadronic cascade. In a very simple Heitler model [146] the hadronic cascade can be approximated by each hadronic interaction producing an energy dependent number m of pions with one $m/3$ of them being neutral pions π^0. The charged pions continue the hadronic cascade with particle production in subsequent hadronic interaction while the neutral pions decay into two photons γ that fuel the electromagnetic cascade. The energy of the interaction is assumed to be distributed equally to the three pions. As soon as the energy of the charged pions falls below a critical energy $E_c \approx 20\,\mathrm{GeV}$ [14] the mean free path length gets longer than the decay length and the hadronic cascades vanishes fueling the muonic component. The charged pion number at the end of the cascade is proportional to E/E_c^α with $\alpha \approx 0.9$. Less than $1\,\%$ of the primary energy reaches the ground carried by hadrons. These hadrons are mostly neutrons.

In this simple model, the fragmentation and higher crosssection of primaries heavier than protons is modelled as the superposition of A protons with the number of nucleons A in the primary.

The muonic component carries about $10\,\%$ of the shower energy reflecting the fraction of the energy in pions at the end of the hadronic cascade. In air shower simulations the fraction of energy carried by muons depends on the hadronic interaction model [25, 27, 201], the energy and the primary mass. Muons are the most penetrating particles that can be detected efficiently on the ground level. They suffer relatively low attenuation through energy loss processes or decay. The decay length of a $10\,\mathrm{GeV}$ muon is $66\,\mathrm{km}$ resulting in a large fraction of air shower muons reaching ground for zenith angles less than $80°$. Also air shower muons of an energy range of $0.5\,\mathrm{GeV} < E_\mu < 500\,\mathrm{GeV}$ are minimally ionising particles (figure 1.7) having only a small energy loss of about $3\,\mathrm{MeV\ g^{-1}cm^2}$ through ionisation. At muon energies of $500\,\mathrm{GeV}$ Bremsstrahlung, pair productions and hadronic

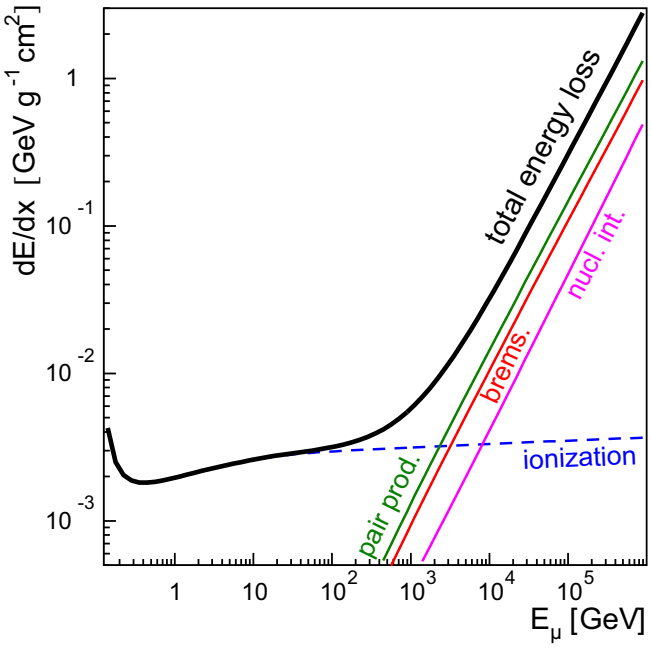

Figure 1.7: The energy loss of muons in air as a function of the particle energy [71, 160].

interaction become significant sources of energy loss. As the critical energy for pion decay is larger in the thinner upper atmosphere very inclined air showers produce muons with higher average energy so that energy loss through the latter effects becomes important at about $80°$ [71].

The divergence of the muons from the shower axis is generated by several effects. Multiple scattering on the Coulomb potential of the air molecules results in an average deflection angle of

$$\langle \alpha^2 \rangle \sim \left(\frac{1}{m\gamma\beta^2} \right)^2 \tag{1.2.1}$$

with the muon mass m and the relativistic factors γ and β [116, 160]. For energetic heavy particles like air shower muons the deflection is dominant only above zenith angles $\theta = 80°$ [77]. Travelling through the atmosphere with a long path length the magnetic deflection of charged particles in the geomagnetic fields becomes an important effect at high zenith angles $\theta > 80°$. Depending on the orientation of the shower with respect to the magnetic field vector the component of the magnetic field perpendicular to the path of the shower particles B_T varies between zero and the full field strength of the field. This introduces an azimuthal dependency of the deflection effect. The deflection can be approximated with [28, 30]

$$\Delta x \sim \frac{B_T d^2}{E_\mu} \tag{1.2.2}$$

with the distance d the muon from its point of production and the muon energy E_μ. With the site of the Pierre Auger Observatory as an example the deviation from a straight line with the maximum perpendicular field of B_T is in the order of $50\,\mathrm{m}$ for travelling distances of $10\,\mathrm{km}$ equivalent to a shower with a zenith angle of $60°$. For showers of $80°$ the travelling distance increases up to $66\,\mathrm{km}$

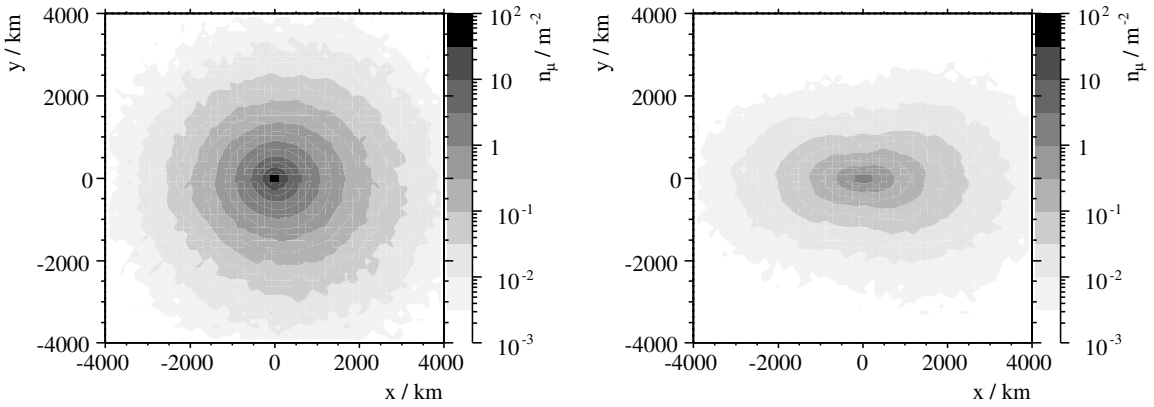

Figure 1.8: The muon density in the shower front as a function of distance from the axis and angle to the projection of the incoming direction on the ground. In the left panel the perpendicular magnetic field is very low, the zenith angle is $60°$*. In the right panel a magnetic field of* $25\,\mu$G *orthogonal to the incoming direction distorts the radial symmetry of a* $80°$ *shower [71].*

and the deflection becomes significant $1.6\,\mathrm{km}$ with respect to the shape of the muonic footprint of the shower without deflection with its muon density reduced to less than $1\,\%$ at $2\,\mathrm{km}$ from the impact point. The muonic lateral profile is distorted from its simple radially symmetric shape by this effect as μ^+ and μ^- are deflected in opposite directions as illustrated in figure 1.8.

Apart from the geomagnetic effects also the evolution of the shower affects the pattern of muon densities seen on the ground. Within the shower disc the lateral shape becomes flatter and broader with propagation through the atmosphere. For inclined showers the difference in path length and therefore in dispersion of the shower disc is significantly different for the early part hitting the ground before the virtual impact point of the primary and the late part. At $60°$ the effect is below $2\,\%$ but at $80°$ the densities in the early part shows $10\,\%$ higher densities than the impact point and regions of equal muonic path length where the late part is attenuated by another $10\,\%$ just by geometric effects.

Moreover the muons have a relatively flat lateral distribution. The muonic component is dominant especially at distances far from the core where the contribution of electromagnetic particles from pion decay is low or after the electromagnetic component is extinct after long propagation through the atmosphere e.g. for showers with large inclinations.

The electromagnetic component is generated by photons produced in π^0 decay. In the electromagnetic cascade particle multiplication by production of an e^+e^- pair by a photon interacting with a nucleus and photon production by $e^\pm$ through Bremsstrahlung is the dominating process until ionisation energy loss dominates and the cascade dies out because of energy loss. The critical energy E_c where ionisation becomes the dominant process determines the number of particles produced by an initiating particle of $E > E_c$. In the simple Heitler model [146] each particle with an energy larger than E_c is assumed to produce two particles of equal energy after a splitting length $\lambda = X_0 \ln 2$. The radiation length is the depth after which the particle has lost half of its energy. For air it is $X_0 = 37\,\mathrm{g\ cm^{-2}}$. After reaching the critical energy particle multiplication ends and the particles start to be absorbed by ionisation energy loss. The maximum particle number in this simple model is 2^n with $n = (\ln E - \ln E_c)/\ln 2$ and the denominator reflecting the number of particles produced. The shower maximum is reached after a depth proportional to $X_{max} \sim n\lambda \sim \ln E$ with

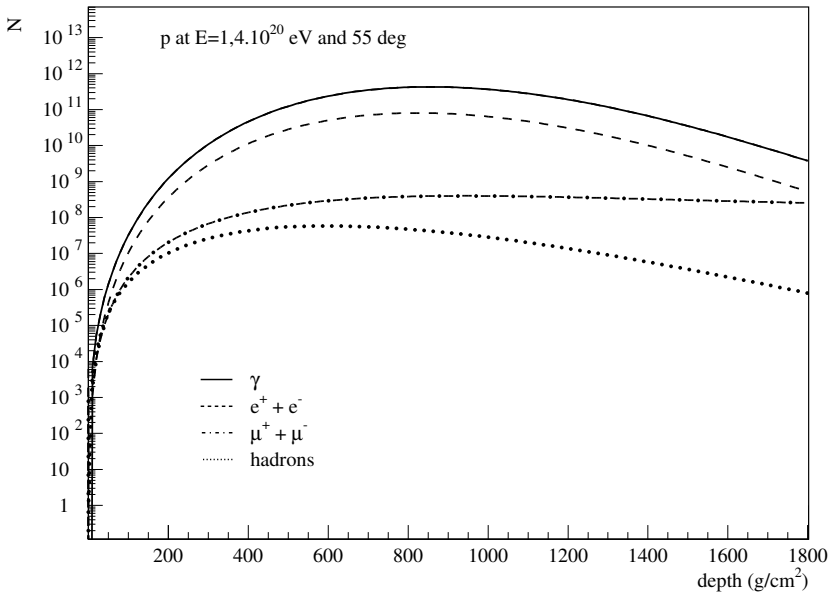

Figure 1.9: The particle content of an extensive air shower as a function of traversed atmospheric depth [140] simulated with CONEX [43].

a number of particles proportional to E. An exact solution of the problem starting with one electron or photon was found by Nishimura, Kamata and Greisen [124, 127, 167]. In an air shower caused by a hadron various electromagnetic subshowers are produced. The lateral shape of the superposition of many electromagnetic showers and the muonic shape can be approximated by a redefinition of the parameters of the shape of a purely electromagnetic shower as found by Nishimura, Kamata and Greisen [16].

The Electromagnetic Component of the signal in the surface detector for a very inclined shower consists of two main contributions. For showers at zenith angles $\theta < 70^\circ$ the electromagnetic cascade produced by hadron decay is not yet completely attenuated. As the elongated profile of an inclined air shower is also a projection of different shower ages this part is highly asymmetrical and concentrated in the earlier region next to the axis [195]. The second contribution visible at all zenith angles is the electromagnetic halo. These photons and electrons are produced by muon decay, Bremsstrahlung, pair production and hadronic interactions [160].

The muonic halo is the simpler part of the electromagnetic correction as it depends on local variables like muon density and also muon energy that roughly follows the shape of the muon density profile [195]. Basically the contribution of the halo is radially symmetric and depends most significantly on the zenith angle as the muon spectrum gets harder with increasing shower age. Above $\theta \approx 80^\circ$ a significant fraction of the muons reaching the ground have very high energy $E > 200\,\mathrm{GeV}$ and can emit very high energetic halo photons causing subshowers and delta radiation. This effect increases not only the expected content of electromagnetically generated signal in the detector station but also its fluctuations [78].

For lower zenith angles the residual primary electromagnetic component has a large contribution to the electromagnetically generated fraction of the signal. Photons and electrons generated by the hadronic cascade are distributed closely around the axis and due to attenuation have an asymmetry with larger

signal contribution in the early part of the shower footprint. Especially very close to the axis the occurence of highly energetic electromagnetic particles causing subshowers in the water of a detector stations is possible. This leads to a similar rise of the signal and its variance as for the halo particles above $\theta \approx 80^{\circ}$.

The three components of the shower differ in their longitudinal development e.g. the atmopheric depth of the hadronic shower maximum is smaller than the maximum of the electromagnetic component as illustrated in figure 1.9. The longitudinal profile of the electromagnetic particles can be observed through fluorescence light. The electrons excite nitrogen molecules by collisions and the de-excitation happens partly via emission of fluorescence light in the UV band. The emission of fluorescence light is proportional to the energy deposit resulting in the possibility of a quasi-calorimetric measurement via detection of fluorescence light. Still some energy is carried away by muons and neutrinos. Thus the fluorescence light does not reflect the complete energy content of the shower. With simulations this *invisible energy* can be determined to be $\approx\ 2 - 7\,\%$ of the total energy in the range of $5 \cdot 10^{18}\,\mathrm{eV} < E < 10^{20}\,\mathrm{eV}$ [32, 161]. The longitudinal development also depends on the primary mass. With the Heitler model, the depth of the shower maximum is dependent on the mass of the primary particle e.g. a heavier primary starts a shower with a larger number of particles and through the superposition model with less fluctuations from shower to shower [111]. A comparison of the measured shower maximum from fluorescence measurements with simulated events allows to infer the average logarithm of the primary atomic mass $\langle \ln A \rangle \sim \langle X_{max} \rangle$ [193]. As the position of the shower maximum is also dependent on the energy $X_{max}\ \sim\ \ln E$ and in case of simulation dependent on the hadronic interaction model, comparisons with known mass of the primary and different hadronic interaction models are compared to the measured average shower maximum as a function of energy.

Chapter 2

The Pierre Auger Observatory

The Pierre Auger Observatory is the cosmic ray detector with the largest detection area of $3000\,\mathrm{km}^2$ and a combination of two detection techniques: Detection of flourescence light and detection of the particles at ground with water Cherenkov detectors [63]. The latter technique has successfully been applied at the Haverah Park detector [133]. A visual impression of both systems is given in figure 2.2. Measuring the same showers with two complementary detection techniques promises not only to resolve the mystery of disagreeing measurements but also offers synergy effects to improve detection beyond just combining two different methods.

The fluorescence detector is described in detail in section 2.1 measures the light emission from nitrogen excitation by shower particles in the atmosphere. This quasi-calorimetric measurement gives an almost simulation independent estimate of the primary energy. However detection of fluorescence light is dependent on low other light sources e.g. in moonless nights. Also the detection volume depends on the brightness of the shower so that the aperture of a fluorescence detector is energy dependent.

The surface detector is explained in section 2.2. Its well-defined size on ground and the stable performance independet of external light sources provide a simulation independent acceptance and high statistics due to a duty cycle of almost $100\,\%$. The energy estimate from surface detector information depends on the relation of particle densities at ground and the primary energy. This relation can be inferred from simulation suffering dependencies on the models used in simulations.

With either the acceptance or the energy scale simulation dependent a combined detector can give results almost independent of simulation. But also compared to standalone components the availability of the other detector component adds a lot of information that improves the results beyond just comparison. The energy determination of the Surface Detector reconstruction uses the normalisation of the energy deposit in the shower footprint at ground. The relation of the normalisation to the primary energy has to be determined either by calibration with simulated showers or with the energy measurement by the fluorescence detector. Also mass dependent parameters as the shape of the signal in the Surface Detector station are less efficient than the Fluorescence Detector measurements. Anyway the Surface Detector has a dury cycle of close to $100\,\%$ and its acceptance is purely geometric above the threshold of full trigger efficiency. Together with hybrid calibration using Fluorescence Detector measurement a robust and almost simulation indepenendent estimate of the shower primary is possible. The two components give complementary information that can be combined at reconstruction level to break degeneracies as a *hybrid detector* and offering possibilites

beyond two standalone components with separate analyses as is described in section 3.5 and chapter 4.

In the domain of UHECR and suggested by AGASA results [186] an anisotropy of cosmic ray arrival at earth is expected. Thus observation on the northern and the southern hemisphere respectively is required as the distribution of galaxies and mass is different. The Pierre Auger Observatory therefore consists of the planned northern observatory in Lamar/CO/USA and the southern observatory in Malargüe/Mendoza/Argentina that has been completed end 2008. A map of the complete setup of the southern observatory is given in figure 2.1. With the analyses of this work based upon data of the southern observatory the detector description is focused on this setup. The northern observatory will complete the full sky coverage of the Pierre Auger Observatory starting in 2011.

Since 2004 data taking at the southern site has provided $12723\,\mathrm{km^2 sry}$ of air shower data allowing tremendous physics results. A collection of results is sketched below to set the analyses presented in this work the context of the achievements of the Pierre Auger Collaboration of about 350 scientists in more than ten countries.

2.1 The Fluorescence Detector

The Fluorescence detector consists of 24 telescopes with Schmidt optics [147] arranged in four buildings at the borders of the array. Six telescopes per building with a field of view of $30^\circ \times 29^\circ$ result in 180° in azimuth overviewing the complete array and 29° of elevation.

The fluorescence measurement gives a very good, quasi-calorimetric estimate of the shower energy and also provides the longitudinal profile of the shower with parameters that allow to determine the mass of the primary particle of the shower. The measurement is restricted to dark nights without moonlight shining directly into the telescopes. This restricts the Fluorescence Detector to a duty cycle of $\approx 13\,\%$. Also the distance a shower can be measured in depends on the shower energy as brighter showers can be seen farther away where fainter low energy showers can only be detected close to the telescope.

Arriving at the telescope from the left in figure 2.3 the light is filtered by a Schott M-GU6 filter that is transparent only in the close UV. As fluorescence light is emitted in this band the filtering reduces the noise generated by other light sources. The Schmidt optics consist of a $3.8\,\mathrm{m}^2$ aperture with a ring-shaped corrector lense [57] at the outer part and a $12\,\mathrm{m}^2$ spherical mirror with a curvature radius of $3.4\,\mathrm{m}$. The corrector ring increases the possible light collection by correcting for spherical aberration. After crossing the aperture and being focused by the mirror the light falls on a pixel camera with $22 \times 20 = 440$ pixels situated in the focal plane. Each pixel consists of a hexagonal photomultiplier Photonis XP-8062 of 1.5° size in the focal plane and its signal is sent via its electronic unit [56] to the analogue board for filtering and processing [19]. Each board controls 22 photomultipliers via programmable potentiometers and adjusts the time response and amplitude for uniform behaviour. The digital front end board of the camera hosts all analogue boards.

Data taking of the Fluorescence Detector is adjusted to variable noise rates. The charge values in the PMTs in the pixels are read out by FADCs in time bins of $100\,\mathrm{ns}$ and the recorded trace is optimised by an algorithm maximising the signal-to-noise ratio in a time window of $100\,\mu\mathrm{s}$. A signal-to-noise ratio of larger than 5 is required to accept the pixel for standard analyses. The timing of the signal is determined to be the centroid of the recorded trace. It is determined already on the level of data taking.

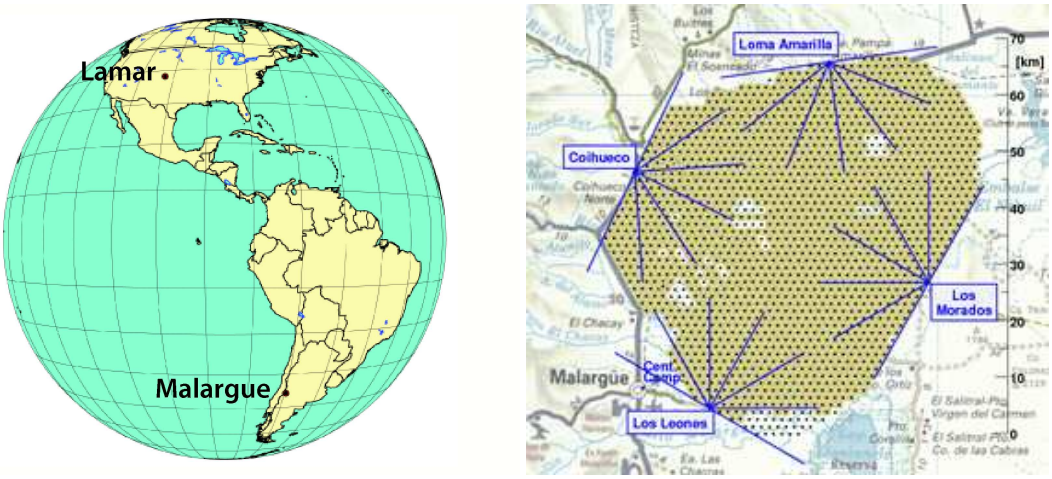

Figure 2.1: Left panel: The two sites of the Pierre Auger Observatory covering both hemispheres of the sky. The northern site in Lamar/CO/USA will be started in 2011 [84]. Right panel: The southern part of the Pierre Auger Observatory with the Surface Detector array and the Fluorescence Detector buildings at the edges. It is located near Malargüe/Mendoza/Argentina. The city is on the map south west of the experiment. The shaded area shows the size of the existing surface array with a solid point at each planned station position. The radial lines from the edges of the array represent the field of view of the fluorescence telescopes.

Figure 2.2: One unit of each of the two detector components of the Pierre Auger Observatory: A water Cherenkov detector station of the surface detector in the foreground an a Fluorescence Detector building containing six telescopes behind. Communication of the surface detectors with the central data acquisition works wireless and with the Fluorescence Detector buildings as relais stations, using the communications tower next to the building.

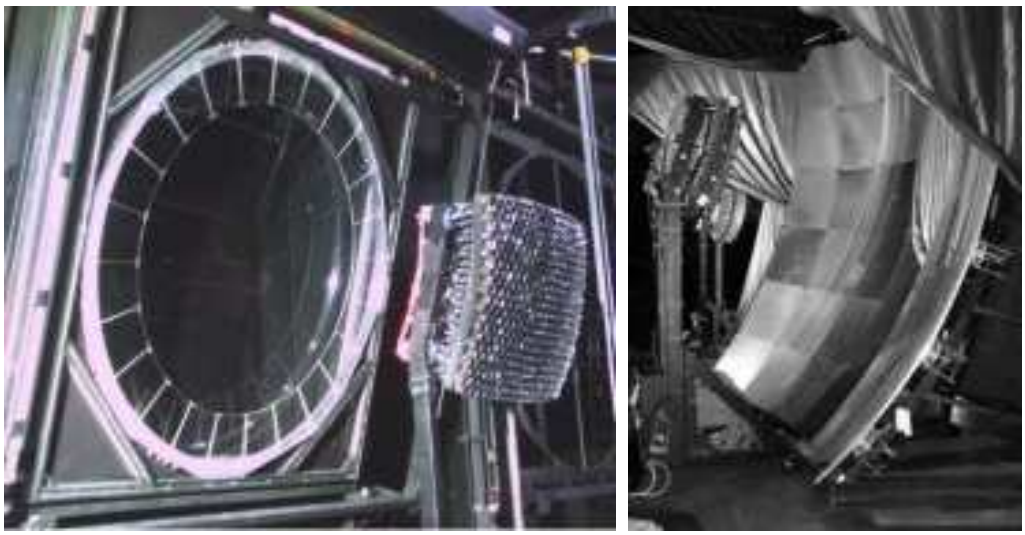

Figure 2.3: The Fluorescence Detector of the southern Pierre Auger Observatory consists of 24 fluorescence telescopes in 4 buildings at the edges of the Surface Detector array. In the left panel the aperture of one telescope with corrector ring and camera is shown. The right panel gives a view on the mirror and the camera.

The first level trigger is a simple threshold trigger for each pixel. For each pixel separately the trigger rate is kept on $100\,\mathrm{Hz}$ by adjusting the threshold. The signal-to-noise ratio in each pixel is reduced by integration over ten time bins resulting in an improvement of $\sqrt{10}$. The second level trigger requires a geometric pattern of four out of five neighbouring pixels within a time window of $20\,\mu\mathrm{s}$ and a time-ordered structure of the pattern [169]. This `T2` is not sent to the central data acquisition (CDAS) but recorded when external triggers by other Fluorescence Detector buildings or the Surface Detector occur. The rate of the pure pattern trigger that is implemented in the hardware is $0.1\,\mathrm{Hz}$. With the requirement of time structure implemented as a software condition the rate is reduced to $0.02\,\mathrm{Hz}$.

A `T3` trigger which is sent to the CDAS is calculated for the complete Fluorescence Detector building. A rudimentary event reconstruction is performed to ensure the compatibility with an extensive air shower. The result also provides the information for the central data acqusition for the read-out of corresponding Surface Detector stations. The status of the experimental setup is stored locally at the Fluorescence Detector building [33]. It provides performance data, calibration tests and operational data for monitoring of the Fluorescence Detector [166].

In order to reconstruct the data recorded by the data acquisition of the fluorescence detector knowledge about the production of the fluorescence light and its relation to the shower processes is required. The propagation processes of light through the atmosphere have to be considered as well as constant conditions of the data taking and a well defined relation of the measured signal to the incoming light intensity.

The fluorescence yield is an essential knowledge for the determination of the energy deposit at the shower track from the light detected at the fluorescence telescope. The yield relates the light emission to the deposited energy by electromagnetic particles. For reconstruction the Pierre Auger Observatory analysis uses the absolute value of the fluorescence yield measured by [149] and its relative dependencies on temperature, pressure and humitiy measured by [24]. Various other

measurements of the yield have been performed [24, 125, 149, 200]. Humidity and pressure at a given altitude vary with the weather conditions as well as the atmospheric density. Because of the dependency of both the shower development and the fluorescence yield on atmsopheric parameters the atmosphere is monitored. The monitoring program consists of a ballooning program with meteorolgical radiosondes [128] and ground based weather stations at the four Fluorescence Detector buildings and one more in the center of the array.

Light propagation through the atmosphere is influenced by scattering and absorption. Thus the opticical properties of the atmosphere are monitored as well. Light Detection and Rangings (LIDAR) systems are situated at each Fluorescence Detector building [39]. The principle of the LIDAR is to observe the backscattered light of a steerable UV laser using a photomultiplier. The timing and intensity of the backscattered light allows to resolve the aerosol content of the atmosphere along the laser path. Other measurements for crosschecks have benn performed by [164].

Detector calibration is performed by various systems: The absolute calibration of the signal in the telescopes is performed approximately every three months using a diffuse light source positioned directly in front of the aperture [37]. The stability of the telescopes is ensured by the relative calibration procedure that is run every night [18]. In addition point-like UV light sources have been positioned in the sky in the atmosphere in front of the telescopes for a more realistic calibration [158] giving a more detailed view on the light collection of the telescopes. The calibration of the fluorescence telescopes includes another laser system: The Central Laser Facility (CLF) [20]. With this system the angular resolution and alignment of the telescopes can be checked. Also the CLF is connected to a single Surface Detector station which gives the possibility to synchronise the timing of both detector components [11]. The CLF is also used for scattering measurements to determine the atmospheric light propagation properties.

2.2 The Surface Detector

The surface detector array consists of roughly 1600 water Cherenkov detectors in a triangular grid with $1500\,\mathrm{m}$ spacing resutling in an array of about $3000\,\mathrm{km}^2$. The detection is based on relativistic air shower particles creating Cherenkov radiation when propagating through an optical dense medium like water [60, 61, 133, 183]. A low energy extension with $750\,\mathrm{m}$ spacing and an area of $50\,\mathrm{km}^2$ is currently built up in front of the *HEAT* [129] site at the western edge of the array, using identical detector stations. Also buried muon detectors are planned for this area [88, 89]. In the context of the following analyses this description is focused on the standard array. The array is situated on a plane with less than $1\,\%$ average ground slope at about $1400\,\mathrm{m}$ above sea level. This ensures the shower age at ground to depend only on the zenith angle but not on the part of the array hit by the shower and gives a ground measurement close to the shower maximum of EeV air showers. The basic elements of the array are the detector stations that are constructed for autonomous operation in power supply, self-calibration and data taking. A single detector unit is shown in figure 2.4.

The componets of the surface detector stations [36, 109] are housed in a cylindric plastic enclosure of $3.6\,\mathrm{m}$ in diameter and $1.5\,\mathrm{m}$ height. They consist of a cylindric water tank with $10\,\mathrm{m}^2$ base area and $1.2\,\mathrm{m}$ height filled with $12000\,\mathrm{l}$ of purified water within a Tyvek liner for diffuse reflection of Cherenkov light and light from converted photons. This light is detected by three $9''$ Photonis

Figure 2.4: A Surface Detector station of the Pierre Auger observatory consisting of water tank, liner, PMTs, electronics, communications and power supply through solar panel and battery. Detailed description of the components is given in the text.

photomultipliers of type XP1805 driven with locally provided high voltage. Both the last dynode and the anode are read out having a nominal ampification of factor 32 in between. So a dynamic range from less than 10 up to 10^5 photoelectrons corresponding to the range of a 15 bit floating point number per time bin is achieved. The signals at dynode and anode are digitised in bins of $25\,\mathrm{ns}$ in units of FADC channels having a pedestal of 50 channels added for baseline monitoring. The clock of the local data taking is synchronised via Global Positioning System (GPS) [165] and provides a common timing among all Surface Detector stations. Local electronics consists of an IBM 403 PowerPC microcontroller, trigger electronics based on the FADC traces and memory for data storage until external read-out. Autonomous operation is ensured by a solar panel and a battery in every station. A solar panel and antennas for the GPS system and communication with the central data acquisition CDAS via GSM are mounted on the enclosure.

Surface Detector calibration

The Surface Detector stations are designed for long-term autonomous operation. Nevertheless the hardware specifications like water quality, liner reflectivity, photomultplier gains and the amplification electronics may change during long-term operation. One or two of the photomultipliers may be temporarily not in data acquisition. The signal calibration procedure makes sure that such changes in the hardware are compensated for on the level of each individual stations. Both hardware settings as the high voltage and the amplification factors for dynode and anode of the photomultipliers are adjusted and a uniform normalisation of tank signal is established. A calibration reference uniform over the whole array is given by atmospheric muons permanently going through the station. A muon passing through the station vertically and centrally is chosen as a reference. So a uniform calibration of the complete array is achieved by using the integrated signal in units of *vertical equivalent muons* VEM. Two basic units are defined within the context of the VEM: Firstly the I_{VEM}^{peak} is the signal created by a vertical and central muon in the first time bin of the recorded signal giving a unit for the

signal intensity in one time bin. Secondly the charge-VEM is defined by the signal of a vertical and central muon integrated over all time bins, representing the whole energy deposited in the station by the muon. The former is needed to for trigger conditions and the latter gives the signal needed for reconstruction.

VEM calibration guarantees to maintain a uniform definition of the VEM independent of drifts in the gain or other changes in the station that might change the signal in FADC channels. Also it guarantees uniform trigger levels as the trigger thresholds in FADC channels are kept constant in units of $\mathrm{I}_{\mathrm{VEM}}^{\mathrm{peak}}$. The peak of the signal in one channel is calibrated to the intensity one vertically and centrally through-going muon produces I_{VEM}^{peak}.

Despite atmospheric muons are present at any time and any place they in general do not hit the detector stations vertically and centrally. For this reason a study of the real signal distribution of atmospheric muons in a reference detector station was performed [5]. The peak position of the signal distribution caused by atmospheric muons in units of the signal of a vertical muon $\mathrm{I}_{\mathrm{VEM}}^{\mathrm{peak}}$ has been determined to be at $1.09\,\mathrm{I}_{\mathrm{VEM}}^{\mathrm{peak}}$ for the full signal determined by all three photomultipliers. With only one of the photomultipliers measuring only the signal that is produced in the vicinity the position of the omindirectional muon peak is at $1.03 \pm 0.02\,\mathrm{I}_{\mathrm{VEM}}^{\mathrm{peak}}$. These values reflect that the vertical muon is by far the mos frequent case and it has the shortest track possible and gives the lowest signal possible for a through-going muon. Muons that are stopped in the detector volume would loose all their energy and produce a much higher signal.

The gain of the photomultipliers is set at deployment by adjusting the high voltage. From the reference tank a single photomultiplier having a signal of $3\,\mathrm{I}_{\mathrm{VEM}}^{\mathrm{peak}}$ is found with a rate of $100\,\mathrm{Hz}$ and so the single photomultipliers are adjusted to a rate of $100\,\mathrm{Hz}$ at 150 FADC channels [12]. Thus one vertically and centrally through-going muon gives a signal of 50 FADC channels which is equivalent to a gain of $3.5 \cdot 10^5$ with 94 photoelectrons per vertical equivalent muon. The three photomulipliers are adjusted by mathching the peak caused by atmospheric muons in their integrated signal distribution [80, 168]. Variations in water-quality, the optical coupling of the photomultiplier to the water and other technical specifications are compensated for in this way.

In a time interval of $t_{cal} = 5\,\mathrm{s}$ the rate of events with more than $1.75\,\mathrm{I}_{\mathrm{VEM}}^{\mathrm{peak}}$ in all three photomultipliers and one photomultiplier above $2.5\,\mathrm{I}_{\mathrm{VEM}}^{\mathrm{peak}}$ with the assumption of $1\,\mathrm{I}_{\mathrm{VEM}}^{\mathrm{peak}} = 50$ FADC channels is recorded. The rate of the three-fold coincidence should be $100\,\mathrm{Hz}$ and the rate for the additional threshold for one of the photomultipliers should be $70\,\mathrm{Hz}$ based on measurements at the reference detector station. A $\sigma - \delta$ algorithm [181] is applied after the counting of the events. The trigger level is increased by $\delta = 1$ FADC channel if the rate is $\sigma = 2\,\mathrm{Hz}$ above the expected value of $70\,\mathrm{Hz}$ and vice versa. The procedure is repeated with t_{cal} increased by $5\,\mathrm{s}$ unto a maximum of $60\,\mathrm{s}$ and δ decreased by 0.1 FADC channel to am minimum of 0.1. The procedure converges robustly and fast. For the full array a calibration of $1\,\mathrm{I}_{\mathrm{VEM}}^{\mathrm{peak}} = 46 \pm 4$ FADC channels is found consistent with the initial setup and showing a small cooldown of the photomultplier gains.

The calibration data are sent to central data acquistion with the event data and so a detailed calibration of the data can be performed in offline analyses that determine the baseline, the integrated signal in VEM and the peak signal in $\mathrm{I}_{\mathrm{VEM}}^{\mathrm{peak}}$. The amplification between the last dynode and the anode is determined by fiiting the signal of large signals from calibration triggers for both outputs respectively determining the amplification factor of ≈ 32 at an accuracy of $2\,\%$. The overall systematic uncertainty of the calibrated signal is $2\,\%$ [136] which is much better than the statistical fluctuations of the signal.

Surface Detector data acquisition

In order to record air showers and not noise generated by atmospheric muons and to keep memory for data storage in acceptable size triggers to select air shower candidates are required. The conditions for storeing an event are organised in the trigger chain of the surface detector. The first two levels are station triggers. Subsequently the central data acquisition checks for compact patterns among the stations that sent a trigger and reads out the array accordingly. Coinciding recorded data is merged offline into an event that contains Surface Detector data and Fluorescence data if available. Two more software trigger conditions are applied in the reconstruction algorithm. They are described in chapter 3.

The station trigger has two trigger levels. On the first level `T1` the three PMTs are required to coincidentally exceed a signal threshold of $1.75\,\mathrm{VEM}$ (`Thr1`) or at least two PMTs to exceed $0.2\,\mathrm{VEM}$ in 13 or more bins out of sliding window of 120 bins (time over threshold `ToT`). The definition of the VEM given in the calibration procedure guarantees a rate of `T1` triggers of about $100\,\mathrm{Hz}$. Data from stations on this trigger level is only read-out if a central trigger is formed.

The subsequent `T2` trigger furtherly reduces the rate of triggers in the station. On this trigger level the station sends a trigger signal to the central data acquisition. There are again two types of the `T2`:

Thr2 The threshold `T2` requires the three PMTs to conincidentally exceed $3.2\,\mathrm{VEM}$. Coincident muons from very inclined showers and fast and large signals close to the shower core are aimed on by this condition. Compared to `Thr1` the rate reduces by a factor of 5 to about $20\,\mathrm{Hz}$.

ToT The time over threshold `T2` requires $0.2\,\mathrm{VEM}$ in at least 13 out of 120 bins in two PMTs. This is equivalent to a sliding window of $3000\,\mathrm{ns}$. The `ToT` rate is about $5\,\mathrm{Hz}$. All `ToT` type `T1` are promoted automatically to `T2` as the condition is the same. In case of both `T2` criteria are fulfilled only `ToT` is recorded.

The three local triggers are illustrated by traces fulfilling the condition shown in figure 2.5. Any station without `T1` is considered as without signal if read-out. One muon or two coincident atmospheric muons giving `Thr1` are likely to accidentally be recorded even though not being part of the shower. The rejection of accidental stations is described in chapter 3.

The central trigger is a coincidence trigger. It checks for triggered stations in a more or less compact pattern in a time window of $50\,\mu\mathrm{s}$. The patterns are designed to include all multi-station triggers caused by air showers. This trigger `T3` is not designed to exclude non air shower events but to include all air showers. So also random coincidences of atmospheric muons and low energy air showers are stored fulfilling a `T3` trigger. The patterns accepted as `T3` [64, 104] are illustrated by examples in figure 2.6:

3ToT Three detector stations with a `ToT` trigger in time intervals according to the distance of the triggered stations.

4C4 Three triggered stations with two of them being next or next to next neighbours to the central one on the grid (`3C2`) and one detector station with any `T2` not farther than four grid points away from the central station within time windows appropriate to the distances.

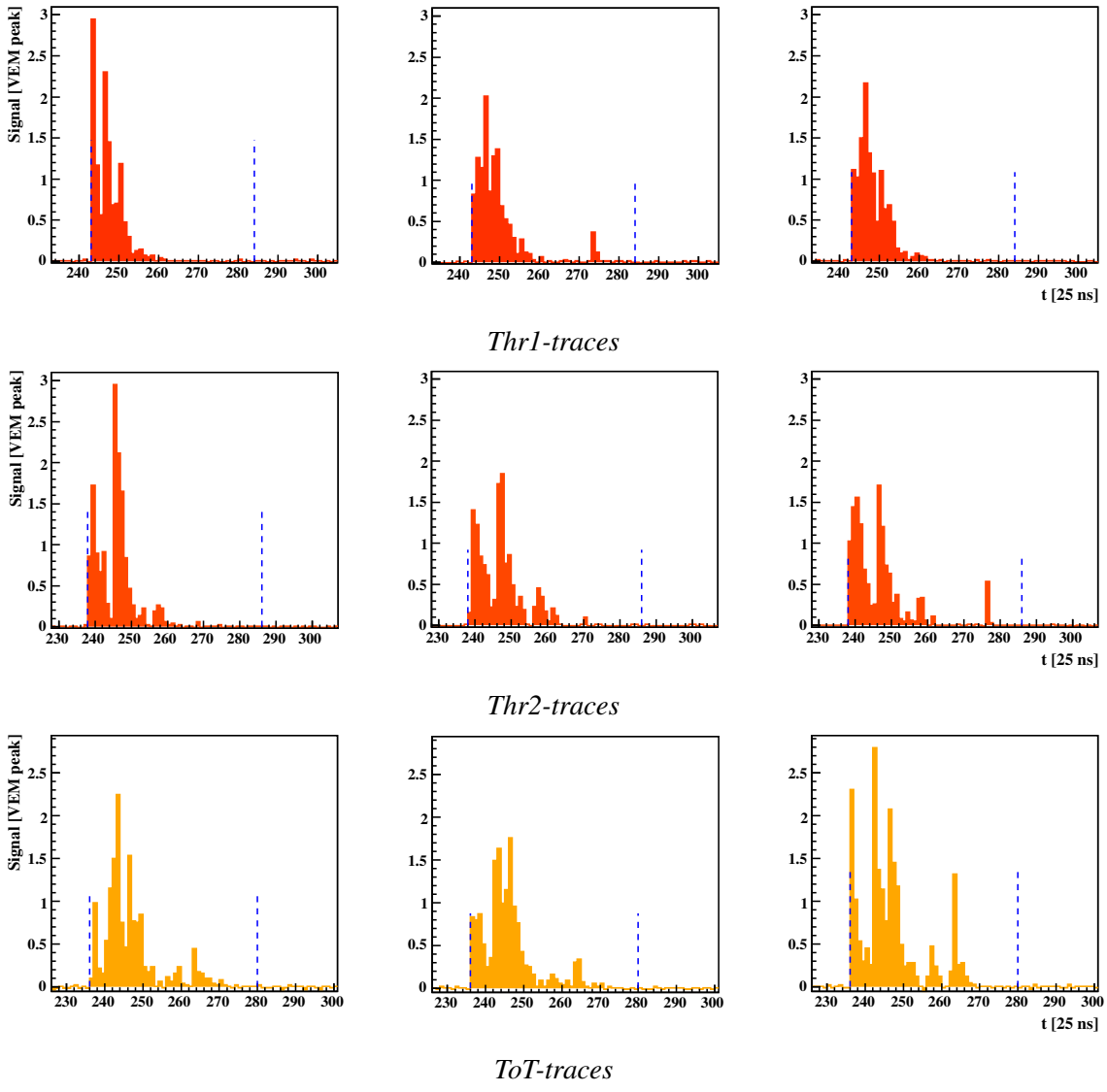

Figure 2.5: FADC traces recorded by a Surface Detector station that fulfil the different local trigger conditions: `Thr1` *(top panel),* `Thr2` *(mid panel) and* `ToT` *(bottom panel)*

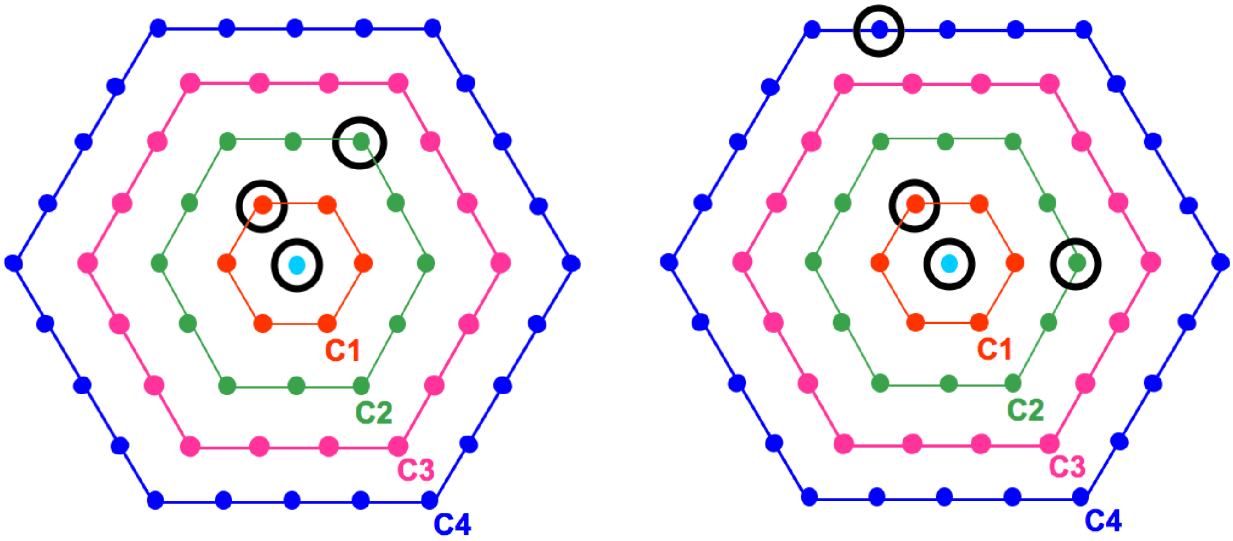

Figure 2.6: Expamples of the possible `T3` *configurations:* `3ToT` *(left panel),* `4C4` *(left panel) [71].*

3C1H Three stations in an aligned and compact configuration.

In addition external triggering of the readout of the array due to a Fluorescence Detector trigger is possible. Events of this option are labelled as `FD`. If multiple conditions are fulfilled all of them are stored as `T3` conditions of the event. The merging of Fluorescence Detector data and Surface Detector data respectively into one event is managed by the CDAS software [134]. Also events that are very elongated can form multiple `T3` triggers which causes the event to be split in several partly readouts of the array. Those events are merged into one single event by the CDAS software too.

Chapter 3

Event Reconstruction

At the Pierre Auger Observatory air showers are recorded as patterns of energy deposit in surface detector stations and fluorescence light detected by pixels of the fluorescence detector. Given the geometry and timing information from the detector components reconstruction provides estimates of incoming direction and the shower size.

The reconstruction of the incoming direction by using the timing information of the signal is introduced for both detector components. For the surface detector, two methods of energy determination using the signal sizes in the detectors and optimised for different zenith angles are described in the following. The shower size parameters S_{1000} and N_{19} are introduced respectively. Also the energy reconstruction using the fluorescence detector is shown.

The geometry reconstruction and the energy reconstruction are only slightly coupled as for all described cases as the geometry reconstruction relies on the timing of the signal but the energy reconstruction is based on the signal size in the detector.

3.1 Surface Detector Reconstruction

The surface detector measures the energy deposit of particles on ground. On the way from surface detector signals to physics data three main steps have to be taken: Rejection of background signal from other sources than the shower, estimation of the incoming direction and the shower size determination by fitting a model of the footprint of the shower to surface detector data. As the requirements on these algorithms are not the same for different incoming directions e.g. zenith angles two methods of station selection and especially shower size determination are presented: The reconstruction using a cylindrical symmetric lateral distribution function (*LDF*) optimised for *low zenith angles* $\theta < 60^\circ$ and the reconstruction method using two-dimensional muon density profiles optimised for *high zenith angles* $\theta > 70^\circ$. The validity of both methods overlaps in the intermediate region of *moderate zenith angles* $60^\circ < \theta < 70^\circ$.

Station Selection

Besides particles from an extensive air shower also accidental muons and coinciding low energy showers triggering few stations can contribute to the station content of an event. Moreover stations

with bad calibration or triggers caused by lightning have to be removed. The latter type of stations in the event is identified and rejected in advance as described in [91, 184]. For removal of physical signals not belonging to the shower two different station selecting algorithms have proven to be superior to the other depending on the zenith angle. Both algorithms incorporate the removal of spatially isolated stations as a first step, but use different parameters for identification of isolation.

Bottom-Up Selection is used for small and moderate zenith angles $0^\circ < \theta < 70^\circ$. It removes accidental stations by spatial isolation and by using a preliminary estimate of the shower front derived from a compact triangle of stations maximising the sum of signals [91, 198].

Stations with no triggered neighbour within a ground distance of $1800\,\mathrm{m}$ or only one within $5000\,\mathrm{m}$ are removed from the event. The algorithm is optimised for compact ground configurations and a high fraction of stations with `ToT` trigger. For high zenith angles the footprint is more sparse. So the criteria for spatial isolation are looser in case of the alternative algorithm for high zenith angles.

Subsequently the *seed* is composed of a compact configuration of three stations maximising the signal. From the timing of the seed stations an initial guess of the planar shower front is done. Using this shower front estimate accidental stations are removed if their start time is not within an interval of

$$-1000\,\mathrm{ns} < t_i - t_{front} < 2000\,\mathrm{ns} \tag{3.1.1}$$

with the expected arrival time of the shower front t_{front} and the start time t_i of the station S_i. The asymmetry in the allowed delay accounts for the planar shower front being only an approximation of the curved shower front. At high zenith angles accidental stations may be errornously part of the seed. In that case the bottom-up selection is not reliable. Thus it is used for low and moderate zenith angles. For high zenith angles the top-down algorithm is used.

Top-Down Selection is preferred for the selection of stations belonging very inclined events $60^\circ < \theta < 80^\circ$ [48]. For highly inclined events, the shower cone covers a huge area on ground, hitting many stations in different development stages of the shower. As the traversed atmospheric depth before hitting ground is large for inclined showers, the muonic component dominates and `ToT` triggers are rarely found. So a possible seed must be composed also of threshold trigger stations. With accidental muons forming `Thr` triggers the seed may be spoiled by accidentals. Thus the angular reconstruction of a three-fold seed has large fluctuations as well making timing compatibility cuts with the seed reconstruction less reliable.

The Top-Down Selection algorithm firstly removes all stations that are isolated from the event in space and time as extensive air showers are compact in the shower plane and also in the projection into the ground plane. A triggered station is regarded as isolated in space if there is no other triggered station within a ground distance of $4700\,\mathrm{m}$ or less than two other triggered stations within $6200\,\mathrm{m}$. Station that have signal start times long before or after all other stations are likely to be triggered by accidental muons or coincident low energy showers triggering only one station. Removal of stations due to isolation in time is applied if one of the criteria

- the start time is more than $15700\,\mathrm{ns}$ earlier or later than any other station in the event or
- the start time is $20700\,\mathrm{ns}$ earlier or later than the start times of any but one other station in the event

Stations removed	Stations, sorted by increasing signal
0	
1	X X X X X X ...
2	X X X X X X ... X X X X ...
3	X X X ...

Figure 3.1: The scheme of the Top-Down selection algorithm. The X are symbols for removed stations in the current subset of the full station sample. In the upper part, 1 out of N stations is removed, starting with the lowest signal stations. Below, the subsequent treatment is illustrated: in each subset, one more station is removed, iterating over all stations in the subset beginning with the lowest signal.

is fulfilled. The criteria of spatial isolation are less strict than in case of the Bottom-Up selection as the Top-Down selection is optimised for high zenith angles that can have more gaps within the footprint of very inclined showers. The Top-Down algorithm is very time consuming for high numbers of triggered stations with a large content of accidental stations because for the removal of k accidentals from n triggered stations the required steps are

$$N = \sum^{k} \binom{n}{k} \tag{3.1.2}$$

with a simplified reconstruction of the shower geometry at each step N. Thus the removal due to temporal and spatial isolation is vital for the performance of the algorithm.

After applying these criteria, the Top-Down algorithm is applied remaining set of stations in the event. Basically it consists of an iteration over the possible subsets of stations and a set of criteria if the subset is compatible with an extensive air shower signature e.g. fulfils a set of compacity criteria.

As the subsets are ordered with descending number of stations and descending sum of signals the first event surviving the criteria is the combination compatible with an extensive air shower pattern maximising number of stations and sum of signal respectively.

The Iteration over subsets starts with the trivial subset of all remaining stations. In the next step all subsets with one station removed are used starting with removing the station with lowest signal. Subsequently each subset from the previous step is treated the same way: One more station is removed, iterating over all stations starting with the one with lowest signal. Figure 3.1 illustrates

the sequence of generation of subsets. The iteration stops with the first subset fulfilling the `T4Has` criterion.

The compacity criteria consist of three main components: Compatibility with a shower plane, spatial compacity of the set stations in the shower frame and temporal compacity of the set of stations in the shower plane. Additionally, the event is required not to consist only of aligned stations.

- A fit of a planar front propagating with the speed of light as described in section 3.1 is applied to the station list subset of this step of the iteration. The subset is rejected if the analytical plane fit fails as the subsequent criteria require a preliminary estimate of the shower geometry.

- Temporal compacity is motivated by the shower front as a characteristic of an extensive air shower. It is fulfilled if the signal start times of all N_{cand} selected stations S_i are compatible with the estimated planar shower front. The time difference between a planar shower front and every candidate station S_i in that subset is required to fulfil

$$t_i - t_0 + \frac{u \cdot d_{xi}}{c} + \frac{v \cdot d_{yi}}{c} \quad < \quad N_{dof} \cdot 250\,\mathrm{ns} \cdot \max(\cos\theta, 0.2) \qquad (3.1.3)$$
$$d_{xi} = x_i - x_c, \quad d_{yi} = y_i - y_c$$

  with the candidate station S_i, its signal start time t_i and its coordinates x_i and y_i in the ground plane, the estimated core coordinates in the ground plane x_c, y_c and the directional cosines $u = \sin\theta$ and $v = \cos\theta$. Events with more stations can have a larger fluctuation in timing which is accounted for by scaling the upper limit of allowed timing difference with the number of degrees of freedom. As u, v and the start time at an arbitrary reference point t_0 are the only free parameters, the number of degrees of freedom is $N_{dof} = N_{cand} - 3$. The curvature of the shower front gets smaller for highly inclined showers represented by the cosine of the zenith angle θ. In order to still account for fluctuations the neglibly small values of $\cos\theta$ at highest zenith angles a lower limit of this factor of 0.2 is introduced corresponding to $\theta = 78°$.

- Spatial compacity is based on the fact that the huge, elongated footprint of an inclined extensive air shower is the result of a projection of the relatively compact particle density into a tilted ground plane defined as shower plane coordinates. Thus stations triggered by air shower particles are grouped around the axis. The size of the shower disc projected into the shower plane scales with the primary energy. At the stage of station selection the best available value proportional to the primary energy is the number of candidate stations N_{cand} or the number of degrees of freedom N_{doF}. Spatial compacity is given if the shower plane distance of all stations S_i to the shower axis

$$\sqrt{d_{xi}^2 + d_{yi}^2 - (u \cdot d_{xi} + v \cdot d_{yi})^2} \quad < \quad N_{dof} \cdot 1300\,\mathrm{m} \qquad (3.1.4)$$
$$d_{xi} = x_i - x_c, d_{yi} = y_i - y_c$$

  has to be smaller than a distance scaled with the number of stations. The coordinates (x_i, y_i) give the position of the station S_i, the barycenter as a core estimation is at the coordinates (x_c, y_c) and (u, v) are the directional cosines of the preliminary shower axis. The square root is the distance of the station to the shower axis.

- With only aligned stations the angular reconstruction is ambiguous. Besides the lack of a unique solution for the directional cosines giving undefined zenith and azimuth angles respectively, further reconstruction steps will fail because of the lack of a two-dimensional lever arm for reconstruction. Moreover aligned events can never fulfil subsequent trigger criteria as both 3 stations in a elementary triangle `3ToT` and 4 Stations in a hexagon containing seven stations `4C1` are two dimensional. Aligned events or station subsets are rejected at this point.

Detector stations outside the regular grid of the surface detector array [88] cause different sampling of lateral distribution function or the two-dimensional muon profile depending on the exact position within the array. So to guarantee the uniformity of the array stations outside the regular grid are rejected. For the same reason stations positioned very close to another station are removed from the event as well. In that case always the station with the lowest detector station id is kept in the event even if it is not triggered but one of the others in the same position has a signal to avoid a bias due to selection of signal only.

Event Selection

The online trigger algorithms at data acquisition are designed to store any air shower event candidate as far as bandwidth for transmitting and data storage permits. The recorded selection has to include as much as possible of potential new phenomena in order to not restrict the results by not storing interesting data. For analysis of data tighter cuts are applied as air shower events show compactness in their ground signature. Also events that hit the array with the core outside the array or at the edge introduce difficulties in both reconstruction and acceptance determination. The software trigger conditions of the physics trigger `T4` and the quality trigger `T5` account for this and reduce the data set for reliable analysis of the spectrum. Also both trigger conditions are applied to the event after station selection as the trigger conditions are designed to be applied on events cleared from detector stations triggered accidentally coincidentally together with an air shower event.

The physics trigger criterion `T4` is a criterion to select spatial compact configurations of triggered stations compatible with a shower front in the surface detector array that characterise air shower signatures [91]. It consists of two minimum criteria of spatial compactness and the compatibility of the timing of these stations with a shower front. The station configurations have to be at least one of the following:

- The `3ToT` configuration requires three non-aligned stations with a `ToT` station trigger with at least one of them being closest neighbour to the other two stations. The two possible configurations are shown in figure 3.2. The `3ToT` criterion selects 99 % of the events at low zenith angles. Due to the dominance of short muonic signals the `ToT` station trigger is not effective for moderate and especially for high zenith angles. Hence `3ToT` configurations are not sufficient to select moderately and highly inclined air shower signatures.

- The `4C1` criterion requires at least four detector stations with any `T2` trigger each with one of them being direct neighbour to the other three stations. The possible configurations are shown in figure 3.3. The fraction of air showers satisfying only `4C1` becomes significant above 55°.

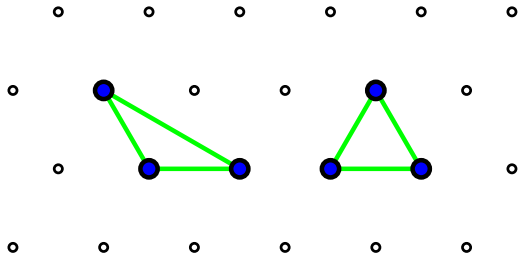

Figure 3.2: The two possible basic patterns of the `3ToT` *criterion on the array. Symmetry transformations of the triangular grid give the complete set. All three stations are required to fulfil the* `ToT` *criterion (see Pierre Auger Chapter). The physics trigger* `T4` *requires this configuration or* `4C1` *(figure 3.3).*

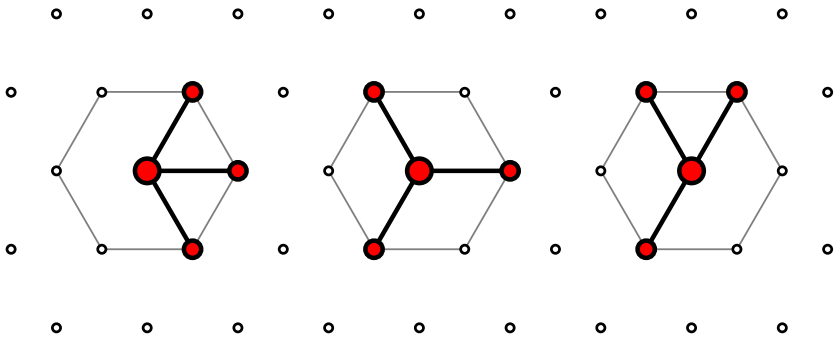

Figure 3.3: The minimum patterns that satisfy the `4C1` *condition plotted on an example piece of the surface detector array. All possible configurations are given by the symmetry transformations of the triangular grid. The physics trigger* `T4` *requires at least one of these configurations or the* `3ToT` *configuration (figure 3.2).*

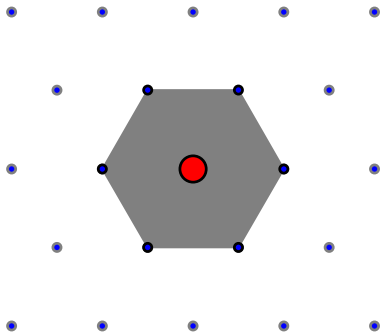

Figure 3.4: The quality trigger `T5` *requires the reference station and its six direct neighbours to be in data taking but not necessarily triggered at the time of the event.*

Additionally all stations that belong to one of these configurations have to be compatible with a shower front propagating with the speed of light giving a maximum timing difference of the distance between the stations divided by speed of light plus a tolerance of 200 ns. With the stricter spatial criteria than at the level of the central `T3` trigger, there are two types of the physics trigger `T4` according to the spatial configurations `3Tot` and `4C1`.

The quality trigger criterion `T5` defines events that can be reconstructed based on the major part of the event being recorded in the array [156]. Basically it is designed to reject events at the edges of the array being contained only partially. The missing part of the event introduces an uncertainty in reconstruction. The design of the `T5` also specifies the active area of the surface detector array as a function of the array geometry. The projected active area for the used solid angle is called acceptance. For determining the flux of cosmic rays the recorded event numbers have to be normalised with the acceptance integrated over time. This quantity is called exposure.Taking into account the different properties considering the core position with respect to the largest expected signal of showers depending on their zenith angle of the `T5` are introduced: The regular `T5` suited for low zenith angles that are reconstructed with the LDF type reconstruction algorithms and the `T5Has` optimised for high zenith angles reconstructed with the muon profile driven reconstruction. However the two criteria differ only in the choice of the *reference station* used for the trigger calculation. Low zenith angle showers that have a steep lateral profile. Thus station with the most energy deposit in the event is always the closest to the core. As shown later this is also reflected in the LDF reconstruction algorithm giving large weight to the station with the most signal and therefore keeping the reconstructed core position close to that *hottest station*. Thus the standard `T5` refers to the hottest station meaning the station with the highest signal in the event and can be calculated prior to the reconstruction. In case of the complex two-dimensional, flatter and elongated profile of inclined showers the core position is not as clearly bound to the hottest station. This is also reflected in the reconstruction algorithm allowing the core position to deviate from the hottest station. The `T5Has` uses the station closest to the reconstructed core as *reference stations* and therefore it has to be calculated a posteriori. Differen definitions of the `T5Has` have been applied in other analyses of very inclined showers [71, 153].

To make sure the event is well contained within the array the reference station and its six neighbours are required to be active but not necessarily triggered at the time of the event (figure 3.4). So at least the first crown around the core gives an accurate picture of the shower without missing signal biasing the reconstruction. The reconstruction algorithms rely heavily on the core position being contained in the array. Depending on the reconstruction algorithm the core position is misreconstucted either

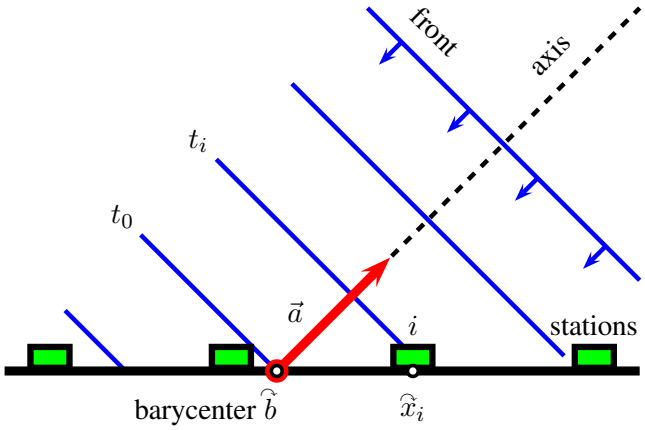

Figure 3.5: The shower front can be approximated by a plane propagating through the atmosphere at the speed of light. With this model the incoming direction can be estimated from arrival times of the shower front at the surface detector stations.

too close to the edge of the array or very far from the array resulting in strong underestimations or overestimations of the energy respectively.

Angular Reconstruction

The determination of the incoming direction of the shower relates a model of the shower front moving at the speed of light with the signal start times of the detector stations. With the model of a planar shower front a first approximation of the shower direction gives input parameters for the reconstruction of the core position and the shower size parameter. Subsequently the angular reconstruction is refined using the more realistic model of a spherical shower front. The reconstruction of the spherical model requires a good estimate of the core position to give reliable results for the incoming direction. Hence it cannot be used before the reconstruction of the core position and the energy respectively.

The Plane Fit stage of angular reconstruction is the first step using the approximation of a planar shower front moving through the atmosphere with the speed of light [199]. With the approximation of a two dimensional surface detector array this fitting can be performed analytically and therefore provides a robust estimation of the incoming direction of the shower. So the time difference of the arrival of the shower front at two points $\widehat{x_i}$ and $\widehat{x_{ref}}$ times the speed of light c is their distance projected on the surface normal $\vec{a}$ defining the plane

$$c(t_i - t_{ref}) = -(\widehat{x_i} - \widehat{x_{ref}}) \cdot \vec{a} \tag{3.1.5}$$

with the surface normal defining the shower axis that is defined as a normalised vector pointing towards the source of the shower. The reference point $\widehat{x_{ref}}$ is set to the signal-weighted barycenter $\widehat{b}$ defining the origin of the core centered coordinate system. The weighted barytime gives the arrival time at origin $t_{ref} = t_b$. So the arrival time at $\widehat{x_i}$ is given by

$$ct(\widehat{x_i}) = ct_0 - (\widehat{x_i} - \widehat{x_{ref}}) \cdot \vec{a}. \tag{3.1.6}$$

In the core centered coordinate system $\widehat{b} = (0, 0, 0)$ with the point $\widehat{x_i} = (x_i, y_i, z_i)$ and the shower axis written using the directional cosines $\vec{a} = (u, v, w)$ a least squares method [199] can be set up to

$$\chi^2_{plane} = \sum_i \frac{ct_i - ct_b + x_i u + y_i v + z_i w}{\sigma_i^2} \tag{3.1.7}$$

with the constraint of the directional cosines being real numbers with $u^2 + v^2 + w^2 = 1$. With the constraint reformulated as $w = \sqrt{1 - u^2 - v^2}$ the three-dimensional χ^2 is non-linear. Using the very flat geometry $z_i \ll x_i, y_i$ of the surface detector array the problem can be linearised and theefore be solved analytically by neglecting the z-component. A solution always exists if aligned events giving a linear dependence of the station coordinates are excluded. A numerical minimisation of the full problem accounting for the z_i is performed subsequently.

Provided the positions of the detector stations are known exactly only the uncertainties in arrival time $\sigma_i = c\sigma_{t,i}$ contribute to the denominator. The timing uncertainty is modelled with an empirical time variance model [51, 175].

More realistic shower front models introduce a curved shower front. Two basic curved shower front have been established: A cylindrical symmetric parabolic extension to the shower plane model and the idea of an expanding sphere. The spherical model is preferred because it provides a simple relation of the curvature of the shower front and the on-going propagation as well as because the fitting procedure of the spherical front depends less heavily on a precise core determination in advance.

A Spherical Shower front is the curved shower front model used within this analysis [199]. All particles are assumed to travel from an idealised first interaction point at the center of the sphere $\widehat{R_c}$ with the speed of light. In reality the origin of the shower particles according to this model is close to the end of the hadronic cascade. That leads to arrival time predictions at a point $\widehat{x_i}$ depending on the distance to the center of the sphere $\widehat{R_c}$:

$$ct(\widehat{x_i}) = ct_0 - \|\widehat{x_i} - \widehat{R_c}\|. \tag{3.1.8}$$

Using this model the center of the sphere $\widehat{R_c}$ can be determined independent of the position of the shower core only by using the timing information of the stations by minimising

$$\chi^2_{sphere} = \sum_i \frac{ct_i + ct_0 - \|\widehat{R_c} - \widehat{x_i}\|}{c^2\sigma_i^2}. \tag{3.1.9}$$

The shower axis $\vec{a}$ and the radius of curvature R_c are given by the spherical model

$$R_c\vec{a} = \widehat{R_c} - \widehat{c} \tag{3.1.10}$$

with the shower core position $\widehat{c}$ on ground. The minimisation of χ^2_{sphere} with the approximation of an ideally flat ground array improves the direction estimate by the order of $0.5°$. A subsequent minimisation with $z_i \neq 0$ treatment gives further axis change in the order of few tenths of a degree.

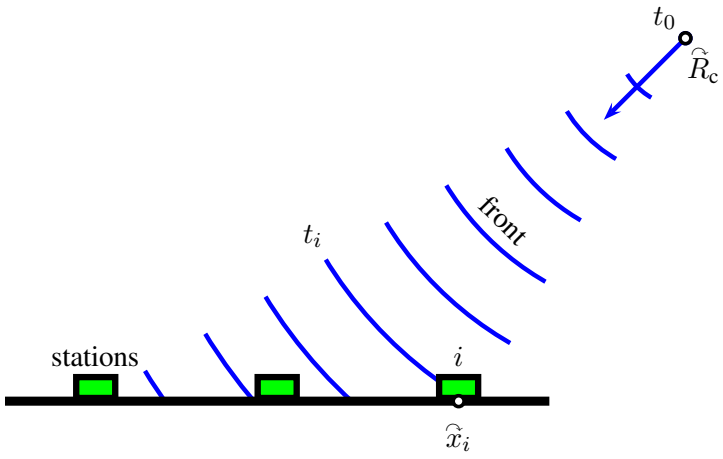

Figure 3.6: The shower front can be modelled as an expanding sphere. The resulting prediction of the arrival time can be used to detemine the virtual origin of the shower particles. With the core position known the incoming direction can be inferred.

3.2 Shower Size Determination For Low And Moderate Zenith Angles

Showers with incident angles up to about $\theta = 65°$ reach the ground with a significant contribution of the electromagnetic component and only small magnetic distortions of the cylindrical symmetry of the shower. The lateral profile is relatively steep and asymmetries in the ground pattern are caused by attenuation during ongoing propagation through the atmosphere and other effects. The signal in the detector station basically depends on the distance from the shower axis thus the pattern can be modelled by a one-dimensional function of the radius.

Fitting method

For low and moderately inclined showers asymmetries in the lateral profile of particle densities on ground are small [44]. A function depending only on the distance to the shower axis

$$S = S_{1000} \cdot f_{LDF}(r, \theta, E, A) \tag{3.2.1}$$

describes the shower footprint with the lateral distribution function $f_{LDF}(r, \theta, E, A)$ and the normalisation S_{1000} which is the expected signal in a detector station at $1000\,\mathrm{m}$ from the shower axis with the requirement $f_{LDF}(1000\,\mathrm{m}) = 1$ [34, 152]. The choice of the lateral distribution function is described in the next section. The distance r of the point $\widehat{x}_i$ to the axis

$$r = |\widehat{x}_i - \widehat{b} \times \vec{a}| \tag{3.2.2}$$

where $\vec{a}$ is normalised axis vector and $\widehat{b}$ is a point on the shower axis is dependent on the position of the shower track in space. Thus the position of the shower core $\widehat{c}$ is a parameter of equation 3.2.1. It is defined as an element of the shower track. The determination of the shower size parameter S_{1000} is coupled with the determination of the position of the shower core. The fitting procedure is implemented as a maximum likelihood method:

The Likelihood function is composed of four terms accounting for the subsets of low signal stations, high signal stations, saturated stations and zero-signal stations respectively

$$L = \prod_i f_{\mathrm{P}}(n_i, S_{exp,i}) \prod_i f_{\mathrm{G}}(n_i, S_{exp,i}) \prod_i F_{\mathrm{sat}}(n_i, S_{exp,i}) \prod_i F_{\mathrm{zero}}(n_i, S_{exp,i}) \tag{3.2.3}$$

with the signal expectation $S_{exp,i} = S_{1000} \cdot f_{LDF}$ described in the next section. The construction of the likelihood function is shown in the following

Provided that the shape of the footprint is described well by $f_{LDF}(r)$ the energy estimator and core position are determined by maximising the probability

$$P(S_i) = f(S_i | x_i - x_c, y_i - y_c, S_{1000}) dS_i \tag{3.2.4}$$

to measure a signal S_i in the detector station i wheras $f(S_i)$ is the probability density function of the measured signals. The probability of measuring a lower signal than a given value $S_{upperlimit}$ or a higher signal than $S_{lowerlimit}$ is given by the integration of the p.d.f. over signal for the respective singal range. So stations without a trigger can be accounted for with an upper limit of the signal. Also stations with signals above the region of linear behaviour of the photomultipliers or the electronics (saturated statiosn) can be used accounting for them as a lower limit to the LDF. For setting up the p.d.f. equation 3.2.4 the number of particles causing the signal in the detector station is estimated. At ground the significant contributions to a signal caused by an extensive air shower come from muons, electrons and photons. So the signal in a surface detector station is given by the number of particles of a kind times the corresponding mean signal contribution a_j per particle

$$\begin{aligned} S &= \sum_j a_j \cdot n_j, \quad j \in \{\mu, e, \gamma\} \\ &= n \cdot \sum_j a_j \cdot \frac{n_j}{n}, \quad n = \sum_j n_j \end{aligned} \tag{3.2.5}$$

with the effective number of particles n in the station and n_j the number of muons μ, electrons e and photons γ respectively. The effective particle numbers are used for the estimation of the statistical behaviour of the signal and are not to be interpreted as realistic particle numbers in the station. Muons and electromagnetic particles give very different contributions to the measured signal. This is accounted for by definition of the Poisson factor p_S. This factor defines the relation between signal and effective particle number and varies with the composition of the particles in the detector e.g. the fraction of muons and electromagnetic particles.

$$p_S = \frac{n \cdot 1\,\mathrm{VEM}}{S} = \begin{cases} f_S^{-2}(\theta) & f_S(\theta) \geq 1 \\ 1 & f_S(\theta) < 1 \end{cases} . \tag{3.2.6}$$

with the signal factor $f_S(\theta)$. For the same signal a different composition out of muons and other particles e.g. a different effective particle number also result in different statistical signal uncertainties [21, 22]

$$\sigma_S(\theta) = f_S(\theta) \cdot \sqrt{S} \tag{3.2.7}$$

with an emprical model of the signal factor

$$f_S(\theta) = (0.32 + 0.42 \cos\theta). \tag{3.2.8}$$

The approximation equation 3.2.6 neglects radial dependencies of the relative contributions to the particle number. In real showers the relative contribution of muons to the signal rises with the distance to the shower core.

The p.d.f. for small and zero signals with effective particle numbers $n < 30$ is modelled with a Poissonian p.d.f.

$$f_P(n_i, S_{exp,i}) = \frac{S_{exp,i}^{n_i} \mathrm{e}^{-S_{exp,i}}}{n_i!} \tag{3.2.9}$$

with the signal expectation $S_{exp,i} = S_{1000} \cdot f_{LDF}(x_i, y_i, \theta)$. For untriggered but active stations the sub-threshold $n_i < n_{th} = 3$ probablities are summed up giving the factor

$$F_{\text{zero}}(n_{\text{th}}, \mu_i) = P(S < S_{thr}) = \int_0^{S_{thr}} f_p dS. \tag{3.2.10}$$

Large signals and saturated stations allow the use of a Gaussian approximation of the p.d.f.

$$f_{\text{G}}(n_i, S_{exp,i}) = \frac{1}{\sqrt{2\pi}\,\sigma_i} \exp\left(-\frac{(n_i - S_{exp,i})^2}{2\sigma_i^2}\right) \tag{3.2.11}$$

with σ_i from equation 3.2.7. For the treatment of the expected particle number n_i of saturated stations as a lower limit for $S_{exp,i}$ an integration of $F_{\text{sat}}(n_i, \mu_i) = \int_{n_i}^{\infty} f_{\text{G}}(n_i, S_{exp,i})$ from n_i to infinity is used.

3.3 Fine Tuning of the LDF parameterisation

As the LDF is used to determine the energy estimator and the core location for a measured air shower, a suitable LDF parameterisation is a crucial requirement for the reconstruction air shower data from the surface detector up to zenith angles $\theta < 70°$. For comparisons of the reconstruction of moderately inclined and very inclined air showers with the LDF reconstruction and the HAS reconstruction the parameterisation of the LDF is optimised in order not to influenced by a flawed parameterisation when comparing. Within this section the parameterisation of the lateral signal profile is optimised and checked using the large statistics of both Surface Detector data alone as well as showers measured by the Fluorescence Detector and the Surface Detector simultaneously.

Within the Pierre Auger collaboration two approaches have been found to be the best candidates for the modelling of Auger surface detector data:

	modified NKG		log-log parabola	
parameter	value	σ	value	σ
a_0	-3.35	0.23	-4.73	0.26
a_1	-0.125	0.151	-0.519	0.154
b_0	1.33	0.31	1.32	0.25
b_1	-0.0324	0.2114	0.405	0.149
c_0	-0.191	0.105	-0.105	0.063
c_1	-0.00573	0.07210	-0.117	0.0401
χ^2/N_{dof}	1.44308		2.43995	

Table 3.1: The values and uncertainties of the constants for the slope parameters β of the modified NKG function and B of the modified power law function derived in [170].

The modified power law function [163] has been inspired by lateral distribution studies on Monte Carlo simulations. For simulated events the logarithm of the signal in a tank as function of the logarithm of the core distance can be modelled by a parabola

$$y = A + Bx + Cx^2 \quad \text{with} \quad y = \lg\left(\frac{S(r_{SP})}{1\,\mathrm{VEM}}\right), x = \lg\left(\frac{r_{SP}}{1000\,\mathrm{m}}\right), \tag{3.3.1}$$

where $S(r_{SP})$ is the signal in a tank at the distance r_{SP} from the shower core in shower plane coordinates. Transforming to plain coordinates, the modified power law structure becomes visible

$$S(r_{SP}) = 10^A \cdot 1\,\mathrm{VEM} \cdot (r_{SP}/1000\,\mathrm{m})^B \cdot (r_{SP}/1000\,\mathrm{m})^{C \lg(r_{SP}/1000\,\mathrm{m})} \tag{3.3.2}$$

factorising the problem into the normalisation term $10^A \cdot 1\,\mathrm{VEM} = S_{1000}$ which is the signal at $1000\,\mathrm{m}$ from the core in shower plane coordinates, the power law term with the slope B and the deviation from the power law in the third factor. For standard reconstruction, the slope parameter B has been tuned using real data [170] using the method described below. Standard reconstruction uses the slope parameters

$$B = (a_0 + a_1 \cdot \lg S_{1000}) + (b_0 + b_1 \cdot \lg S_{1000}) \cdot \sec\theta + (c_0 + c_1 \cdot \lg S_{1000}) \cdot \sec^2\theta \tag{3.3.3}$$

$$C = 0.05 \cdot \sin(8 \cdot (\cos\theta - 0.6)) - 0.5 \tag{3.3.4}$$

with the constants in the parameterisation of B in table 3.1 and the parameterisation of C from [198].

The modified Nishimura Kamata Greisen (NKG) function [124, 127] is based on the theoretical calculations of Nishimura, Kamata and Greisen about the longitudinal and lateral development of an extensive air shower caused by an electron or photon. After defining the propagation parameter of the *shower age* the lateral particle density profile of an electromagnetic air shower is

$$\rho_{ch}(r) = \frac{N_{ch}}{2\pi r_0^2} \cdot C \cdot \left(\frac{r}{r_0}\right)^{s-2} \cdot \left(1 + \frac{r}{r_0}\right)^{s-2} \tag{3.3.5}$$

with the charged particle density ρ_{ch} at a distance r from the shower axis, the total number of charged particles N_{ch} and the Molière radius r_0. The parameter s is called lateral age parameter. For hadron primaries the situation is mor complicated. A hadronic shower consists mainly of a superposition of purely electromagnetic showers and the muonic component. After the end of the hadronic cascade the latter has a flatter LDF than the electrons as muons can travel longer paths than electrons without interaction e.g. farther away from the shower axis. The pattern is approximated by a modified NKG function [34]

$$\rho(r) = \rho(r_{opt}) \cdot \left(\frac{r}{r_{opt}}\right)^{\beta} \cdot \left(\frac{r + r_{scale}}{r_{opt} + r_{scale}}\right)^{\gamma}. \tag{3.3.6}$$

Assuming the signal in a detector station being proportional to the particle density, equation 3.3.6 can be written for the lateral profile of the signal in the detectors:

$$S(r) = S(r_{opt}) \cdot \left(\frac{r}{r_{opt}}\right)^{\beta} \cdot \left(\frac{r + r_{scale}}{r_{opt} + r_{scale}}\right)^{\gamma}, \tag{3.3.7}$$

where $r_{opt} = 1000\,\mathrm{m}$ is the optimum distance for $S(r_{opt}) = S_{1000}$ being the best energy estimator (refs and cites), $r_{scale} = 700\,\mathrm{m}$ is the modified replacement of the Molière radius. The *slope parameters* β and γ are parameters that represent a redefinition of the shower age as defined in [124,127]. They are connected to the shower age as the lateral profile of the shower gets flatter while propagating through the atmosphere but the shower age cannot be inferred from the slope parameters. Reconstruction of data with less than five stations requires a parameterisation of the slope parameters as three parameters have to be determined by the fit in any case: the core location and the normalisation S_{1000}. In [170] the slope parameters have been determined based on real data:

$$\beta = (a_0 + a_1 \cdot \lg S_{1000}) + (b_0 + b_1 \cdot \lg S_{1000}) \cdot \sec\theta + (c_0 + c_1 \cdot \lg S_{1000}) \cdot \sec^2\theta \tag{3.3.8}$$

$$\gamma = \beta \tag{3.3.9}$$

with the constants shown in table 3.1 for the β parameterisation. Since then statistics has tripled. For determining the parameterisation shown in equation 3.3.9 statistics was not sufficient after the strict cuts from [170] for the determination of the second slope parameter γ independently of β. Also the fit ist dominated by the energy region just above the cutting energy as the statistics is by far highest there due to the steeply falling spectrum.

Fitting a slope parameter additionally to the core location and the normalisation requires at least five stations. Also fitting the slope parameters requires a wide-spread distribution of the triggered stations in core distance in order to give a well-determined fit. A criterion to ensure the station distribution to give enough lever arm for the fit of the slope parameters β and B respectively has been formulated [47]. The event is required to contain

- at least two stations $n \in \{i, j\}$ with $500\,\mathrm{m} < r_n < 1500\,\mathrm{m}$ and $|r_i - r_j| > 500\,\mathrm{m}$,
- at least three stations $n \in \{i, j, k\}$ with $500\,\mathrm{m} < r_n < 1500\,\mathrm{m}$ and at least one pair of those with $|r_n - r_o| > 400\,\mathrm{m}$ with $o \in \{i, j, k\}$ or

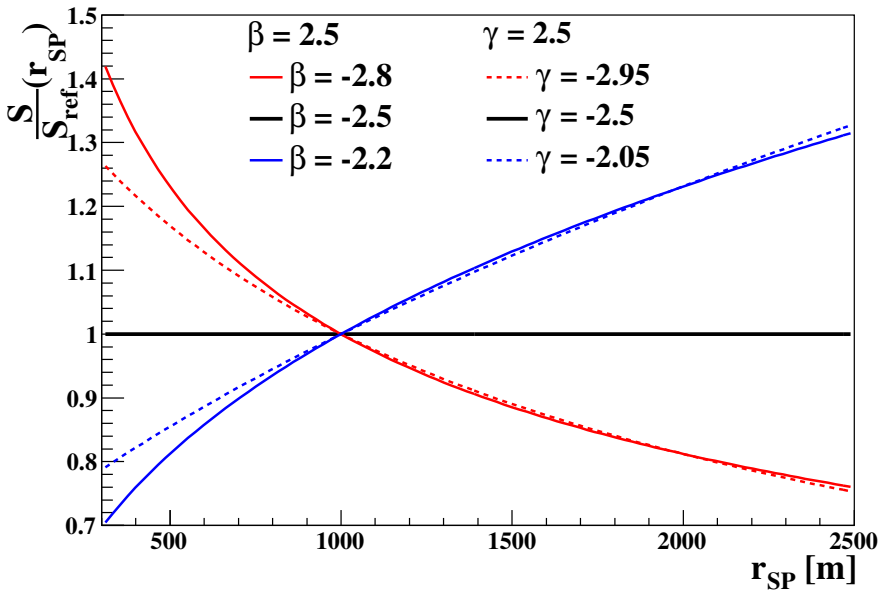

Figure 3.7: The relative influence of variation of β and γ on the modified NKG function as a function of distance from the core. For the solid lines, $\gamma = 2.5$ ist kept fix while β varies around $\beta = 2.5$, for the dashed lines, γ varies around $\gamma = 2.5$ for a constant $\beta = 2.5$. The black solid line represents $\beta = \gamma = 2.5$.

- at least four stations $n \in \{i, j, k, l\}$ with $500\,\mathrm{m} < r_n < 1500\,\mathrm{m}$
  and at least one pair of those with $|r_n - r_o| > 300\,\mathrm{m}$ with $o \in \{i, j, k, l\}$

(3.3.10)

with the distance r_i of the station i from the shower core in shower plane coordinates.

For the modified NKG function equation 3.3.7, the first term dominates the LDF at low core distances. For higher core distances, the influence of the second term with the exponent γ gains influence. This can be seen varying β for a given γ and vice versa. An example is shown in figure 3.7. Accounting for that, a similar condition at higher core distances is required to select events for fitting γ. The event must contain

- at least two stations $n \in \{i, j\}$ with $1000\,\mathrm{m} < r_n < 2000\,\mathrm{m}$
  and $|r_i - r_j| > 500\,\mathrm{m}$,
- at least three stations $n \in \{i, j, k\}$ with $1000\,\mathrm{m} < r_n < 2000\,\mathrm{m}$
  and at least one pair of those with $|r_n - r_o| > 400\,\mathrm{m}$ with $o \in \{i, j, k\}$ or
- at least four stations $n \in \{i, j, k, l\}$ with $1000\,\mathrm{m} < r_n < 2000\,\mathrm{m}$
  and at least one pair of those with $|r_n - r_o| > 300\,\mathrm{m}$ with $o \in \{i, j, k, l\}$

(3.3.11)

By requiring these conditions, the statistics is largely reduced as shown in table 3.2. For fitting both slope parameters simultaneously both criteria on station distribution with respect to the core position have to be fulfilled simultaneously.

Cut	value	sample to fit β	sample to fit γ
$N_{stations} \leq 5$ Lever arm cut	(eqn 3.3.10,3.3.11)	122262	52503
Quality trigger	T5	98030	41685
Reject saturation		96123	39951
Threshold	$\lg E\text{eV} > 18.8$	10903	9163
Zenith angle	$\theta < 70°$	10831	9097

Table 3.2: Cut efficiencies for data sets to fit the slope parameters β and γ respectively. The motivation and implementation of the cuts is described in the text.

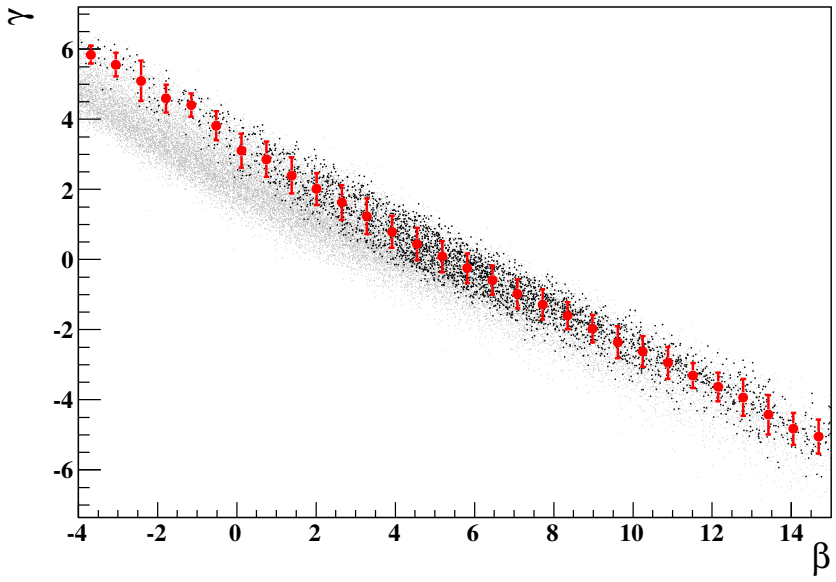

Figure 3.8: The reconstruction of real data shows the strong correlation of the values of β and γ. Events that did not fulfil the quality criteria for the fitting of both slope parameters respectively are shown in grey. Events that fulfilled the criteria shown in table 3.2 are shown in black. The big red points are given by the mean of the distribution fulfilling the quality criteria with the sample variance as error bars.

The best result for events with both enough stations and enough lever arm can be expected for fitting the core, S_{1000} and both slope parameters β and γ at once. But as shown in figure 3.7 the slope of the LDF is determined by both β and γ in any core distance, only the relative influence of the first and the second term of the LDF varies. Thus the correlation of β and γ is large as figure 3.8 illustrates. So the slope parameters are a function not only of the zenith angle and S_{1000}, but also their contributions do not factorise. A simple and robust parameterisation for β and γ only depending on preliminary reconstructed shower data hence is impossible to derive from data with both slope parameters fitted to data simultaneously. Thus the parameterisations of the slope parameters are derived iteratively: Using the estimate of β by the parameterisation from [170] γ is fitted to the data fulfilling the criterion in equation 3.3.11 using the parameterised β. As a second stage, β is fitted to the data set fulfilling equation 3.3.10 using the γ parameterisation. If necessary these steps are iterated until the parameterisations can be confirmed.

In figures 3.9, 3.10 all data surviving the cuts on number of triggered stations and station distribution for β and γ respectively are plotted as a function of $\lg S_{1000}$ and $\cos^2\theta$. At energies below $E = 3 \cdot 10^{18}\,\mathrm{eV}$, not all showers trigger three stations to fulfill the `T4` condition. This threshold rises for higher numbers of required stations and additional criteria on the station distribution. It also depends on the zenith angle as more stations are triggered by more inclined showers.

The trigger probability for a shower depends on the slope of its LDF. Steeper events trigger less stations as the particles are more concentrated near the shower axis for equal energy but steeper LDF. The selection of flat events below the threshold is demonstrated by two features in figures 3.9, 3.10:

- A steepening of the slope parameter as a function of $\lg S_{1000}$ in figure 3.9.
- The lower average slope parameter for low S_{1000} and low zenith angles θ also illustrates the zenith angle dependency of the threshold.

Flatter events e.g. events with lower values of the slope parameters are preferred by the requirement of at last five stations. For events with lower numbers of triggered Surface Detector stations the slope parameters are extrapolated from the unbiased parameterisations. To avoid the selection bias events with energies below the threshold of $E =$ eV corresponding to $S_{1000} =$ for vertical showers are rejected. Due to attenuation in the atmosphere for inclined showers the corresponding S_{1000} is lower as will be shown in chapter 4.

For the fitting of the slope parameter the station closest to the core has a large influence as the LDF parameterisations diverge at zero. Unrecovered saturated stations give only a lower limit to the signal and therefore bias the fitting of the slope parameter. Events containing a Surface Detector with unrecovered saturated signal are not used for the determination of the slope parameterisations. At high zenith angles the radial symmetry of the article densities in the shower front is broken by attenuation effects, geometrical effects and the geomagnetic field. Thus events at high zenith angles $\theta > 70^\circ$ are excluded.

In the lower part of table 3.2 the antibias cuts accounting for threshold effects, saturation and validity of the assumption of a radial symmetry respectively are summarised. After these cuts parameterisations of the slope parameters can be fitted to the remaining data set. For β, a polynom of second order in $\sec\theta$ and a linear dependency on $\lg S_{1000}$

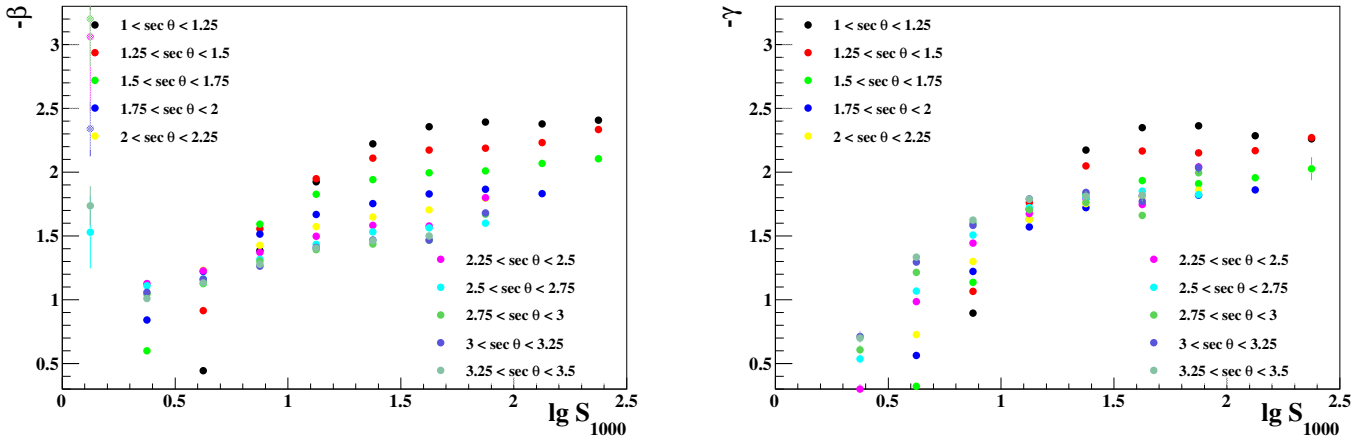

Figure 3.9: The slope parameters β and γ fitted to the data surviving the cuts on number of stations and station distribution (table 3.2) as a function of $\lg S_{1000}$. Below the zenith angle dependent threshold of full trigger efficiency after cuts only a subclass of flat events with low absolute values of β and γ can pass the lever arm cuts. This behaviour can be seen as a larger slope of the dependency of the slope parameters on $\lg S_{1000}$ below a zenith angle dependent threshold in $\lg S_{1000}$.

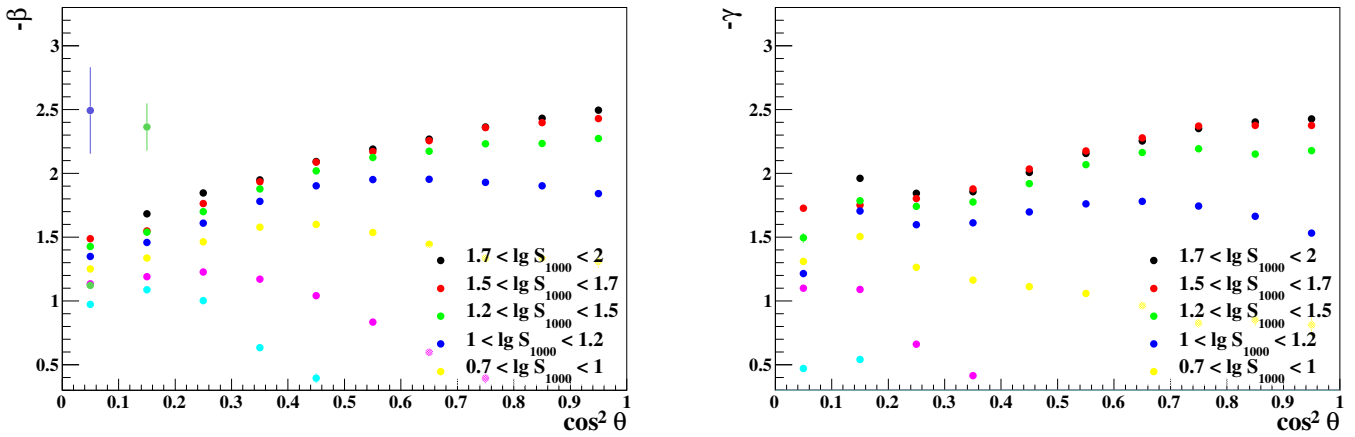

Figure 3.10: The slope parameters β and γ fitted to the data surviving the cuts on number of stations and station distribution (table 3.2) as a function of $\cos^2\theta$. For low energies and low zenith angles both slope parameters show lower absolute values. This illustrates the selection of flat events for energies below the zenith angle dependent threshold of full trigger efficiency.

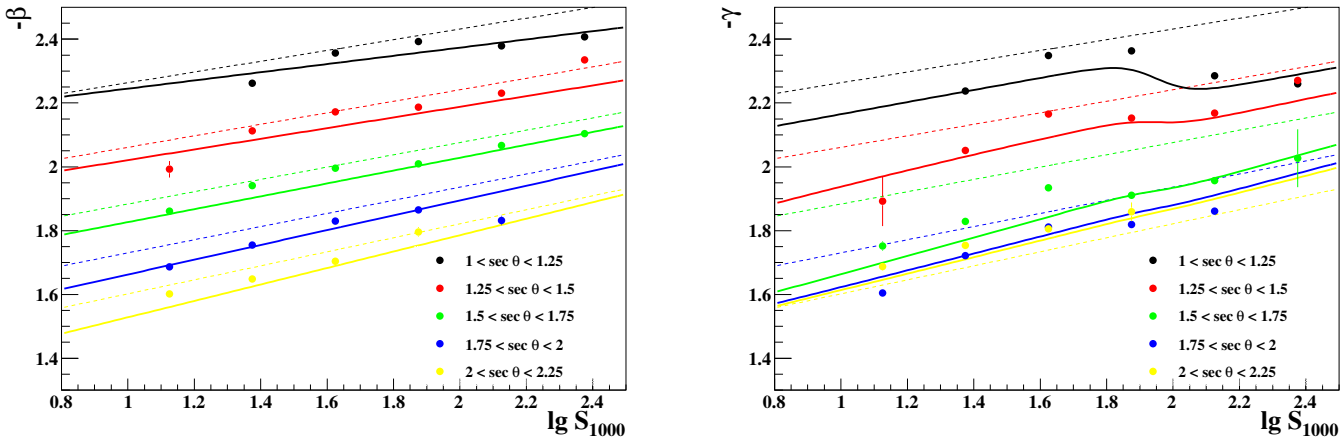

Figure 3.11: The slope parameters β and γ of data after all cuts in table 3.2 as a function of $\lg S_{1000}$. Besides the small dip in the distribution of γ, the behaviour can be modelled by a linear function. Details are explained in the text. For comparison the previously used parameterisation from [170] is shown as dashed lines.

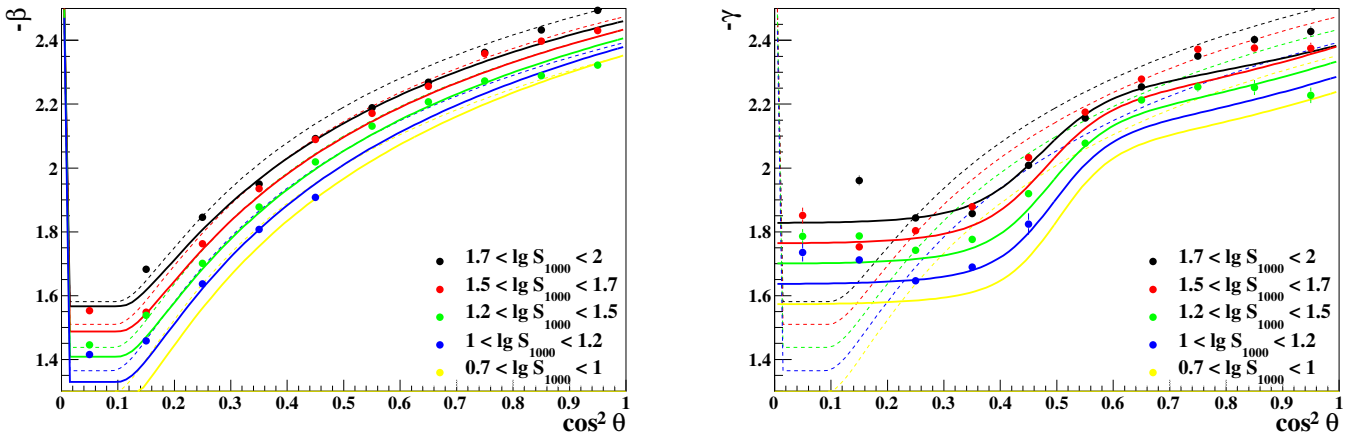

Figure 3.12: The slope parameters after the quality cuts as a function of $\cos^2\theta$. A quadratic function in $1/\cos\theta$ fits the β distribution well. For γ a fermi function with a modification for low zenith angles and high energies is used. Details of the fit are described in the text. For comparison the previously used parameterisation from [170] is shown as dashed lines.

$$\beta(\theta, S_{1000}) = (a_0 + a_1 \cdot \lg S_{1000}) + \tag{3.3.12}$$
$$(b_0 + b_1 \cdot \lg S_{1000}) \cdot \sec\theta + \tag{3.3.13}$$
$$(c_0 + c_1 \cdot \lg S_{1000}) \cdot \sec^2\theta \tag{3.3.14}$$

with constant parameters. For the second slope parameter, a Fermi function in $\cos^2\theta$ has been chosen, modelling the dependence on the zenith angle. Both the offset and the amplitude depend linearly on $\lg S_{1000}$. The dip at low zenith angles and high energies is modelled by adding another Fermi function in $\lg S_{1000}$ with an amplitude varying as a power law of $\cos^2\theta$

$$\gamma(\theta, S_{1000}) = (o_0 + o_1 \cdot \lg S_{1000}) \tag{3.3.15}$$
$$d_1 \cdot \frac{1}{\exp((s_1 - 4.1 \lg S_{1000}) \cdot (cos^2\theta - p_1)) + 1} + \tag{3.3.16}$$
$$d_2 \cdot \cos^4\theta \cdot \frac{1}{\exp(s_2 \cdot (\lg S_{1000} - p_2)) + 1}. \tag{3.3.17}$$

The fit has been performed without binning by minimising a χ^2 defined as

$$\chi^2 = \sum_i{}^N \frac{(\beta_i - \beta(\theta_i, S_{1000,i}))^2}{\sigma_i^2}, \tag{3.3.18}$$
$$\sigma_i^2 = \sigma_\beta^2 + \left(\frac{d\beta(\theta_i, S_{1000,i})}{d\theta} \cdot \sigma_\theta\right)^2 + \left(\frac{d\beta(\theta_i, S_{1000,i})}{dS_{1000}} \cdot \sigma_{S1000}\right)^2. \tag{3.3.19}$$
$$\tag{3.3.20}$$

In figures 3.11 and 3.12 the parameterisation is compared to the underlying data set. For demonstration the data has been binned and the curves using the bin center in the parameterisation is shown in the corresponding colour. The resulting parameters and χ^2 values are shown in tables 3.3 and 3.4, where the data set for β is reconstructed with a γ fixed on the value given by the parameterisation in equation 3.3.17.

The reconstruction of S_{1000} with β and γ fixed to the values given in the parameterisations 3.3.14, 3.3.17 is consistent with the reconstruction with one of the slope parameters as a free parameter in the fit and the other one defined by the parameterisation as shown in figure 3.13. The full data set with only lever arm cuts and five stations minimum has been used. The reconstruction modes with one of the slope parameters fitted to the event agree with the parameterised reconstruction. For low energies a structure is visible as only data fulfilling the conditions 3.3.10, 3.3.11 can be compared. Gaussian fits to the distribution give mean deviations of less than $-0.5\,\%$ with $\sigma < 3\,\%$ respectively. Data reconstructible with both slope parameters as free parameters is shown for comparison. The mean shift of $S_{1000}^{\beta,\gamma free}$ with respect to the parameterised LDF is $5\,\%$ with $\sigma_{fix,free} = 14\,\%$.

The uncertainty of the slope parameters in case of the parameterised LDF consists of two contributions: The uncertainty from the fitting procedure and uncertainty from event-to-event

Parameter	value	uncertainty
a_0	-3.72	0.11
a_1	0.097	0.068
b_0	1.74	0.12
b_1	-0.242	0.077
c_0	-0.274	0.030
c_1	0.035	0.021

Table 3.3: The constants of the parameterisation of the slope parameter β as in equation 3.3.14 derived from a χ^2 fit to high-quality data from the surface detector. The fit results in $\chi^2/N_{dof} = 1.03$

Parameter	value	uncertainty
o_0	-1.73	$\pm$ 0.09
o_1	-2.48	$\pm$ 0.03
d_1	0.43	$\pm$ 0.08
p_1	0.498	$\pm$ 0.008
s_1	20.6	$\pm$ 1.7
d_2	-0.26	$\pm$ 0.04
p_2	1.94	$\pm$ 0.03
s_2	17.0	$\pm$ 3.5

Table 3.4: The parameters derived from high quality data of the surface detector for the parameterised γ as in equation 3.3.17. The fit results in $\chi^2/N_{dof} = 1.1$.

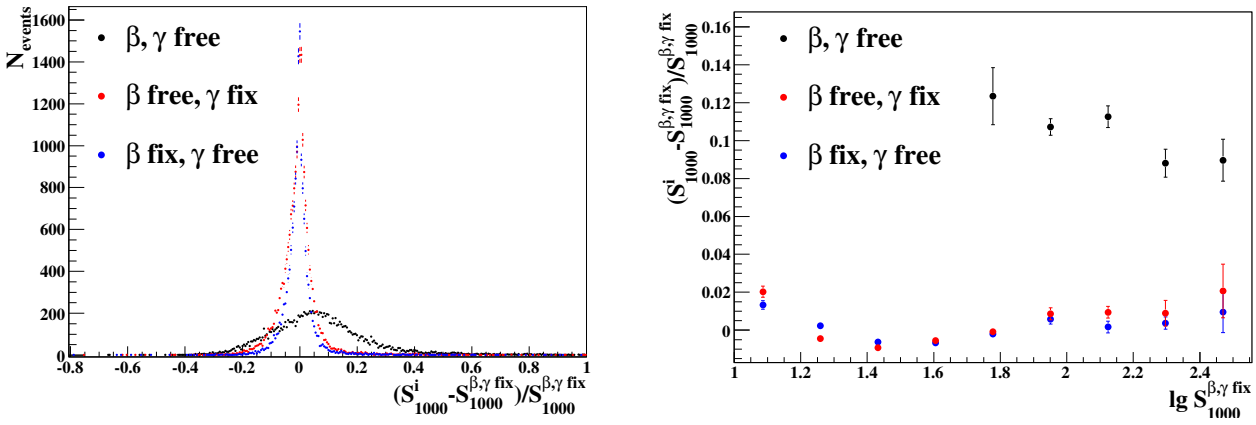

Figure 3.13: The difference in S_{1000} for one or both slope parameters fitted to the data with respect to the fit with a parameterised LDF. The right panel shows the overall distribution including all data reconstructible with the according fitting mode above $S_{1000}^{\beta,\gamma fix} > 15$ VEM. The left panel shows the behaviour as a function of the energy estimator.

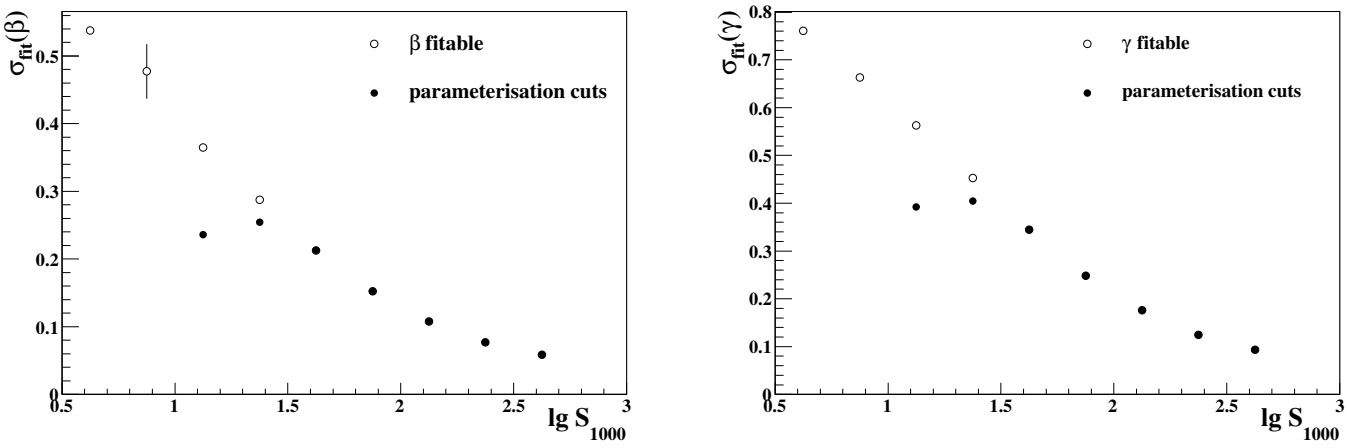

Figure 3.14: The uncertainties derived from the fitting procedure for the slope parameters β (right panel) and γ (left panel) of the modified NKG function used for reconstruction.

fluctuations. In figure 3.14 the uncertainty from the numerical fitting procedure is shown as a function of the energy estimator. The uncertainty depends only slightly on the zenith angle.

The second contribution to the uncertainty in the slope parameters is their intrinsic spread. Shower-to-shower fluctuations as well as different primary masses contribute to the spread of the slope parameters beyond fluctuations due to reconstruction. As the primary mass and intrinsic fluctuations cannot be determined on an event-by-event basis using only surface detector events the two contributions cannot be seperated. A hidden dependency on X_{max} can be expected but statistics of hybrid events passing the cuts for free slope parameters are not sufficient for conclusive studies on that [171]. In figure 3.15 the slope parameter spread is shown as a function of the energy estimator. For the determination of the spread the events have been weighted with the propagated fitting uncertainties from the reconstruction procedure from equation 3.3.20. The systematic uncertainty due to the intrinsic spread of the slope parameters around the parameterisation can be estimated by varying the slope parameters by their spread in the LDF fit. For this purpose the spread is parameterised as a function of the slope parameter

$$\begin{aligned} \sigma_i(S_{1000}) &= \exp(C_i + b_i \cdot \lg S_{1000}), \\ C_\beta = -0.733 \pm 0.003 &\qquad b_\beta = -0.895 \pm 0.003, \\ C_\gamma = -0.221 \pm 0.002 &\qquad b_\gamma = -0.783 \pm 0.003. \end{aligned} \tag{3.3.21}$$

The spread of the slope parameters depends only slightly on the zenith angle thus this dependency can be neglected. The variation of S_{1000} due to the variation of the slope parameter gives the propagation of the uncertainty caused by the parameterised slope parameters on the energy estimator. Together with the fitting uncertainty it gives the uncertainty on S_{1000} for the determination of the energy uncertainty of $2\,\%$ [170].

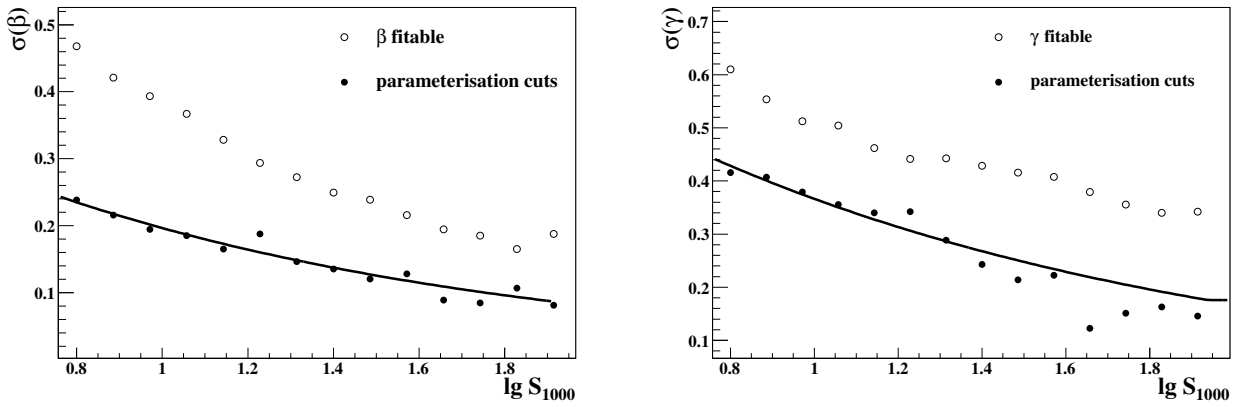

Figure 3.15: The event-to-event fluctuations of the slope parameters β (right panel) and γ (left panel) of the modified NKG function. Events are weighted with the uncertainty on the slope parameter from the LDF fit. The error bars give one standard deviation of the distribution. For comparisons the paramterisation from [170] is included.

Fitting Accuracy

The quality of the SD reconstruction depends on an LDF parameterisation that models the real LDF in the most realistic way. The slope parameterisations of different LDF parameterisation have been shown in the previous sections. In order to find the least biased LDF parameterisation quality criteria have to be defined for comparison. Approaches based on the fitting residuals of stations with signal and a method based on likelihood ratios [123, 170] have been studied.

Residual distributions of the lateral distribution function especially for high numbers of stations in the fitting procedure give a handle on the suitability of the assumed model. The residual of the fit

$$R_i = \frac{S_i - f_{LDF}(r_{SP,i}, \theta, S_{1000})}{\sigma_i} \tag{3.3.22}$$

with the signal S_i of station i, the LDF prediction f_{LDF} and the uncertainty of the signal $\sigma_i = 1.06\sqrt{S_i}$ [35] is plotted as a function of the core distance $r_{SP,i}$ in shower plane coordinates. If the LDF models the real distribution of the signal well, the distribution of the residuals does not only meet the conditions

$$\langle R \rangle = 0, \quad \sigma_R = 1 \tag{3.3.23}$$

over all core distances r_{SP} but also has a flat behaviour as a function of r_{SP}. Only stations with measured signal are accounted for in residual distributions. For stations without signal e.g. an unknown signal between 0 VEM and the threshold value of 3 VEM no residual can be defined. As the reconstruction algorithm accounts for stations without signal integrating over the probabilities for sub-threshold signals the residual distribution contains only a part of the full information used in the fit. Especially far away from the core the signals are low and only upward fluctuations of the particle density in a detector station are triggered. Therefore at high core distances a rise of the residuals is expected.

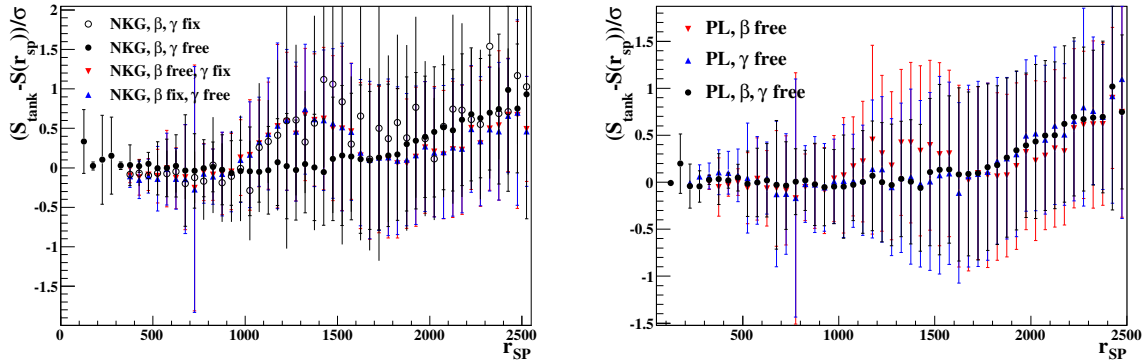

Figure 3.16: The mean residuals of the lateral distribution fit for the modified NKG function (left panel) and the modified powerlaw (right panel) as a function of the distance r_{SP} to the shower axis. A bump or wiggle is visible for all modes with one or more parameterised slope parameters.

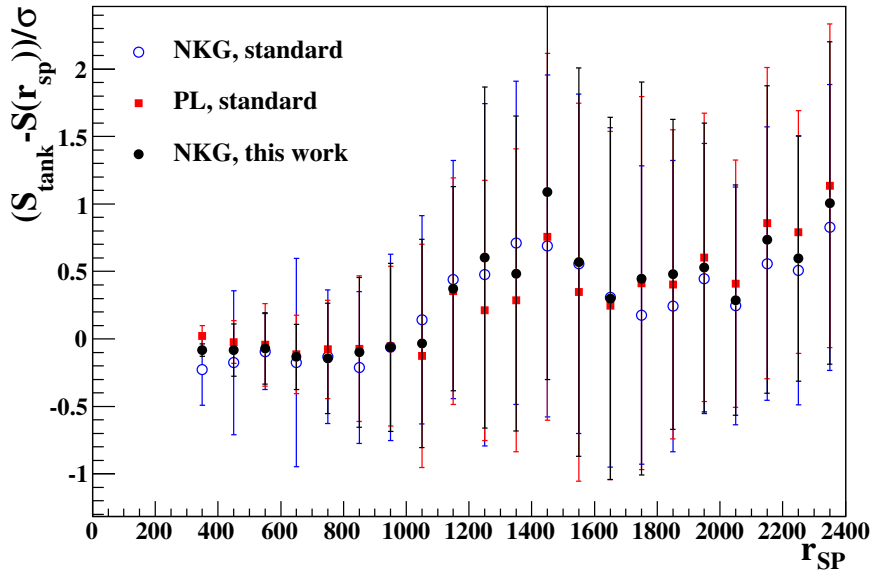

Figure 3.17: The residual distribution for various LDF parameterisations. The feature is visible consistently for all parameterisations.

Besides the predicted feature of rising residuals far from the core for both the modified NKG function and the modified powerlaw a bump at $1000\,\mathrm{m} < r_{SP} < 1500\,\mathrm{m}$ is observed if one or both slope parameters are fixed to a parameterisation. This bump is not visible in case of both slope parameters fitted to the data as free parameters. As stated above the parameters are highly correlated so no slope parameterisation can be derived from data reconstructed with both slope parameters fitted to the data. The bump is subject to further investigation.

In figure 3.13 the reconstructed values of S_{1000} for the slope parameters fitted or parameterised are shown. The deviation of S_{1000} for the different fitting modes contributes to the systematic uncertainty introduced by parameterised slope parameters.

When investigating the bump in the residuals the influence of the silent stations and therefore the contribution of upward fluctuations to the residuals has to be avoided. For this purpose a cut based on the signal expectation from the LDF model is introduced. The cut of $S_{LDF} = 10\,\mathrm{VEM}$ makes sure to sample only that part of each event that is free of an influence of the silent stations on the shape of the LDF residuals as a function of distance to the core. For better visualisation of the effect on S_{1000} the relative deviation of the signal from the LDF $S_{meas}/S_{LDF} - 1$ is used. In figure 3.18 the relative deviations for the old parameterisation [170], the updated parameterisation from this work, and an LDF fit with free parameters are compared. The structure of the bump is revealed to be basically a wiggle and not only a bump. The structure was fitted with a Fermi type function imitating the structure of the wiggle and being basically constant closer and farther from the core than the wiggle occurs.

For an event sample of (number of events) the NKG type LDF was fitted using the parameterisation from this work and fixing the core to the position given by the Fluorescence Detector. Additional to the regular cuts of `T4` and `T5` trigger and the event being reconstructed including silent stations, only non-saturated events were used. Also a quality cut on the Fluorescence Detector was required using the area of the error ellipse of FD given by the core uncertainty in direction of the SDP and the SDP uncertainty. The error ellipse was required to be not larger in area than m^2 equivalent to a symmetric core uncertainty of $100\,\mathrm{m}$. The distribution of the area of the error ellipse is shown in figure 3.19. For the Fermi function of the form

$$f(r) = \frac{1}{1 + \exp(\frac{r-\mu}{\tau})} \tag{3.3.24}$$

the values of $\mu =$ and $\tau =$ were found for a distance cut of $S_{LDF}(r) > 10\,\mathrm{VEM}$. The fit was performed neglecting upward fluctuations by a variable cut in $S_{LDF}(r)$. In figure 3.20 the evolution of the Fermi parameters as a function of the cut value is illustrated. For very low cut values the rejection of upward fluctuation is not efficient and for high cut values the lack of statistics at relevant core distances biases the fit. With the Fermi extension the wiggle in residuals and relative deviations from the LDF can be further reduced with respect to the updated parameterisation as visible through the relative deviations shown as *Fermi extension* in figure 3.18. The systematic uncertainty of S_{1000} due to the bias in the LDF parameterisation is reduced to $4\,\%$.

The likelihood ratio method [123] uses the likelihood as defined in equation 3.2 that is actually optimised in the LDF fit. As described above, the estimated number of particles in signal stations is used as well as the stations without signal in range of the shower are considered with the trigger threshold as upper limit. For saturated stations with the signal not being recovered the likelihood takes the saturated signal as a lower limit. As both LDF parameterisations diverge at the core position. So

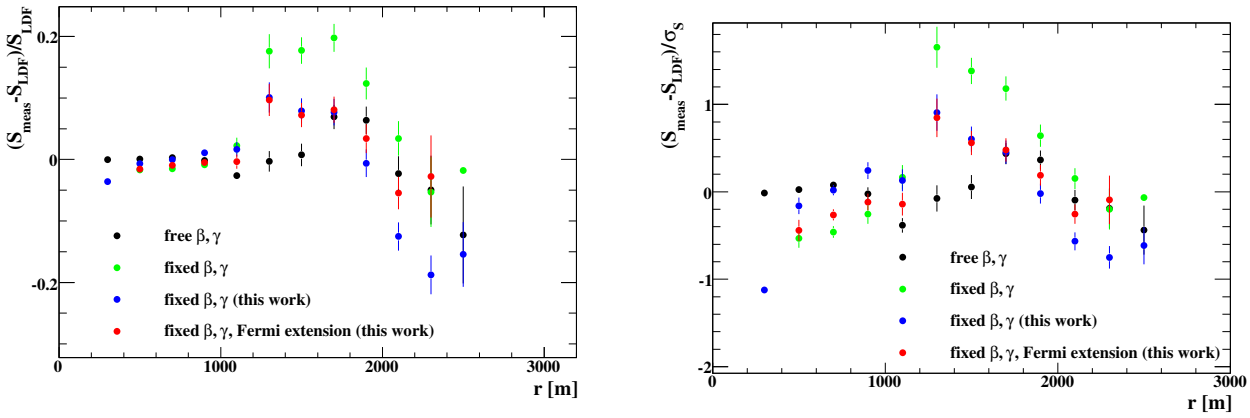

Figure 3.18: Relative deviations (left panel) and residuals (right panel) of stations with respect to the LDF fit with different parameterisations of the LDF. With the new parameterisation given in this work and the Fermi extension the non-flatness can be significantly reduced [139].

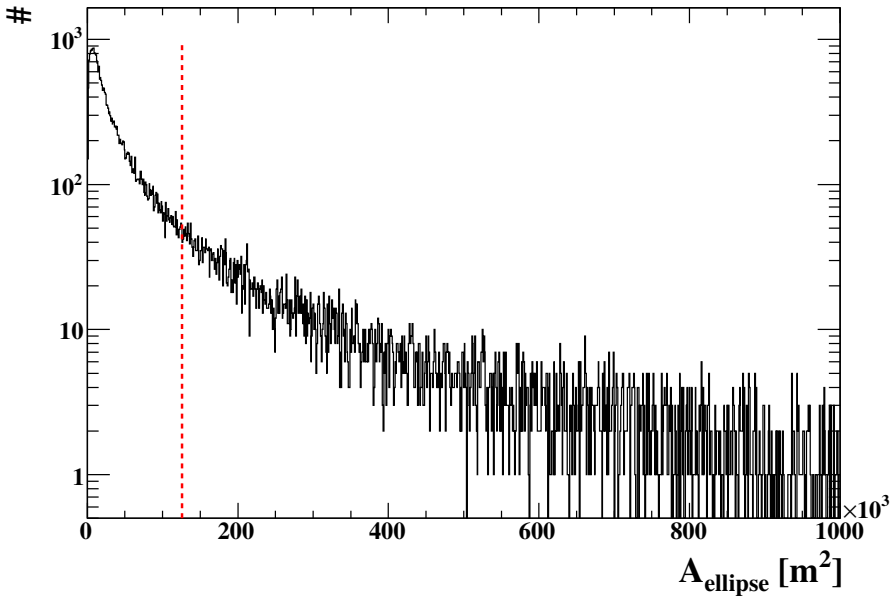

Figure 3.19: The uncertainty of the core position given by Fluorescence Detector reconstruction is asymmetric. The area of an ellipse accounting for both orthogonal uncertainties can be used to cut on the quality of the core position. The cut line is equivalent to a symmetric core uncertainty of 100 m.

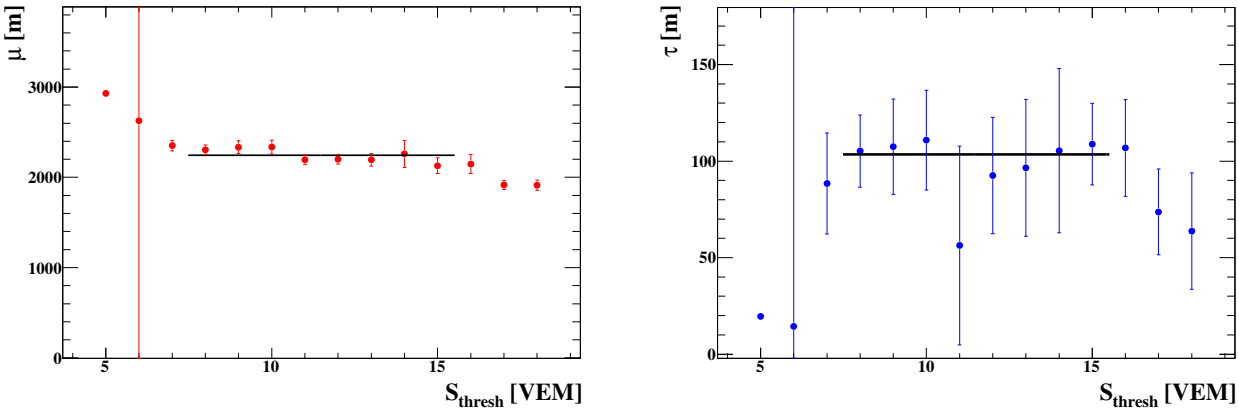

Figure 3.20: The parameters of the Fermi-type extension of the LDF function as derived from golden hybrid data. The fit values are shown as a function of the anti-silent-cut threshold. The fitting values are $\mu = (2243 \pm 24)$ VEM *with a* $\chi^2/N_{dof} = 8.14/7$ *and* $\tau = (103.5 \pm 9.5)$ VEM *with a* $\chi^2/N_{dof} = 1.19/7$.

unlike the residuals, the likelihood L includes everything as it is considered in the actual fit. A higher maximised likelihood on average indicates a better agreement of the statistical model with the data. For comparisons the ratio of the maximised likelihood of one model and the maximised likelihood of a reference model is defined as the likelihood ratio

$$R = \frac{L_{test}}{L_{ref}} \begin{cases} R > 1 & \Rightarrow \text{ test suits better} \\ R \approx 1 & \Rightarrow \text{ test and ref about equally fitting} \\ R < 1 & \Rightarrow \text{ ref suits better} \end{cases} . \tag{3.3.25}$$

As the value that is actually extremised is $-\lg L$ it is preferred to use the quality criterion actually applied in the fit. The condition can be transformed

$$D = -\lg R = (-\lg L_{test}) - (-\lg L_{ref}) \begin{cases} D < 0 & \Rightarrow \text{ test suits better} \\ D \approx 0 & \Rightarrow \text{ test and ref about equally fitting} \\ D > 0 & \Rightarrow \text{ ref suits better} \end{cases} . \tag{3.3.26}$$

As the fit gets more and more sensitive to the details of the fitted function the loglikelihood difference gains significance for higher numbers of triggered Surface Detector stations. The change with the parameterisation derived for the slope parameters of the modified NKG function above is very low with respect to [170]. Especially for moderate zenith angles and high numbers of triggered stations figures 3.21,3.22 shows the modified NKG function to be better than the modified powerlaw.

3.4 Shower Size Determination For Moderate And High Zenith Angles

Reconstruction algorithms for very inclined showers rely on different methods the reconstruction methods developed for low zenith angles [26, 46, 54, 71, 92, 94, 153]. At moderate zenith angles, the muonic component of an air shower becomes more and more dominant over the electromagnetic

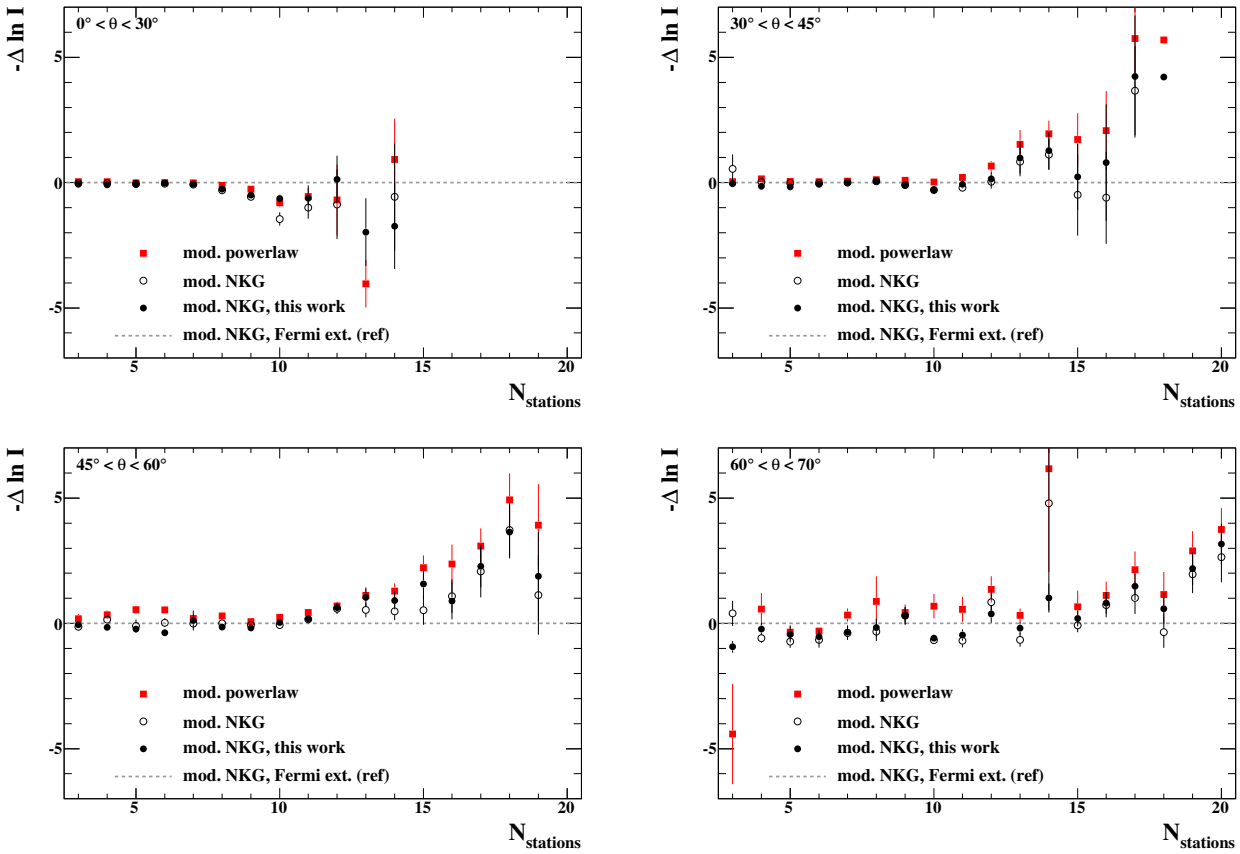

Figure 3.21: Likelihood ratios of the LDF fit. The loglikelihood differences for reconstruction with the modified powerlaw and the modified NKG function with slope parameterisations given in [170] are compared with reconstruction using the modified NKG function parameterised as derived above. With more detector stations the fit gets more sensitive to deviations of the LDF model from the distribution in data. Three low zenith angle bins and one moderately inclined bin are shown. The error bars give the standard deviation for each bin.

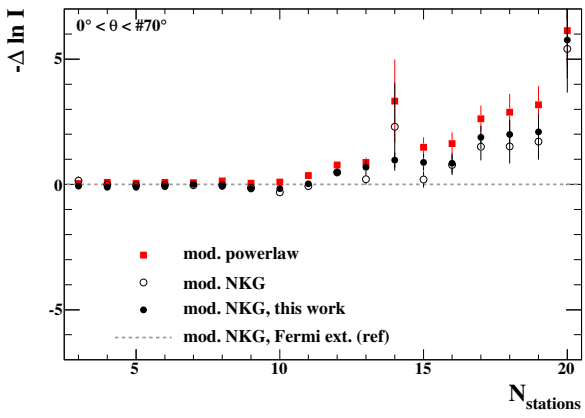

Figure 3.22: Likelihood ratios of the LDF fit for the whole zenith angle interval. The loglikelihood differences Give a measure of the accuracy of the LDF model with respect to data. Especially with high numbers of stations deviations of the model from the true are reflected in worse optimised likelihood using a worse function.

particles. Muons are the only surviving component at high zenith angles. In addition muons travel very long distances in the atmosphere and therefore a significant deflection by the geomagnetic field can be observed. The two-dimensional pattern of measured signal caused by muons at moderate and high zenith angles in Surface Detector stations is modelled from Monte Carlo simulations. The pattern of signal prediction is fitted to Surface Detector data using a maximum likelihood method giving a shower size parameter as the normalisation.

Fitting procedure

As for vertical and moderately inclined air showers the reconstruction of the shower size is based on a model of the shower footprint in energy deposit depending on the incoming direction and the primary energy. In addition to the dependency of the LDF on the zenith angle the two-dimensional footprint of an inclined air shower also depends on the azimuth angle ϕ as the radial symmetry of the muon LDF is broken by the geomagnetic field. Thus the probability P_i of observing a signal S_i in a station at the position (x_i, y_i) neglecting the altitude is

$$P_i = P_i(S_i(x_i, y_i)|E, x_c, y_c, \theta, \phi) \tag{3.4.1}$$

with the core position (x_c, y_c) on ground. With the incoming direction reconstructed seperately as described at 3.1 there are only three free parameters: The shower core position and the energy E. Assuming a model for P_i the P_i are combined in a *Likelihood function* [29, 71, 73, 153]

$$L(\{S_i\}|E, x_c, y_c; \theta, \phi) = \prod_i P_i(S_i(x_i, y_i)|E, x_c, y_c, \theta, \phi). \tag{3.4.2}$$

The function defined in equation 3.4.2 reaches its maximum for the best estimate of the free parameters E, (x_c, y_c). In event reconstruction the Likelihood function has to be maximised numerically to obtain the free parameters. Most numerical optimisation packages implement minimisation instead of maximisation and as summation provides better numerical stability the actual implementation uses a *Loglikelihood method* minimising

$$\ell = -\lg L = -\sum_i \lg P_i(S_i(x_i, y_i)|E, x_c, y_c, \theta, \phi). \tag{3.4.3}$$

The dependency on the shower footprint model is completely within the individual probabilities P_i. So the information can be used station by station reflecting the content of information better than in a multiplication of probabilities. The probabilities are built of models derived from Monte Carlo simulations as described below.

The Likelihood function is composed of the *Muon Profile*, the *Tank Response* and the *EM Correction*. *Silent Stations* that were in data acquition when the event occured but had no signal are included as upper limit. In order to keep the fit fast they are only accounted for within a radius from the core $r_{silent} = 1000\,\mathrm{m}$. For stations in range but without signal the p.d.f. is integrated from zero to the signal threshold of a detector station giving the probability for a sub-threshold signal given an expected muon number from the muon profile.

Putting everything together the Likelihood function to maximise is composed of two products for the triggered stations and the silent stations respectively:

$$
\begin{aligned}
& L(\{S_i\}|R_\mu, x_c, y_c, \theta, \phi) = L_{\text{triggered}} \cdot L_{\text{silent}} \\
L_{\text{triggered}} &= \prod_i \sum_{k=0}^{\infty} f\big(S_i/(1+\epsilon(x_i,y_i,\theta,\phi))|\theta_{\mu,i},k\big)\, dS\, P\big(k|\lambda(x_i,y_i,\theta_{\mu,i},\theta,\phi)\big) \\
L_{\text{silent}} &= \prod_j \sum_{k=0}^{\infty} (1+\epsilon(x_j,y_j,\theta,\phi)) \int_0^{S_{\text{th}}/(1+\epsilon(x_j,y_j,\theta,\phi))} \mathrm{d}s\, f\big(s|\theta_{\mu,j},k\big)\, P\big(k|\lambda(x_j,y_j,\theta_{\mu,j},\theta,\phi)\big).
\end{aligned}
\tag{3.4.4}
$$

The three components are described in the following.

The Muon Profile is the basic element of the shower footprint as for high zenith angles muons give the largest particle content on ground. So the predicted signal and the probability to observe a signal S_i is dominated by the prediction of the muon density

$$n_\mu = n_\mu(x - x_c, y - y_c, \theta, \phi, E, A) \tag{3.4.5}$$

with the geomagnetic field and the altitude assumed to be constant. Besides the primary energy E, the position relative to the core $(x - x_c, y - y_c)$ and the arrival direction (θ, ϕ) muon density also depends on the atomic number of the primary A. It can be shown from simulations [26, 27, 72] that n_μ factorises into the total muon number N_μ and a normalised density profile

$$n_\mu \approx N_\mu(\theta, E, A) \cdot p_\mu(x - x_c, y - y_c, \theta, \phi) \tag{3.4.6}$$

neglecting effects lower than $5\,\%$. Besides the primary energy E and the atomic mass of the primary A the total muon number depends on the zenith angle θ due to muon loss while propagating through the atmosphere. The muon lateral distribution, its distortion by geomagnetic deflection and the elongation of the footprint by projection on ground are modelled by the normalised profile. Hence the profile p_i is strongly dependent on the zenith angle. So the density profile can be separated into a normalisation factor and the profile also separating the three free parameters. Introducing the ratio of the total muon number of an example shower to the total muon number of a reference shower with the primaries atomic mass A_{ref} and the primary energy E_{ref}

$$R_\mu(E, A, E_{ref}, A_{ref}) = \frac{N_\mu(\theta, E, A)}{N_\mu(\theta, E_{ref}, A_{ref})} \tag{3.4.7}$$

the zenith angle dependency of the normalisation factor can be removed through rewriting the muon profile

$$
\begin{aligned}
n_\mu &\approx R_\mu(E, A, E_{ref}, A_{ref}) \cdot N_\mu(\theta, E_{ref}, A_{ref}) \cdot p_\mu^{ref}(x - x_c, y - y_c, \theta, \phi) && (3.4.8) \\
&= R_\mu(E, A, E_{ref}, A_{ref}) \cdot n_\mu^{ref}(x - x_c, y - y_c, \theta, \phi, E_{ref}, A_{ref}). && (3.4.9)
\end{aligned}
$$

	E_0	γ
proton, QGSJET-II	10.3	1.02
iron, QGSJET-II	7.3	1.05

Table 3.5: The constants of equation 3.4.14 for simulated data sets [75]. For real data the atomic mass is not known on an event by event basis. The uncertainty of calibration using the energy input to Monte Carlo generation therefore is large. The values are derived in chapter 4

The choice of the reference energy E_{ref} and the reference atomic mass A_{ref} is arbitrary. For the typical energy range of the Pierre Auger Observatory in UHECR ($10^{18}\,\mathrm{eV} < E < 10^{20}\,\mathrm{eV}$) the choice of $E_{ref} = 10^{19}\,\mathrm{eV}$ aims on using a reference profile n_μ^{ref} as closely to the bulk of the measured showers as possible. As the atomic mass of the primary particle can not been determined on an SD event-by-event basis the choice of the reference atomic mass $A_{ref} = 1$ is arbitrarily. These parameters of the reference profile are common for various analyses of very inclined air showers [26, 27, 72] and so the abbreviation

$$N_{19} = R_\mu(E, A, E_{ref} = 10^{19}\,\mathrm{eV}, A_{ref} = 1) \tag{3.4.10}$$

is defined consistently with the parallel analyses. The total muon number of a shower at a given state of development e.g. zenith angle θ and for a given primary is correlated with the shower energy

$$E \sim \cdot N_\mu^\gamma(\theta, E, A) \tag{3.4.11}$$

via a power-law. As attenuation of muons is not dependent on the total number of muons, γ is independent of the zenith angle. Using N_{19} or any other $R_\mu(E, A, E_{ref}, A_{rf}$ equation 3.4.11 can be rewritten

$$\frac{E}{E_{ref}} = \frac{N_\mu(\theta, E, A)}{N_\mu(\theta, E_{ref}, A_{ref})}^{\gamma} \quad \text{or} \tag{3.4.12}$$

$$E = E_{ref} \cdot R_\mu^\gamma \overset{E_{ref}=10^{19}\,\mathrm{eV}, A_{ref}=1}{=} E_{ref} \cdot N_{19}^\gamma \tag{3.4.13}$$

with the assumption of the primary mass A being equal to the reference primary mass $A_{ref} = 1$. For SD only events the primary mass is not known on an event-by-event basis. Also hadronic interaction models used in simulation do not perfectly reproduce real data. A more general relation between N_{19} and the primary energy leaves the scale energy E_0 as a free parameter

$$E = E_0 \cdot N_{19}^\gamma. \tag{3.4.14}$$

For different combinations of primary mass and interaction models in reference data and reconstructed data E_0 can vary at a level of $70\,\%$. The slope γ is less sensitive, it scales from $1.05 < \gamma < 1.10$ [71, 78, 93, 95, 153]. The actual values for simulated data are shown in table 3.5. The values for real data are determined using high quality events measured simultaneously with the fluorescence

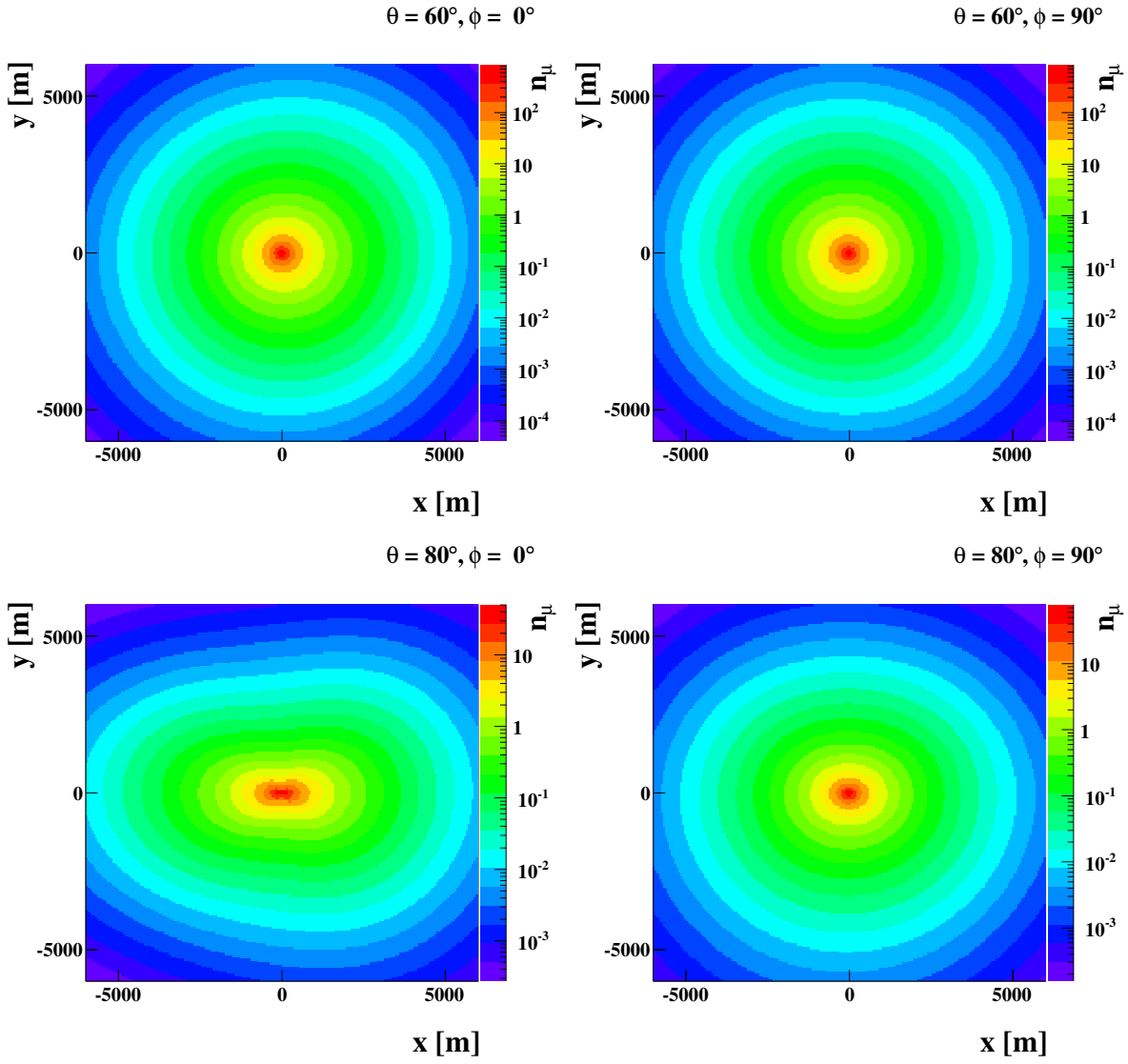

Figure 3.23: Muon density profiles used in reconstruction of moderately and very inclined extensive air showers in shower plane coordinates. The two-dimensional structure depends on the zenith angle θ and on the azimuth angle ϕ. A comparison of this paramererised model with other models [153, 159] has been performed in [70, 71].

and surface detectors respectively and by using the overlap region with the LDF reconstruction for cross-calibration in chapter 4.

The reference muon profile $n_\mu(x-x_x, y-y_c, \theta, \phi, E_{ref} = 10^{19}\,\mathrm{eV}, A_{ref} = 1)$ used for reconstruction has been extracted from Monte Carlo simulated extensive air showers. The profiles are are a high-dimensional parameterisations of the shape depending on the zenith angle θ and the azimuth angle ϕ [72]. The muon density is given in ground plane coordinates and shown in figure 3.23. The air shower library the parameterisation was fitted to was produced using the air shower simulation code `CORSIKA` [114] using the hadronic interaction models `QGSJET-II` [154] for high energy and `FLUKA` [96, 97] for low energy interactions. The muon densities are only defined in the ground plane neglecting the curvature of the surface of the earth and altitude differences respectively. A three-dimensional parameterisation is aimed for as soon as planar and horizontal observation level definitions in simulation codes are replaced by more flexible structures.

With the muon density $N_{19} \cdot n_\mu(x - x_c, y - y_c, \theta, \phi, E = 10^{19}\,\mathrm{eV}, A = 1)$ on ground a prediction for the muon number in each tank depending on core position, energy and arrival direction of the shower is available.

The Tank Response function couples the muon density n_μ to a signal prediction and a probability for the measurement of a signal S_i given the primary energy, incoming direction and core position. For the calculation of the signal only the muon density is taken into account. The treatment of the electromagnetic halo and the residual electromagnetic component is given in the next paragraph.

As pointed out in section 1.2, nearly all air shower muons that reach the ground are approximately minimally ionising particles propagating through Water-Cherenkov-Detectors without hard interactions [114]. So they produce Cherenkov radiation on their full path length traversing a surface detector station $l_{\mu,i}$ [13]. The signal created by multiple air shower muons in a detector station is

$$S_\mu \sim \sum_i^k l_{\mu,i} \tag{3.4.15}$$

with the total number k of muons hitting the tank. For the determination of the individual track length of each muon the entry point and the muon direction has to be known. The muon inclination is modelled depending on the incoming direction and the distance to the impact point [71, 159]. Still the point of entering the volume of the detector station is not known, so a probability density function of the track lengths $l_{\mu,i}$ and the average muon incoming direction is used instead. With the radial symmetry of surface detector stations with three photomultipliers working the probability density function is only a function of the local muon inclination θ_μ and not on the local muon azimuth. Muon dominated data is described well by the convolution of the track length distribution with an empirical charge-collection function [87, 180] although full Monte Carlo simuations are used instead of an analytical approach. From the probability distribution function for a single muon $f(S_\mu|\theta_\mu, 1)$ the probability function for k muons is derived via autoconvolution [78]

$$\begin{aligned} f(S_\mu|\theta_\mu, k) = & \int \mathrm{d}s_{k-1} \int \mathrm{d}s_{k-2} \ldots \int \mathrm{d}s_2 \int \mathrm{d}s_1 \cdot \\ & f(S_\mu - s_{k-1}|\theta, 1) f(s_{k-1} - s_{k-2}|\theta, 1) \ldots f(s_2 - s_1|\theta, 1) f(s_1|\theta, 1) \end{aligned} \tag{3.4.16}$$

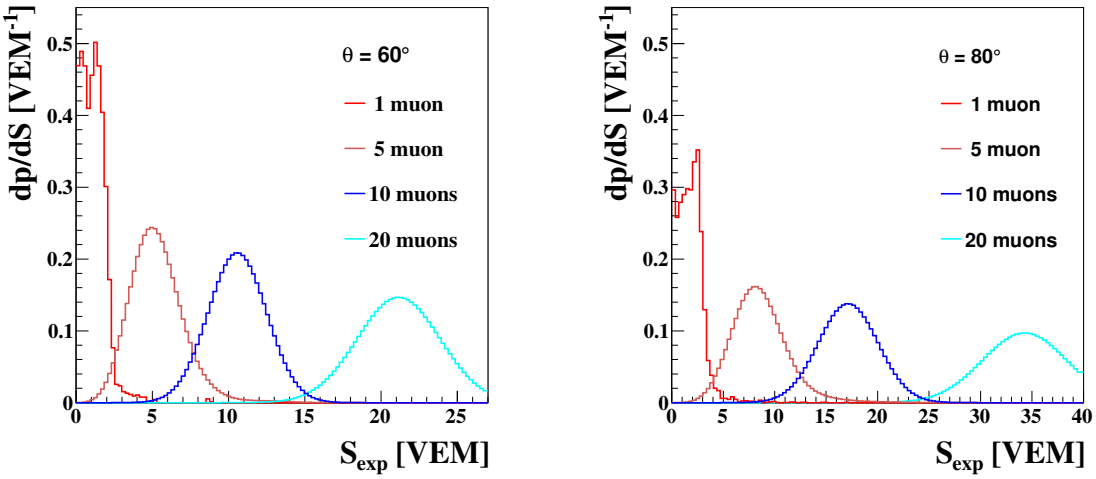

Figure 3.24: The probability for measuring a given signal if N muons hit the tank. Electromagnetic particles are not accounted for but fluctuations due to the electromagnetic component are included in the p.d.f. [71] The tank response function is zenith angle dependent through the different mean track length of muons in the tank.

The actual probability density functions for the one muon tank response were extracted from the air shower library [75]. The fluctuations of the electromagnetic component are included into the muon tank response for now [71]. For this purpose detector stations hit by one muon with known muon incident angle from the Monte Carlo set were used to build the one muon p.d.f. following the development in [26, 46, 54, 71, 92, 94, 153]. Figure 3.24 gives an example of the one muon p.d.f. at two zenith angles. Also the p.d.f.s for more muons derived through autoconvolution are shown. As an example the ten muon p.d.f. is emphasised.

The muon-only likelihood function can now be written down with the probabilities for measuring the actual signal being the sum over the tank response to k muons and the probability of having k muons in that surface detector station given by a Poissonian:

$$\begin{aligned} L_\mu(\{S_{\mu,i}\}|R_\mu, x_c, y_c, \theta, \phi) &= \prod_i \sum_{k=0}^{\infty} f(S_{\mu,i}|\theta_{\mu,i}, k)\, P\big(k|\lambda(x_i - x_c, y_i - y_c, \theta_{\mu,i}, \theta, \phi)\big) dS \\ \text{with} \quad P(k|\lambda) &= \frac{1}{k!}\lambda^k e^{-\lambda} \\ \lambda(x_i - x_c, y_i - y_c, \theta_{\mu,i}, \theta, \phi) &= A_{\text{eff}}(\theta_{\mu,i}) \times R_\mu \times n_\mu^{\text{ref}}(x_i - x_c, y_i - y_c, \theta, \phi) \end{aligned} \tag{3.4.17}$$

with the effective ground area A_{eff} of a detector station seen by muons at an incident angle of θ_μ, the expected muon number λ in the detector station and the positions of the station (x_i, y_i) and the core (x_c, y_c) respectively. For the purely muonic signal this Likelihood function is sufficient. However even old showers with only muons reaching the ground show an electromagnetic contribution to the signal. Thus a realistic signal modelling needs a treatment for this effect.

The local muon incoming direction is calculated from the spherical shower model (see section 3.1). By assuming the estimated origin of the shower $\vec{R_c}$ being the origin of all shower muons the local muon incoming direction is

$$\vec{a_\mu} = \frac{\vec{R_c} - \vec{s_i}}{\|\vec{R_c} - \vec{s_i}\|} \tag{3.4.18}$$

with the position of the station $\vec{s_i}$. Due to the cylindrical symmetry of the detector stations only $\theta_\mu = \arccos(\vec{a_\mu} \cdot \vec{e_z})$ with the local normal vector of ground is required.

The Electromagnetic Component of the signal in the surface detector for a very inclined shower consists of two main contributions as shown in section 1.2: The primary electromagnetic component that is dominant close to the shower axis for zenith angles below 65° and the electromagnetic halo of muons.

The primary electromagnetic component and the halo cannot be distinguished on ground. The whole electromagnetic component is modelled by an increase of the signal by the expectation value of the ratio between electromagnetic contribution and muonic signal [195]:

$$\begin{aligned} S_{tot} &= S_\mu \cdot (1 + \epsilon) \\ \epsilon(x - x_c, y - y_c, \theta, \phi, E, A) &= \left\langle \frac{S_{em}}{S_\mu} \right\rangle \end{aligned} \tag{3.4.19}$$

If the variance of the electromagnetic content of the signal caused by a shower in a detector station is lower than the variance of the muonic signal the electromagnetic contribution to the signal can be modelled on average

$$g(S_{tot}) \approx f(S_\mu + \epsilon) \approx f\left(\frac{S_{tot}}{1 + \epsilon}\right) \tag{3.4.20}$$

with the probability g to measure a total signal S_{tot} approximated by the probability to measure the estimated muonic signal S_μ which is the full signal reduced by the expected value of the electromagnetic contribution. Figure 3.25 shows the profile of ϵ in two dimensions. The averaged contribution neglecting the asymmetries is shown in figure 3.26 to demonstrate the different absolute influence depending on zenith angle. For $\theta = 60^\circ$ the asymmetry due to the primary electromagnetic component is obvious. The parameterisation has been extracted from simulations in [195]. Its dependencies on primary mass, hadronic interaction model and energy have been studied. For now those dependencies are neglected in the implementation giving a systematibias of less than $10\,\%$ [196].

As the detector stations are not on exactly the same altitude and for large footprints the curvature of the earth gives a significant deviation from the ground plane in core-centered coordinates the detector stations are projected into the ground plane along the local muon incoming direction $\vec{a_\mu}$.

For the actual implementation initial values for the core position are given by the position of the barycenter of the station signals in the event. An initial value for R_μ is found by a one parameter χ^2 method using the signal expectation from the models used in the Likelihood function while the

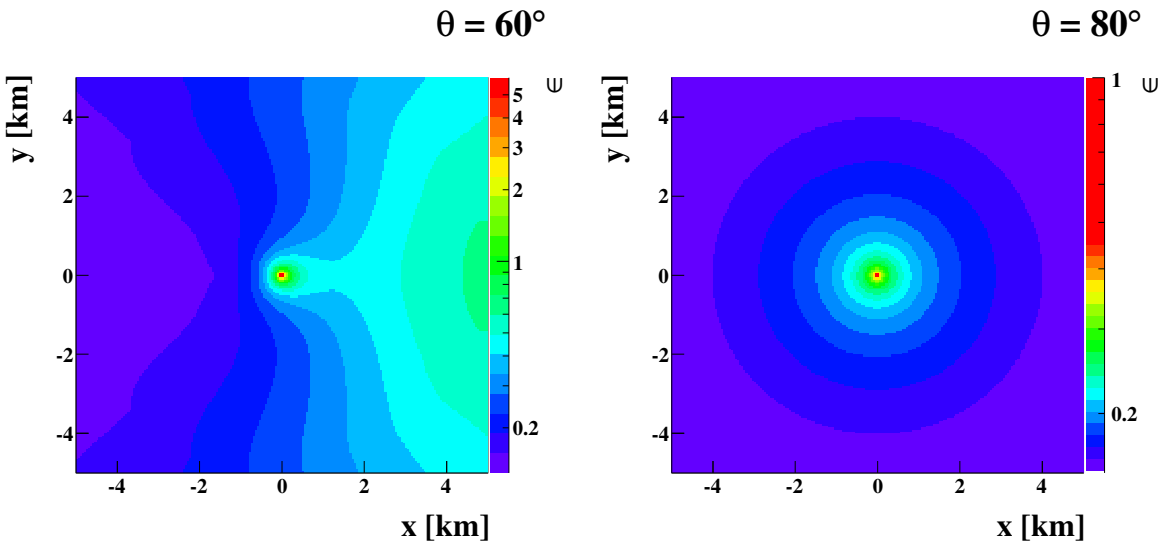

Figure 3.25: The expectation value ϵ of the contribution of electromagnetic particles to the signal in a station divided by the signal contribution by muons projected into the shower plane. Asymmetries occur especially for the low zenith angle range. The asymmetries are due to the primary electromagnetic component. The radial decrease of the electromagnetic contribution is caused by the muon energy distribution at high zenith angles. At lower zenith angles the decrease is due to the lateral shape of the primary electromagnetic component.

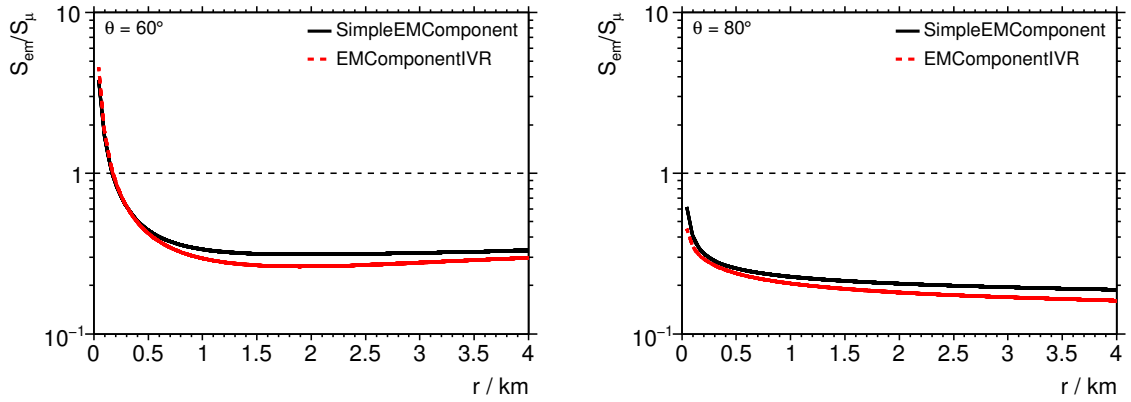

Figure 3.26: The average radial dependency of the electromagnetic content of an inclined shower on ground for two different zenith angles θ.

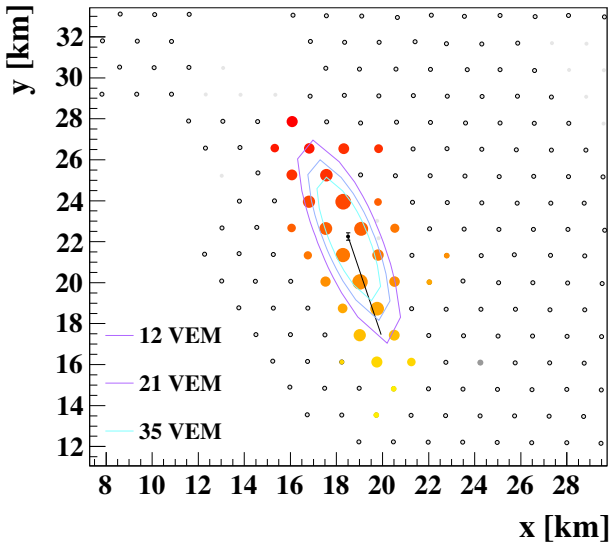

Figure 3.27: An example event (Event Id 6606282, recorded 2008/10/15, $E = (2.57 \pm 0.17) \cdot 10^{19}$ eV, energy estimator $N_{19} = 5.0 \pm 0.3$, zenith angle $\theta = 78.16° \pm 0.06°$, azimuth angle $\phi = 286.62° \pm 0.04°$) reconstructed using the reconstruction for very inclined air showers. The expected signal is drawn on the array via contour lines.

core is fixed to the position of the maximum. As the muon profile, the tank response function and the electromagnetic component term are very sensitive on changes in zenith angle θ the reconstruction procedure is carried out iteratively. After a first shower size determination by the log likelihood method the incoming direction is refined with a fit of the spherical model using the refined core position. These two steps are repeated until convergence. An example event with the expected signal map visualised by contour lines is shown in figure 3.27. The resulting resolution of the reconstructed shower properties is discussed in chapters 4, 5.

3.5 Fluorescence Detector Reconstruction

As pointed out in chapter 2, the concept of Fluorescence Detector measurements is a complementary approach to detecting extensive air showers by Surface Detector arrays. The measurement of the longitudinal profile leads to a quasi-calorimetric measurement of the primary energy of an extensive air shower. Air showers measured with the Fluorescence Detector and the Surface Detector simultaneously can be used for calibration of the Surface Detector energy estimate not depending on air shower simulations. The shower direction is determined using the calibrated timing information from the Fluorescence Detector pixels and additional timing information from one Surface Detector station. The determination of the deposited energy in the atmosphere is performed subsequently as it depends strongly on the knowledge of the reconstructed shower track.

Geometry Reconstruction

As described in [179, 189] the shower geometry is determined by the *Shower Detector Plane* (SDP) and the position of the shower track within this plane as illustrated in figure 3.28. The determination

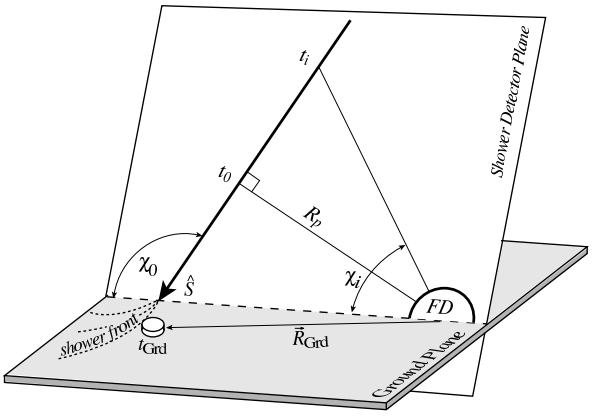

Figure 3.28: The Fluorescence Detector geometry reconstruction. The shower-detector plane (SDP) is determined from the pixel pointing directions of the camera. The position of the shower within the SDP is given by the timing of the triggered pixels of the fluorescence telesope together with the timing and position of a single Surface Detector station [189].

of the SDP containing the fluorescence telescope and the shower track requires the pointing directions $\vec{p_i}$ of each pixel i weighted with the total integrated signal of the pixel S_i. The normal vector of the SDP is found by minimising

$$Q^2 = \sum_i S_i \quad |\vec{p_i} \cdot \vec{n}|. \tag{3.5.1}$$

The position of the shower track within the SDP is identified using the timing information of the pixels. It is defined by the minimum distance of the shower track from the detector R_p and the angle between the shower axis and the line of intersection of the ground plane and the SDP χ_0. The origin in time t_0 is defined by the time the shower front reaches the closest point to the telescope at R_p. With the timing uncertainty $\sigma(t_i)$ the minimisation function is defined as

$$\chi^2 = \sum_i \left(\frac{t_i^{\text{exp}} - t_i^{\text{meas}}}{\sigma(t_i)} \right)^2 . \tag{3.5.2}$$

The expected time t_i^{exp} is calculated from geometrical considerations in the frame of the SDP with the shower moving along the axis with the speed of light

$$t_i^{\text{exp}} = t_0 + \frac{R_p}{c} \cdot \tan\left(\frac{\chi_0 - \tilde{\chi_i}}{2} \right). \tag{3.5.3}$$

The elevation angle $\tilde{\chi_i}$ is given as the angle between the pixel pointing direction $\vec{p_i}$ and the line of intersection of the SDP with the ground plane. The parameters t_o, R_p and χ_0 are highly correlated and therefore a simultaneous fit gives results with large uncertainties. With the timing information of a Surface Detector station the χ^2 can be extended to

$$\chi^2 = \sum_i \left(\frac{t_i^{\text{exp}} - t_i^{\text{meas}}}{\sigma(t_i)} \right)^2 + \left(\frac{t_{SD}^{\text{exp}} - t_{SD}^{\text{meas}}}{\sigma(t_{SD})} \right)^2 \tag{3.5.4}$$

with the expected start time of the Surface Detector station t_{SD}^{exp} determined by the propagation of the shower along the shower track defined by the shower axis $\vec{a}$

$$t_{SD}^{\text{exp}} = T_0 + \frac{(\widehat{SD}_i - \widehat{FD}) \cdot \vec{a}}{c} \tag{3.5.5}$$

with the position $\widehat{SD}_i$ of the Surface Detector station and the position of the Fluorescence Detector telescope $\widehat{FD}$. With the additional information from the well defined position $\widehat{SD}_i$ and the corresponding timing information t_{SD}^{meas} the correlation is broken. The Surface Detector station in hybrid reconstruction is required to be closer than $2\,\text{km}$ to the intersection of the shower track with the ground plane. The station with the highest signal is used. The angular resolution is of the order of 0.5° [50] for typical events.

Energy Reconstruction

The light flux at the aperture of the Fluorescence Detector is not point-like because of the extensive shower disc, projection effects and scattering in the atmosphere. A signal-over-noise maximisation algorithm [101] gives the optimum radius ζ for the integration over the camera image at any time time. The integration over the signal of all pixels within ζ from the center of the shower image on the camera gives the number of photons at the aperture $N_\gamma^{\text{ap}}(t)$ as a function of time.

The light detected at the aperture is produced in two major processes: fluorescence of Nitrogen molecules and Cherenkov radiation [31, 65–67, 176]. During propagation through the atmosphere the photons are scattered and partly absorbed. The direct and scattered light components are shown schematically in figure 3.29. The two relevant scattering effects are Rayleigh scattering of photons by particles smaller than the wavelength and Mie scattering by particles larger than about ten times the wavelength of the photons. With scattering the light at aperture is composed of three main contributions: fluorescence light partly attenuated by scattering, scattered and direct Cherenkov light.

The amount of fluorescence light N_γ^f produced is directly proportional to the energy deposit in the atmosphere $\mathrm{d}E/\mathrm{d}X$. The proportionality factor is the *fluorescence yield* Y^f as described in section 2.1. So

$$N_\gamma^f(X_i) = Y^f \frac{\mathrm{d}E_i}{\mathrm{d}X} \Delta X_i \tag{3.5.6}$$

fluorescence photons are produced at an atmospheric depth X_i traversed by the shower. Y^f depends on the temperature, the pressure and the relative humidity [24,125,149,200] at the point of production of fluorescence photons. The systematic uncertainties of the fluorescence yield of $14\,\%$ dominate the uncertainty of the energy scale of the Pierre Auger Observatory [2]. Due to the relatively low intensity of fluorescence light the effects of Rayleigh scattering and Mie scattering result approximately only in attenuation of the direct fluorescence light. The transmission factor of T_i is used to describe these effects. With the aperture A and the detection efficiency ϵ the fluorescence light flux y_i measured [172, 189] is

$$y_i^f = \frac{A\epsilon T_i}{4\pi r_i^2} Y_i^f \frac{\mathrm{d}E_i}{\mathrm{d}X} \Delta X_i. \tag{3.5.7}$$

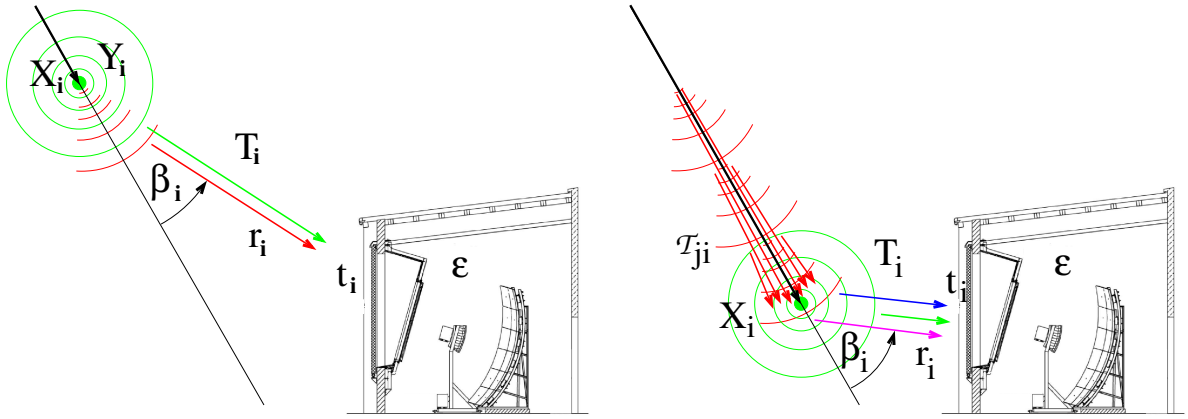

Figure 3.29: A schematic view of the direct (left) and indirect light components (right) to the light at the aperture of the fluorescence detector [189, 192]

Cherenkov radiation is produced by charged particles above an energy threshold corresponding to the propagation faster than the speed of light in air [60, 61, 183]. Basically all electrons and positrons N_e in an extensive air shower have velocities above the Cherenkov threshold in air. So the number of produced Cherenkov photons at X_i is

$$N_\gamma^C(X_i) = Y^C N_e(X_i) \tag{3.5.8}$$

with the Cherenkov yield Y_C depending on the altitude [82, 105, 120, 151]. $N_e(X_i)$ is the number of electrons and positrons at the traversed depth X_i. With the Cherenkov cone described by the fraction $f^C(\beta_i)$ of photons emitted with an angle β_i to the shower axis

$$y_i^{C,d} = \frac{A\epsilon T_i}{4\pi r_i^2} Y_i^C f^C(\beta_i) N_e(X_i) \tag{3.5.9}$$

is the measured direct Cherenkov light. The angular distribution $f^C(\beta_i)$ of Cherenkov photons with respect to the shower axis is wider than the narrow Cherenkov cone because the directions of the emitting particles deviate from the shower axis. Nevertheless the Cherenkov emission is dominant in forward direction building up an intense Cherenkov beam along the shower axis. In a simplified one-dimensional approach the Cherenkov beam at a depth X_i builds up from the Cherenkov emission at the previous depths attenuated by an attenuation coefficient τ_{ji} giving the number of photons

$$N_\gamma^{C,beam}(X_i) = \sum_{j=0}^{i} \tau_{ji} Y_j^C \Delta X_j N_e(X_j). \tag{3.5.10}$$

Even with a low fraction $f_S(\beta_i)$ of light scattered towards the detector a significant contribution of scattered Cherenkov light can result from the beam. The contribution of scattered Cherenlov light $y_i^{C,s}$ can be expressed similarily to the direct contributions

$$y_i^{C,s} = A\epsilon T_i f_s(\beta_i) \sum_{j=0}^{i} \tau_{ji} Y_j^C \Delta X_j N_e(X_j). \tag{3.5.11}$$

Adding all direct and scattered contributions the total measured light flux in the detector at time t_i is

$$y_i = y_i^f + y_i^{C,d} + y_i^{C,s}. \tag{3.5.12}$$

The different light contributions at the detector are composed of energy losses in the atmosphere w_i that can be expressed by the number of electrons N_i^e

$$w_i = N_i^e \cdot \alpha_i \tag{3.5.13}$$

with the average energy loss of a single electron α_i. With this relation the light fluxes at the detector can be combined and expressed by the *Cherenkov-fluorescence matrix* [190] accounting for the light emission and transmission mechanisms respectively:

$$y_i = \sum_j C_{ij} w_i. \tag{3.5.14}$$

The profile of energy deposit in the atmosphere observed by the Fluorescence Detector is obtained by matrix inversion of C_{ij}. In general the limited field of view of the fluorescence telescopes does not allow the observation of the complete shower development in the atmosphere. With the *Gaisser-Hillas function* [101]

$$f_{GH} = \left(\frac{\mathrm{d}E}{\mathrm{d}X}\right)_{max} \cdot \left(\frac{X - X_0}{X_{max} - X_0}\right)^{\frac{X_{max}-X_0}{\Lambda}} \cdot \exp\left[\frac{X_{max} - X}{\Lambda}\right] \tag{3.5.15}$$

the profile of energy deposit by the electromagnetic component is modelled empirically for the whole shower development. X_0 corresponds to the atmospheric depth of the first interaction while Λ corresponds roughly to the attenuation of the shower in the atmosphere. If the depth of the shower maximum X_{max} and therefore the point with the maximal energy deposit $(\mathrm{d}E/\mathrm{d}X)_{max}$ and a significant part of the shower development are observed within the camera of the fluorescence telescope, all four parameters of the Gaisser-Hillas function can be fitted to the profile. In other cases the parameters X_0 and Λ are constained to their average values deduced from very high quality showers measured by the Fluorescence Detector [192]. The total electromagnetic energy deposit of the shower is available via the integral of the Gaisser-Hillas function. The primary energy E_{tot} of the shower can be obtained by modelling the energy deposited without emission of light e.g. the muonic component and energy carried away by neutrinos. The total energy of the quasi-calorimetric measurement by the Fluorescence Detector is therefore given by

$$E_{tot} = f_{inv} \cdot E_{em} = f_{inv} \cdot \int_0^\infty f_{GH}(X)\mathrm{d}X. \tag{3.5.16}$$

The f_{inv} gives the correction for energy deposit invisible for the Fluorescence Detector. The correction is of the order of $5\,\%$ In figures 3.32,3.34 an example event measured by the fluorescence detector is given. The energy resolution of the fluorescence detector of $22\,\%$ is dominated by the uncertainty of the fluorescence yield of $14\,\%$ [137, 138, 149]. A more detailed description of the energy uncertainty of the fluorescence detector is given in chapter 4 in the context of hybrid calibration of the surface detector.

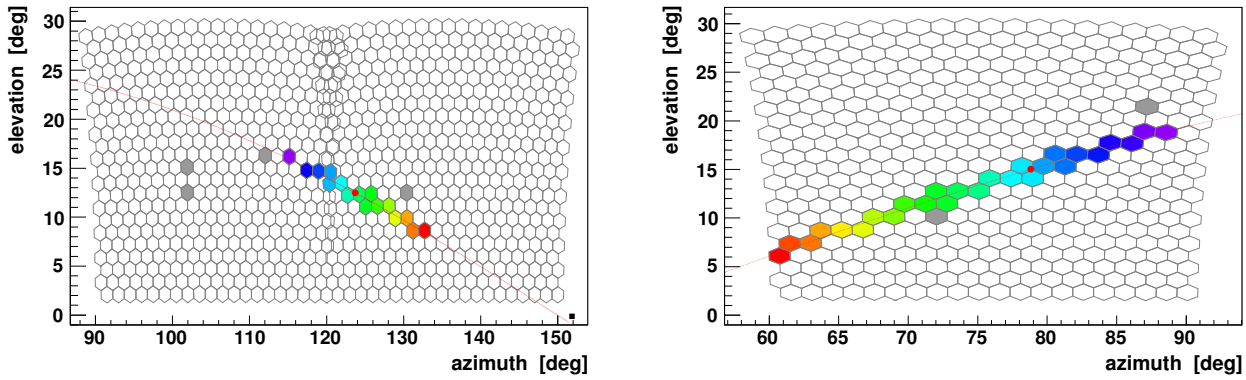

Figure 3.30: The shower track on the fluorescence detector camera. The colour code shows the timing from cold to warm colours.

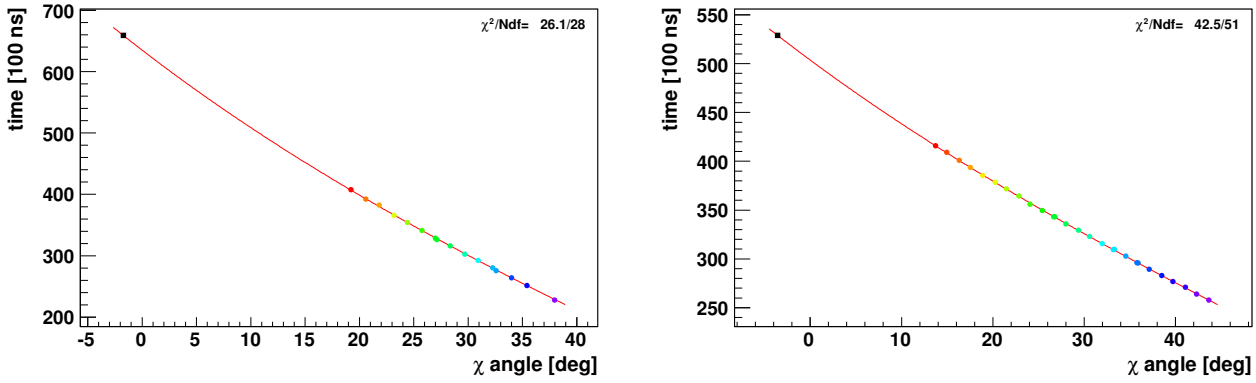

Figure 3.31: The timing of the pixels in colour coding from cold to warm. The black square represents the surface detector station used for hybrid reconstruction.

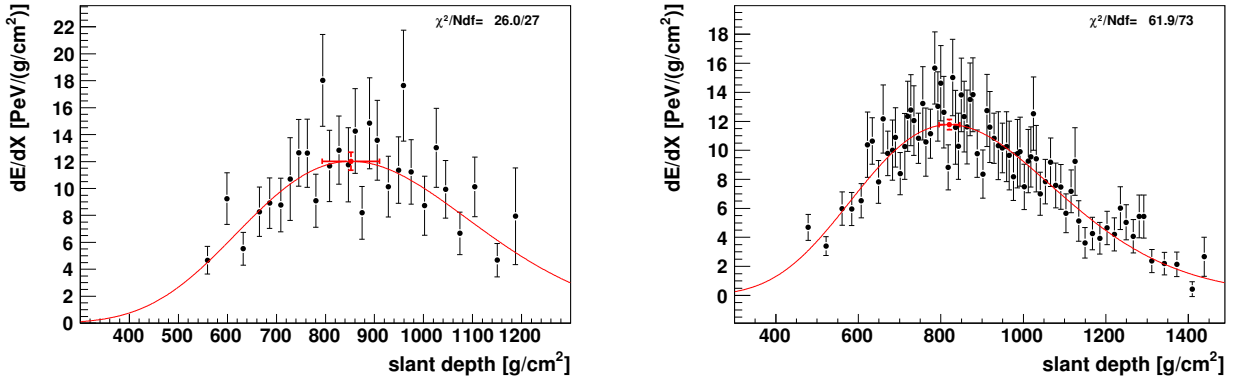

Figure 3.32: The shower profiles of the event with the id 200809504543 with a zenith angle $\theta \approx 63.5°$. The event triggered two seperate fluorescence detector which is referred to as a stereo event. The energy reconstruction of both fluorescence detector building agrees at $E \approx 8.5\,\mathrm{EeV}$ and is compatible with the result of the surface detector reconstruction at $E \approx\approx 8.5\,\mathrm{EeV}$. A three dimensional view of the event and the surface detector reconstruction is given in figure 3.34.

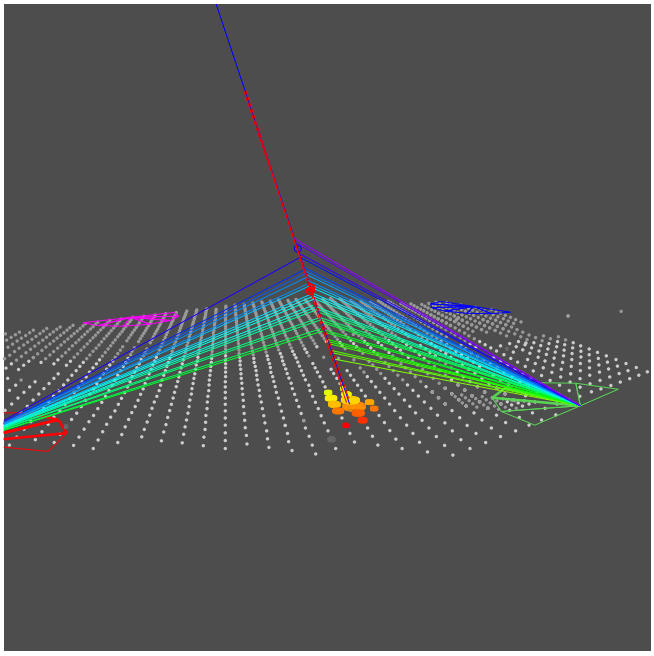

Figure 3.33: A three dimensional view on event 200809504543 with two triggered fluorescence detectors and the surface detector triggered as well.

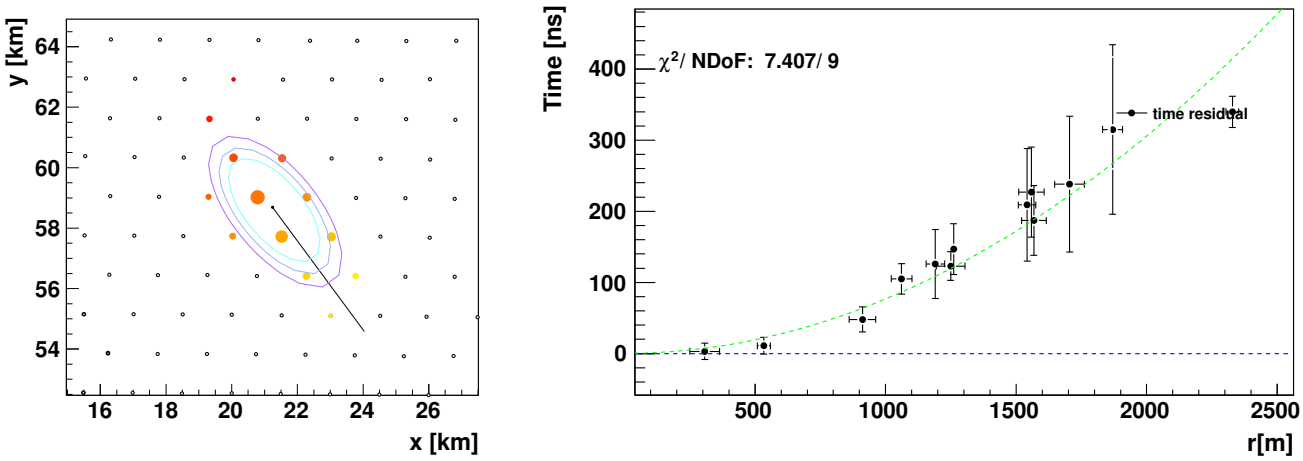

Figure 3.34: The surface detector reconstruction of event 200809504543 using the HAS reconstruction algorithm. In the left panel, the surface detector array with the triggered stations are shown. The size of the marker corresponds to the signal in the station. The lines are lines of equal signal expectation according to the HAS reconstruction algorithm. In the right panel the timing information from the surface detector stations with the fit of a curved shower front is shown. The reconstructed data is given in figure 3.32.

Chapter 4

Comparison of the Surface Detector Energy Determination

The reconstruction methods suited for moderately and very inclined air showers measured with the surface detector of the Pierre Auger Observatory provide the shower size parameters S_{1000} and N_{19} respectively. Both parameters basically characterise the shower size in particles or energy deposit respectively. Therefore the methods to calculate the primary energy of the shower are very similar and the shower size parameter

$$S_{SD} = \begin{cases} S_{1000} & \text{from the LDF reconstruction} \\ N_{19} & \text{from the HAS reconstruction} \end{cases} \tag{4.0.1}$$

can be introduced. The shower size parameter is required to be independent of shower parameters other than the energy e.g. the arrival direction. As the particle densities depend on the shower development in the atmosphere the particle densities on ground vary. The dependency of the raw shower size parameters S_{SD} on the shower geometry is investigated and a conversion into a valid energy estimator $S_{SD,ref}$ independent of the incoming direction is derived using a *Constant Intensity Method* [119].

The energy conversion function $E(S_{SD,ref})$ is obtained by relating $S_{SD,ref}$ with the independent determination of the primary energy of a reference data set. The different reconstruction methods have been applied to both hybrid data and sets of simulated showers, using the energy estimate of the fluorescence detector and the input energy of the simulations as references respectively.

4.1 Event Selection and Data Sets

The determination of the energy estimater $S_{SD,ref}$ can either happen through the determination of the conversion $S_{SD,ref} = f(S_{SD})$ or the the validation of $f(S_{SD})$ to be the identity function. In either case an unbiased set of surface detector events is required for the determination of $f(S_{SD})$. Events with their core position e.g. the maximum of the signal strength on ground not contained in the surface detector array are rejected for being biased. Also below the threshold of full trigger efficiency only a subset of events can trigger the array. This selection biases the average properties of

the showers towards the properties of the subsample e.g. only upward fluctuations of the signal in the surface detector are recorded resulting in an energy bias. The *Surface Detector data set* is used for the determination of $f(S_{SD}) = S_{SD,ref}$ and the determination of the cosmic ray flux in chapter 6. For the surface detector only basic cuts are necessary, requiring

- the physics trigger condition `T4` being fulfilled,
- the quality trigger `T5` for the LDF reconstruction or `T5Has` for the HAS reconstruction respectively being fulfilled and
- the zenith angle being within the validity range of the models used in the reconstruction algorithm, giving $0^\circ < \theta < 70^\circ$ for the LDF reconstruction and $60^\circ < \theta < 80^\circ$ for the HAS reconstruction.

These data sets are used not only to infer a valid energy estimator but also for the determination of the energy spectra of cosmic rays. The overlap of both sets in events forms the basis for comparisons of reconstruction accuracy using real data.

The subset of the events in the Surface Detector samples having at least one triggered Fluorescence Detector is the basis for calibration with the energy determination from the Fluorescence Detector. Besides the Surface Detector related cuts described above a high quality Fluorescence Detector reconstruction to be used as independent energy estimate is vital. The cuts are based on the fluorescence detector quality cuts from [71, 140, 191, 194]. The first simple set of cuts is based on detector effects, the monitoring of the reliability of the detector and the data taking. It is designed to reject events detected in non-reliable states of the detector or events with poor information recorded by the fluorescence detector.

- A measurement of the vertical optical depth, the Mie scattering length and the Mie attenuation length available is required. The fluorescence detector measurement is highly sensitive on the atmospheric conditions and so the energy reconstruction is not reliable without a measurement of the actual atmospheric conditions.
- The calibration of the absolute fluorescence detectors is vital for a reliable energy determination. Events that lack an absolute calibration of the fluorescence detector that detected them are rejected.
- In order to guarantee a good reconstruction five or more triggered pixels belonging to the event are required. With few pixels a reliable reconstruction cannot be achieved.

After data taking and the properties of the detector and the atmosphere, cuts on the quality of the reconstruction are applied. A reliable reconstruction is ensured by requirements on the uncertainties and the majority of the information given by the event contained within the used and reconstructed data.

- The hybrid reconstruction is using the timing inforamtion of a surface detector station. A large distance between the reconstructed hybrid core and the corresponding surface detector station may indicate poor geomatry reconstruction. Also the fluorescence detector reconstruction algorithm approximates the shower front with a plane leading to biases if the used surface detector station is too far away. The surface detector station used in hybrid reconstruction is required to be closer than $1000\,\mathrm{m}$ to the reconstructed shower core.

- In order to ensure enough information observed by the fluorescence detectior the observed track on the fluorescence camera has to be equivalent to a significant tracklength of the shower in the atmosphere. Very close showers may be well reconstructed but the reconstruction may be dominated by only a small fraction of the shower development introducing an uncertainty. The observed shower track has to be equivalent to at least $400\,\mathrm{gcm}^{-2}$ observed atmospheric depth the shower propagated through.

- The angle between the shower axis and the line of sight from the shower to the telescope has to be at least 20°. This makes sure the shower development has been sampled from many pixels and excludes showers that are dominated by direct Cherenkov light in the camera i.e. shower tracks hitting the camera.

- The longitudinal profile modelled by the Gaisser Hillas function is the basis for the energy determination. In order to make sure the reconstruction not to be relying only on the rising or falling edge of the longitudinal profile the shower maximum X_{max} e.g. the maximum value of the fitted Gaisser Hillas function must be within the part of the shower observed in the flourescence detector. In order to exclude events with X_{max} erroneously reconstructed within the observed track, X_{max} must be at least $50\,\mathrm{gcm}^{-2}$ from the borders of the observed shower track.

- With the propagation of the light flux and geometrical uncertainties to the reconstructed longitudinal profile, the uncertainties of the reconstructed parameters are good estimators for the reliability of the reconstruction. The uncertainty in the shower maximum $\sigma(X_{max})$ has to be smaller than $40\,\mathrm{gcm}^{-2}$ and

- the relative uncertainty of the reconstructed energy $\sigma(E)/E$ must be smaller than $40\,\%$.

- The minimised χ^2 of the profile reconstruction as an indicator of the compatibility of the detected profile with the Gaisser Hillas function is required to be smaller than 2.5. Deviations from the Gaisser Hillas profile due to clouds, fog or other bad weather conditions are rejected by this cut as well as poor fits.

- Faint and distant showers may not have a well defined Gaisser Hillas form in the recorded data. In order to reject this source of uncertainties the χ^2 of the Gaisser Hillas fit is required to be at least 4 smaller than the χ^2_{line} of the fit of a straight line to the data in analogy to $\chi^2 = \chi^2_{min} + 4$ indicating a 2σ deviation [123]. A linear shape in contradiction to the Gaisser Hillas shape is therefore excluded by $95\,\%$.

The cut efficiencies are shown in table 4.1 for the *Hybrid data sets* using the valid zenith angles of the LDF reconstruction and the HAS reconstruction respectively. For moderate and especially for high zenith angles the set of hybrid events that satisfy those cuts is small so the overlap of both full range hybrid data sets is basically identical to the hybrid set for the HAS reconstruction.

For cross-checks of the energy determination and for the comparison of the reconstruction accuracies of both reconstruction methods two *Monte-Carlo data sets* constructed from data given in the HAS library [76] have been reconstructed using the LDF reconstruction and the HAS reconstruction respectively. The shower simulation was performed using `CORSIKA` [115,117,118] with the hadronic interaction models `FLUKA` [96,97] for low energy interactions and `QGSJET-II` [126,154] for high energy interactions respectively. 2700 proton and 540 iron showers were used as those primaries are

Cut	LDF		HAS	
	events left	efficiency	events left	efficiency
full set	1670000		349828	
$\theta > 60°$	not applied		162648	46.5
$\theta < 80°$	not applied		140157	86.2
$\theta < 70°$	1650388	98.9	not applied	
`T5`	1443396	87.5	not applied	
`T5Has`	not applied		103760	74.0
FD available	57108		5759	
Atm. database available	50004	87.6	5180	89.9
$n_{pixels} > 5$	43343	86.7	2926	56.5
$d(\text{core, SD})$	40972	94.5	2583	88.3
tracklength $> 400\,\mathrm{gcm}^{-2}$	15445	37.7	2000	77.4
viewing angle $> 20°$	12025	77.9	559	27.9
$\lvert X_{max} - X_{border}\rvert < 50\,\mathrm{gcm}^{-2}$	11184	93.0	505	90.3
$\sigma(X_{max}) < 40\,\mathrm{gcm}^{-2}$	9901	88.5	288	57.0
$\sigma(E)/E < 40\,\%$	9901	100.0	288	100.0
$\chi^2_{GH} < 2.5$	9709	98.1	275	95.5
$\chi^2_{GH} + 4 < \chi^2_{line}$	8115	83.6	246	89.5

Table 4.1: The cuts on the data set recorded at the Pierre Auger Observatory and the cut efficiencies. In the upper part the SD cuts are shown, resulting in the surface detector data set. In the lower part, the subset of these events having fluorescence data and the quality cuts are shown.

the two extremes expected for hadronic cosmic rays. The simulated showers cover moderate and high zenith angles $60° < \theta < 88°$, all azimuth angles and the domain of ultra high energy cosmic rays $10^{18}\,\mathrm{eV} < E < 10^{19}\,\mathrm{eV}$. The detector response of the Surface Detector of the Pierre Auger Observatory has been simulated using the `Offline` [99, 162] framework using every shower ten times varying the core position randomly. The distributions of the simulated zenith angles, azimuth angles and primary energies of the resulting data set are shown in figures 4.1, 4.2 and in appendix A. In table A.1 the borders of the bins are listed. For each combination five proton showers and one iron shower were used. The larger amount of protons is motivated by larger fluctuations in proton showers. Within the bins the input parameters to the simulations are distributed randomly.

With the shower geometry and the primary energy as well as the nature of the primary known the Monte Carlo data set allows the determination of the influence of the primary mass on the relation between shower size parameter and primary energy. As the hadronic interaction models cannot reproduce ultra high energy cosmic ray air shower data well [45] the Monte Carlo data set cannot be used to derive the energy calibration curve for real data of the Pierre Auger Observatory [74].

4.2 Validating the Energy Estimator

A valid energy estimator is independent on other shower parameters than the energy. Except for shower to shower fluctuations and the different muon number related to different primary mass the dependencies can be checked even on real data by assuming that the cosmic ray flux does not depend on the incoming direction. Despite the observation of anisotropic arrival directions for cosmic rays of the highest measured energies $E > 56\,\mathrm{EeV}$ in galactic coordinates [185], the assumption of equal cosmic ray flux per solid angle at a given energy holds for lower energies $E < 20\,\mathrm{EeV}$ [112] and in local coordinates. So the flux per solid angle $dJ/d\Omega$ is equal for any incoming direction in the energy region above the threshold of full trigger efficiency. With the solid angle element in spherical coordinates $d\Omega = \sin\theta d\theta d\phi$ an equidistant binning in the azimuth angle ϕ results in bins of equal solid angle with an equal expected flux. Figure 4.3 illustrates this behaviour for both reconstruction algorithms.

The model of the LDF has a cylindrical symmetry around the shower axis independent of the azimuth angle but with a dependeny on the zenith angle. The muon profiles used in the HAS reconstruction depend on the zenith angle as well as on the azimuth angle. The flat behaviour of the flux in equidistant bins of azimuth angle above different thresholds in the shower size parameter demonstrates that the models do not introduce an azimuth angle dependent bias in the shower size parameter e.g. $f(S_{SD})$ is not a function of the azimuth angle.

For the LDF reconstruction the shower size parameter S_{1000} is the normalisation of the function f_{LDF} fitted to the signal distribution on ground. As the signal distribution on ground corresponds to the particle densities on ground S_{1000} is affected by shower development as the rise of the particle density before the shower maximum and the attenuation in the atmosphere thereafter. For N_{19} the signal is compared to the signal expected at ground. So with a realistic model of the longitudinal development of the shower used in the determination of N_{19} a dependency on the zenith angle is not expected and its presence would indicate a discrepancy of the shower evolution between reality and the models used in simulation.

The dependence of the energy estimator on the zenith angle is determined using the assumption of constant flux in bins of equal solid angle again. It can be written as

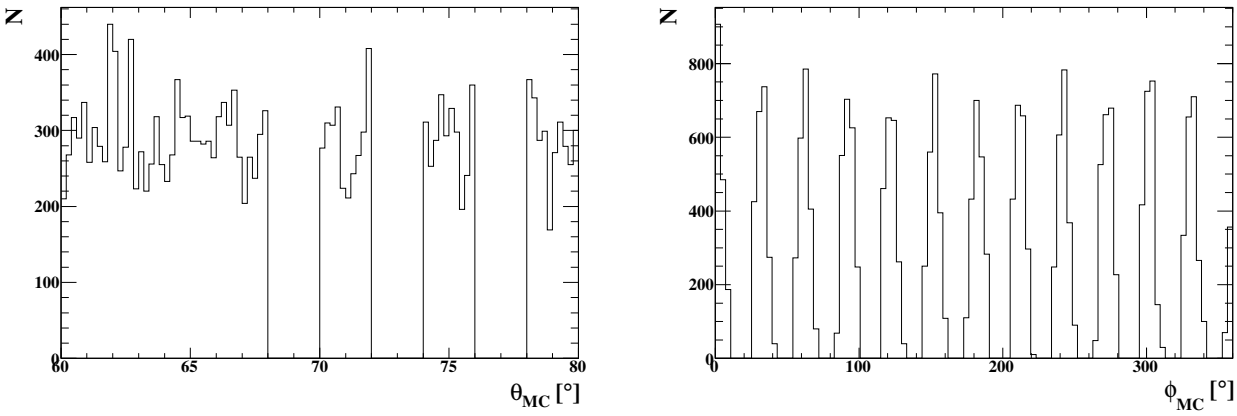

Figure 4.1: The distribution of the simulated zenith angle θ_{MC} (right panel) and the simulated azimuth angle ϕ_{MC} of the simulated data sets for protons and iron primaries respectively. The distributions shows the number of simulated events with every simulated shower giving ten events with randomised shower cores.

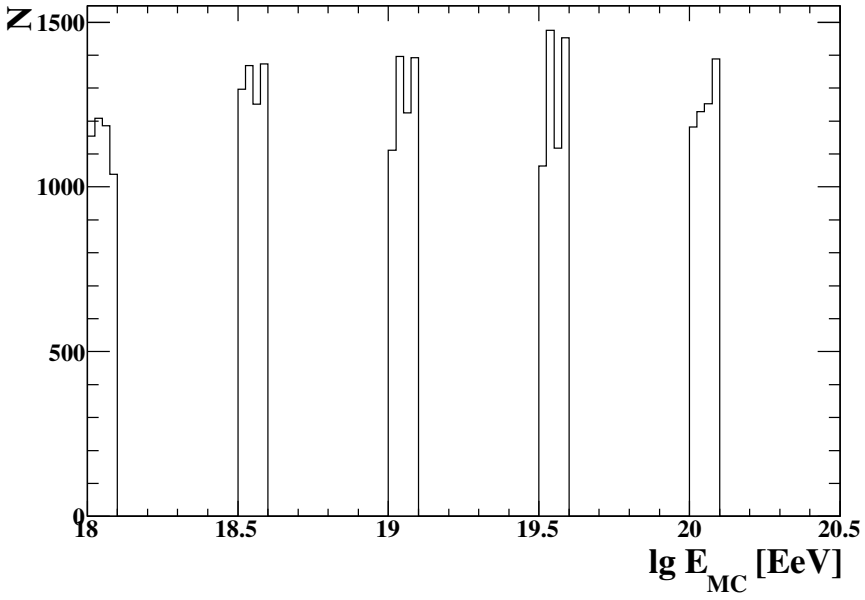

Figure 4.2: The energies of the simulated events for proton and iron primaries respectively. Each shower gives ten events with random core positions with respect to the simulated Surface Detector array.

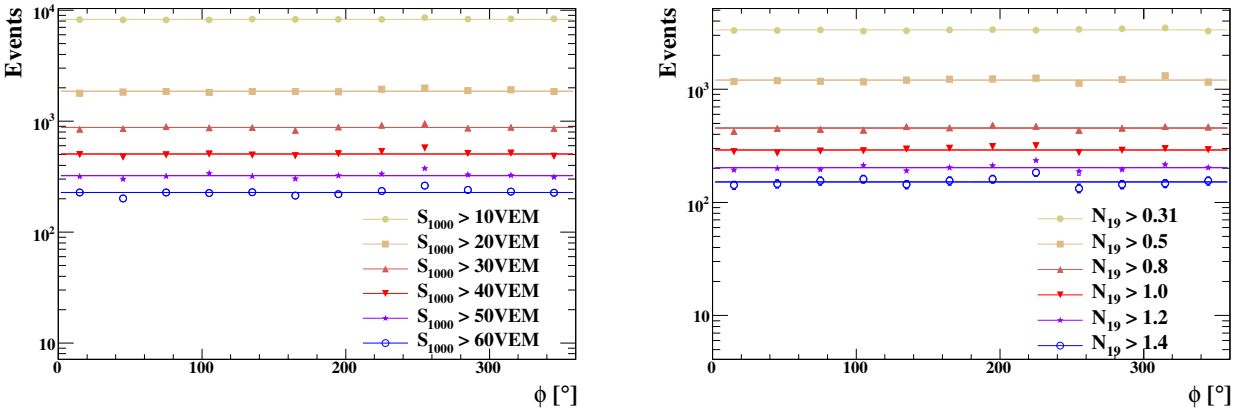

Figure 4.3: The number of events detected by the Surface Detector with a shower size parameter above a threshold in equidistant bins in azimuth angle ϕ for reconstruction using the LDF reconstruction (left panel) and the HAS reconstruction (right panel) respectively. With the assumption of isotropic arrival of cosmic rays in local coordinates the flat distribution verifies the energy estimators S_{1000} and N_{19} as not dependent on the azimuth angle.

$$\frac{d}{d\Omega}J = \frac{d}{d\theta}\left(\frac{1}{A\cdot\cos\theta}\frac{d^3N}{dt\ dE\ \sin\theta d\theta d\phi}\right) = 0 \tag{4.2.1}$$

with the zenith angle θ and the effective area $A_{eff} = A\cos\theta$. The area A and the time t are neglected as these variables are not zenith angle dependent. As shown above, no dependence on the azimuth angle is seen. So after trivial integration over ϕ with the solid angle element $d\Omega = \sin\theta d\theta d\phi$ equation 4.2.1 becomes

$$\frac{dN}{dE\ \sin\theta\cos\theta d\theta} = \text{constant}. \tag{4.2.2}$$

With the influence of anisotropy at highest energies being small due to the steeply falling spectrum of cosmic rays, the integration above a threshold energy E_0 gives

$$\left.\frac{dN}{\sin\theta\cos\theta d\theta}\right|_{E>E_0} = \text{constant}. \tag{4.2.3}$$

So for any energy threshold above the threshold for full trigger efficiency, equistant bins in $\cos^2\theta$ contain a equal intensity which means equal number of events above this threshold. If the shower size parameter does not depend on the zenith angle, equation 4.2.3 can be integrated leading to

$$\left.\frac{N(\theta\in[\theta_1,\theta_2])}{\cos^2\theta_2-\cos^2\theta_1}\right|_{S_{SD}>S_{SD,0}} = \text{constant}. \tag{4.2.4}$$

Figure 4.4 shows intensities for various threshold values in the shower size parameters S_{1000} and N_{19} respectively. The intensity per $\cos^2\theta$ bin being non-constant implies a dependency of the shower size parameters on the zenith angle θ. The estimator given by LDF reconstruction S_{1000}

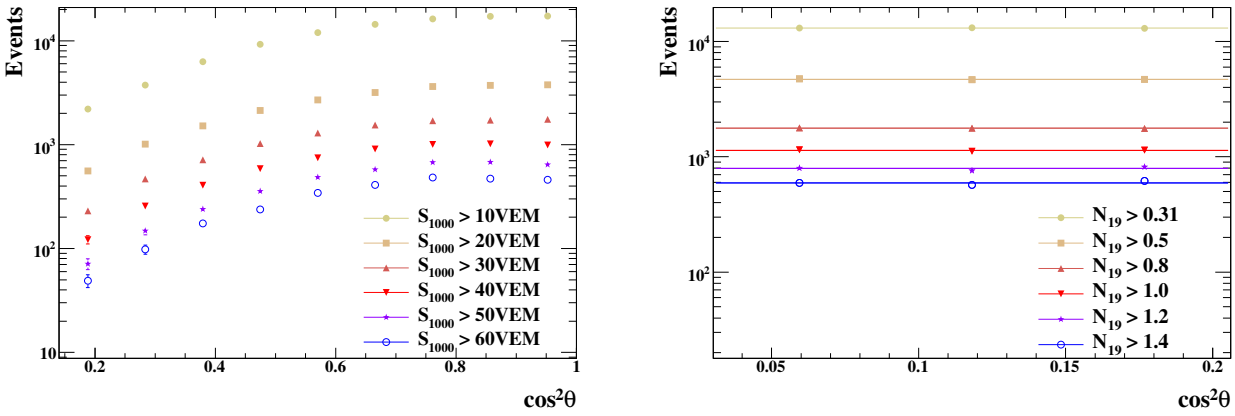

Figure 4.4: Intensities for different threshold values in S_{1000} (left) and N_{19} (right) respectively. If the shower size parameter is not zenith angle dependent, equidistant bins in $\cos^2\theta$ contain equal numbers of events.

is the normalisation of a cylindrical symmetric model of the signal and therefore is influenced by geometrical effects and attenuation during proapgation in the atmosphere both dependent on the zenith angle. N_{19} is constructed in correlating the overall muon number with a shape from simulation already accounting for attenuation and geometrical effects according to the interaction models used in the shower simulation. By applying the method of *Constant Intensity* [119], the zenith angle dependency in S_{1000} can be accounted for by defining an energy estimator $S_{SD,ref} = f(S_{1000}, \theta) \neq S_{SD,ref}(\theta)$.

The constant intensity method is based on the assumption of isotropic arrival of cosmic rays of all energies in the local coordinate system. As shown in equation 4.2.3 with this assumption in bins of equal acceptance of the detector i.e. equidistant bins in $\cos^2\theta$ and above the threshold of full trigger efficiency equal numbers of events $N(S_{SD} > S_{SD,thr}, \theta)$ correspond to equal primary energy E. So the threshold shower size parameter $S_{SD,thr}(N, \theta)$ maps the zenith angle dependency of S_{SD} for given energy. To infer the zenith angle dependent shower size parameter for constant energy $S_{SD}(N, \theta)$ the data is binned equidistantally in $\cos^2\theta$. Each bin i contains the intensity I_i being the integrated flux with the logarithm of the energy estimator larger than $\lg S_{SD,i}$. The intensity is the sum

$$I_i = \sum_{j=0}^{i} n_j \tag{4.2.5}$$

of the differential fluxes n_j in bins at higher $\lg S_{SD,j}$. The flux above the highest bin is represented by n_0. The intensities I_i are not statistically independent. The integrated spectra for the LDF and HAS reconstructions are shown in figure 4.5 for lowly and moderately inclined events and moderate and high zenith angles respectively. The spectra are shifted in $\lg S_{SD}$ because of the zenith angle dependency of the estimator. The values of S_{SD} corresponding to an intensity N are calculated from the integrated spectra. To avoid biases due to spectral features seen in different positions in the shifted integrated spectra the estimator $S_{SD}(I, \theta)$ as a function of intensity i and zenith angle θ is not derived from a fit to the spectra but by interpolation with a local power law corresponding to a line in double logarithmic coordinates

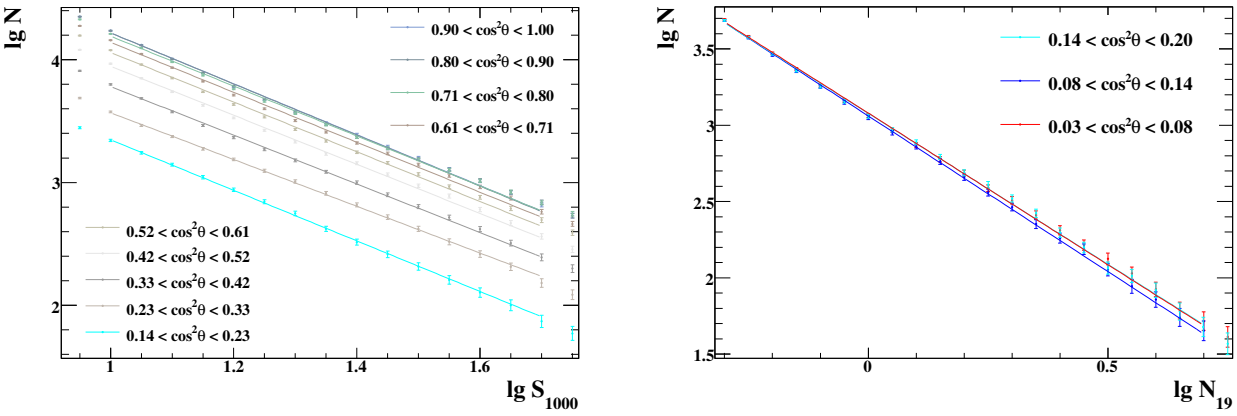

Figure 4.5: Integrated spectra of the raw energy estimators S_{1000} (left) and N_{19} (right) respectively. With the assumption of constant intensity, equal intensity corresponds to equal energy. Statistical uncertainties under the assumption of poissonian fluctuations only give the error bars. The power law fit lines are restricted to an estimator range corresponding to the energy range of constant spectral index between $5 \cdot 10^{18}\,\mathrm{eV} < E < 5 \cdot 10^{19}\,\mathrm{eV}$. The spectral indices are fitted seperately for each zenith angle bin.

$$\ln S_{SD,i} = a + b \cdot lnI_i, \quad i \in \{k, k+1\} \tag{4.2.6}$$

with $I_{k+1} \leq I > I_k$ being the closest neighbouring bins of the chosen intensity I. The problem can be reformulated using the differential flux n_{k+1} and the integrated flux above bin $k+1$

$$I_k = \sum_{j=0}^{k} n_j \tag{4.2.7}$$

which are statistically independent. The parameters of the local powerlaw can be determined analytically:

$$\begin{aligned} S(I) &= e^a \cdot I^b \\ a &= \ln S_{SD,k+1} + \ln \frac{S_{SD,k+1}}{S_{SD,k}} \left(\ln \frac{n_k + n_{k+1}}{n_{k+1}} \right) \ln n_{k+1} \\ b &= \ln \frac{S_{SD,k+1}}{S_{SD,k}} \left(\ln \frac{n_k + n_{k+1}}{n_{k+1}} \right). \end{aligned} \tag{4.2.8}$$

The intensities I_i are correlated but the differential flux n_{k+1} and the intensity n_k are statistically independent. With the covariance matrix [145]

$$U = \begin{pmatrix} \left(\frac{\partial a}{\partial n_0}\right)^2 \cdot n_0 + \left(\frac{\partial a}{\partial n_1}\right)^2 \cdot n_1 & \frac{\partial a}{\partial n_0} \cdot \frac{\partial b}{\partial n_0} \cdot n_0 + \frac{\partial a}{\partial n_1} \cdot \frac{\partial b}{\partial n_1} \cdot n_1 \\ \frac{\partial a}{\partial n_0} \cdot \frac{\partial b}{\partial n_0} \cdot n_0 + \frac{\partial a}{\partial n_1} \cdot \frac{\partial b}{\partial n_1} \cdot n_1 & \left(\frac{\partial b}{\partial n_0}\right)^2 \cdot n_0 + \left(\frac{\partial b}{\partial n_1}\right)^2 \cdot n_1 \end{pmatrix} \tag{4.2.9}$$

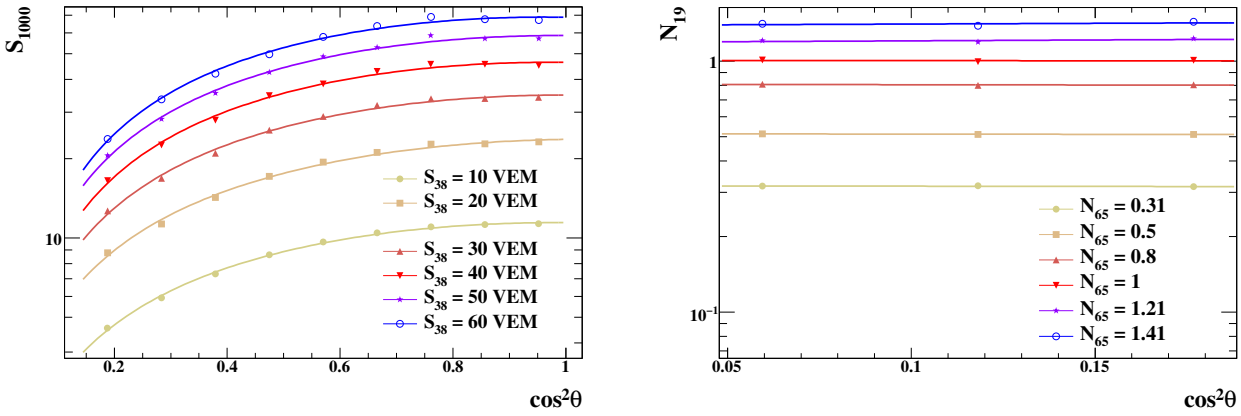

Figure 4.6: The raw energy estimator S_{1000} (left) and N_{19} (right) as a function of $\cos^2\theta$ for various intensities and the full validity range of the reconstruction algorithm giving the energy estimator N_{19} and S_{38} respectively.

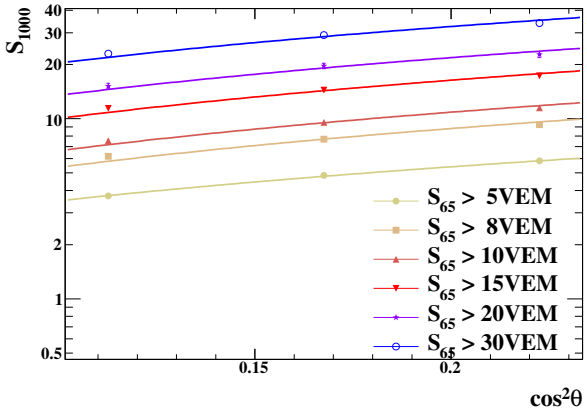

Figure 4.7: The raw energy estimator S_{1000} as a function of $\cos^2\theta$ for various intensities. The angular range was restricted to the zenith angle range of $60° < \theta < 70°$. Considering the reduced zenith angle range only a linear term was fitted.

and assuming Poissonian fluctuations of the independent fluxes only $\sigma_n^2 = n$ the uncertainties can be propagated. The derived uncertainties are shown as the error bars in figure 4.6.

The values of $S_{SD}(I, \theta_i)$ for each intensity I correspond to the same energy as I corresponds to one value of the primary energy. The zenith angle independent energy estimator $S_{SD,ref}(I)$ is defined as the value of $S_{SD}(I)$ measured at the reference zenith angle θ_{ref}. So the problem factorises:

$$S_{SD}(I,\theta) = S_{SD,ref}(I) \cdot f(\theta) \Leftrightarrow \quad (4.2.10)$$

$$S_{SD,ref}(I) = S_{SD}(I,\theta)/f(\theta). \quad (4.2.11)$$

Knowing $f(\theta)$ the corrected energy estimator can be calculated by using equation 4.2.11. Fitting the $S_{SD}(I, \theta_i)$ with equation 4.2.10 both the reference estimator $S_{SD,ref}(I)$ and the zenith angle dependency $f(\theta)$ are determined. The zenith angle dependency is modelled by a polynomial of nth degree in $\cos^2\theta$ normalised at the reference zenith angle θ_{ref}

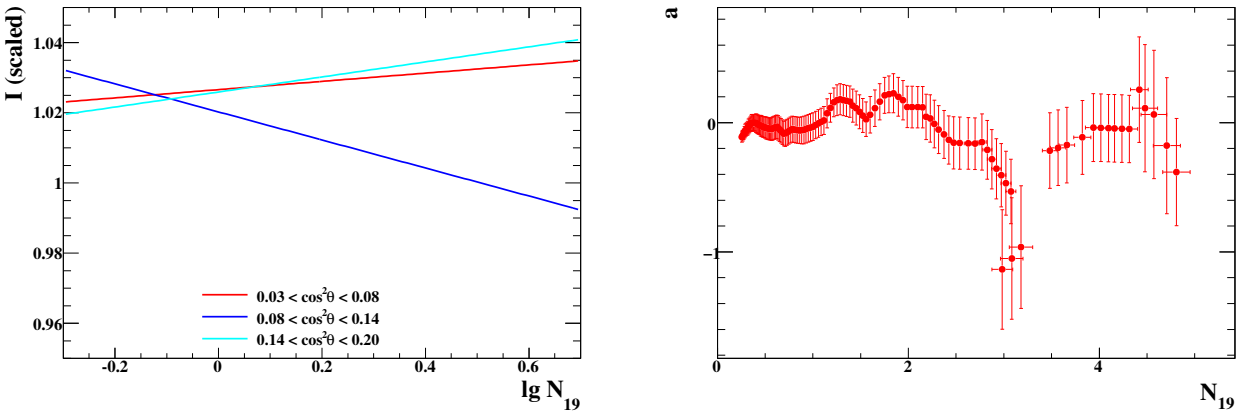

Figure 4.8: In the left panel the powerlaw fits of the integrated spectra used for the constant intensity method in the energy range of constant spectral index in the primary spectrum are shown. In the right panel the slope of the zenith angle correction for the HAS reconstruction energy estimator N_{19} derived with the constant intensity method is shown. The error bars represent the fitting uncertainty and the propagated uncertainty from interpolation of the integrated spectra. As the intensity values used are not statistically independent, also the fitting errors for different intensities are correlated. The low deviations of the spectral shapes and the compatibility of the slope with zero over the whole energy range indicate N_{19} to be independent of the zenith angle in the whole energy range.

$$S_{SD}(I,\theta) = S_{SD,ref}(I) \cdot \left(1 + \sum_{i=1}^{n} a_i \cdot (\cos^2\theta - \cos^2\theta_{ref})\right). \tag{4.2.12}$$

For the LDF reconstruction the shape is modelled best with $n = 2$. For the HAS reconstruction a line ($n = 1$) is fitted for comparison. In figures 4.7 a linear function fitted to the $S_{1000}(\theta)$ in the range of moderate zenith angles $60° < \theta < 71°$ is shown for comparison.

With N_{19} based on the muon number in the shower and the corresponding muon densities on ground a dependency on zenith angle can be a hint on differences between the real evolution of a shower and the modelling in air shower simulation and the used hadronic interaction models. Also the correlation between N_{19} and the primary energy depends on the mass of the primary particle A as the muon content differs at constant energy. As the evolution of the mass composition of cosmic rays cannot depend on the zenith angle but on the energy a changing mass composition does not affect the zenith angle dependency at constant intensity. According to studies on simulations [71] the zenith angle dependency of the muon number $N_\mu \approx a(\theta) \cdot N(E, A)$ factorises. Thus even a change of the zenith angle dependency with energy cannot give hints on primary mass. The spectral index of the integrated spectra derived for N_{19} for different zenith angles as well as the evolution of deviations from a negligible slope of the zenith angle correction of N_{19} in figure 4.8 show no hint for a dependence of the estimator on primary energy and zenith angle.

The estimator S_{1000} given by the LDF reconstruction is not corrected for shower evolution e.g. it depends on the stage of shower development on ground due to the particle multiplication and subsequently attenuation in the atmosphere as well as geometrical effects. With increasing energy of the primary particle the shower maximum shifts to higher depths traversed by the shower. Thus higher energetic showers at the same zenith angle are less developed than showers with lower energy of the

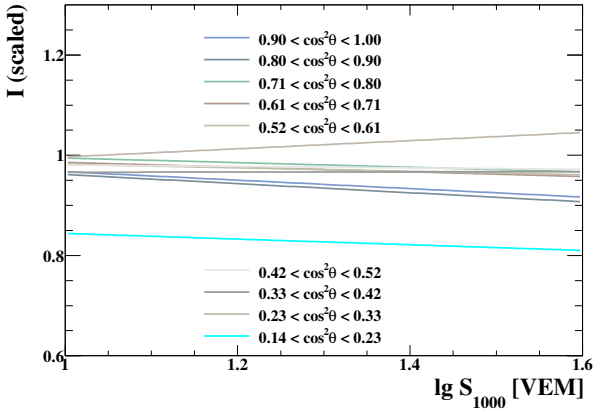

Figure 4.9: The relative differences of the power law fits to the integrated spectra in the energy estimator of the LDF reconstruction S_{1000}. The difference for low zenith angle indicates the showers being measured at ground increasingly significantly before the shower maximum.

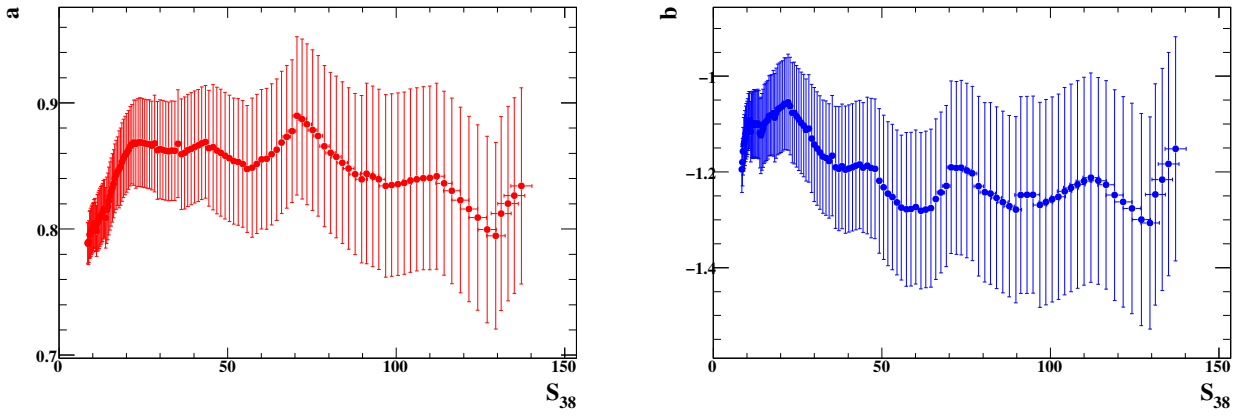

Figure 4.10: The parameters of the second degree polynomial modelling the dependence of S_{1000} on the zenith angle. The evolution of the attenuation curve in energy is the largest uncertainty of the correction of the energy estimator for effects of different shower age at ground. The error bars show the fitting uncertainty of the parameter in the vertical direction and the fitting uncertainty of S_{38} in the horizontal direction. The errors are correlated.

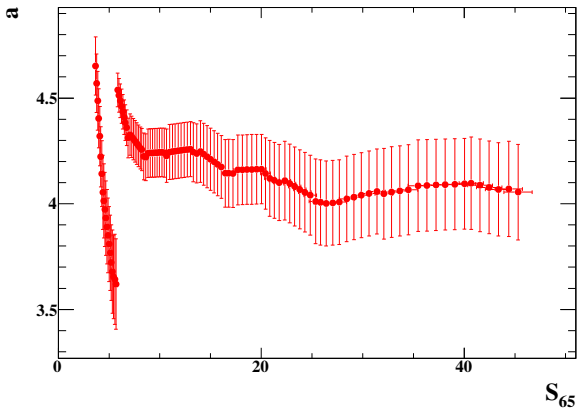

Figure 4.11: The slope parameter of the attenuation curve for S_{1000} only using moderately inclined showers. The energy dependent effect of showers reaching ground before their maximum is excluded as it occurs only at low zenith angels in this energy range. This part of the attenuation curve is universal as the constant slope illustrates.

primary. The Pierre Auger Observatory is situated at an altitude of $1400\,\mathrm{m}$ or a vertical atmospheric depth of $840\,\mathrm{gcm}^{-1}$. Air showers caused by UHECR nuclei show similar or even higher atmospheric depths for their shower maxima. Vertical showers of energies above $3{\cdot}10^{18}\,\mathrm{eV}$ reach ground before the shower maximum having lower particle densities than maximally developed showers. As this effect increases for higher energies the attenuation curve of S_{1000} is dependent on the primary energy. This can be observed both in the spectral indices of the integrated spectra in figure 4.9 and the evolution of the parameters of the correction curve in figure 4.10. At moderate zenith angles the effect of showers reaching ground before reaching the maximum is negligible at the primary energies relevant for the Pierre Auger Observatory. The evolution of a first degree polynomial fit to the attenuation curve restricted to moderately inclined showers in figure 4.11 illustrates that with a constant slope of the attenuation curve.

4.3 Calibration

The calibration of the energy estimator $S_{SD,ref}$ means to define a function $E(S_{SD})$ relating the energy of the shower primary to the energy estimator S_{SD} from the reconstruction algorithm. For both N_{19} and S_{38} the calibration curve $E = f(S_{SD})$ with the S_{SD} independent of the shower geometry is a power law

$$E_{SD} = E_0 \cdot S_{SD,ref}^{\gamma}. \tag{4.3.1}$$

The method to determine the energy E_0 for a value of the estimator $S_{SD,ref} = 1$ and the exponent γ requires a data sample having an independent measurement of a reference energy to calibrate with. Two methods are applied in this work:

- Plain Calibration assuming an energy estimater $S_{SD,ref}$ that does not depend on the zenith angle [142, 145, 178].

- Calibration with angular correction using S_{SD} regardless of its potential zenith angle dependency and determining the angular correction and the calibration curve in one fit [145].

With the second method an independent check of the results of both angular correction as derived in section 4.2 as well as the energy calibration curve derived with the first method is possible. This allows to estimate systematic uncertainties introduced by the method of sequential determination of the correction and calibration curves respectively. Also for Monte Carlo set with no continuous spectrum a constant intensity method is not applicable. Therefore the calibration with angular correction is applied for this purpose.

Both methods basically fit the available data with the calibration curve. Although equation 4.3.1 in principle holds for any energy, the available data below the threshold of full trigger efficiency of the detector does not reflect the true calibration curve. Below full trigger efficiency the distribution of S_{SD} only upward fluctuations are seen in the data while the downward fluctuation do not trigger. The bias introduced to the calibration curve fit by this effect can be eliminated by cutting sub-threshold events. A bias by introducing the cut is avoided by an optimisation of the cut inclination with respect to the calibration curve according to the relative uncertainties in S_{SD} and E_{FD} respectively using a toy Monte Carlo.

Another method based on a likelihood fit has been developed in [74, 144].

Methods

Plain Calibration determines the relation between the energy estimator $S_{SD,ref}$ and the primary energy as in equation 4.3.1. It requires the energy estimator to be not dependent on the shower geometry e.g. the $S_{SD,ref}$ derived with the constant intensity method. Besides the requirement of an unbiased reference energy threshold effects of the Surface Detector can influence the result of the method. The determination of a cut to eliminate this bias is shown in the next subsection.

The calibration curve is derived with an unbinned χ^2 method [123]

$$\begin{aligned} \chi^2 &= \sum_i \frac{\left(E_{ref} - E_0 \cdot S_{SD,ref}^{\gamma}\right)^2}{\sigma_{FD}^2 + \sigma_{SD}^2} \\ \sigma_{FD}^2 &= \sigma^2(E_{FD}) \\ \sigma_{SD}^2 &= \sigma_{fit}^2(S_{SD}) + \sigma_{LDF,\theta}^2(S_{SD}) + \sigma_{att}^2(S_{SD}) \end{aligned} \tag{4.3.2}$$

accounting for the uncertainties in the Fluorescence Detector measurement as well as the uncertainties from the Surface Detector reconstruction, the models used in reconstruction and the attenuation curve.

For cross-calibration of N_{19} with the energy estimate by the LDF reconstruction as shown in section 4.3 the cut optimisation is described in section 4.3.

Direct Energy Calibration [141] of the shower size parameter S_{SD} includes the correction of effects in zenith angle into the calibration procedure. With the energy calibration curve $E = g(S_{SD,ref})$ and the corrected energy estimator $S_{SD,ref} = f(S_{SD}, \theta)$ a least squares method can be defined using

$$\chi^2 = \sum_i \frac{(E_i - g(f(S_{SD}, \theta)))^2}{\sigma_i^2} \tag{4.3.3}$$

with the reference energy E_i and the sum of the quadratic uncertainties and quadratic propagated uncertainties

$$\sigma_i^2 = \sigma^2(E_i) + \left(\frac{\mathrm{d}S_{SD,ref}}{\mathrm{d}S_{SD}} \cdot \sigma(S_{SD,i}^{\text{reco}})\right)^2 + \left(\frac{\mathrm{d}S_{SD,ref}}{\mathrm{d}S_{SD}} \cdot \sigma(S_{SD,i}^{\text{fluctuation}})\right)^2 + \left(\frac{\mathrm{d}S_{SD,ref}}{\mathrm{d}\theta} \cdot \sigma(\theta_{SD,i}^{\text{reco}})\right)^2 . \tag{4.3.4}$$

The method does not require to bin the data and gives a handle on the calibration curve and the zenith angle dependency of the energy estimator at once. With all the parameters of both the calibration curve $g(S_{SD,ref})$ and the angular dependency $f(S_{SD}, \theta)$ being fitted to the data set this method is of limited use for very low statistics e.g. the sparse set of high quality hybrid events at moderate and high zenith angles.

As the method deals with the raw energy estimator without any zenith angle correction a cut in S_{SD} is introduced with analoguous slope with respect to the calibration curve as for $S_{SD,ref}$ in the previous section. For the actual implementation of the fit function the same parameterisations are used: The calibration $g(S_{SD,ref})$ curve as defined in equation 4.3.1 and an angular correction $f(S_{SD}, \theta)$ as in function 4.2.12. For the LDF reconstruction with an angular range of $0° < \theta < 70°$ f is an polynomial of second order $N = 2$, for the HAS reconstruction with the much smaller angular validity range of $60° < \theta < 80°$ a linear angular correction function $n = 1$ is used.

Cut optimisation

All extensive air showers of energies above $E = 6 \cdot 10^{18}\,\mathrm{eV}$ and zenith angles up to $\theta = 80°$ trigger the Surface Detector array as will be shown in chapter 6. For lower energies especially in the range of moderate and high zenith angles the trigger efficiency is less than one. Thus only upward showers with fluctuations of the particle densities at ground are recorded. Therefore below the threshold of full trigger efficiency also upward fluctuations of S_{1000} and N_{19} respectively enter the data set. So for low energies the distribution of the energy estimator is biased. For a cut removing these events below the threshold the uncertainties of both the energy estimator and the reference energy have to be accounted for. With an evolution of the uncertainties with energy also the energy distribution of the calibration data set becomes important as the number of events in an energy range together with the uncertainties gives the weight of that energy region in the fit of the calibration curve.

Analogue to the power law form of the calibration curve the rejection of sub-threshold events uses a straight line in doublelogarithmic coordinates. If the relative uncertainties of $S_{SD,ref}$ and E_{ref} were equal a threshold cut perpendicular to the calibration curve in doublelogarithmic coordinates would guarantee an unbiased fit cutting the of $S_{SD,ref}$ and E_{ref} distributions due to statistical fluctuations symmetrically. Any ratio σ_y/σ_x of relative uncertainties constant in energy can be rescaled so that a

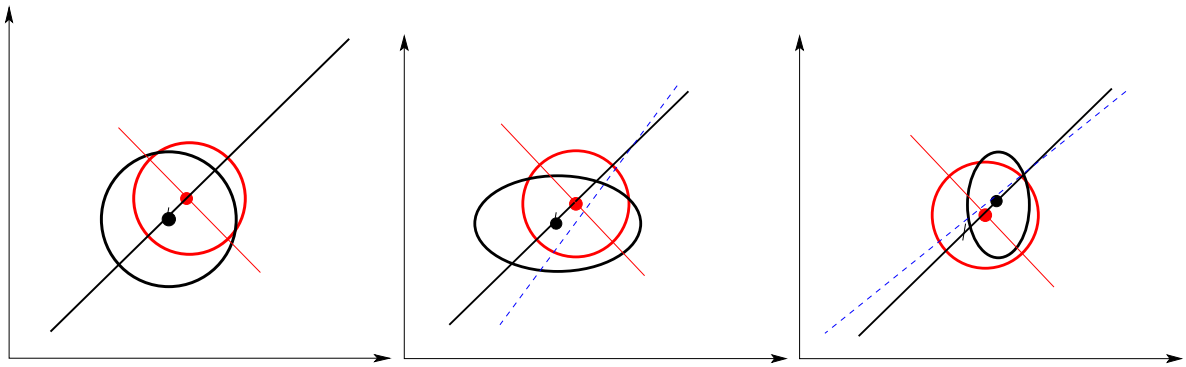

Figure 4.12: The effect of energy dependent uncertainties on a linear fit. All cases are rescaled to equal uncertainties at the intersection point of cut line and fit line [74, 144].

perpendicular cut in rescaled doublelogarithmic coordinates can be used. With the calibration curve equation 4.3.1 the cutting line transformed to plain coordinate is a powerlaw with the index

$$\gamma_{cut} = -\frac{\sigma_{SD}^2}{\sigma_{FD}^2}\frac{1}{\gamma} \tag{4.3.5}$$

In case of energy dependent uncertainties a rescaling in a frame of equal uncertainties is not possible. The bias by using a perpendicular cut in rescaled coordinates is illustrated in figure 4.12 for the case of energy dependent uncertainties.

Sticking to the concept of a linear cut in doublelogarithmic coordinates or equivalently a power law cut is optimised by varying the slope around a perpendicular cut with the cut parameter $-1 < \Delta < 1$ [74] giving

$$\gamma_{cut} = -\left(\frac{1}{\gamma} + \Delta\right). \tag{4.3.6}$$

In case of using the input energy to a simulation as reference energy to calibrate the reconstructed energy estimator S_{SD} the uncertainties in the reference energy are zero by construction. Therefore a horizontal line $\Delta = -1/\gamma$ is used for the cut as it does not affect distribution of the energy estimator. In case of a reconstructed energy the ratio of the uncertainties is energy dependent as stated above. For cut optimisation a toy Monte Carlo has been set up to create simulated data samples using the realistic uncertainties of the calibration sample. The uncertainty of the energy estimator is energy dependent as rising energy and therefore rising number of triggered stations give stronger constraints to both the LDF fit as well as the fit of the muon profile. As the uncertainties show an analogous behaviour the dependency of the uncertainty $\sigma_{fit}(S_{SD})$ on the logarithm of the estimator $\lg S_{SD}$ that can be parameterised as an exponential

$$\begin{aligned} \sigma_{fit}(S_{38}) &= \exp -1.94 \pm 0.67 \cdot S_{38}^{(-1.26\pm1.06)} \\ \sigma_{fit}(N_{19}) &= \exp -0.95 \pm 1.20 \cdot N_{19}^{(-0.94\pm1.04)}, \end{aligned} \tag{4.3.7}$$

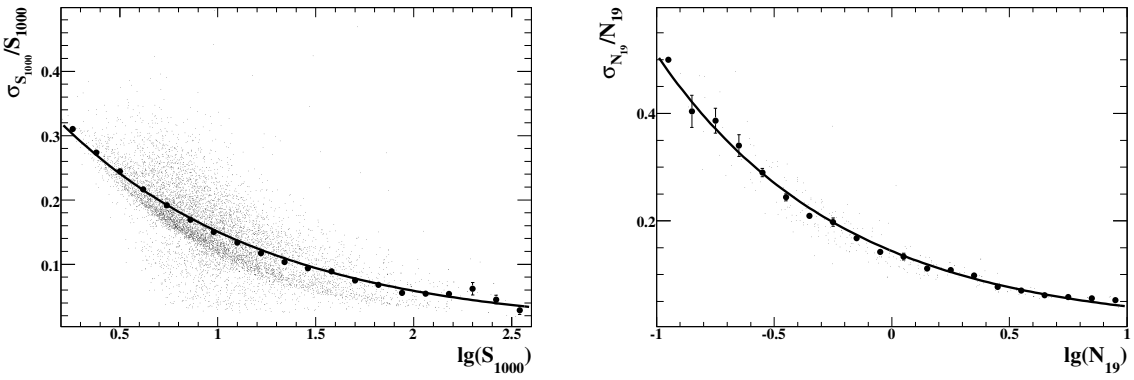

Figure 4.13: The uncertainty of the energy estimator from the fitting procedure is energy dependent and can be modelled by an exponential in $\lg S_{SD}$

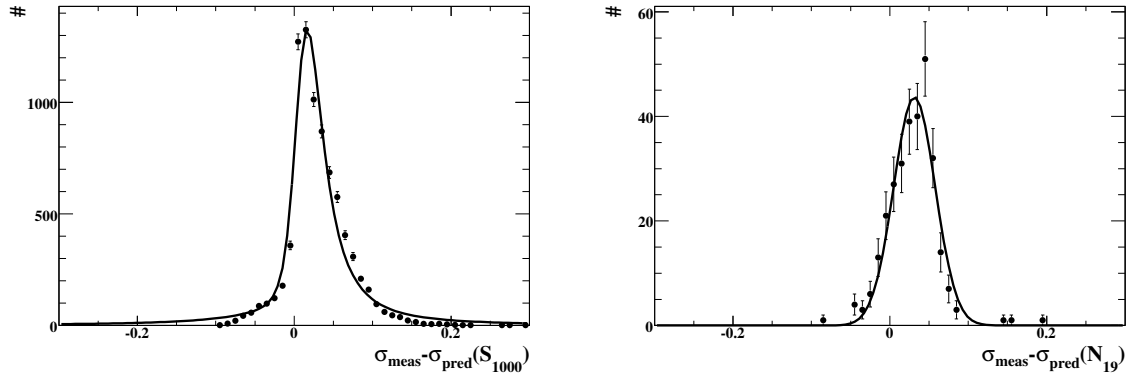

Figure 4.14: The deviation of the uncertainty from the parameterisation given in equation 4.3.7 follows a ratio distribution. The uncertainty of the estimator is drawn from this distribution around the parameterisation with an exponential in the toy Monte Carlo.

the spread around a exponential parameterisation of the uncertainty as a function of the energy and the systematic uncertainty due to the footprint model in parallel in figures 4.13, 4.14for real data and the full validity range of each reconstruction method respectively. The uncertainty in the energy estimate from the Fluorescence Detector and the spread of the error of S_{SD} around the parameterisation were parameterised using a ratio distribution. The parameters used for the toy Monte Carlo and their uncertainties are shown in detail in appendix B.

For the shower-to-shower fluctuation the value of $\sigma_{sh2sh} = 10\,\%$ given by [23] is used indepently of the zenith angle and energy for low zenith angles. For high zenith angles the value of $14\,\%$ from [71, 74] is used. For the Fluorescence Detector measurement as reference energy the uncertainy was assumed to be ratio-distributed independently of the energy as shown in figure 4.15. The energy distribution of the simulated calibration sets was drawn from the distribution of the reference energies measured by the Fluorescence Detector as shown in figure 4.16.

For each reconstruction method a number of fake samples have been created using the toy Monte Carlo and reconstructed with different values of the cut parameter Δ. For the LDF reconstruction 60 sets of the 8134 events after cuts were created. For the HAS calibration it was 250 sets of 296 events. The input calibration curve to the toy Monte Carlo was chosen as the expected values derived before

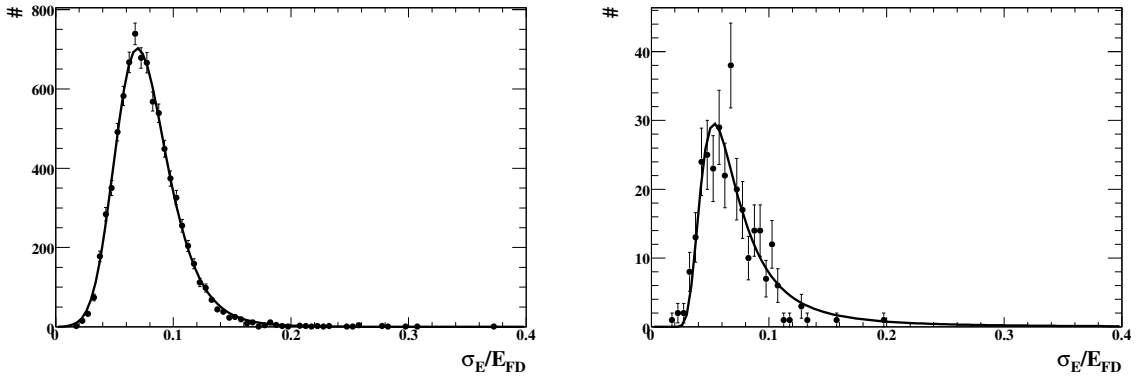

Figure 4.15: The uncertainty of the reference energy given by the Fluorescence Detector for the two data sets. The lines show a ratio distribution as parameterisation.

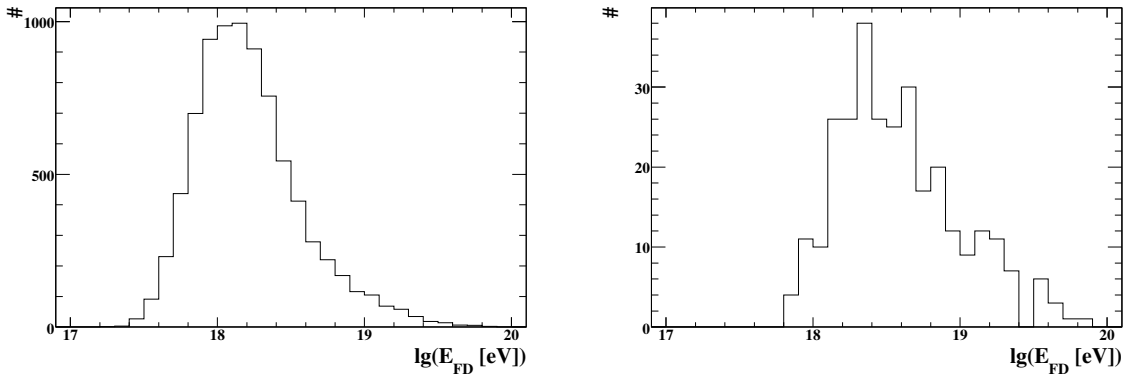

Figure 4.16: The distributions of the reference energy given by the Fluorescence Detector measurement for low and moderate zenith angles and moderate and high zenith angles respectively. This energy distribution is used to create simulated calibration sets for cut optimisation.

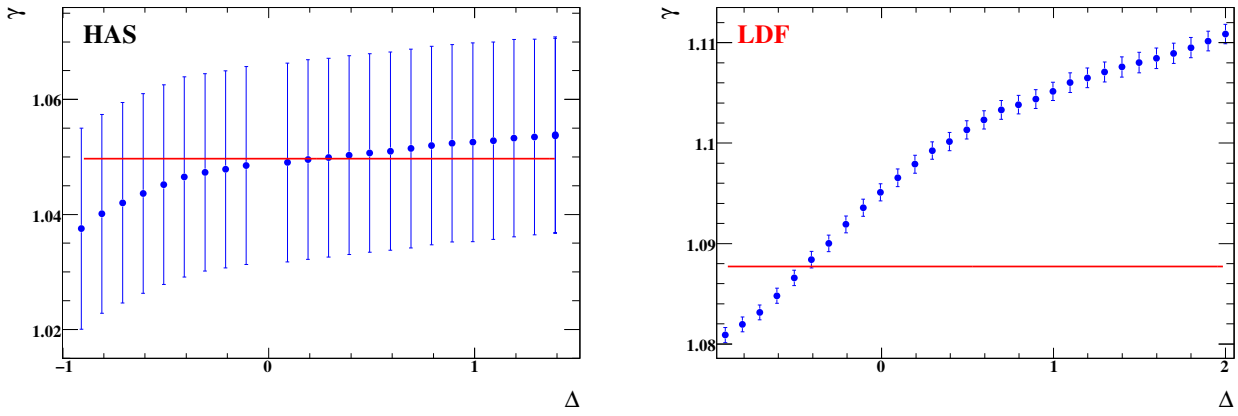

Figure 4.17: The mean slope of the calibration curve as a function of the inclination Δ of the anti-bias cut for a large number of calibration data sets using a toy Monte Carlo. The true slope of the data sets is plotted as a horizontal line. Left panel: The HAS calibration data set with 296 events between zenith angles $60°$ and $80°$ was used to create 256 fake calibration sets. Right panel: 64 sets of 6800 events were created using the distributions of the calibration set for the LDF reconstruction spanning over a zenith angle range up to $71°$.

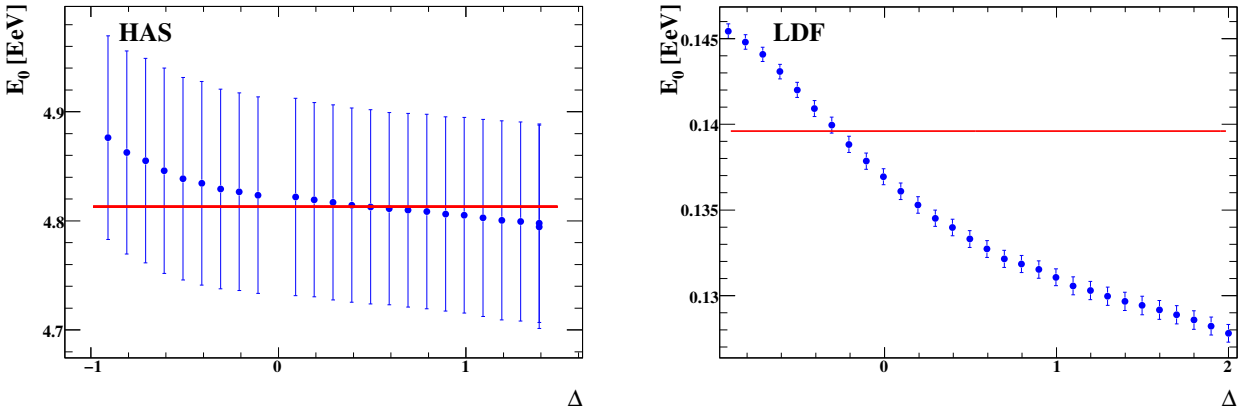

Figure 4.18: The same toy Monte Carlo data sets as in figure 4.17 were used to derive the energy E_0 at $S_{SD} = 1$. The input of E_0 is illustrated by a horizontal line.

using a cut with $\Delta = 0$

$$E_{SD}^{LDF} = 0.140 \cdot S_{1000}^{1.09}$$
$$E_{SD}^{HAS} = 4.82 \cdot N_{19}^{1.05}. \tag{4.3.8}$$

The resulting slopes and normalisations for different cut slope parameters Δ are shown in figures 4.17, 4.18. The input values are shown as a horizontal line. The optimum cut parameters Δ for the calibration of real data are given as the intersection of the reconstructed mean calibration curve parameters from the toy Monte Carlo generated sets with the input value

$$\Delta_{LDF} = -0.3, \Delta_{HAS} = 0.2. \tag{4.3.9}$$

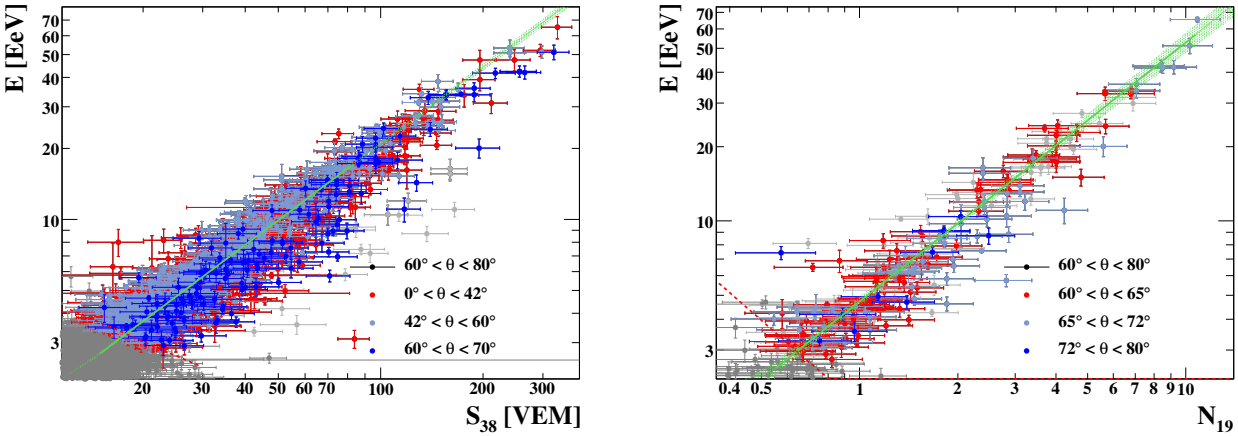

Figure 4.19: The calibration data set and the calibration curves for the LDF reconstruction in the left panel and the HAS reconstruction in the right panel. For subsets in different zenith angle ranges the points are colour coded. Independent calibration curves for those subsets are shown in the same colour as the corresponding points.

Application to real hybrid data

This method is using high quality hybrid data from the Pierre Auger Observatory as described in section 4.1. As the reference energy is based on the quasi-calorimetric FD measurement this method gives a simulation independent calibration avoiding the propagation of biases in the hadronic interaction models [45] or primary mass.

For the LDF reconstruction the correction of the energy estimator is vital as S_{1000} depends on the particle density on ground which is influenced by attenuation. For N_{19} no zenith angle dependent correction is required as shown in figure 4.19. The resulting calibration curves

$$\begin{aligned} E_{LDF}^{CAL} &= (0.147 \pm 0.004)\,\mathrm{EeV} \cdot S_{38}^{(1.077\pm0.004)} \\ E_{HAS}^{CAL} &= (4.72 \pm 0.15)\,\mathrm{EeV} \cdot N_{19}^{(1.049\pm0.009)} \end{aligned} \tag{4.3.10}$$

are cross-checked by fits to subsets of the zenith angle range. The derived values again agree with the overall fit within the uncertainties as shown in table 4.2. The correlation of the overall parameters is $cov_{LDF}(E_0, \gamma) = 2.9 \cdot 10^{-5}$ for the LDF reconstruction and $cov_{HAS}(E_0, \gamma) = 0.0005$ in case of the HAS reconstruction.

The calibration with determination of the zenith angle dependency from hybrid data uses the raw estimator S_{SD} and converts it to $S_{SD,ref}$ internally. The attenuation parameters and the calibration constants are determined at once. For the hybrid data set the calibration curves

$$\begin{aligned} E_{LDF}^{DEC} &= (0.139 \pm 0.004)\,\mathrm{EeV} \cdot S_{1000}^{(1.101\pm0.008)} \\ E_{HAS}^{DEC} &= (4.71 \pm 0.11)\,\mathrm{EeV} \cdot N_{19}^{(1.050\pm0.025)} \end{aligned} \tag{4.3.11}$$

	$0^\circ < \theta < 41^\circ$	$0^\circ < \theta < 70^\circ$	$41^\circ < \theta < 70^\circ$
E_0^{CAL}	0.139 ± 0.005	0.147 ± 0.004	0.157 ± 0.006
γ_0^{CAL}	1.084 ± 0.005	1.077 ± 0.004	1.065 ± 0.005
E_0^{DEC}	0.133 ± 0.004	0.139 ± 0.004	0.147 ± 0.005
γ_0^{DEC}	1.114 ± 0.007	1.101 ± 0.008	1.083 ± 0.008
	$60^\circ < \theta < 65^\circ$	$60^\circ < \theta < 80^\circ$	$65^\circ < \theta < 80^\circ$
E_0^{CAL}	4.62 ± 0.16	4.72 ± 0.15	4.77 ± 0.16
γ_0^{CAL}	1.032 ± 0.011	1.049 ± 0.009	1.069 ± 0.010
E_0^{DEC}	4.76 ± 0.11	4.71 ± 0.11	4.63 ± 0.13
γ_0^{DEC}	1.070 ± 0.026	1.050 ± 0.025	1.032 ± 0.031

Table 4.2: The values of the calibration constants derived with various methods for the LDF reconstruction (upper table) and the HAS reconstruction (lower table) respectively. Fits for subsets giving about equal hybrid acceptance are given for comparison.

are determined. The zenith angle correction for the LDF reconstructed sample results in an attenuation curve of $a = 0.949 \pm 0.024$ and $b = -0.765 \pm 0.066$. For the HAS reconstructed data set the slope of the zenith angle correction $a = -0.02 \pm 0.36$ is not significant e.g. N_{19} is verified not to be zenith angle dependent. The data sets and resulting calibration curves are are shown in figure 4.20. The solid points show the original values of the energy estimator and after correction of the zenith angle dependency they move to the positions marked in light colours.

The relative deviations of the energy determined by the calibration curve and the Surface Detector reconstruction E_{SD} from the reference energy E_{FD} are shown for all methods and both data sets and therefore both reconstruction methods in figure 4.21. The deviations as a function of energy and zenith angle respectively are shown in figure 4.22 and figure 4.23 respectively. The flat behaviour is expected for an unbiased calibration.

For the LDF reconstruction the mean of the distribution is $\mu_{CAL,LDF} = 0.034 \pm 0.006$ and $\mu_{DEC,LDF} = 0.030 \pm 0.006$ with the direct energy calibration resulting in a bias where calibration after constant intensity cut gives almost no bias. The width of the distributions is $\sigma_{CAL,LDF} = 0.187 \pm 0.004$ and $\sigma_{DEC,LDF} = 0.181 \pm 0.004$ also compatible within the uncertainty giving an overall resolution of about $18\,\%$. For the HAS reconstruction the mean of the distribution is $\mu_{CAL,HAS} = 0.048 \pm 0.023$ and $\mu_{DEC,HAS} = 0.048 \pm 0.023$ giving a small bias due to poor statistics. The width of the distributions is $\sigma_{CAL,HAS} = 0.199 \pm 0.030$ and $\sigma_{CI,HAS} = 0.198 \pm 0.031$ also compatible within the uncertainty giving an overall resolution of about $20\,\%$.

Cross-Calibration of the surface detector

As the application of both reconstruction methods, the LDF method and the HAS method respectively, is valid for moderate zenith angles a calibration of N_{19} with the energy estimate determined using the LDF reconstruction is possible. There are mor than 21000 events in the overlap region at zenith angles $60^\circ < \theta < 70^\circ$ reconstructable with both surface detector reconstruction algorithm. This exceeds the number of 300 high quality hybrid events by a factor of 70. Also the only source of differences between the reference parameters and the parameters to be calibrated is the reconstruction algorithm.

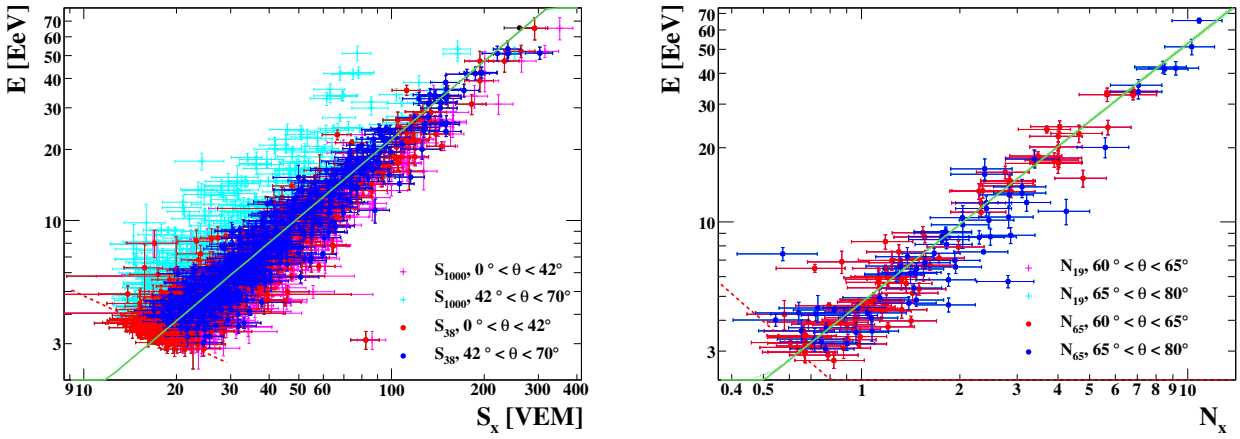

Figure 4.20: Illustration of the calibration curve with respect to the data set used for calibration. The movement of the points due to the zenith angle dependent correction is illustrated by the points in light colors. The LDF reconstructed data set is shown in the left panel and the HAS reconstructed data set in the right panel.

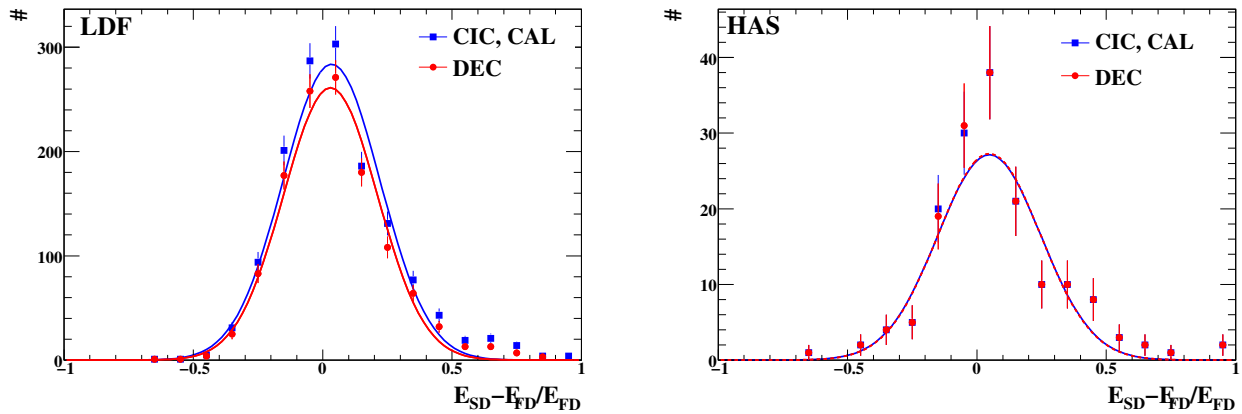

Figure 4.21: The pull distributions giving both the bias and the resolution of the energy calibration methods using the energy measurement from the Fluorescence Detector respectively. In the left panel the situation for the data set reconstructed with the LDF algorithm is shown. The calibration pull of the HAS reconstruction for the different methods is shown in the right panel.

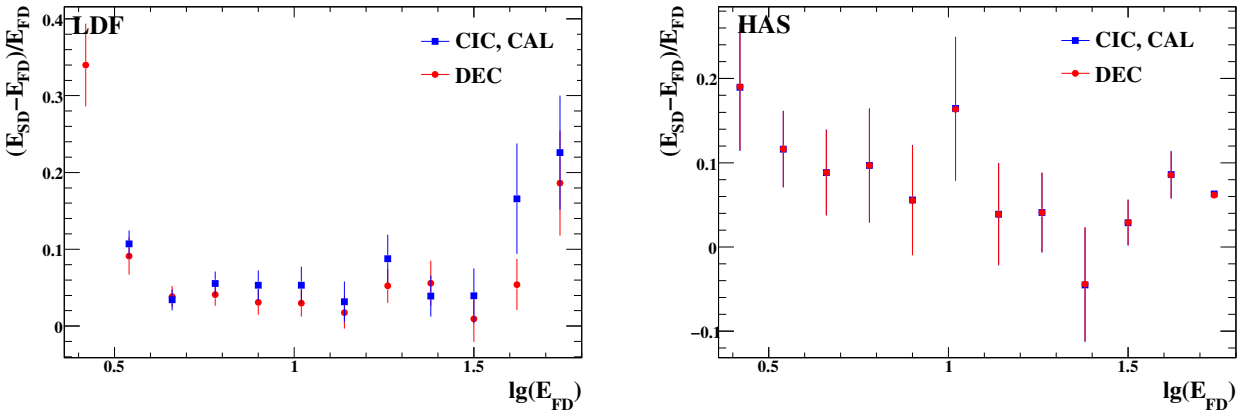

Figure 4.22: The residuals of the calibration curve fit for the different calibration methods as a function of energy. For the LDF reconstruction the calibration with corrected $S_{1000}(\theta = 38°)$ by the constant intensity method and the method deriving energy calibration and attenuation curve from hybrid data are shown in the left panel. In the right panel the calibration of the uncorrected N_{19}, the $N_{19}(\theta = 65°)$ determined by the constant intensity method and the energy calibration with determination of the zenith angle determination from hybrid data are shown.

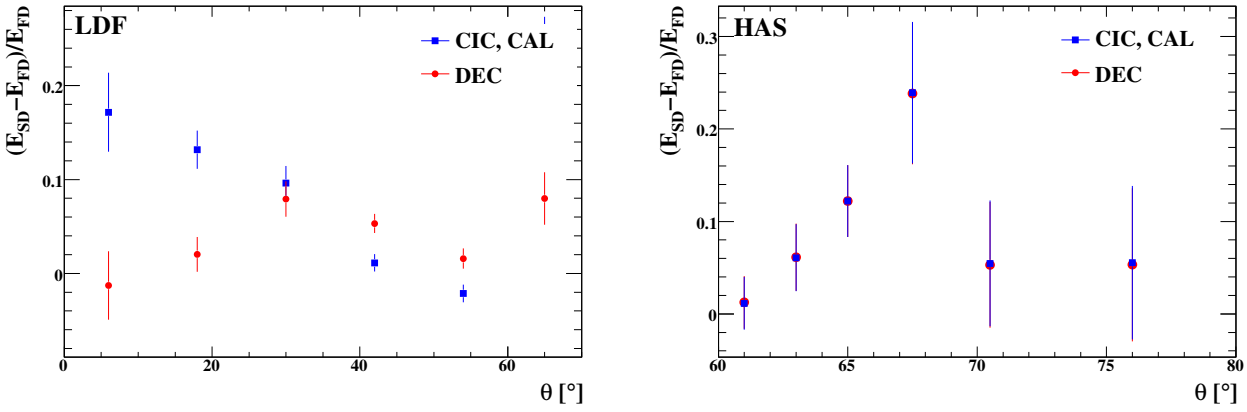

Figure 4.23: The residuals of the calibration curve fit for the different calibration methods as a function of the zenith angle θ. For both reconstruction mehods the energy calibration residuals for both methods using a zenith angle correction are shown respectively. For the HAS reconstruction the calibration of the uncorrected energy estimator N_{19} is shown too. The flat behaviour of the residuals illustrates the correct zenith angle corrections or in case of the HAS reconstruction the energy estimator to be independent of the zenith angle.

Effects of the shower evolution and the properties of the detector are identical for reference and test event. Thus effects like shower-to-shower fluctuations do not affect cross-calibration.

The uncertainty of the reference energy has four major contributions: The uncertainty from the fluorescence detector measurement that is the basis for the energy estimate using the LDF reconstruction $E_{SD,LDF}$, the uncertainty from sampling introduced in the reconstruction algorithm, the uncertainty due to the LDF model and the uncertainties introduced by the angular correction and the energy calibration respectively. As both energy estimators are deduced using the same real showers shower-to-shower fluctuations give no additional contribution and therefore are properly included into the latter uncertainty. The systematic uncertainty on the energy given by the systematics of the Fluorescence Detector measurement defining the energy scale is accounted for externally. The statistical uncertainty and the uncertainty from the reconstruction procedure is included into the uncertainty coming from the beforehand hybrid calibration procedure. The error bars on $E_{SD,LDF}$ are given as

$$\begin{aligned}\sigma^2(E_{SD,LDF}) &= \left(\frac{\mathrm{d}E_{SD.LDF}}{\mathrm{d}S_{1000}}\right)^2 \sigma^2_{reco}(S_{1000}) + \left(\frac{\mathrm{d}E_{SD.LDF}}{\mathrm{d}S_{1000}}\right)^2 \sigma^2_{LDF}(S_{1000}) \\ &+ \left(\frac{\mathrm{d}E_{SD.LDF}}{\mathrm{d}S_{38}}\right)^2 \sigma^2_{CI}(S_{38}) + \sigma^2_{cali}(E_{SD,LDF}.\end{aligned} \tag{4.3.12}$$

The uncertainty of N_{19} consists of a statistic contribution calculated by the reconstruction algorithm $\sigma_{reco}(N_{19})$ and the uncertainty due to the choice of the muon profile based on the zenith angle $\sigma_\theta(N_{19})$. Both the uncertainty on $E_{SD,LDF}$ and on N_{19} depend on the energy. The overall reconstruction uncertainty for the energy estimators has been estimated as a function of energy estimators in figure 4.13. Together with the energy estimate given by the calibration algorithm in the previous sections the exponential behaviour of σ_{SD} in $\lg S_{SD}$ can be reformulated as a function of energy

$$\sigma_{SD}(E) = \exp a + \frac{b}{\gamma} \lg \frac{E}{E_0} \tag{4.3.13}$$

using the parameters a and b from equation 4.3.7 and the calibration constants E_0 and γ from the corresponding calibration curve. The result is shown in the left panel of figure 4.24. The fraction of the uncertainties is only weakly dependent on energy and close to 1 for the energy range used for calibration as is shown in the right panel of figure 4.24. With equation 4.3.5 the slope of the cutting line can be determined resulting in a $\Delta = 0.8$ according to equation 4.3.6 to be used for cross-calibration.

The resulting calibration curve deduced with the simple calibration method and the method with included zenith angle correction on N_{19} are based on largely increased statistics of 21540 events in the overlap region of the validity of both reconstruction algorithms for Surface Detector events. In the left panel of figure 4.25 the curves from both methods are shown on top of the underlying data points. The calibration constants

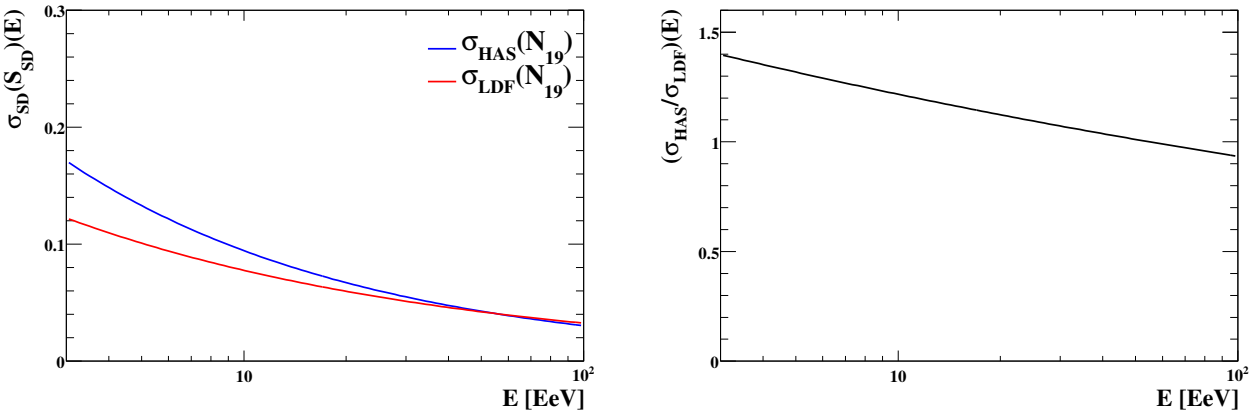

Figure 4.24: For calibration of the HAS reconstruction with the LDF reconstruction energy estimate only the uncertainties introduced by the reconstruction algorithm are relevant. Left panel: The relative uncertainties of the energy estimators N_{19} and S_{1000}. Right panel: The ratio of the reconstruction uncertainty is close to 1 almost constant in energy.

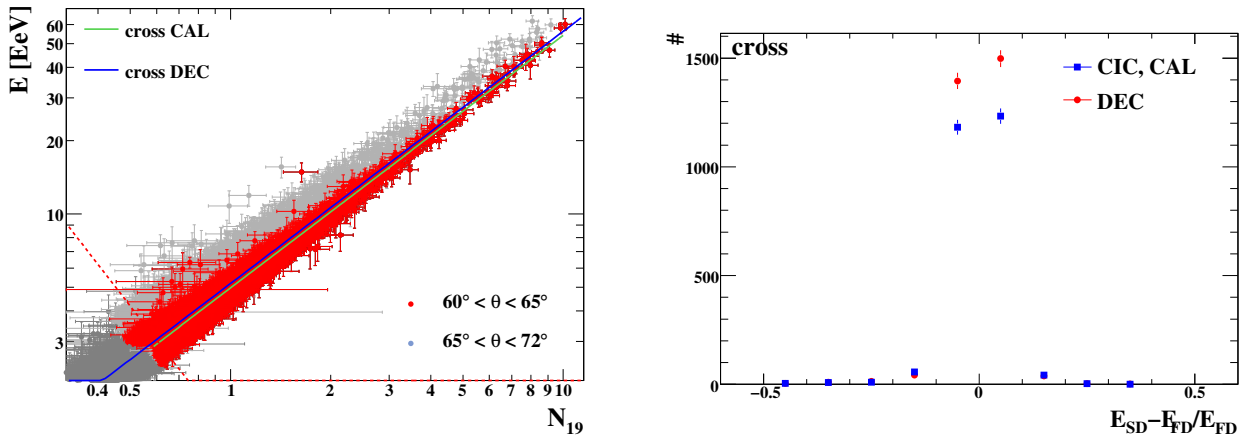

Figure 4.25: In the left panel the calibration curves deduced with and without zenith angle correction are shown together with the calibration data set. The error bars give the propagated uncertainties of $E_{SD,LDF}$ from the calibration procedure and the uncertainty of N_{19} due to reconstruction. The right panel shows the relative deviation of the calibrated energy $E^{cross}_{SD,HAS}$ from the reference energy $E_{SD,LDF}$.

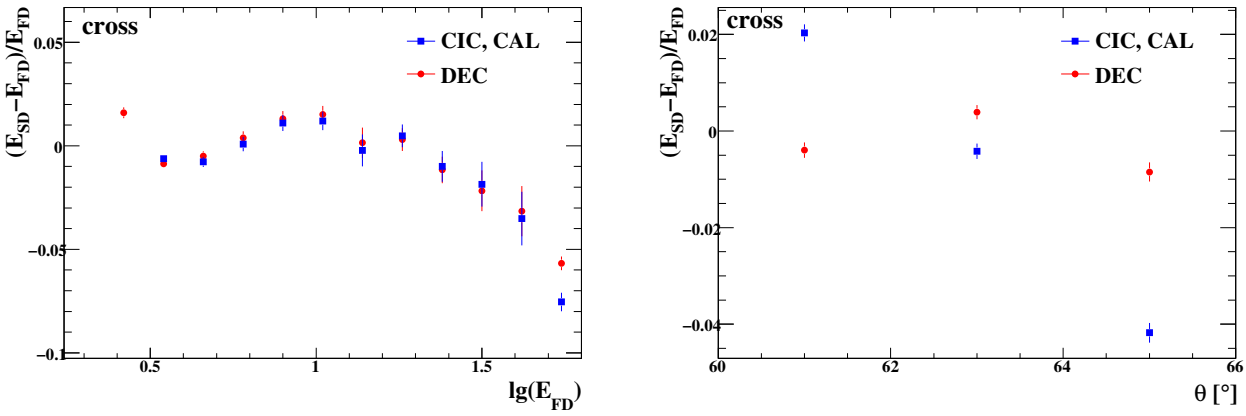

Figure 4.26: The deviation of the calibrated energy using cross-calibration as a function of the energy (left panel) and the zenith angle (right panel) with and without zenith angle correction. The deduced zenith angle correction from the overlap data set is small.

$$E_{cross}^{CAL} = 4.96 \pm 0.02\,\mathrm{EeV} \cdot S_{1000}^{(1.039\pm0.005)}$$
$$E_{cross}^{DEC} = 5.18 \pm 0.04\,\mathrm{EeV} \cdot N_{19}^{(1.035\pm0.005)} \tag{4.3.14}$$

deduced from the overlap data set of 1610 events above the diagonal cut agree well. The deduced slope for a N_{19} correction for zenith angle dependent effects is $a = 1.17 \pm 0.17$ giving an effect of $8\,\%$ in the range of the fit. An extrapolation to higher zenith angles is not done. In figure 4.25 the relative deviation of the resulting calibrated energy from the reference energy $E_{SD,LDF}$ is shown. The Gaussian fits to the curves result in $\mu_{CAL} = 0.01 \pm 0.1\,\%$ and $\sigma_{CAL} = 5.5 \pm 0.1\,\%$ for the calibration algorithm without angular correction and in case of the method including an angular correction $\mu_{DEC} = 0.1 \pm 0.1\,\%$ and $\sigma_{DEC} = 5.3 \pm 0.1\,\%$. Consistently the systematic uncertainty due to the two different reconstruction algorithms is $5.4\,\%$ in the overlap region of $60° < \theta < 80°$. With the flat behaviour of the relative deviation versus energy and zenith angle respectively in figure 4.26 no systematic bias as a function of the geometry or primary energy can be verified.

Application to Monte Carlo data

With the input parameters of shower simulations well known simulated events can be calibrated using the input energy. The simulated data set is not a continuous spectrum and therefore the constant intensity method can not be applied. With every simulated event having the input energy to the simulation available as reference, direct energy calibration can be used. The curves of calibration and attenuation are derived in the regime of moderately and highly inclined showers using the combined fit of the direct energy calibration, assuming a common threshold of $5 \cdot 10^{18}\,\mathrm{eV}$ in both cases. The reference energy has no error so the horizontal cut can be applied. The calibration curves are shown in figures 4.27,4.28 for proton and iron simulations respectively. The calibration constants are shown in table 4.3. As the zenith angle range extends only from 60° to 80° the angular correction was chosen according to equation 4.2.12 with $n = 1$

	a	E_0	γ
proton, HAS reconstruction	0.0	10.3667 ± 0.05	1.021 ± 0.003
iron nuclei, HAS reconstruction	0.0	7.28 ± 0.04	1.055 ± 0.003
proton, LDF reconstruction	-4.21 ± 0.05	0.217 ± 0.003	1.05 ± 0.002
iron nuclei, LDF reconstruction	-4.69 ± 0.05	0.385 ± 0.002	0.99 ± 0.001

Table 4.3: The slope of the angular correction function a and the parameters of the energy calibration curve as described in equation 4.3.15 for all combinations of two simulated primaries and two reconstruction methods respectively.

$$S_{SD} = \frac{S_{SD,raw}}{1 + a \cdot (\cos^2\theta - \cos^2 65^\circ)} \tag{4.3.15}$$

with the reference angle of 65° within the angular range of the simulated showers.

Both reconstruction methods show a strong dependency of the absolute normalisation of the energy on the primary mass. Also the zenith angle dependency differs for different primary masses as well as the index of the calibration function. Even though simulations do not reproduce real data consistently the dependency on primary mass indicates a systematic uncertainty in energy determination due to the unknown primary mass in real data. At 10^{19} eV the energies determined assuming protons or iron respectively differ by more than $40\,\%$ for both LDF and HAS reconstructions.

4.4 Results and Comparison

The determination of an energy estimator given by the reconstruction of Surface Detector data and a calibration function relating the energy estimator using a reference data set has been shown using two different reference sets and two different methods respectively.

The zenith angle dependency of the energy estimator S_{SD} has been determined using the constant intensity method and by a method making use of hybrid events by fitting both the zenith angle dependency of the estimator and the energy calibration function at once. The different curves at a reference value of the energy estimator are shown in figure 4.29. Above a threshold of about $S_{1000} > 30\,\mathrm{VEM}$ the results for attenuation of the shower seen in S_{1000} are stable. The values deduced for the whole angular range are

$$S_{38} = S_{1000} \cdot (1 + a(cos^2\theta - cos^2 38^\circ) + b(cos^2\theta - cos^2 38^\circ)^2) \tag{4.4.1}$$

$$\begin{aligned} &\text{CAL:} \quad a_{CIC} = 0.86 \pm 0.05 \quad b_{CIC} = -1.23 \pm 0.15 \\ &\text{DEC:} \quad a_{DEC} = 0.949 \pm 0.024 \quad b_{DEC} = -0.765 \pm 0.066. \end{aligned} \tag{4.4.2}$$

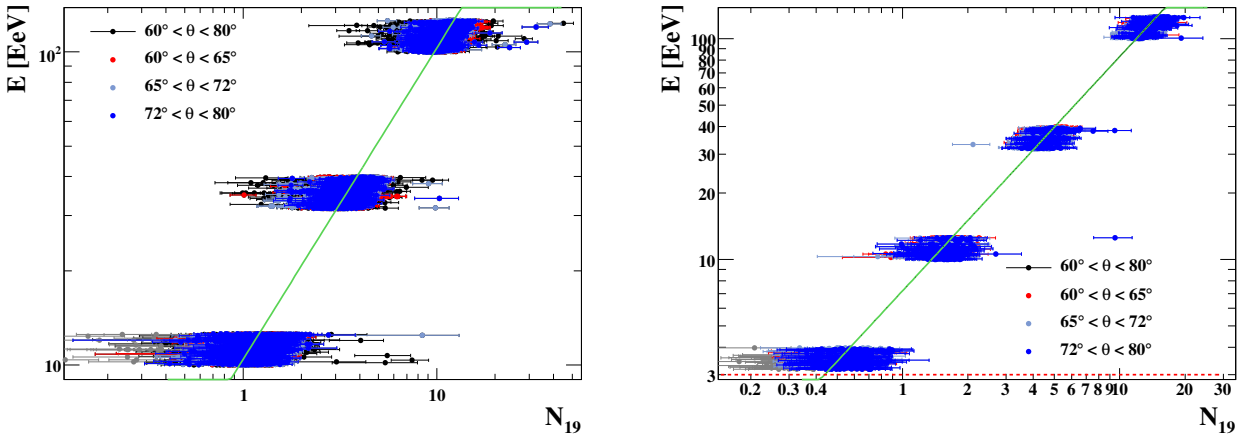

Figure 4.27: The calibration curves for simulated protons (left) and iron nuclei (right) showers reconstructed with the HAS reconstruction respectively. The antibias cut has been set at an energy of $5 \cdot 10^{18}$ eV. *The error bars give the reconstruction uncertainties of the single events, an error band is calculated from the fit and the propagation of the uncertainties in the angular correction curve. Its width is of the order of the linewidth of the calibration curve.*

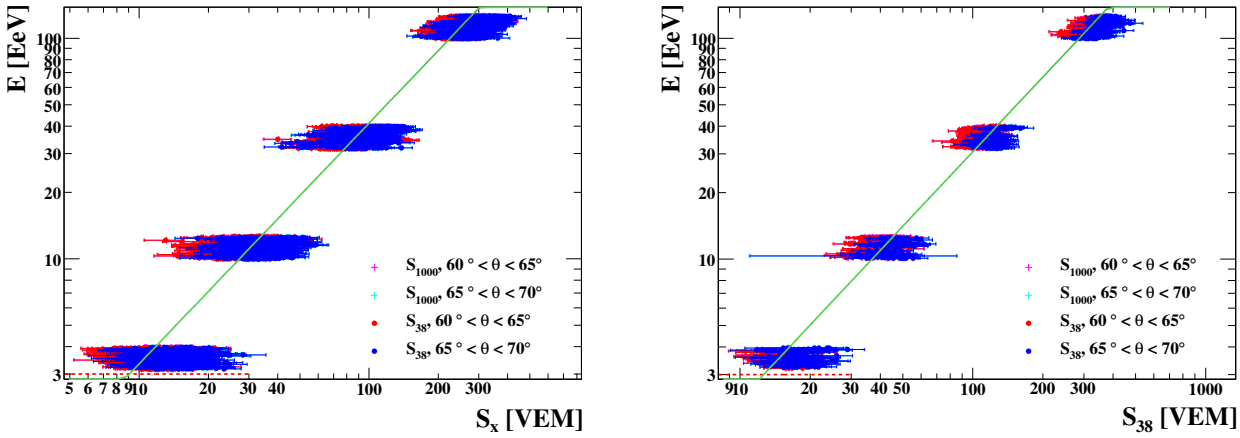

Figure 4.28: The calibration curves for simulated protons (left) and iron nuclei (right) showers reconstructed with the HAS reconstruction respectively. The antibias cut has been set at an energy of $5 \cdot 10^{18}$ eV. *The error bars give the reconstruction uncertainties of the single events, an error band is calculated from the fit and the propagation of the uncertainties in the angular correction curve. Its width is of the order of the linewidth of the calibration curve.*

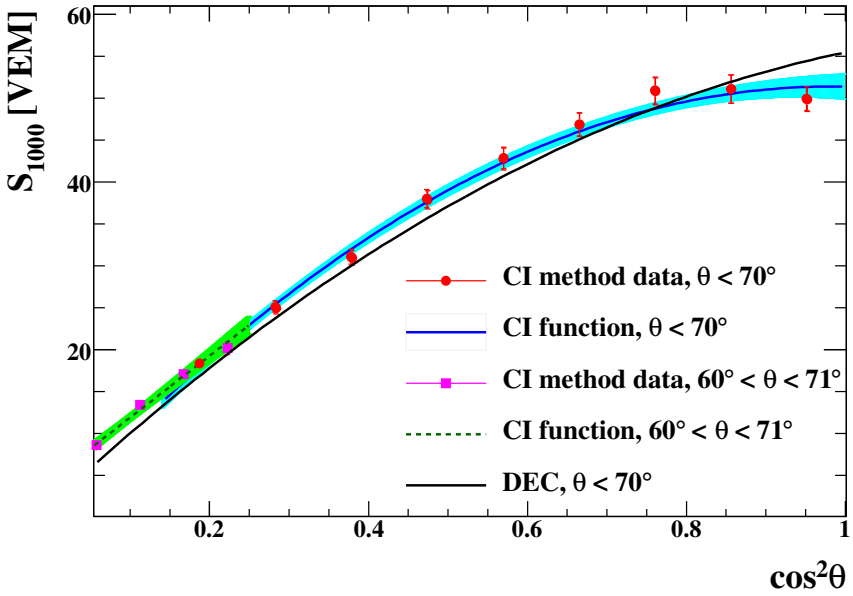

Figure 4.29: The attenuation curves deduced with the constant intensity method and with the direct energy calibration from hybrid data respectively for the LDF reconstruction. The error bands show the one σ uncertainty of the functions. The error bars of the data points are the propagated uncertainties from interpolation of the integrated spectra.

In case of the constant intensity method the reference value of $S_{38} = 50\,\mathrm{VEM}$ was chosen providing enough statistics while avoiding threshold effects on the attenuation curve. The discrepancy of the two methods is assumed to define the width of the systematic uncertainty of the determination of the attenuation curve. So the atttenuation parameters according to equation 4.4.2 are

$$a = 0.86 \pm 0.05_{stat} \pm 0.05_{syst} \quad b = -1.23 \pm 0.15_{stat} \pm 0.22_{syst}. \tag{4.4.3}$$

For the HAS reconstruction basically no zenith angle dependency of N_{19} is expected as the estimator is a ratio of the measured muon number with respect to the muon number at this zenith angle and a reference energy. For the range of 62° to 80° the slope of a linear zenith angle correction depending of N_{19} is compatible with zero using the constant intensity method. Also the calibration of N_{19} using the energy estimate from the LDF reconstruction reveals no zenith angle dependence of N_{19}. Using the direct energy calibration the slope of a linear function in $cos^2\theta$ is $a_{DEC} = -0.02 \pm 0.36$ while the cross-calibration using the DEC algorithm results in $a_{cross} = 1.17 \pm 0.17$ which is due to biases in the LDF reconstruction starting to occur at $\theta > 65^\circ$ as shown in chapter 5.

The muon dominated regime of moderately and highly inclined air showers is very sensitive to the primary mass composition. Independently of the reconstruction method the energy estimator is basically a measure for the muon number in the shower as the electromagnetic component is strongly suppressed by attenuation compared to the muonic component at moderate zenith angles. At high zenith angles the primary electromagnetic component is extinct. With the higher number of muons produced by heavier primaries the relation between the energy estimator and the true energy changes. The extreme cases of protons and iron nuclei have been examined using simulated showers. For iron primaries the muon number is higher. Thus an iron shower produces a higher energy estimated

than a proton shower of the same energy. The calibration curves for Monte Carlo showers caused by proton and iron primaries respectively and reconstructed with both the LDF reconstruction and the HAS reconstruction are shown in figure 4.30. For both reconstruction methods the calibration curves deviate significantly. An estimate of the uncertainty under the assumption of no information on mass composition used in the energy determination is given in figure 4.31. The curves show the offset in the energy assigned to a proton shower assuming an iron shower and vice versa. Independent of the reconstruction method the reconstructed energy deviates up to $40\,\%$ from the true value if reconstructing under the assumption of a wrong primary.

In case of hybrid calibration the energy assigned to the event by Fluorescence Detector reconstruction does not depend explicitly on the primary mass. A change of the average primary mass with the energy is compensated in a shift of the parameters of the calibration curve with respect to a constant composition as shown in [74]. In case of the LDF reconstruction the determination of the energy from the estimator S_{38} the parameters

$$\begin{aligned} E(S_{38}=1) = E_0 &= (0.147 \pm 0.005_{stat} \pm 0.004_{syst})\,\mathrm{EeV} \\ \gamma &= 1.077 \pm 0.008_{stat} \pm 0.012_{syst} \end{aligned} \tag{4.4.4}$$

$$\tag{4.4.5}$$

are found. The systematic errors account for the results of the two different methods. The values are calculated by using the interval of the values derived with different methods and assuming the uncertainty to be one half of the span.

The cross-calibration of N_{19} by using S_{38} the statistics for determinating the calibration curve largely increases statistics from $\sim$ 200 events to more than 1600 events. From the methods of cross-calibration and direct energy calibration the calibration determined with hybrid events as described above has been cross-checked. The resulting parameters for determining the energy from N_{19} are

$$\begin{aligned} E(N_{19}=1) = E_0 &= (4.72 \pm 0.02_{stat} \pm 0.23_{syst})\,\mathrm{EeV} \\ \gamma &= 1.049 \pm 0.020_{stat} \pm 0.007_{syst} \end{aligned} \tag{4.4.6}$$

$$\tag{4.4.7}$$

with the differences of the various methods used as an estimate of the systematic error. The resulting error bands are shown in figure 4.32. The uncertainties are calculated event by event by propagating the uncertainties in reconstructed values, angular correction and calibration and summation over these uncertainties

$$\begin{aligned} \sigma(E) &= \sqrt{\sigma^2_{stat}(E) + \sigma^2_{syst}(E)} \\ \sigma_{stat}(E) &= \sqrt{\sum_i \sigma^2_{i,syst}(E)} \\ \sigma_{syst}(E) &= \sqrt{\sum_j \sigma^2_{j,syst}(E)}. \end{aligned} \tag{4.4.8}$$

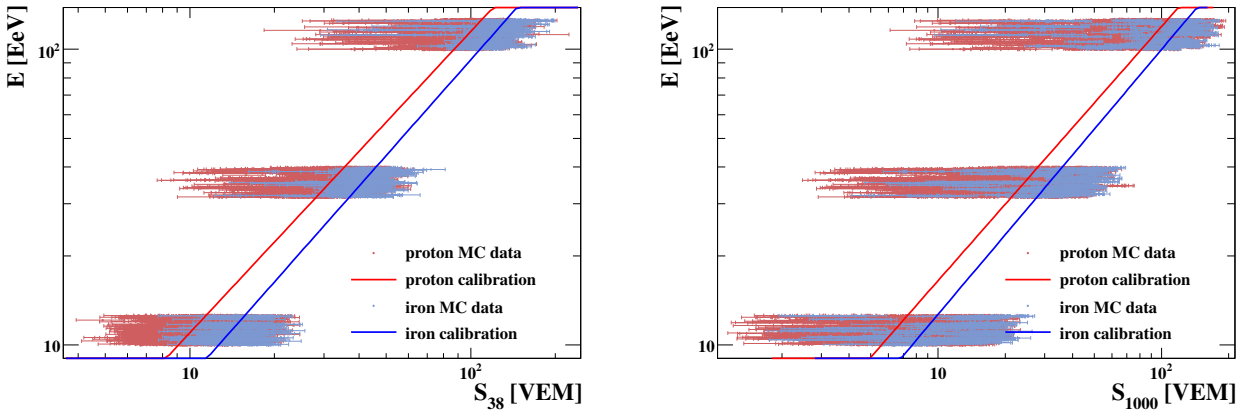

Figure 4.30: The calibration curves of simulated showers for the LDF reconstruction (left panel) and the HAS reconstruction (right panel) for moderately inclined events respectively. The normalisation E_0 differs about $40\,\%$ depending on the primary mass. This effect is accounted for as systematic uncertainty.

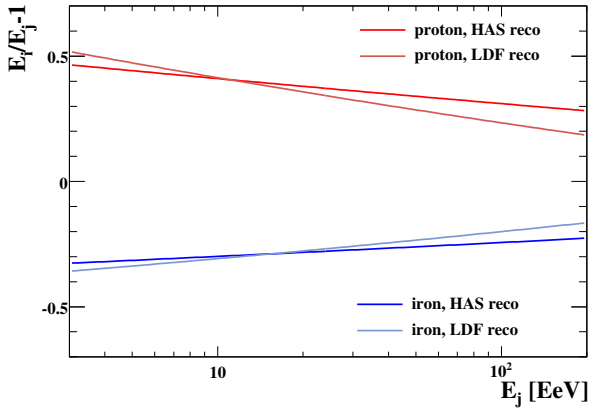

Figure 4.31: The overall relative uncertainty of the energy estimate by the Surface Detector reconstruction algorithms as a function of energy due to the primary mass. In case of the hybrid reconstruction the reference energy from Fluorescence Detector measurement is independent of the primary and compensates for this effect (see text).

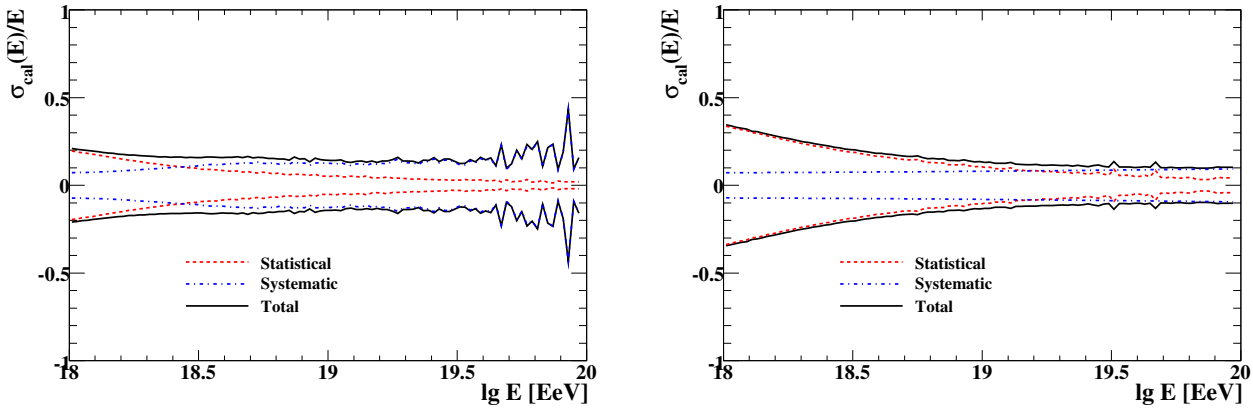

Figure 4.32: The uncertainty in the energy determination for zenith angles larger than $\theta = 60°$ due to the statistic and systematic uncertainties of the calibration curves for the LDF reconstruction (left panel) and the HAS reconstruction (right panel) respectively.

Contribution		$\Delta E/E\%$
Fluorescence yield	Absolute calibration	14
	Pressure dependence	1
	Humidity dependence	1
	Temperature dependence	5
FD calibration	Absolute calibration	11
	Wavelength dependence	3
Atmosphere	Rayleigh	1
	Wavelength dependence of aerosol scattering	1
	Aerosol phase function	1
FD reconstruction	Method	10
	Invisible energy	4
Total		22

Table 4.4: The contributions to the uncertainty of the energy scale from the Fluorescence Detector measurement as reference energy for calibration [53].

Contribution		$\Delta E/E\%$
Fluorescence detector		22
LDF parameterisation		5
Angular correction	Method	10
	Systematic	5
Energy calibration	Method	10
	Systematic	5
Total		27

Table 4.5: The contributions to the uncertainty of energy given by the Surface Detector after cross-calibration.

The uncertainties given here are propagated to the energy spectrum in chapter 6. The statistical uncertainties decrease rapidly with increasing energy while the systematic uncertainties of the calibration increase due to the fit procedures being dominated by the high statistics in the lower energy region.

Chapter 5

Comparison of Reconstruction Methods

In a moderate zenith angle interval $\theta \in [60^\circ, 70^\circ]$ the validity range of the LDF reconstruction and the HAS reconstruction overlaps. Both methods can be applied for air showers in this range making about $14\,\%$ of the total geometrical acceptance of the Surface Detector array. The Monte Carlo data sets described in section 4.1 provide good statistics in the overlap region where also the input energy is known as reference for cross-checks. These data can be used to cross-check the compatibility of both reconstruction methods and and their accuracies respectively. When comparing accuracies as a function of zenith angle the arbitrary choice of $\theta = 60^\circ$ as the upper limit of validity of LDF reconstruction and lower limit of HAS reconstruction respectively can be replaced by a more elaborate transition angle. Also the agreement of reconstructed parameters used for physics analysis for both reconstruction methods in and outside the overlap range is checked. This agreement is vital for using Surface Detector data for physics analysis in the whole zenith angle range.

5.1 Geometry

With increasing zenith angle the number of triggered stations rises as a result of the projection of the shower disc on the ground. With more supporting points the accuracy of the fit rises naturally. In the first step of the angular reconstruction the shower plane fit is applied to the data surviving the station selection giving starting values of the zenith and azimuth angles respectively. Subsequently the determination of the energy estimator also gives an estimate of the core position $\widehat{c}$. The reconstruction of the origin $\widehat{R}_c$ of the shower assuming a spherical expansion of the shower front in the atmosphere is in principle independent of the estimate of the position of the shower core. The algorithm is the same for both the LDF reconstruction and the HAS reconstruction. Nevertheless the shower direction estimate using the origin is constructed as the direction vector of the line connecting the estimated positions of the core and the shower origin respectively

$$\vec{a} \;=\; \frac{\widehat{R}_c - \widehat{c}}{|\widehat{R}_c - \widehat{c}|} \tag{5.1.1}$$

Differences in the reconstructed shower direction must depend on the differences of the reconstruction algorithms only. So the set of stations after station selection and the core position given by the

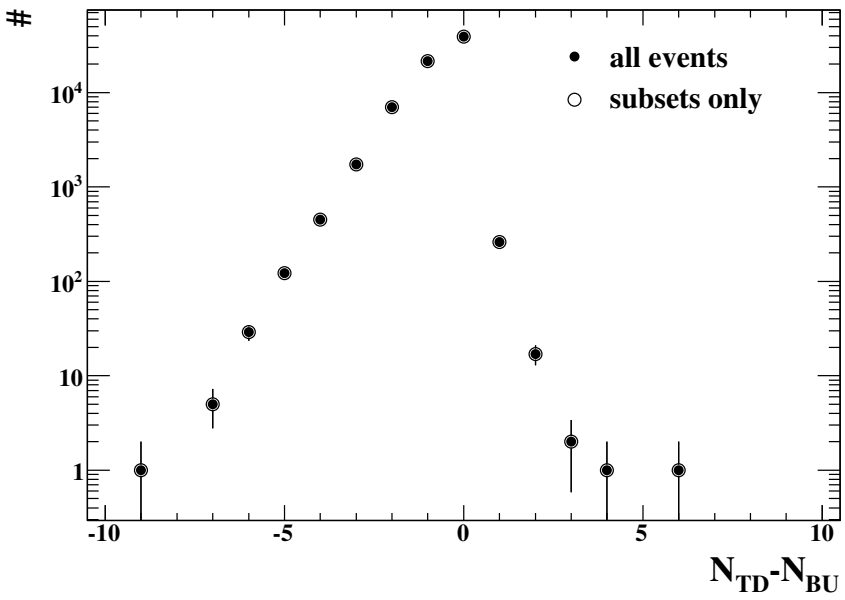

Figure 5.1: The difference of the number of selected stations by Top-Down selection and Bottom-Up selection. The red circles mark the events with one selection being a subset of the other one. The error bars illustrate Poissonian errors.

shower size reconstruction are the only sources of differences in the determination of the shower axis. As both the angular reconstruction and the determination of the core position depend on the station set in reconstruction the two contributions cannot be seperated easily. The difference of the number of selected stations after Top-Down selection and Bottom-Up selection respectively is shown in figure 5.1. The selection algorithms might select stations the other one deselects. The difference in station number can not distinguish events for which one of the selection algorithm selects a subset of the selection by the other one. As shown in the figure for all events the Top-Down algorithm selects the same stations or a subset of the selection by the Bottom-Up selection or vice versa.

The selection algorithms differ in the way they reject stations. In the Bottom-Up selection rejection of accidental stations depends on the reconstruction of the seed. A seed spoiled by accidental stations or accidental muons leads to errornous rejection of stations. Bottom-Up selection works best with `TOT` stations. This results in the behaviour of the discrepancies in station multiplicity in zenith angle and energy shown in figure 5.2. With the signal of a station being its weight in the reconstruction of the core position and the energy estimator the influence of a station on the reconstructed values depends on its signal value. Therefore also the impact on the final reconstructed shower direction is given by the total signal of the station. In figure 5.3 the signal distribution of all stations that have been selected by only one of the selection algorithms is shown. The selection algorithms differ in a negligible way for Surface Detector stations with high signals. So the influence of the selection algorithm on the core position is low.

In order to compare the difference of the axes given by different reconstruction algorithms or the input axis of a simulated shower the angular separation ψ is defined as the opening angle of the axes vectors

$$\cos\psi_{i,j} = \vec{a_i} \cdot \vec{a_j}. \tag{5.1.2}$$

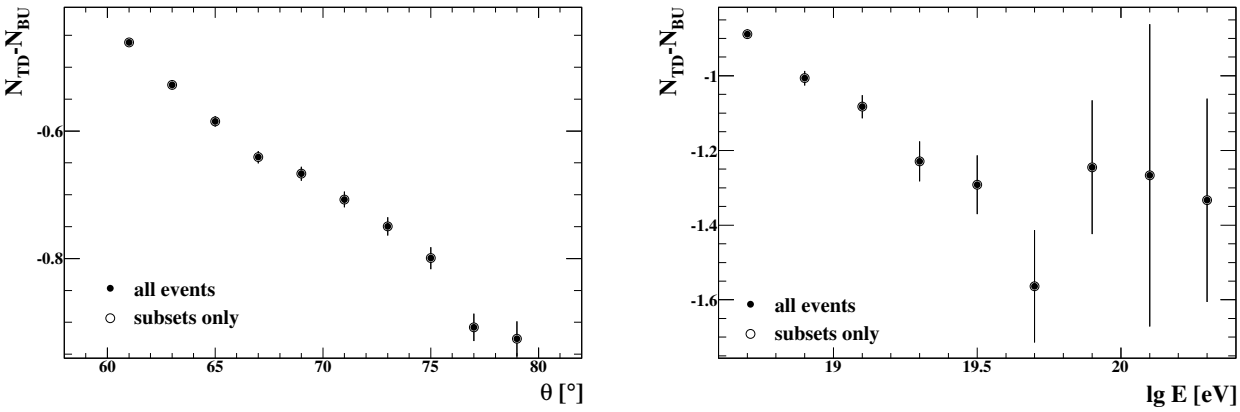

Figure 5.2: The discrepancy of the Top-Down selection and Bottom-Up selection respectively as a function of zenith angle and energy. The full symbols show the mean of the absolute difference with one standard deviation as the error bars. The open symbols show the abolute difference of station number only for events with one selection giving a subset of the stations selected by the other.

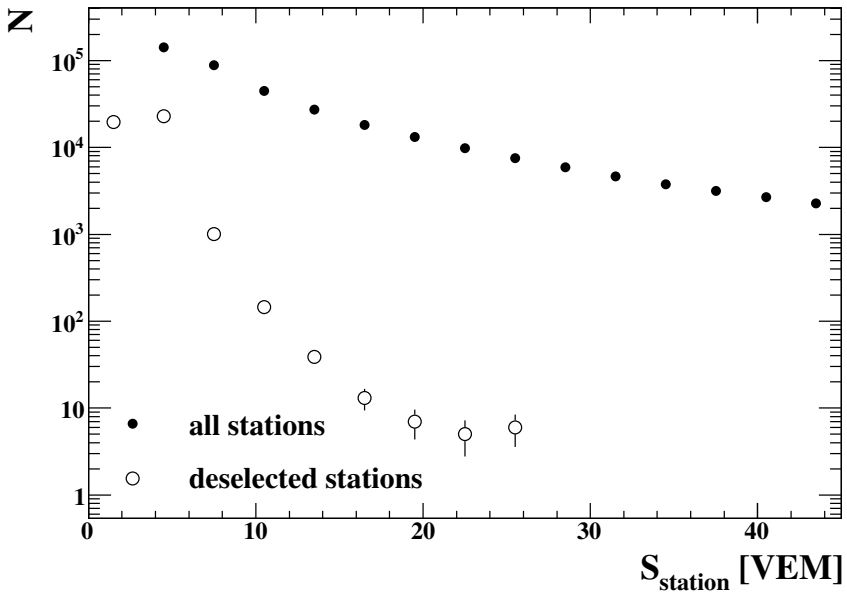

Figure 5.3: The signal distribution of all Surface Detector stations compared to the signal distribution of the stations that have been selected by only one of the two selection algorithms.

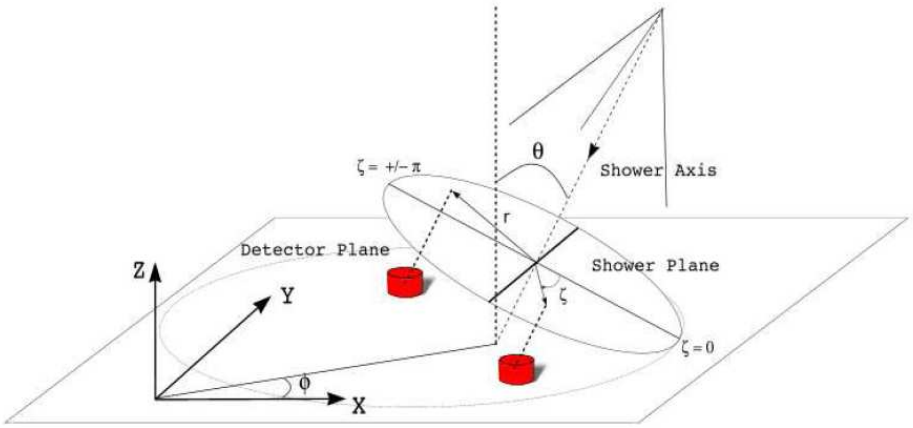

Figure 5.4: Shower geometry and deviations from a reference geometry. With the fit of a curved shower front deviations of the core position and the incoming direction are coupled and can be seperated in components along the shower development and orthogonal to the shower development [55].

As the angular separation can be decomposed into the differences in zenith angle $\Delta\theta$ and the azimuth angle $\Delta\phi$ respectively the distance of the reconstructed or simulated core positions can be decomposed into the projections on the coordinate axes of the shower plane frame. Besides the shower axis $\vec{a}$ the shower plane coordinates are defined by the direction vector of the intersection line of the shower plane and the ground plane $\vec{b_{ri}}$ and the vector $\vec{b_{up}}$ pointing into the ground vertically to the shower axis. With the vector $\vec{v}$ pointing in the local zenith direction the shower plane base vectors are

$$\begin{aligned} \vec{b}_{ri} &= \frac{\vec{a} \times \vec{v}}{|\vec{a} \times \vec{v}|} \\ \vec{b}_{up} &= \vec{a} \times \vec{b}_{ri}. \end{aligned} \tag{5.1.3}$$

Figuratively this definition gives the vector $\vec{b}_{ri}$ pointing to the right looking along the axis in upright position and the vector $\vec{b}_{up}$ pointing in the upstream direction i.e. the early region of shower development at ground. Considering only the core position a shift in the $\vec{b}_{up}$ direction decreases the zenith angle θ and vice versa. Deviations of the azimuth angle ϕ due to a shift in core position scale with the shift in $\vec{b}_{ri}$ direction as illustrated in figure 5.4. Neglecting other effects than the core shift the angular deviations can be written as

$$\begin{aligned} \sin\Delta\theta &= \frac{r_{SP,up}}{R_c} \\ \sin\Delta\phi &= \frac{r_{SP,ri}}{R_c} \\ \sin\psi &= \frac{r_{SP}}{R_c} = \frac{\sqrt{r_{SP,up}^2 + r_{SP,ri}^2}}{R_c} \end{aligned} \tag{5.1.4}$$

with the radius of curvature R_c as described in section 3.1 and the core shift vector projected into the shower plane $\vec{r}_{SP} = (r_{SP,up}, r_{SP,ri}, 0)$. So for small deviations $r_{SP} \ll R_c$ a linear dependency of the angular deviations due to core shift effects is expected. Also the dependency of the angular resolution and systematic angular shifts on the shower parameters is expected to be proportional to the core resolution and systematic core shifts as a function of the shower parameters.

In case of the Monte Carlo data set not only the input energy is known but also the shower geometry i.e. the incoming direction $\vec{a}$ and the core position $\widehat{c}_{MC}$ representing the virtual impact point of the shower primary. With the generated shower geometry as a reference frame the accuracy of the reconstructed values can be determined and the correlations of the deviations can be verified. Figure 5.5 illustrates the linear dependency of the angular separation of the reconstructed and simulated axes respectively as function of the core shift introduced by reconstruction with respect to the simulated core position. In figure 5.6 both the angular deviation and the core shift is shown separated into its respective components along and vertical to the direction of the shower development. As the resolutions of the core position and the reconstructed incoming direction are coupled their behaviour as a function of the shower parameters is similar besides effects of station selection on the shower origin $\widehat{R}_c$ given by the spherical model.

The main differences considering the reconstruction of the shower core position between the LDF and HAS reconstructions respectively are features of the footprint model: The LDF function diverges at the estimated core position binding the core to the station with the highest measured signal and the LDF function is not accounting for deviations from the cylindrical symmetry with respect to the shower axis. The muon profiles used in the HAS reconstruction do not diverge at the impact point and therefore core positions distant from the station with the highest signal are possible. Also the muon profiles and the electromagnetic content model account for asymmetries in the shower footprint due to geometrical effects and attenuation. Due to this effect both the core resolution and the angular resolution of showers with moderate and high zenith angles are better using the HAS reconstruction in all azimuth angles as shown in figure 5.7 and all energies as shown in figure 5.8. With rising energy also the number of stations and therefore the accuracy of both reconstruction methods increase. Anyway the effect of the systematic core shift does not depend on the number of stations. Thus this effect is present even at highest energies.

Moderately and especially highly inclined air showers show the station with the highest signal shifted into the early region of the shower footprint on ground with respect to the impact point due to asymmetries in the particle density and the expected signal. The shift of the reconstructed core position using the LDF reconstruction with respect to the impact point therefore rises with the strength of these effects. As shown in figure 5.9 the deviation of the reconstructed core and therefore also the deviation of the reconstructed direction using the spherical model are almost constant for the HAS reconstruction that accounts for asymmetries. Using the LDF reconstruction the reconstructed core position as well as the shower direction show a rising deviation from the simulated values with the zenith angle. As shown in figure 5.10 a systematic shift of the reconstructed core position into the early region of the shower compromises the zenith angle determination using the LDF reconstruction resulting in a systematic underestimation of the zenith angle.

5.2 Energy Resolution

The energy reconstruction based on the signals of the Surface Detector stations relies on the modelling of the footprint of the shower. The models are dependent on the shower parameters as the incoming

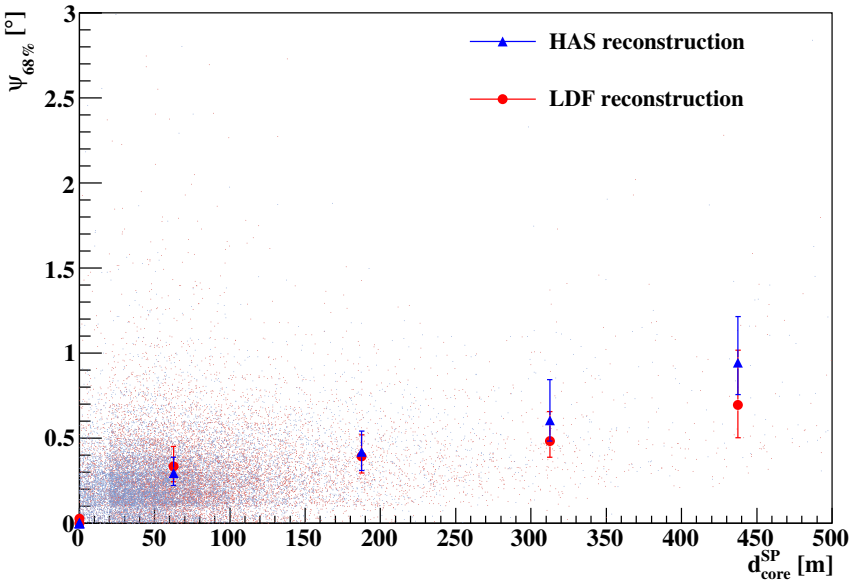

Figure 5.5: Besides effects of station selection the angular separation between the simulated and the reconstructed axes is linearly dependent on the distance of the reconstructed core to the simulated impact point for both reconstruction methods. The points give the 68 % quantile for the intervals with the median as lower error bar and the 82 % quantile as upper error bar.

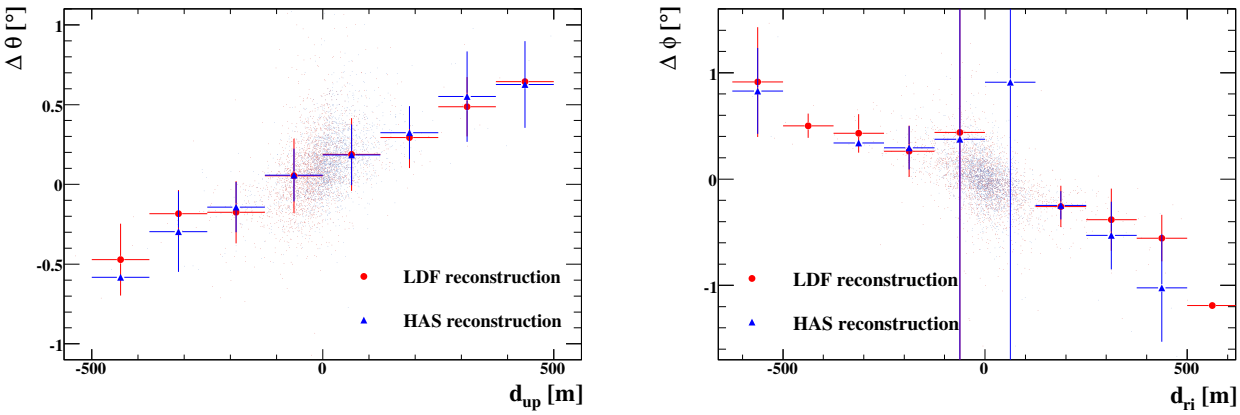

Figure 5.6: In shower plane coordinates the deviations of the reconstructed zenith angle and the reconstructed azimuth angle with respect to the simulated axis are related to the deviation of the reconstructed core position from the simulated impact point. The solid points represent the mean of the distribution in each bin. The error bars show one standard deviation.

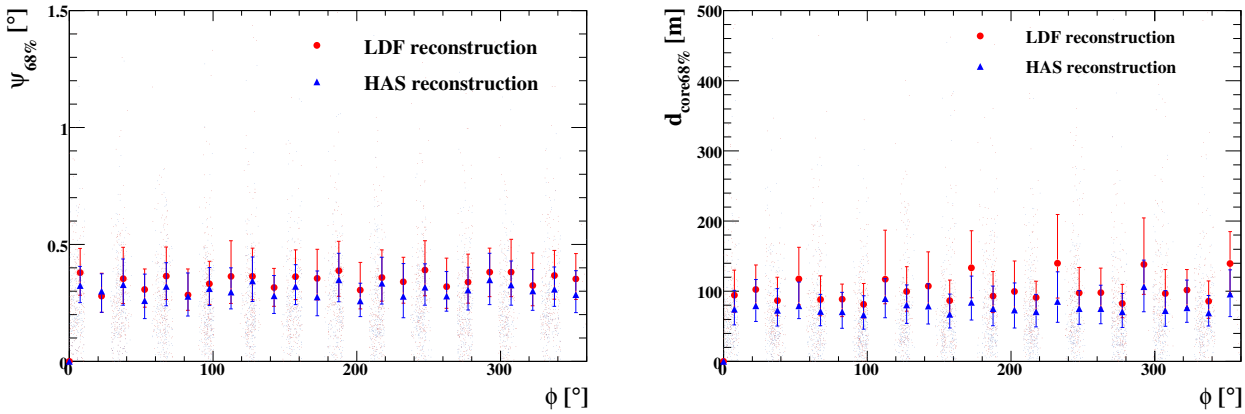

Figure 5.7: The angular resolution (left panel) and the core resolution (right panel) respectively do not depend on the azimuth angle.

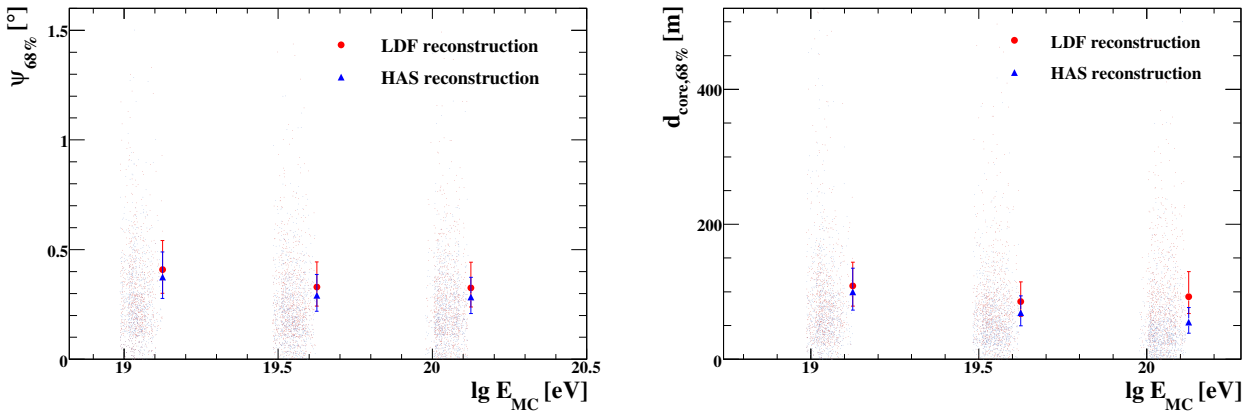

Figure 5.8: The angular resolution (left panel) and the core resolution (right panel) as a function of the input energy of simulated showers. With increasing energy the core resolution improves resulting in a better angular resolution.

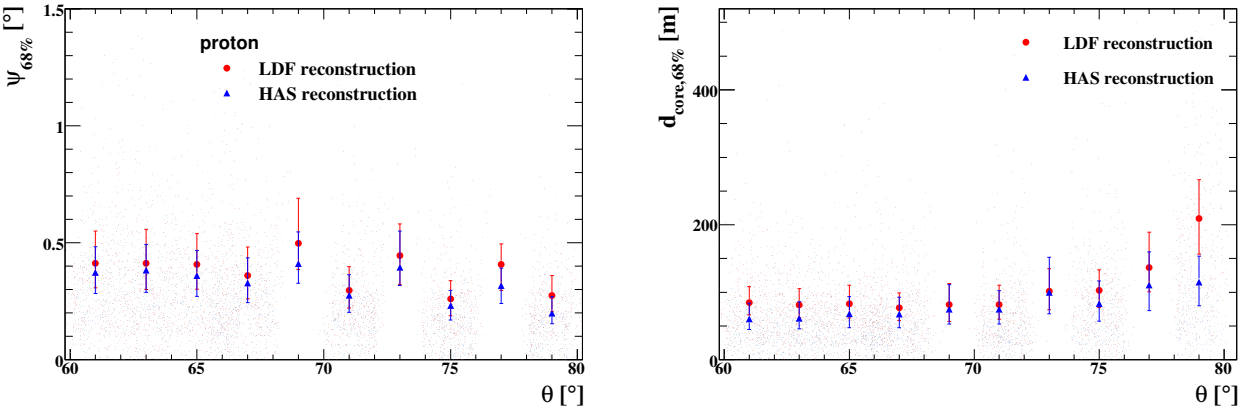

Figure 5.9: Left panel: The angular resolution derived from Monte Carlo events with proton primaries for both the LDF and the HAS reconstruction algorithms as a function of the zenith angle. Right panel: The major source of angular deviations under the assumption of correctly reconstructed $\vec{R}_c$ is the shift of the reconstructed core position with respect to the impact point. Zenith angle dependent asymmetries are accounted for in the HAS reconstruction but not in the LDF reconstruction.

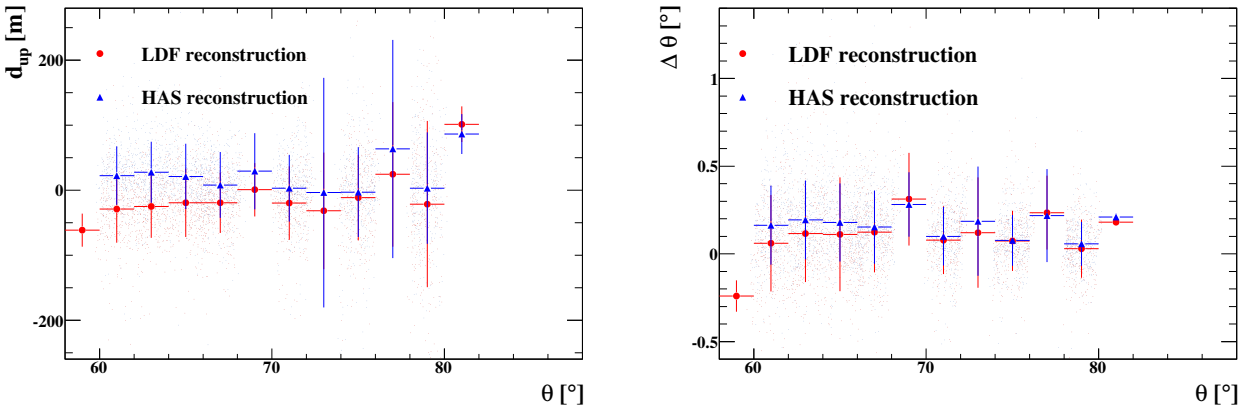

Figure 5.10: The components of the deviation of the reconstructed values of the shower direction (left panel) and the core position (right panel) as a function of the zenith angle. The points give the mean of the distributions. The error bars show one standard deviation. A systematic shift in the θ and upstream directions respectively is present especially applying the LDF reconstruction at high zenith angles.

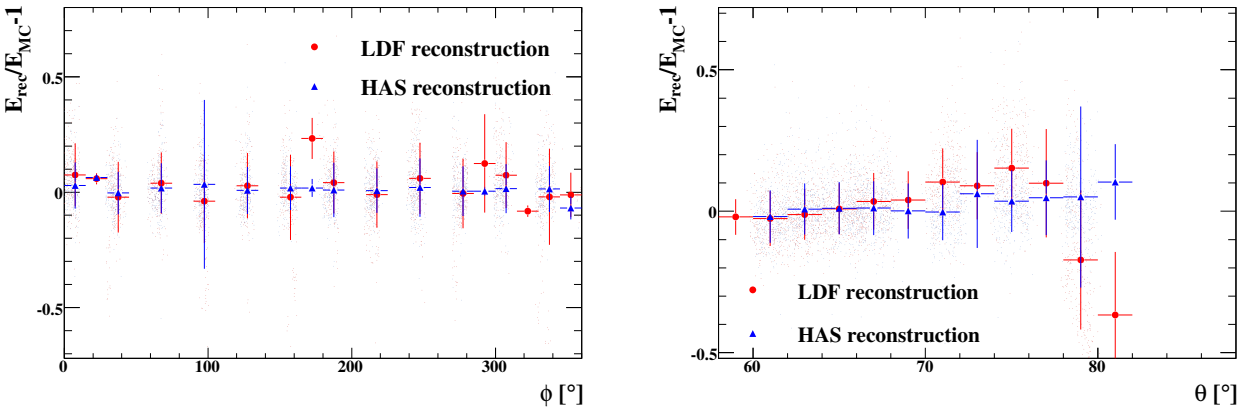

Figure 5.11: The reconstructied bias (points) and standard deviation (error bars) of the reconstructed energy with respect to the simulated values as a function of the azimuth angle (left panel) and the zenith angle (right panel) for the different reconstruction methods and two differen primaries.

direction in both reconstruction algorithms. The estimation of the energy of the cosmic ray primary is not only influenced by fluctuations due to the reconstruction algorithm but also by intrinsic shower-to-shower fluctuations of the particle densities in the shower development.

The energy estimators $S_{SD,ref}$ used for energy determination are not intrinsic parameters of the shower but give a handle on the energy. In order to have a reference value the energy estimate from the calibration process as described in chapter 4 is compared to the input energy used for generation of simulated showers in the Monte Carlo data set. For each primary mass the respective calibration curve is applied neglecting the systematic uncertainty introduced by the unknown primary mass of a single shower measured by the Surface Detector already determined through the offset in the energy calibration curves for the two extreme primary masses proton and iron respectively. Anyway the intrinsic fluctuations of the showers are decreasing with increasing mass. Therefore the simulations for proton and iron primaries are analysed seperately.

The asymmetries not accounted for in the LDF model increase with zenith angle implying a zenith angle dependent decrease of the accuracy. Geomagnetic distortions at high zenith angles give an additional asymmetry modulated with the angle between the shower axis and the geomagnetic field vector. The relative geomagnetic angle changes not only with the zenith angle but also with the azimuth angle. In figure 5.11 the mean and the spread of the relative deviation of the reconstructed energy from the simulated value are shown as a function of the zenith and azimuth angles respecitvely. No significant variation is visible in the azimuth angle implying that the geomagnetic effects become dominant at highest zenith angles above $\theta = 80°$ only since no compensating core shift as a function of azimuth angle is observed in figure 5.7. For the LDF reconstruction the energy determination is biased for highly inclined showers. Both the lack of a verified attenuation curve for high and highest zenith angles due to decreasing reconstruction efficiency and the rising shift of the core position into the upstream direction cause this bias. Therefore the energy estimate by the LDF reconstruction is not reliable for zenith angles above 70°.

With increasing primary energy the influence of both intrinsic and statistical fluctuations due to few surface detector stations decrease. Both the number of particles and the number of triggered detector stations increase with energy. In figure 5.12 the bias and the resolution assuming a Gaussian

behaviour is shown for both reconstruction methods as function of the primary energy. The decrease of the fluctuations is clearly visible for the HAS reconstruction. Anyway the large spread of the reconstructed values using the LDF reconstruction is dominated by the high zenith angle range above $\theta = 70^\circ$ as shown in figure 5.13 for zenith angle sub-ranges. The energy resolution is comparable in the overlap region of the applicability of the two reconstruction method.

The energy resolution and the energy bias are coupled with the geometry reconstruction mainly due to the fact that the core position and the energy estimator are determined in a combined fitting procedure (see figure 5.14). Deviations of the reconstructed geometry result in an increase of the fluctuations of the reconstructed energy as well as in a bias increasing with the deviations from the true geometry. Especially the effect of the core shift towards the early region giving an an overestimation of the energy is visible. For the HAS reconstruction a shift in the core position results in an underestimation of the energy.

Using simulated data the energy resolution $\sigma(E)$ can be parameterised as a function of the zenith angle for both reconstruction methods using only moderately inclined proton showers

$$\begin{aligned} \sigma_{LDF}(E) &= -0.162 + 0.005 \cdot \theta[^\circ] \\ \sigma_{HAS}(E) &= 0.06 + 0.001 \cdot \theta[^\circ]. \end{aligned} \tag{5.2.1}$$

For $60^\circ < \theta < 80^\circ$ $\sigma_{HAS}(E)$ is approximately constant ≈ 0.184. This results in the angle of the same energy resolution being $\theta = 68^\circ$ as demonstrated in figure 5.15. The extremes of the overall resolution are defined by the cosmic ray primaries inducing air showers with the largest and the smallest fluctuations. The valid zenith angle range of the LDF reconstruction covered with the Monte Carlo data set spans over showers of zenith angles $\theta \in [60^\circ, 80^\circ]$. In figure 5.16 the resolutions for proton and iron primaries and the LDF and HAS reconstructions respectively are shown above the threshold of $5 \cdot 10^{18}\,\mathrm{eV}$. A fit of a normal distribution results in

$$\begin{aligned} \mu_{LDF,proton} &= 0.054 \pm 0.002 & \sigma_{LDF,proton} &= 0.190 \pm 0.002 \\ \mu_{LDF,iron} &= 0.026 \pm 0.003 & \sigma_{LDF,iron} &= 0.122 \pm 0.003 \\ \mu_{HAS,proton} &= 0.062 \pm 0.002 & \sigma_{HAS,proton} &= 0.174 \pm 0.002 \\ \mu_{HAS,iron} &= 0.005 \pm 0.003 & \sigma_{HAS,iron} &= 0.095 \pm 0.003 \end{aligned} \tag{5.2.2}$$

for the angular range of $\theta \in [60^\circ, 68^\circ]$. For the full range of the HAS reconstruction the deviations are shown in figure 5.17. The fits result in

$$\begin{aligned} \mu_{HAS,proton} &= 0.036 \pm 0.002 & \sigma_{HAS,proton} &= 0.160 \pm 0.001 \\ \mu_{HAS,iron} &= 0.003 \pm 0.002 & \sigma_{HAS,iron} &= 0.083 \pm 0.002 \end{aligned} \tag{5.2.3}$$

Assuming a mixed composition the mean energy resolution using the LDF reconstruction on moderately inclined showers is $\sigma_{LDF} = 0.16$. For the HAS reconstruction a resolution of $\sigma_{HAS} = 0.12$ for a zenith angle range of $\theta \in [60^\circ, 80^\circ]$ and mixed composition is derived.

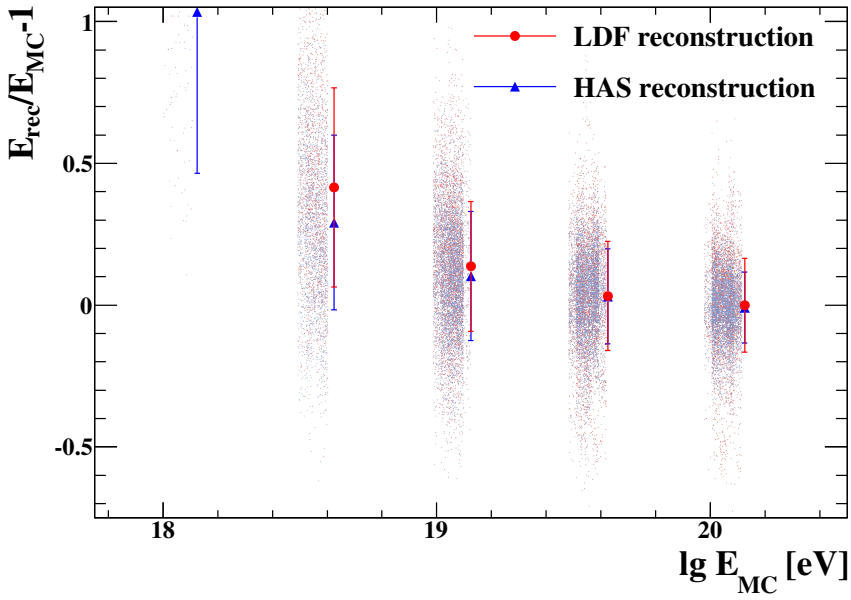

Figure 5.12: The energy bias (points) and one standard deviation of the energy deviation distribution (error bars) as a function of energy for moderately and highly inclined air shower simulations.

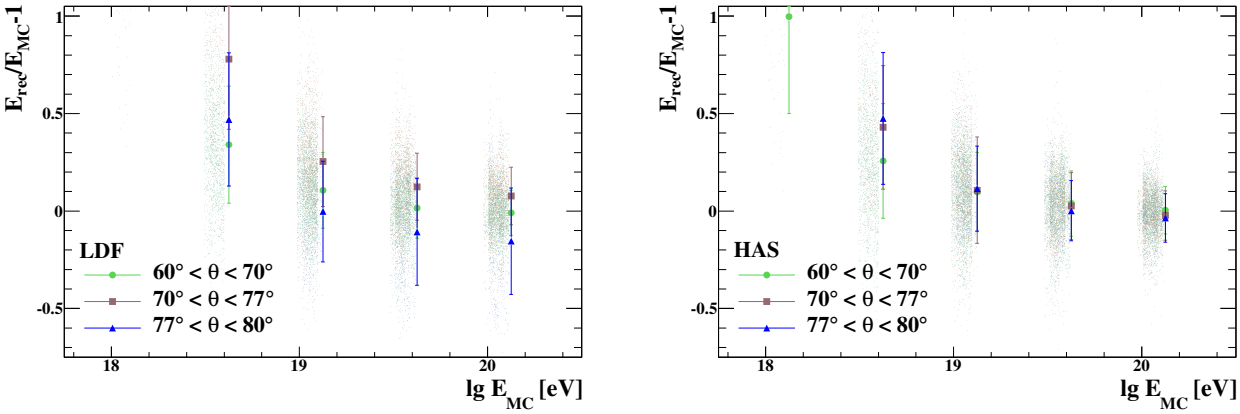

Figure 5.13: The energy resolution assuming a Gaussian distribution of the deviations (error bars) and the energy bias (points) as a function of energy for various zenith angle ranges. For larger zenith angles than $\theta = 70°$ the HAS reconstruction (right panel) is clearly superiour to the LDF reconstruction (left panel) in all energies. The positive LDF bias in the energy due to asymmetry reverts at $\theta = 70°$ to a negative.

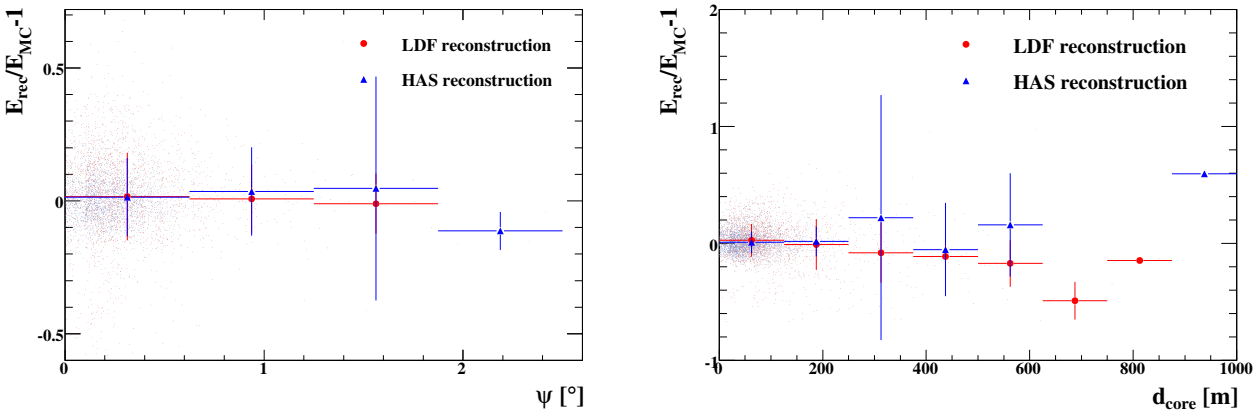

Figure 5.14: The deviation of the reconstructed energy from the simulated primary energy as a function of the deviation of the axis (left panel) and the core position (right panel) from the input values to the simulation.

The agreement of the reconstructed energy in the LDF and HAS reconstruction methods respectively is a prerequisite for the cross calibration shown in section 4.3. The deviation of the energy estimate from the true energy consists of three components: The shower-to-shower fluctuations, detector effects and the bias introduced by reconstruction methods. As the reconstructions can be compared event by event shower to shower fluctuations and detector effects do not affect the difference in the energy estimate of HAS reconstruction and LDF reconstruction. The deviation from the true energy

$$\Delta E = \frac{E_{SD} - E_{MC}}{E_{MC}} \tag{5.2.4}$$

depends on the fluctuations, detector and sampling effects and the uncertainty from the reconstruction algorithm. For moderately inclined showers the validity and agreement of both reconstructed energies has a signature of a linear correlation of ΔE_{LDF} and ΔE_{HAS}. In figure 5.18 the correlation of the reconstructed energy and the correlation of the deviation from the true energy is shown for various zenith angle ranges.

For the zenith angle range of the overlap region the reconstructed energies are proportional to each other showing neither a constant bias nor an energy dependent shift. For higher zenith angles biases and a larger spread arise as the LDF no longer describes the shape of the shower footprint accurately at this inclinations. The correlation of the reconstructed energies is well reflecting the relatively low impact of the reconstruction algorithm to the deviation from the true energy. A linear fit has been performed using only the overlap region of the validity resulting in

$$\Delta E_{HAS} = 0.0119 \pm 0.0009 + (0.909 \pm 0.005) \cdot \Delta E_{LDF}. \tag{5.2.5}$$

The energies derived from both reconstruction methods show almost equal deviations from the true energy with the LDF reconstruction pronouncing fluctuations $10\,\%$ stronger and a mean bias of $1\,\%$. In figure 5.19 the difference of the deviation from the true energy

$$\Delta E_{LDF} - \Delta E_{HAS} = \frac{E_{LDF} - E_{HAS}}{E_{MC}} \tag{5.2.6}$$

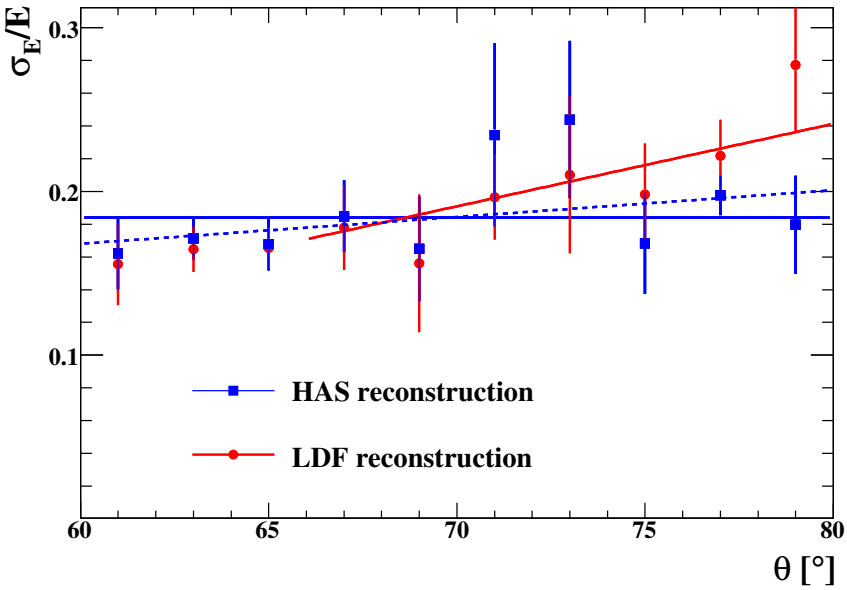

Figure 5.15: The energy resolution of the two reconstruction algorithms for protons as a function of the zenith angle. The lines are fits of a constant and a linear function in θ to the energy resolution $\sigma(E)$. The resolution given by the HAS reconstruction is better than the LDF reconstruction above $\theta = 68°$.

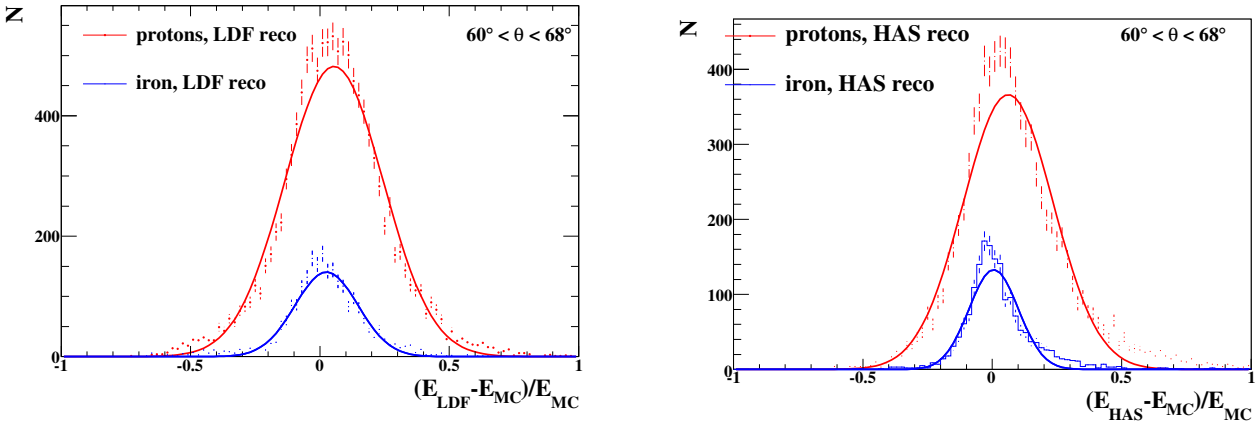

Figure 5.16: The energy resolution of the two reconstruction algorithms for proton and iron showers for the overlapt angular range $\theta \in [60°, 68°]$.

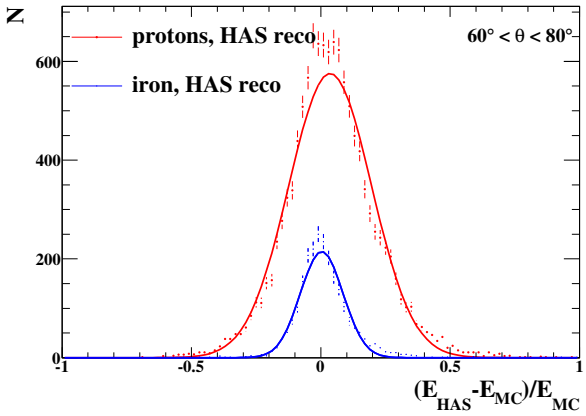

Figure 5.17: The energy resolution of the HAS reconstruction for proton and iron showers respectively. The full angular range of $\theta \in [60°, 80°]$ is used.

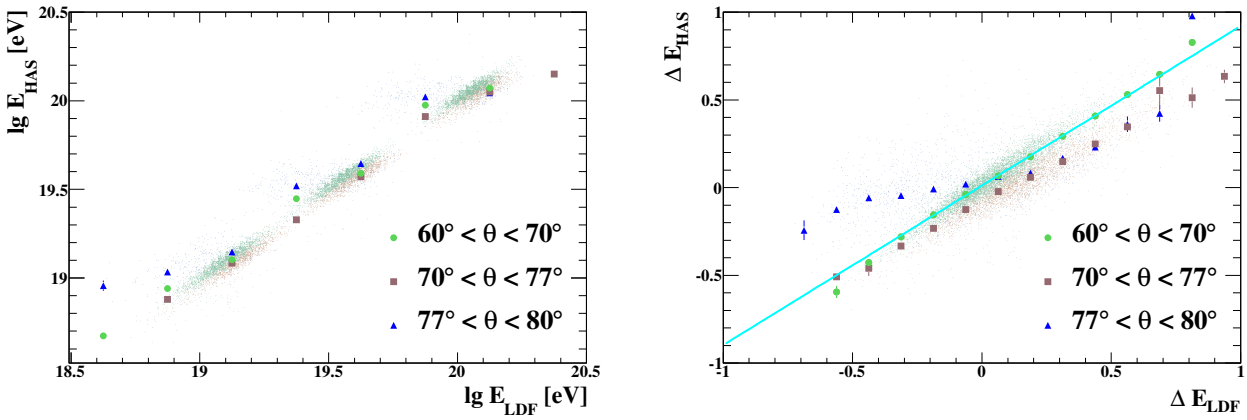

Figure 5.18: Left panel: The correlation of the reconstructed energy between the LDF and HAS reconstructions from simulated data. The error bars show the error of the mean of the distribution. Right panel: The correlation of ΔE of the two reconstruction algorithms after calibration. The error bars again illustrate the error of the mean of the distribution.

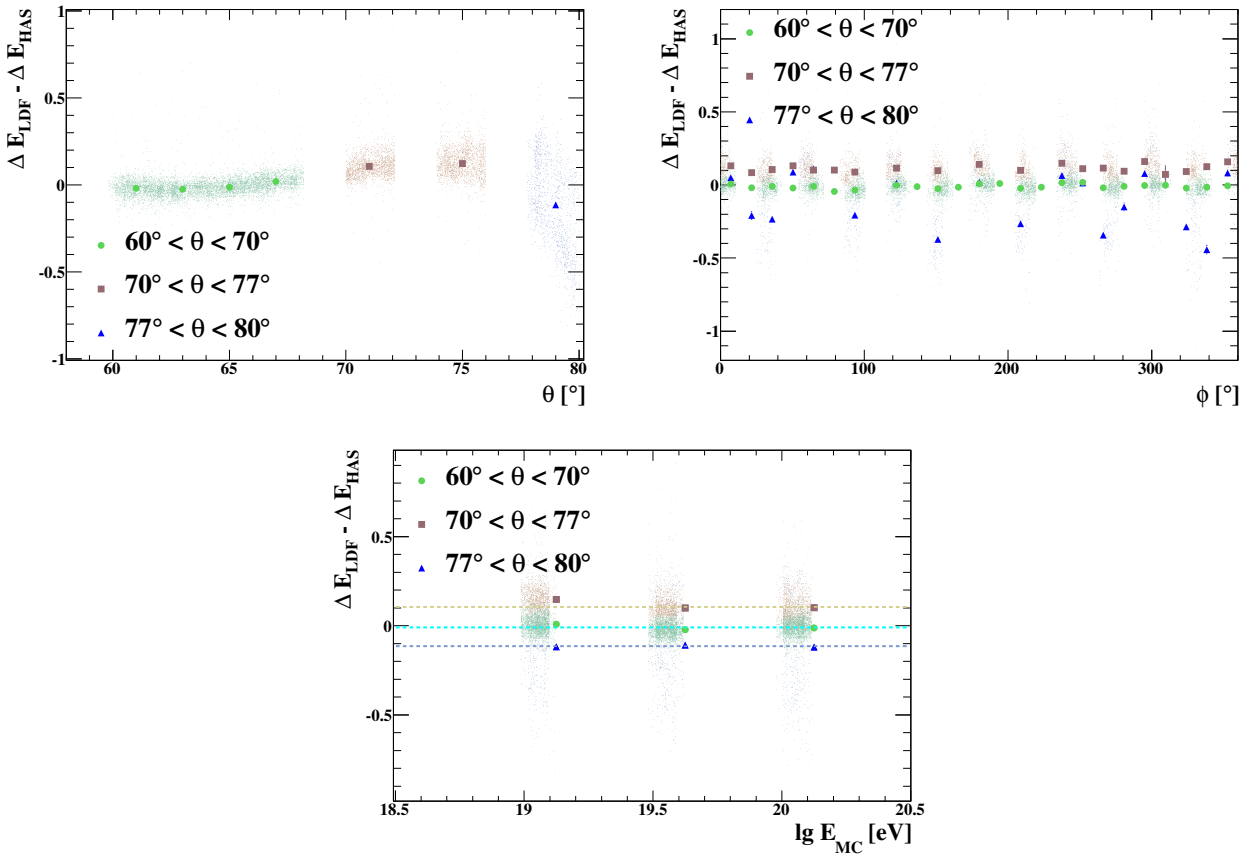

Figure 5.19: The difference of the deviations of the reconstructed energies from the true energy normalised by the true energy. The parameter is shown event-by-event as a function of the zenith angle, the azimuth angle and the energy. The dots reflect the mean of the distribution and the error bars reflect the error of the mean. The horizontal lines in the lower panel are printed to guide the eye.

is shown as a function of the zenith angle, the azimuth angle and the primary energy. The dependency of the bias and the increasing spread i.e. the decreasing correlation of the reconstructed energies with increasing zenith angle is clearly visible. For zenith angles above 70° a bias towards $10 - 20\,\%$ larger LDF energy estimate reflects the shift of the core postition to the upstream region as shown above. The LDF reconstruction fails above 77° resulting in the vanishing correlation of the reconstructed energies. In highest zenith angles a deviation caused by assymmetry not accounted for in the LDF is seen as a function of azimuth angle. The effect is constant in energy as illustrated by horizontal lines fitted to the whole energy range for the the three zenith angle ranges seperately.

Chapter 6

Energy Spectrum

The determination of the cosmic ray flux with data from moderately and highly inclined air showers measured by the Pierre Auger Observatory includes a consistent energy determination for events up to zenith angles $\theta = 80^\circ$ shown in chapter 4 and the calculation of the acceptance of the array for very inclined air showers. The acceptance calculation is closely connected to the definition of the quality trigger that defines the fiducial area of the array. For very inclined showers a different quality trigger is applied than for extended air shower of zenith angles $\theta in [0^\circ, 70^\circ]$. The acceptance calculation is adjusted based on the behaviour of the different quality trigger conditions on real data. The threshold of full detection efficiency of the surface detector is estimated for inclined air showers using simulation. With the acceptance as a normalisation the flux of ultra high energy comsic rays as a function of energy is calculated using the optimal reconstruction method with respect to the zenith angle intervals.

6.1 Acceptance Calculation

The acceptance calculation for air showers of zenith angles $\theta in [0^\circ, 70^\circ]$ has been established in [8] based on the geometric acceptance of a surface detector array above the threshold of full trigger efficiency. Basically the quality trigger `T5` guarantees a station to be completely within the array i.e. being surrounded by 6 other stations of the regular grid as demonstrated in figure 6.1. For each station the `T5` criterion can be calculated and each station fulfilling the criterion is inside the array and therefore contributes to the acceptance of the surface detector. The hexagon-shaped blue in figure 6.1 area of $A_{cell} = (1.5\,\mathrm{km})^2 \cdot \sqrt{3}/2 = 1.95\,\mathrm{km}^2$ around a surface detector station is the area this individual station contributes to the surface detector acceptance. It is defined as the area being closer to the reference station than to any other of the six surrounding stations in regular grid i.e. fulfilling the `T5`. The effective area for a given incoming direction scales with the Cosine of the zenith angle so that a single elementary hexagon contributes

$$a_{cell} = A_{cell} \cdot \int_0^{2\pi} \int_{\theta_1}^{\theta_2} \cos\theta \sin\theta d\theta d\phi = A_{cell} \cdot (\sin^2\theta_2 - \sin^2\theta_1) \tag{6.1.1}$$

to the total acceptance in the zenith angle range from θ_1 to θ_2. With the acceptance of a single cell known for any zenith angle range the exposure calculation above the threshold of full trigger efficiency

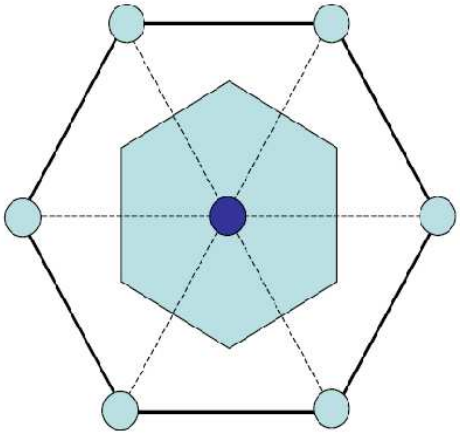

Figure 6.1: A station fulfilling the T5 *quality trigger condition i.e. being completely inside the array. The station used for calculating the* T5 *condition is selected to be closest to the core position of the reconstructed shower.*

can be performed by summation of the number of hexagons at a given moment and integration over time

$$E = a_{cell} \int_{T_1}^{T_2} N_{cell}(t)dt \approx a_{cell} \sum_i N_{cell,i} \Delta t_i, \tag{6.1.2}$$

with the number of active stations fulfilling the T5 criterion N_{cell} and the duration stable periods Δt_i with constant $N_{cell,i}$ within the measuring time interval from T_1 until T_2. The configuration of the array changes because of various effects like the growing array during the build-up of the surface detector until 2008, detector dead-times and dead-times of the central data acquisition. The monitoring of the array stability is written to the T2-files giving the status of each surface detector station over time with the precision of 1 s based on the single station trigger rates [131]. Besides the information from the single station trigger rates also the status of the central data acquisition and the availability of T2 information have to be accounted for. If the central data acquisition does not record the data i.e. due to trigger problems considering real events there are zero stations available although the single station trigger rates indicate otherwise and leads to an overestimation of the exposure. On the other hand the the single station trigger rates not being available during regular data taking leads to an underestimation of the exposure. Both effects are of the order of $1\,\%$. Unstable periods of the detector i.e. the data acquisition are rejected completely to get a clean data set. The rejection of unstable periods contributes $0.5\,\%$ to the uncertainty of the exposure [52] which is the largest contribution. Together with trigger effects and imperfections of the array grid [8] the uncertainty sums up to $1\,\%$. With the assumption of constant T5 trigger rates per hexagon the corresponding dead times of the array are estimated in [52, 59]. A seasonal modulation of the trigger rate with an amplitude of $3.8\,\%$ has been observed in [68, 143]. In early 2009 problems in data acquisition caused an interruption in the reliable data collection of cosmic ray showers that is still in the process of being recovered [135]. Hence the data of 2009 have not been used in this work.

The hexagon counting including all effects and rejecting all unstable periods of the detector has been automatised [108]. For the period including the complete years from 2004 until 2008 $(87.5 \pm 2.6) \cdot 10^9$

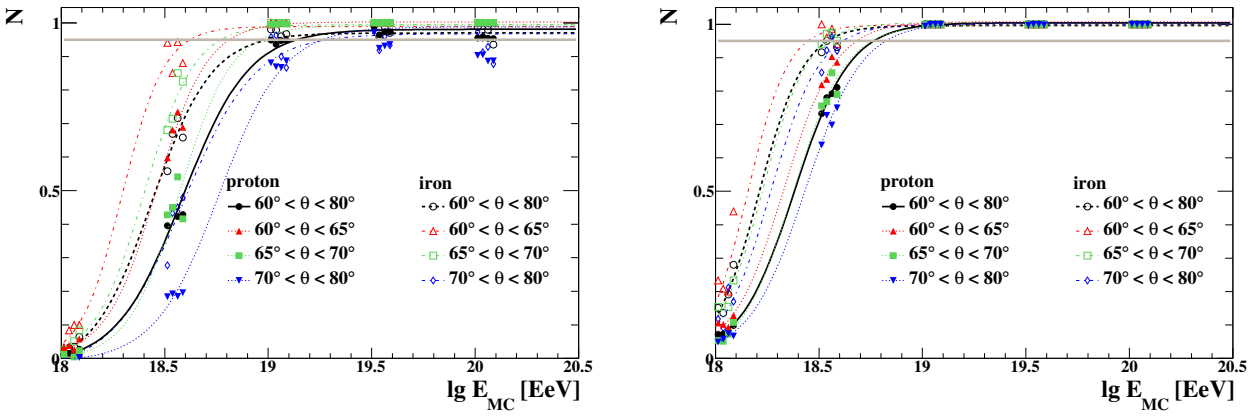

Figure 6.2: The threshold of full reconstruction efficiency for proton and iron primaries and different zenith angle intervals respectively. In the left panel the LDF reconstruction efficiency is shown. It does not reach $100\,\%$ *for the highest zenith angles even at high energies. In the right panel the efficiencies for the HAS reconstruction are shown.*

hexagon-seconds contribute to the exposure. This results in values for the exposure of

$$\begin{aligned} E(0^\circ, 70^\circ) &= 14980 \pm 450\,\mathrm{km}^2\ \mathrm{sr\ yr} \\ E(60^\circ, 80^\circ) &= 3730 \pm 110\,\mathrm{km}^2\ \mathrm{sr\ yr} \\ E(60^\circ, 68^\circ) &= 1860 \pm 56\,\mathrm{km}^2\ \mathrm{sr\ yr} \\ E(68^\circ, 80^\circ) &= 1870 \pm 56\,\mathrm{km}^2\ \mathrm{sr\ yr} \end{aligned} \tag{6.1.3}$$

for the different zenith angle intervals the spectrum is inferred with in this work.

Trigger efficiency and reconstruction efficiency

Full trigger efficiency is the prerequesite for the simple geometric acceptance calculation described above. The trigger efficiency in the region of moderately and highly inclined showers is influenced by two major effects: On the one hand due to geometrical effects the area of the shower footprint increases with the zenith angle. Thus more stations can be triggered. On the other hand with increasing zenith angle attenuation and geometrical effects play an increasing role. The particle density and therefore the trigger probability in a tank gets lower. The increasing number of stations hit by the shower footprint rise the possibility of a central trigger while the decreasing particle density decreases the probability of a single station trigger. Also at increasing zenith angle asymmetries not included into the LDF model and other effects reduce the reconstruction efficiency and therefore the efficiency of the a posteriori `T5Has` trigger condition. Thus full reconstruction efficiency is relevant for the acceptance calculation instead of only full trigger efficiency.

Simulated showers allow the determination of the threshold of full reconstruction efficiency in an infinite surface detector array. For proton and iron primaries the reconstruction efficiency of the

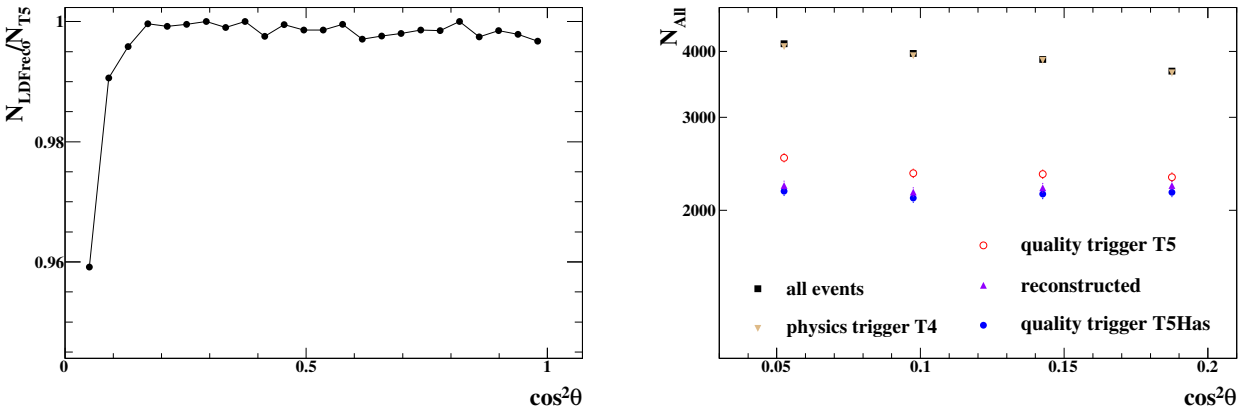

Figure 6.3: The reconstruction efficiency for data fulfilling the `T5` *quality trigger as a function of zenith angle. Left panel: Reconstruction efficiency of* `T5` *events using the LDF reconstruction. Right panel: The event numbers with* `T5` *trigger, with reconstruction and with* `T5Has` *are shown in zenith angle invervals of equal acceptance.*

two reconstruction algorithms are shown in figure 6.2. For muon-rich iron showers the threshold is lower than for proton showers. Also the threshold increases with zenith angle for both reconstruction methods. For highest zenith angles the LDF reconstruction cannot reconstruct every shower even at highest energies due to the larger asymmetries. Considering the LDF reconstruction only for zenith angles up to 70°, both reconstruction algorithms show a reconstruction efficiency of more than 95 % for energies above $E_{thresh} = 6.3\,\mathrm{EeV} \approx 10^{18.8}\,\mathrm{eV}$.

Another possibility to address the question of trigger efficiency would be to infer $P(SD|FD)$ which is exactly the trigger probability given full trigger efficiency of the FD. For showers up to zenith angles of 60° this method has been used [143]. In the regime of moderately inclined showers the statistics of fluorescence detector events with well reconstructed energy is poor due to various effects described in chapter 4. Especially for very inclined showers nearly no reliable event from the fluorescence detector is available. Other analyses with Monte Carlo data sets and fluorescence data have been performed in [72, 157] leading to similar values of the threshold.

The zenith angle dependent reconstruction efficiency is adressed using surface detector `T5` data. The determination on real data allows to address the effect of a finite array with its borders defined using the `T5` quality trigger criteria. The reconstruction efficiency depends on the reconstruction method. The assumption of a cylindrical symmetry of the particle densities with repect to the shower axis is the basis of the LDF reconstruction. Asymmetries due to attenuation in the atmosphere, geometrical effects and geomagnetic distortion influence the accuracy of the reconstruction algorithm resulting in a larger fluctuation as well as a biased mean. For high zenith angles the symmetrical model and the asymmetric shower footprint differ significantly. This can cause the reconstruction algorithm i.e. the fitting procedure of LDF to fail. In figure 6.3 the reconstruction efficiency of the LDF and HAS reconstruction algorithms respectively is shown for events fulfilling the quality trigger `T5` as a function of the zenith angle for energies above the threshold of $E = 5\,\mathrm{EeV}$.

As demonstrated in figure 6.3 left panel for highly inclined air showers the reconstruction efficiency of the LDF reconstruction does not significantly drop below 100 % for energies above $E = 5\,\mathrm{EeV}$

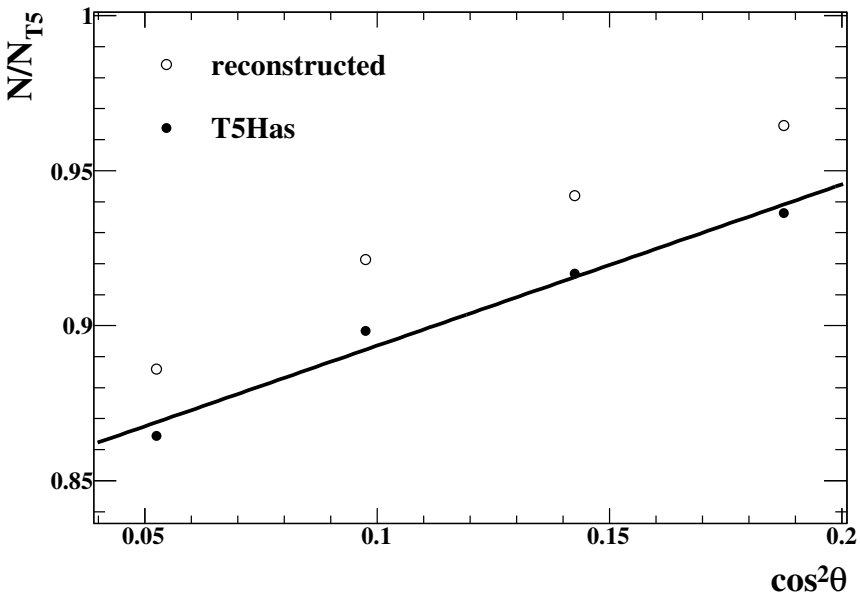

Figure 6.4: The `T5Has` *trigger condition requires six active stations around the station closest to the core. For standard acceptance calculation counting hexagons the* `T5` *requiring six active stations around the station with the highest signal in the event is used. The ratio and therefore the correction for the acceptance as a function of zenith angle is shown.*

at zenith angles larger than $\theta = 70°$. For the HAS reconstruction a stricter `T5Has` quality trigger is applied a posteriori. All events that fulfill `T5Has` are reconstructable by construction. The event statistics for the different triggers and the reconstruction efficiencies for zenith angles larger than $\theta = 60°$ or $cos^2\theta < 0.25$ are shown in figure 6.3 right panel.

The quality triggers `T5` and `T5Has` are designed to guarantee the shower core to be inside the array as described in section 3.1. The criteria make sure no significant information is missing as this might lead to wrong results of reconstruction. For low and moderate zenith angles the core position is close to the station with the largest signal in the event. At high zenith angles the signals get lower and as they are muon dominated the fluctuations increase for showers of the same energy. Also the lateral profile gets flatter than for less inclined showers. Hence the station closest to the core and the station with the highest signal are not necessarily identical.

The quality triggers differ only by the refence station. As the station closest to the core is only known a posteriori `T5Has` requires reconstruction while `T5` does not. Using real data the ratio of events fulfilling `T5Has` with respect to the rate of `T5` events can be inferred. The geometrical acceptance using the `T5` condition is corrected with this ratio to infer the final acceptance using HAS reconstruction and `T5Has`. The `T5Has`-to-`T5` ratio is zenith angle dependent as the effects that lead to the core being outside the cell of the station with the highest signal increase with increasing zenith angle. The effect is shown in figure 6.4. To infer the ratio for a zenith angle range the zenith angle dependent ratio is integrated

$$R_{T5Has} = \frac{1}{cos^2\theta_2 - cos^2\theta_1} \int_{\theta_1}^{\theta_2} r_{T5Has}(\theta) d\cos^2\theta \tag{6.1.4}$$

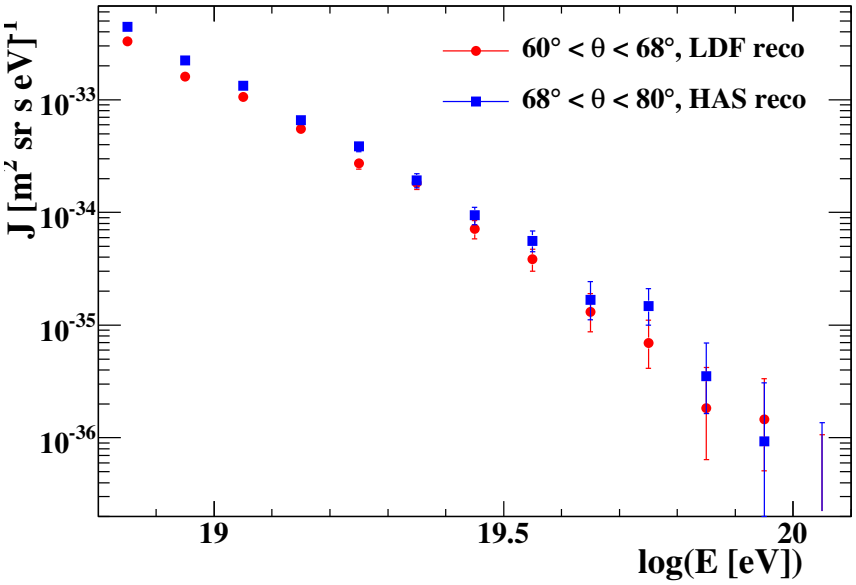

Figure 6.5: The cosmic ray flux measured with moderately inclined showers and very inclined showers. For the different zenith angle domains different optimum reconstruction methods are used. The error bars show only the statistical uncertainty.

over $\mathrm{d}\cos^2\theta$ proportional to the acceptance. The function fitted to the values in figure 6.4 is a linear function

$$r_{T5Has} = 0.8415 \pm 0.0001 + \cos^2\theta \cdot (0.5204 \pm 0.0003) \tag{6.1.5}$$

that reaches one only at $\theta = 60°$. For different zenith angle ranges the correction of the acceptance due to usage of `T5Has` can thus be calculated. For the zenith angle intervals used in this chapter the values are

$$\begin{aligned} R_{T5Has}(60°, 80°) &= 0.91 \pm 0.0001 \\ R_{T5Has}(60°, 68°) &= 0.94 \pm 0.0001 \\ R_{T5Has}(68°, 80°) &= 0.89 \pm 0.0001. \end{aligned} \tag{6.1.6}$$

In case of using the `T5Has` instead of the a priori `T5` the standard acceptance has to be corrected with R_{T5Has} to get a correct result. The parameterised r_{T5Has} reaches one at zenith angles slightly below $\theta = 60°$ accounting for the strong correlation of the core and the station with the largest signal.

6.2 The cosmic ray spectrum with inclined shower data

With the energy determination and the acceptance at hand the cosmic ray flux as a function of energy can be determined. With the results from chapter 5 the optimal result is achieved by using the LDF

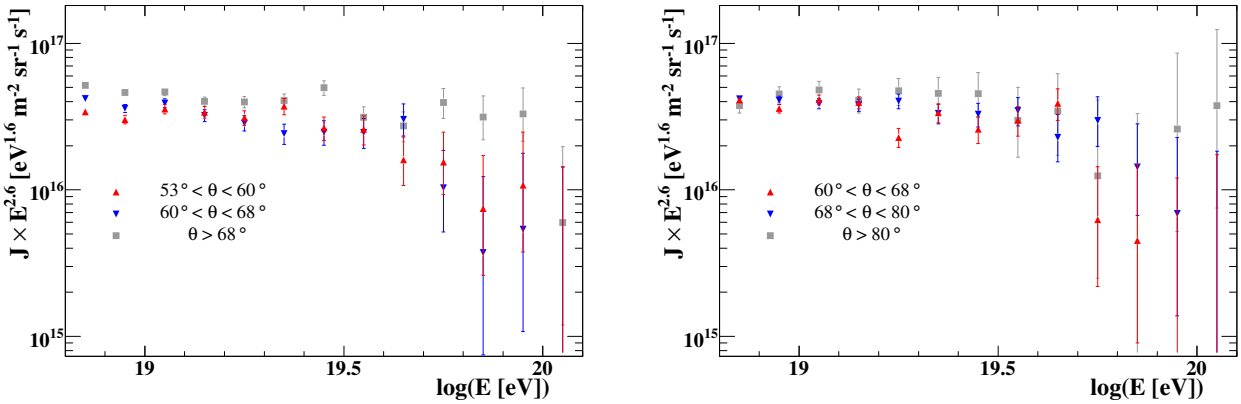

Figure 6.6: The cosmic ray flux estimated with different methods and for different zenith angle intervals. The spectra in the left panel were created using the LDF reconstruction and the corresponding calibration, the ones in the right panel give the results of the HAS reconstruction.

reconstruction for showers up to zenith angles of $\theta = 68°$ while for more inclined showers the results using the HAS reconstruction are superior. In figure 6.5 the spectra using the LDF reconstruction for $60° < \theta < 68°$ and the HAS reconstruction for $68° < \theta < 80°$ are shown. The offset is within the systematic uncertainty due to the acceptance calculation as shown below. The correction due to the use of the `T5Has` in case of very inclined showers gives a slight overcompensation of the acceptance reduction due to the a posteriori trigger condition.

Two major sources contribute to the uncertainty of the derived spectrum: The exposure calculation and the energy determination. The latter will be discussed below considering various contributions. The exposure calculation for energies of more than $E = 6.3\,\mathrm{EeV}$ depends only on hexagon counting. The uncertainties of the exposure are caused by various effects included into the uncertainties in equation 6.1.3.

Reconstruction algorithms and calibration methods have been shown to be optimised for different zenith angle ranges in chapter 5 but in the zenith angle range of $60^\circ < \theta < 80^\circ$ basically both reconstruction methods have close to full reconstruction efficiency, but only between $60^\circ < \theta < 80^\circ$ both methods are in unbiased. Also different calibration methods are valid and the differences give an estimate of the systematic uncertainty of the calibration algorithm. In figure 6.6 the flux spectra derived with the different methods are shown for the subsamples $60^\circ < \theta < 68^\circ$ and $68^\circ < \theta < 80^\circ$. For the LDF reconstruction also the zenith angle interval from $53^\circ < \theta < 60^\circ$ is shown. The three intervals are chosen to have equal geometrical acceptance i.e. above the threshold of full trigger efficiency the normalisation factors due to the exposure are equal. The difference of the reconstructed spectra with different methods give the systematic due to reconstruction.

The different calibration algorithms result in slightly different parameters for the angular correction and energy calibration. These effects have been studied in chapter 4 and give another important contribution to the uncertainty of the reconstructed energy. Also the propagation of the uncertainties in the energy estimator through the energy determination procedure contribute to the uncertainty. The largest contribution is given by the uncertainty of the fluorescence energy determination that provides the energy estimate used for calibration directly in case of hybrid calibration and through the calibration constants of the reference surface detector reconstruction in case of cross calibration. The resulting error bands from all these uncertainties are summarised in figure 6.7 giving the uncertainties of the energy determination propagated to the flux values. The uncertainty of the energy scale due to the fluorescence detector energy is by far the largest contribution. A detailed description of the contribtions to the uncertaintiesis given in section 4.4 and tables 4.4, 4.5 . Also the systematic uncertainties in the zenith angle dependency of the energy estimator give a large contribution especially for the LDF reconstruction with the reference angle at $\theta = 38^\circ$ and therefore large uncertainties due to the angular correction at moderate zenith angles.

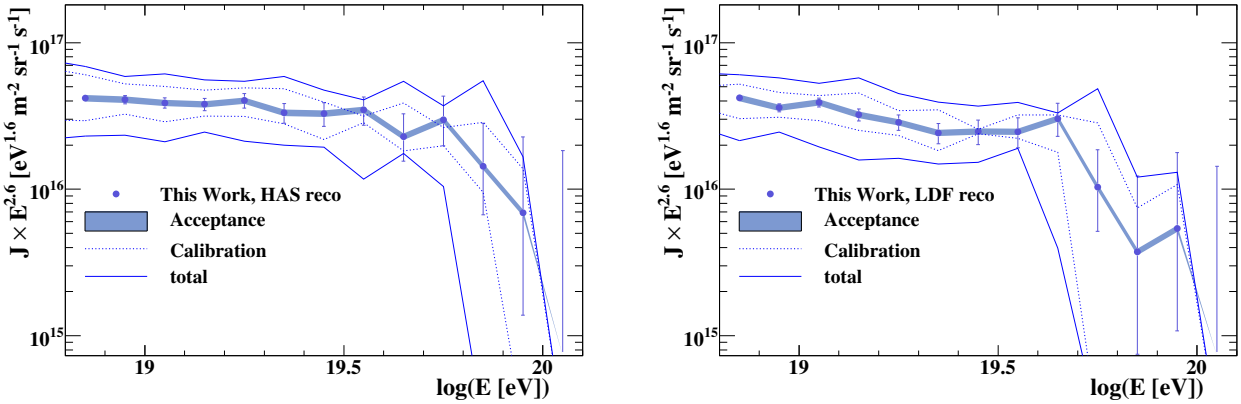

Figure 6.7: The cosmic ray flux at ultra high energies with systematic and statistical uncertainties using air showers in the zenith angle intervals $60° < \theta < 68°$ *(left panel) and* $68° < \theta < 80°$ *(right panel). The error bars of the points show the statistical uncertainty of the flux, the error bands show the contributions of the systematic uncertainties.*

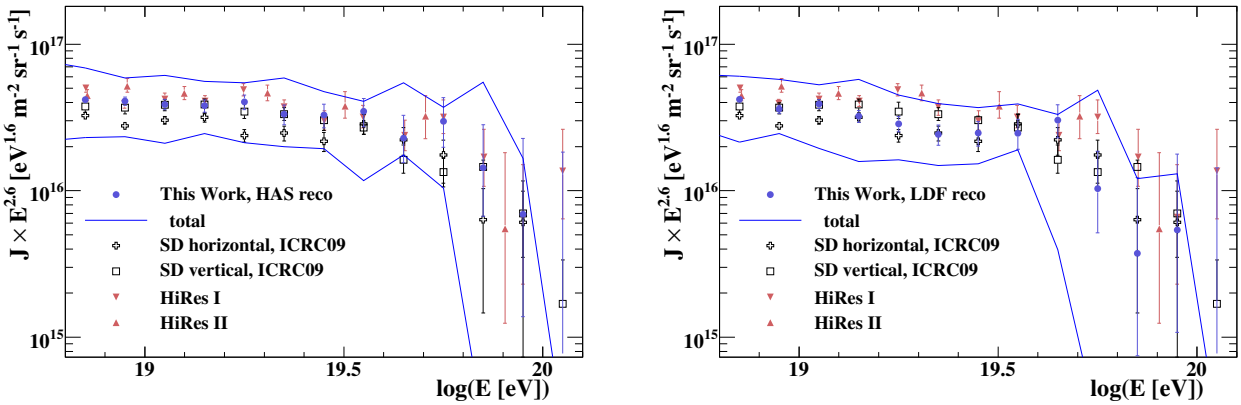

Figure 6.8: The cosmic ray flux derived with extensive air showers at moderate and high zenith angles using the least biased reconstruction chain respectively. The error bars give the statistical uncertainty, the dotted lines are the systematic uncertainty derived in this work. The previous results [4, 173, 197] are included with only statistical uncertainties drawn as error bars.

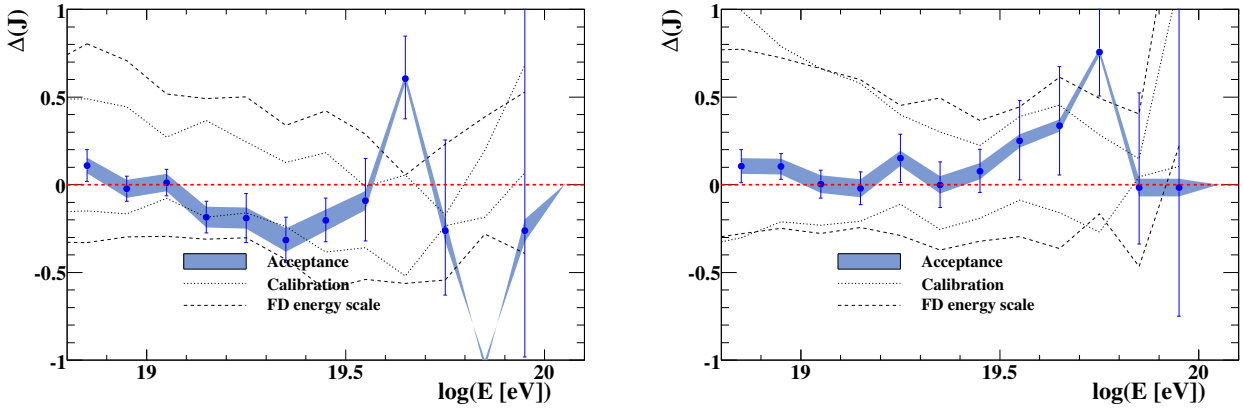

Figure 6.9: The difference in the flux scaled with the energy as defined in equation 6.2.1 with respect to [173]. The systematic uncertainties derived in this work are shown as error bands. The statistical uncertainties of both spectra are propagated and shown as error bars. In the left panel the situation for moderate zenith angles $60° < \theta < 68°$ *is shown, in the right panel the interval* $68° < \theta < 80°$ *is displayed.*

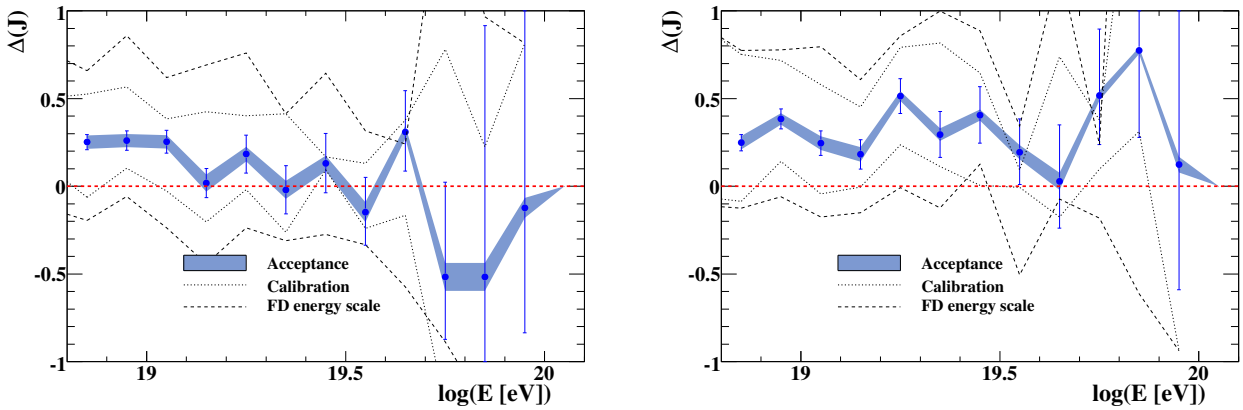

Figure 6.10: The difference in flux as defined in equation 6.2.1 with respect to the result in [197]. Systematic uncertainties are shown as error bands. The error bars are the propagated statistic uncertainties of both spectra. In the left panel the situation for moderate zenith angles $60° < \theta < 68°$ *is shown, in the right panel the interval* $68° < \theta < 80°$ *is displayed.*

Previous results published by the Pierre Auger Collaboration and other experiments like HiRes [4] have shown the primary cosmic ray spectrum for different zenith angle intervals. The results from [4, 173, 197] are shown compared to the flux derived with the results of this work in figure 6.8. The shape of the spectra is in good agreement with previous results, especially the flux suppression at $50\,\mathrm{EeV}$ is confirmed using the range of moderately and highly inclined air showers.

In figures 6.9,6.10 the relative difference of the flux scaled with the energy

$$\Delta(J) = \frac{J_{ref} \cdot E - J_{thiswork} \cdot E}{J_{ref} \cdot E + J_{thiswork} \cdot E} \tag{6.2.1}$$

with respect to the results in [173, 197] is shown. The differences to the previously measured spectra are shown to be within the statistic uncertainties so the spectra are compatible. Especially at energies of the kink in the spectrum due to flux suppression the differences of the spectra show a structure that is caused by an energy offset of 0.1 in logarithmic energy which corresponds to $\approx 19\,\%$ energy shift between the flux spectrum derived in this work and the vertical spectrum.

This work derives the flux of ultra-high energy cosmic rays as shown in figure 6.11 scaled with the energy E to the power of 2.6. The systematic uncertainties give a shift in the same direction for the whole energy range and are given in form of the arrows in the upper right corner of the plot. The flux suppression is seen consistently in both angular ranges.

The good agreement of both reconstruction methods in the overlap region $60^\circ < \theta < 68^\circ$ is shown in figure 6.12. It indicates a robust reconstruction of very inclined showers with both methods applied and shows the flux suppression consistently with each other and previous results.

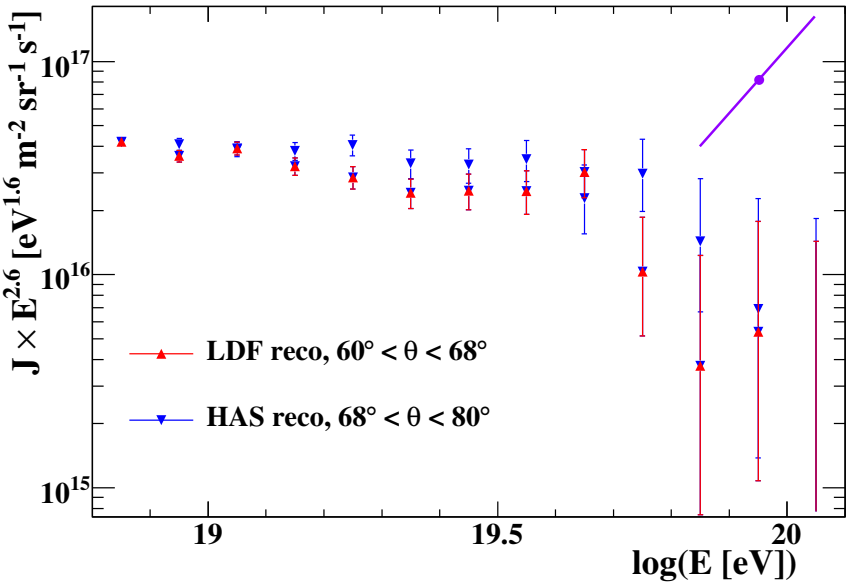

Figure 6.11: The ultra-high energy cosmic ray flux derived with air showers of zenith angles $\theta \in [60°, 80°]$. The error bars show the statistical uncertainty. The systematic uncertainties are shown as the diagonal error bars in the upper right corner.

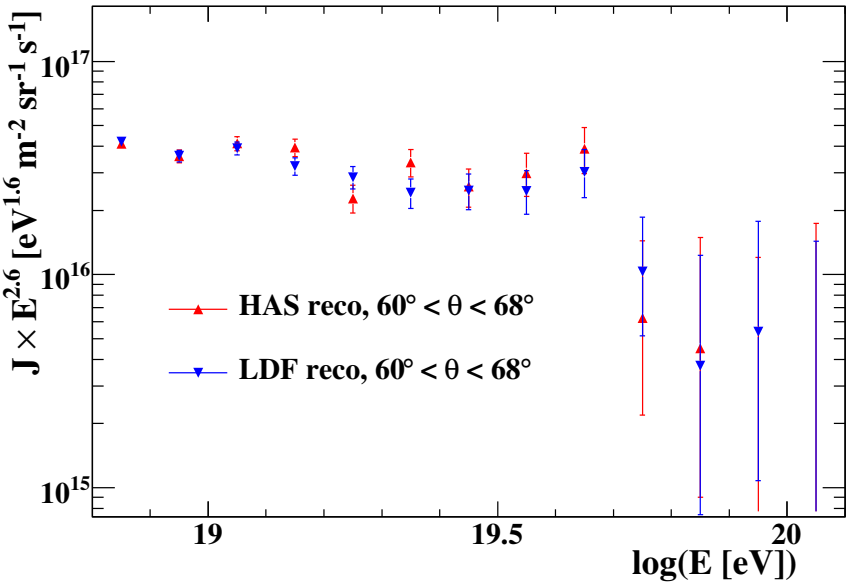

Figure 6.12: For air showers at zenith angles $60° < \theta < 68°$ both the LDF and the HAS reconstruction are applicable. The spectra determined with the two methods are shown for this zenith angle interval.

Summary and Conclusion

The determination of the flux of Ultra High Energy Cosmic Rays using very inclined air showers measured at the Pierre Auger Observatory has been the aim of this work. The water Cherenkov detectors of the surface array have an effective detection area of $4.3\,\mathrm{m}^2$ even for horizontal travelling particles. Thus very inclined air showers can be detected with full trigger efficiency for primary energies larger than $E = 6.3\,\mathrm{EeV}$ even at large zenith angles. In a zenith angle interval of $60^\circ < \theta < 70^\circ$ the reconstruction method for less inclined showers can still be applied, while a further method suited to reconstruct inclined showers can be used at zenith angles $\theta > 60^\circ$.

For optimisation of the reconstruction procedures, the two methods have been presented. During this thesis the method used for less inclined events has been improved generally and in the light of the application to very inclined data. Also the HAS reconstruction and improvements of this algorithm have been implemented into a general reconstruction framework.

- A method to determine the parameterisation of the lateral distribution function from data has been developed. A modified NKG function [124, 127] is used and both slope parameters are parameterised using real data.
- The current LDF parameterisations used in surface detector analyses show a systematic bias in the residuals of the LDF fit, causing an $8\,\%$ offset in the energy estimator for some event classes. An extension of the LDF by multiplying with a Fermi function has been introduced and the parameters of the extension have been determined using hybrid data. The non-flat residuals have been strongly reduced, resulting in a reduction of the bias to $4\,\%$.
- As a measure of the fitting quality a likelihood ratio analysis of the lateral distribution function has been set up. The method is designed to compare the performance of different functional shapes and parameterisations of the LDF. A modified NKG function has been proven superiour to other parameterisations. The parameterisation of the slope parameters given in this work and the effect of the Fermi extension are shown to further improve the performance of the modified NKG function.
- The uncertainty of the slope parameters with respect to the parameterisation due to different LDF shapes for different primary masses, fluctuations and detector effects has been calculated. These effects causing an intrinsic spread of the slope parameters around the parameterisation as well as the fitting uncertainty of the slope parameters of single events have been accounted for. The slope parameter uncertainty is propagated to to the uncertainty of the energy estimator and results in a systematic uncertainty of S_{1000} of $4\,\%$.
- The station selection and energy reconstruction algorithms of the HAS reconstruction have been improved while being implemented into the Offline reconstruction framework.

The surface detector measurement is based on the particle densities on ground. With data from the quasi-calorimetric energy measurement by the fluorescence detector the surface detector energy estimate can be derived independently of simulations.

- Using the constant intensity cut method the attenuation of the shower size parameter S_{1000} given by the LDF reconstruction has been extended up to a zenith angle of $\theta = 70^\circ$

  $$S_{38} = S_{1000}/(1 + (0.86 \pm 0.05^{+0.02}_{-0.05})\, x - (1.23 \pm 0.15^{0.10}_{-0.22})\, x^2.$$

  with $x = cos^2\theta - cos^2 38^\circ$. The parameters are compatible with those found in for the interval $\theta < 60^\circ$.

- A zenith angle dependency of the energy estimator N_{19} given by the muon profile based HAS reconstruction was falsified by application of the constant intensity method.

- The conversion from the surface detecor energy estimators S_{38} and N_{19} are power laws. The power law index for the conversion of S_{38} is $\gamma_{LDF} = 1.077 \pm 0.008^{+0.012}_{-0.012}$ and the normalisation is $E_{0,LDF} = 0.147 \pm 0.005^{+0.004}_{-0.004}\,\mathrm{EeV}$. For the HAS reconstruction the index is $\gamma_{HAS} = 1.049 \pm 0.020^{+0.007}_{-0.007}$ and the normalisation is $E_{0,HAS} = 4.72 \pm 0.02 \pm^{+0.23}_{-0.05}\ \mathrm{EeV}$.

- Using the direct energy calibration [141] the energy conversion function and the zenith angle correction can be determined fromm hybrid data without using the assumption of constant intensity. The results are in good agreement with the standard method.

- The cross-calibration of N_{19} with the energy estimate from the LDF reconstruction is also in very good agreement with the results of calibration with hybrid data.

- The energy resolution using the LDF reconstruction is $\sigma_{LDF}(E) = 19\,\%$ and for the HAS reconstruction, it is $\sigma_{HAS}(E) = 20\,\%$. The energy difference of the two methods has a spread of only $4\,\%$ giving an estimate of the contribution of the reconstruction method to the overall resolution.

- The different station selection algorithms do not influence the reconstructed energy significantly. The discrepancies of the station selections affectes only low signal stations.

A comparison of the reconstruction of a common data set of real data as well as simulated data with the two methods has been used to determine the optimum validity ranges and the properties of the methods.

- With simulated showers in the angular range of $60^\circ < \theta < 80^\circ$ the energy estimate using the surface detector is shown to dependend on the primary mass. For both reconstruction methods the difference of the measured energy for showers of the same energy having iron and proton primaries respectively is $40\,\%$. Using the hybrid calibration this bias is avoided.

- The performance of the LDF reconstruction at high and highest zenith angles is affected by asymmetries due to shower development. The asymmetries lead to an overestimation of S_{1000} and hence the energy at zenith angles $68^\circ < \theta < 72^\circ$. At higher zenith angles the reconstruction efficiency of the LDF algorithm drops and the energy is strongly underestimated and the resolution gets poor. in contrast the HAS reconstruction accounts for all these effects.

- In the range of moderately inclined air showers the energy estimates derived with the two methods are strongly correlated. The deviation of the energy estimate from the true value in simulations is also strongly correlated. In agreement with this result the cross-calibration of the HAS reconstruction using the LDF energy estimate results in a low spread. This spread of $4\,\%$ gives contribution of the energy uncertainty coming from the reconstruction algorithm.
- By comparing the zenith angle dependent energy resolution derived from simulated showers assuming a mixed mass composition for both reconstruction algorithms, the HAS algorithm has been proven to give better results at zenith angles above $\theta > 68°$. For lower zenith angles the LDF reconstruction should be used.

In order to derive the cosmic ray flux as a function of energy the event numbers detected by the Pierre Auger Observatory have to be normalised by the exposure.

- The muon-map based HAS reconstruction has full reconstruction efficiency at $E > 6.3\,\mathrm{EeV}$ for moderately and very inclined air showers of $60° < \theta < 80°$ regardless of the primary particle. The LDF reconstruction is fully efficient above $E > 6.3\,\mathrm{EeV}$ for showers with less than $\theta < 68°$, for higher zenith angles full reconstruction efficiency is not achieved in the energy range measured by the Pierre Auger Observatory.
- The well-established surface detector exposure calculation was modified according to the definition of the `T5Has` quality trigger for very inclined events. The ratio of events fulfilling `T5Has` and `T5` respectively was calculated for different zenith angle intervals. The `T5Has` acceptance is $9\,\%$ lower than the standard acceptance. Using `T5`, $1860 \pm 110\,\mathrm{km^2\ sr\ yr}$ of exposure have been collected in the zenith angle interval $60° < \theta < 68°$. For the full range zenith angle range $60° < \theta < 80°$, $3394 \pm 100\,\mathrm{km^2\ sr\ yr}$ of integrated exposure are accumulated using `T5Has`.

For the zenith angle interval of $60° < \theta < 68°$ using the LDF reconstruction and the HAS reconstruction respectively the energy spectrum and its statistical and systematic uncertainties coming from the acceptance, the calibration procedure, the reconstruction and the uncertainty of the fluorescence detector energy scale have been determined. The result is in agreement with previous results of the Pierre Auger Observatory and the the HiRes experiment respectively within the uncertainties. The derived flux based on the data taken by the Pierre Auger Observatory is consistent with the GZK feature.

Bibliography

[1] J. Abraham et al. Correlation of the highest energy cosmic rays with nearby extragalactic objects. *Science*, 318:938–943, 2007.

[2] J. Abraham et al. Observation of the suppression of the flux of cosmic rays above 4×10^{19}eV. *Phys. Rev. Lett.*, 101:061101, 2008.

[3] T. Abu-Zayyad et al. Measurement of the cosmic ray energy spectrum and composition from 10**17-eV to 10**18.3-eV using a hybrid fluorescence technique. *Astrophys. J.*, 557:686–699, 2001.

[4] T. Abu-Zayyad et al. Measurement of the spectrum of uhe cosmic rays by the fadc detector of the hires experiment. *Astropart. Phys.*, 23:157–174, 2005. astro-ph/0208301.

[5] M. Aglietta et al. Response of the Pierre Auger Observatory water Cherenkov detectors to muons. Presented at 29th International Cosmic Ray Conference (ICRC 2005), Pune, India, 3-11 Aug 2005.

[6] F. Aharonian. Primary particle acceleration above 100-TeV in the shell- type supernova remnant RX J1713.7-3946 with deep HESS observations. *Astron. Astrophys.*, 464:235–243, 2007.

[7] D. Allard, N. G Busca, G. Decerprit, A. V. Olinto, and E. Parizot. Implications of the cosmic ray spectrum for the mass composition at the highest energies. *JCAP*, 0810:033, 2008.

[8] D. for the Pierre Auger Collaboration Allard. The trigger system of the Pierre Auger surface detector: operation, efficiency and stability. *Proc. 29th Int. Cosmic Ray Conf., Pune, India*, 2005.

[9] Denis Allard, A. V. Olinto, and E. Parizot. Signatures of the extragalactic cosmic-ray source composition from spectrum and shower depth measurements. 2007.

[10] Denis Allard, E. Parizot, and A. V. Olinto. On the transition from Galactic to extragalactic cosmic- rays: spectral and composition features from two opposite scenarios. *Astropart. Phys.*, 27:61–75, 2007.

[11] P. Allison et al. Timing calibration and synchronization of surface and fluorescence detectors of the Pierre Auger Observatory. Presented at 29th International Cosmic Ray Conference (ICRC 2005), Pune, India, 3-11 Aug 2005.

[12] P.S. Allison, P. Bauleo, X. Bertou, and C. Bonifazi. Surface detector calibration in the engineering array. Internal Note of the Pierre Auger Collaboration GAP-2002-028, 2002.

[13] J. Alvarez-Muñiz, G. Rodríguez-Fernández, I. Valiño, and E. Zas. An alternative method for tank signal response and s(1000) calculation. GAP-2005-054, 2005.

[14] Jaime Alvarez-Muniz, Ralph Engel, T. K. Gaisser, Jeferson A. Ortiz, and Todor Stanev. Influence of shower fluctuations and primary composition on studies of the shower longitudinal development. *Phys. Rev.*, D69:103003, 2004.

[15] C. D. Anderson. The positive electron. *Phys. Rev.*, 43:491–494, 1933.

[16] T. Antoni et al. Electron, muon, and hadron lateral distributions measured in air-showers by the KASCADE experiment. *Astropart. Phys.*, 14:245–260, 2001.

[17] T. Antoni et al. Kascade measurements of energy spectra for elemental groups of cosmic rays: Results and open problems. *Astropart. Phys.*, 24:1–25, 2005. astro-ph/0505413.

[18] Carla Aramo et al. Optical relative calibration and stability monitoring for the Auger fluorescence detector. 2005.

[19] S. Argiro et al. The analog signal processing system for the Auger fluorescence detector prototype. *IEEE Trans. Nucl. Sci.*, 48:444–449, 2001.

[20] F. Arqueros et al. 2005.

[21] M. Ave, P. Bauleo, J. L. Harton, R. Knapik, A. Castellina, G. Navarra, and A. S. Chou. The accuracy of signal measurement with the water Cherenkov detectors of the Pierre Auger Observatory. *Nucl. Instrum. Meth.*, A578:180–184, 2007.

[22] M. Ave, P. Bauleo, and T. Yamamoto. Signal fluctuation in the auger surface detector array. Internal Note of the Pierre Auger Collaboration GAP-2003-030, 2003.

[23] M. Ave, N. Busca, L. Cazon, and F. Schmidt. Monte carlo and hybrid studies of shower-to-shower fluctuations. Internal Note of the Pierre Auger Collaboration GAP-2007-052, 2007.

[24] M. Ave et al. Measurement of the pressure dependence of air fluorescence emission induced by electrons. *Astropart. Phys.*, 28:41, 2007.

[25] M. Ave, J. A. Hinton, R. A. Vázquez, A. A. Watson, and E. Zas. The rate of cosmic ray showers at large zenith angles: a step towards the detection of ultra-high energy neutrinos by the Pierre Auger Observatory. *Astroparticle Physics*, 14:109, 2000. arXiv:astro-ph/0003011.

[26] M. Ave, J. A. Hinton, R. A. Vázquez, A. A. Watson, and E. Zas. The rate of cosmic ray showers at large zenith angles: a step towards the detection of ultra-high energy neutrinos by the Pierre Auger Observatory. *Astroparticle Physics*, 14:109, 2000. arXiv:astro-ph/0003011.

[27] M. Ave, J. A. Hinton, R. A. Vázquez, A. A. Watson, and E. Zas. Constraints on the Ultra High Energy Photon flux using inclined showers from the Haverah Park array. *Phys. Rev.*, D 65(0110613):63007–63007, 2002.

[28] M. Ave, R. A. Vazquez, and E. Zas. Modelling horizontal air showers induced by cosmic rays. *Astropart. Phys.*, 14:91, 2000.

[29] Maximo Ave. PhD thesis, Universidade de Santiago de Compostela, 2004.

[30] Maximo Ave. *PhD. Thesis, University of Santiago de Compostela*. PhD thesis, Universidade de Santiago de Compostela, 2004.

[31] R. M. Baltrusaitis et al. THE UTAH FLY'S EYE DETECTOR. *Nucl. Instrum. Meth.*, A240:410–428, 1985.

[32] Henrique M. J. Barbosa, F. Catalani, J. A. Chinellato, and Carola Dobrigkeit. Determination of the calorimetric energy in extensive air showers. *Astropart. Phys.*, 22:159–166, 2004.

[33] N. Barenthien et al. The slow control system of the Auger fluorescence detectors. Prepared for 28th International Cosmic Ray Conferences (ICRC 2003), Tsukuba, Japan, 31 Jul - 7 Aug 2003.

[34] D. Barnhill et al. Measurement of the lateral distribution function of UHECR air showers with the Pierre Auger observatory. 2005.

[35] P. Bauleo, A. Castellina, R Knapik, G. Navarra, and J. Harton. Auger surface detector signal accuracy - results from production tanks data. Internal Note of the Pierre Auger Collaboration GAP-2004-047, 2004.

[36] P. Bauleo et al. A water tank cerenkov detector for very high energy astroparticles. GAP-1997-023, 1997.

[37] P. Bauleo et al. Absolute calibration of the Auger fluorescence detectors. 2005.

[38] J. Bellido et al. Measurement of the average depth of the shower maximum and its fluctuations with the pierre auger observatory. Proc. of the 31th ICRC, 2009.

[39] S. Y. BenZvi et al. Measurement of Aerosols at the Pierre Auger Observatory. 2007.

[40] E. G. Berezhko, Leonid T. Ksenofontov, V. S. Ptuskin, V. N. Zirakashvili, and H. J. Voelk. Cosmic ray production in supernova remnants including reacceleration: The secondary to primary ratio. *Astron. Astrophys.*, 410:189–198, 2003.

[41] V. Berezinsky. Transition from galactic to extragalactic cosmic rays. 2007.

[42] V. S. Berezinsky, S. I. Grigoreva, and B. I. Hnatyk. Extragalactic UHE proton spectrum and prediction of flux of iron-nuclei at 10**8-GeV - 10**9-GeV. *Nucl. Phys. Proc. Suppl.*, 151:497–500, 2006.

[43] T. Bergmann et al. One-dimensional hybrid approach to extensive air shower simulation. *Astropart. Phys.*, 26:420–432, 2007. astro-ph/0606564.

[44] Xavier Bertou and Pierre Billoir. On the origin of the asymmetry of ground densities in inclined showers. GAP-2000-017, 2000.

[45] P. Billoir and O. Blanch Bigas. About a possible muon excess in real data compared to simulations. Internal Note of the Pierre Auger Collaboration GAP-2006-055, 2006.

[46] P. Billoir, O. Deligny, and A. Letessier-Selvon. A complete procedure for the reconstruction of inclined air showers. GAP-2003-003, 2003.

[47] Pierre Billoir. Email to the auger collaboration mailing list. Auger Collaboration Mailing List.

[48] Pierre Billoir. Top-down selection of events and stations in surface detector triggers. GAP-2006-072, 2006.

[49] D. J. Bird et al. The Cosmic ray energy spectrum observed by the Fly's Eye. *Astrophys. J.*, 424:491–502, 1994.

[50] C. Bonifazi and for the Pierre Auger Collaboration. The angular resolution of the Pierre Auger Observatory. *Nucl. Phys. Proc. Suppl.*, 190:20–25, 2009.

[51] C. Bonifazi and A. Letessier-Selvon. De-biasing the station start time. Internal Note of the Pierre Auger Collaboration GAP-2006-050, 2006.

[52] Carla Bonifazi and Piera Luisa Ghia. Selection of data periods and calculation of the sd geometrical acceptance. GAP-2006-101, 2006.

[53] Bruce Dawson for the Pierre Auger Collaboration. Hybrid performance of the pierre auger observatory. Proc. of the 30th ICRC, 2007.

[54] N. Busca, V. M. Olmos-Gilbaja, P. Privietra, R. A. Vázquez G. Rodríguez-Fernández, and E. Zas. An estimate of the cosmic ray spectrum using inclined data of the pierre auger observatory. GAP-2006-025, 2006.

[55] K. Caballero Mora. Private communication. Private Communication.

[56] D.V. Camin, M. Cuautle, M. Destro, and R. Gariboldi. Fabrication of the first 150 head electronics units-results of the acceptance tests. Internal Note of the Pierre Auger Collaboration GAP-1999-043, 1999.

[57] D.V. Camin, M. Cuautle, D. Mestro, and R. Gariboldi. Fabrication of the first 150 head electronics units results of the acceptance tests. Internal Note of the Pierre Auger Collaboration GAP-2004-018, 1999.

[58] Julian Candia, Silvia Mollerach, and Esteban Roulet. Cosmic ray drift, the second knee and galactic anisotropies. *JHEP*, 12:032, 2002.

[59] C.Bonifazi and A. Letessier-Selvon. Event selection using the t5 time distribution. Internal Note of the Pierre Auger Collaboration GAP-2006-042. GAP-2006-042.

[60] P. A. Cherenkov. Dokl. Akad. Nauk SSSR **2** (1934), p. 451. Dokl. Akad. Nauk SSSR **3** (1936), p. 413. Dokl. Akad. Nauk SSSR **14** (1937), p. 103. Dokl. Akad. Nauk SSSR **14** (1937), p. 99. Izv. Akad. Nauk SSSR Ser. Phys. OMEN (1937) 455.

[61] P. A. Cherenkov, 1937.

[62] R. W. Clay, S. Cook, B. R. Dawson, A. G. K. Smith, and R. Lampard. The angular deviation of ultra high energy cosmic rays in intergalactic magnetic fields. *Astropart. Phys.*, 9:221–225, 1998.

[63] Pierre Auger Collaboration. Pierre auger project design report. Fermilab, 1997. `http://www.auger.org/admin/DesignReport/index.html`.

[64] S. Dagoret-Campagne. The central trigger naming convention. Internal Note of the Pierre Auger Collaboration GAP-2002-062, 2002.

[65] B. Dawson. Fluorescence detector techniques. Internal Note of the Pierre Auger Collaboration GAP-1996-017, 1996.

[66] B. Dawson. Present and possible future implementations of fluorescence yield in fd analysis. Internal Note of the Pierre Auger Collaboration GAP-2002-067, 2002.

[67] B. Dawson. Suggested improvements for the treatment of fd light in the offline. Internal Note of the Pierre Auger Collaboration GAP-2004-055, 2004.

[68] M. De Domenico, M. Scuderi, T. Trovato, R. Caruso, A. Insolia, and S. Riggi. Periodic modulation on the sd event rate. GAP-2009-066, 2009.

[69] Daniel De Marco and Todor Stanev. On the shape of the UHE cosmic ray spectrum. *Phys. Rev.*, D72:081301, 2005.

[70] H. Dembinski. Comparing Models of the Muon Ground Density of Very Inclined Showers with Simulations and Data. Presentation in collaboration meeting, Malargüe, Argentina, Nov. 2008.

[71] H. Dembinski. PhD thesis, RWTH Aachen, 2009.

[72] H. Dembinski, P. Billoir, O. Deligny, and T. Hebbeker. Inferring Average Ground Profiles of the Muon Density of Inclined Air Showers from Monte-Carlo Simulations at Ultra-High Energy. in preprint, 2009.

[73] H. Dembinski, J. Gonzalez, V. Olmos-Gilbaja, I. Valiño, M. Roth, and T. Schmidt. Reconstruction of very inclined air showers with offline. GAP-2009-008, 2009.

[74] H. Dembinski, T. Hebbeker, and T. Schmidt. Determination of the energy calibration function and primary composition of very inclined air showers. GAP-2009-048, 2009.

[75] H. Dembinski and M. Leuthold. The inclined corsika proton shower library. GAP-2006-094, 2006.

[76] H. Dembinski and Matthias Leuthold. The inclined corsika proton shower library. GAP-2006-094, 2006.

[77] Hans Dembinski, Pierre Billoir, Olivier Deligny, and Thomas Hebbeker. Inferring Average Ground Profiles of the Muon Density of Inclined Air Showers from Monte-Carlo Simulations at Ultra- High Energy. 2009.

[78] Hans Dembinski, Javier Gonzalez, Victor Olmos-Gilbaja, Markus Roth, Talianna Schmidt, and Inés Vali no. Reconstruction of horizontal events within offline. Internal Note of the Pierre Auger Collaboration GAP-2009-008, 2009.

[79] V.A. Derbina et al. Cosmic-ray spectra and composition in the energy range of 10-tev - 1000-tev per particle obtained by the runjob experiment. *Astrophys. J.*, 628:L41–L44, 2005.

[80] J. C. D'Olivo et al. Calibration of WCDs for the Auger observatory. Prepared for 26th International Cosmic Ray Conference (ICRC 99), Salt Lake City, Utah, 17-25 Aug 1999.

[81] V. P. Egorova et al. The spectrum features of UHECRs below and surrounding GZK. *Nucl. Phys. Proc. Suppl.*, 136:3–11, 2004.

[82] J. W. Elbert et al. Proc. 18^{th} Int. Cosmic Ray Conf., Bangalore (India), **1** (1983).

[83] J. Engel, T. K. Gaisser, Paolo Lipari, and Todor Stanev. Nucleus-nucleus collisions and interpretation of cosmic-ray cascades. *Phys. Rev. D*, 46(11):5013–5025, Dec 1992.

[84] R. Engel. Private communication. Private Communication.

[85] A. D. Erlykin and A. W. Wolfendale. A single source of cosmic rays in the range 10**15-eV to 10**16-eV. *J. Phys.*, G23:979–989, 1997.

[86] A. D. Erlykin and A. W. Wolfendale. Properties of cosmic ray interactions at PeV energies. *Astropart. Phys.*, 18:151–164, 2002.

[87] A. Etchegoyen. Track geometry and smearing of the bump calibration. GAP-2002-078, 2002.

[88] A. Etchegoyen. AMIGA, Auger Muons and Infill for the Ground Array. 2007.

[89] A. Etchegoyen, Diego G. Melo, A. D. Supanitsky, and Maria Clementina Medina. Pierre Auger enhancements: Transition from galactic to extragalactic cosmic ray sources. *AIP Conf. Proc.*, 917:210–218, 2007.

[90] Lyndon Evans, (ed.) and Philip Bryant, (ed.). LHC Machine. *JINST*, 3:S08001, 2008.

[91] Event Selection Group. The Official SD Event Selection as of March 2005. GAP-2005-023, March 2005. GAP-2005-023.

[92] P. Facal San Luis, V. M. Olmos-Gilbaja, G. Parente, G. Rodríguez-Fernández, I. Vali no, R. A. Vázquez, E. Zas, and L. Cazón. Cosmic ray spectrum with inclined showers: November 2006 update. GAP-2007-027, 2007.

[93] P. Facal San Luis, V. M. Olmos-Gilbaja, G. Parente, G. Rodriguez-Fernandez, I. Valino, R. A. Vazquez, E. Zas, and L. Cazon. Cosmic ray spectrum with inclined showers: November 2006 update. GAP-2007-027, 2007.

[94] P. Facal San Luis, V. M. Olmos-Gilbaja, G. Rodríguez-Fernández, I. Valiño, R. A. Vázquez, and E. Zas. Cosmic ray spectrum using inclined showers: Update presented in september 2006. GAP-2006-107, 2006.

[95] P. Facal San Luis, V. M. Olmos-Gilbaja, G. Rodríguez-Fernández, I. Valinño, R. A. Vázquez, and E. Zas. Cosmic ray spectrum using inclined showers: Update presented in september 2006. GAP-2006-107, 2006.

[96] A. Fassó, A. Ferrari, J. Ranft, and P.R. Sala. Fluka: a multi-particle transport code. CERN-2005-10 (2005), INFN/TC 05/11, SLAC-R-773, 2005.

[97] A. Fassó, A. Ferrari, S. Roesler, P.R. Sala, G. Battistoni, F. Cerutti, E. Gadioli, M.V. Garzelli, F. Ballarini, A. Ottolenghi, A. Empl, and J. Ranft. The physics models of fluka: status and recent developments. Computing in High Energy and Nuclear Physics 2003 Conference (CHEP2003), La Jolla, CA, USA, March 24-28, 2003, (paper MOMT005), eConf C0303241 (2003), arXiv:hep-ph/0306267, 2003.

[98] Enrico Fermi. On the Origin of the Cosmic Radiation. *Phys. Rev.*, 75:1169–1174, 1949.

[99] A. Fernandez, E. Gamez, S. Roman, and A. A. Zepeda. Aires/corsika - root interface. Internal Note of the Pierre Auger Collaboration GAP-2002-043, 2003.

[100] T. K. Gaisser. IceTop: The surface component of IceCube. Prepared for 28th International Cosmic Ray Conferences (ICRC 2003), Tsukuba, Japan, 31 Jul - 7 Aug 2003.

[101] T. K. Gaisser and A. M. Hillas. Reliability of the Method of Constant Intensity Cuts for Reconstructing the Average Development of Vertical Showers. In *Proc. 15th Int. Cosm. Ray Conf.*, volume 8, page 353, Plovdiv, Bulgaria, 1977.

[102] T. K. Gaisser, R. J. Protheroe, and Todor Stanev. Gamma-ray production in supernova remnants. *Astrophys. J.*, 492:219, 1998.

[103] R. C. Geary. The frequency distribution of the quotient of two normal variates. *Journal of the Royal Statistical Society*, 93:442–446, 1930.

[104] P. Ghia. The compact 3tot as sd physics trigger for vertical showers. Internal Note of the Pierre Auger Collaboration GAP-2004-018, 2004.

[105] M. Giller, G. Wieczorek, A. Kacperczyk, H. Stojek, and W. Tkaczyk. Energy spectra of electrons in the extensive air showers of ultra-high energy. *J. Phys.*, G30:97–105, 2004.

[106] Kenneth Greisen. End to the cosmic ray spectrum? *Phys. Rev. Lett.*, 16:748–750, 1966.

[107] N.L. Grigorov, V.E. Nesterov, I.D. Rapoport, I.A. Savenko, and G.A. Skuridin. Investigation of energy spectrum of primary cosmic particles with high and superhigh energies of space stations *proton*. *Yad. Fiz.*, 11:1058–1069, 1970.

[108] Pierre Auger Acceptance Group. Exculator - the pierre auger acceptance calculator, 2006. `http://ipnweb.in2p3.fr/~auger/AugerProtected/formulaire1.html`.

[109] A.M.J. Guerard, C. K. andFerrero, P. Bauleo, et al. Segmentation of a water cerenkov tank. GAP-1997-031, 1997.

[110] J. D. Hague et al. Correlation of the highest energy cosmic rays with nearby extragalactic objects in pierre auger observatory data. Proc. of the 31th ICRC, 2009.

[111] P. M. Hansen, R. A. Vazquez, and J. Alvarez-Muniz. Studying shower to shower fluctuations with simulations. Proc. of the 31th ICRC, 2009.

[112] Diego Harari, Silvia Mollerach, and Esteban Roulet. Correlation of cosmic rays with astronomical objects in the pierre auger observatory data. GAP Note 2006-046, 2006.

[113] Andreas Haungs et al. Investigating the 2nd knee: The KASCADE-Grande experiment. *J. Phys. Conf. Ser.*, 47:238, 2006.

[114] D. Heck and J. Knapp. Upgrade of the monte carlo code corsika to simulate extensive air showers with energies $> 10^{20}$ ev. Report FZKA 6097B, Karlsruhe, 1998.

[115] D. Heck and J. Knapp. Upgrade of the monte carlo code corsika to simulate extensive air showers with energies $> 10^{20}$ ev. Report FZKA 6097B, Karlsruhe, 1998.

[116] D. Heck, J. Knapp, J.N. Capdevielle, G. Schatz, and T. Thouw. Corsika: A monte carlo code to simulate extensive air showers. Report FZKA 6019, Karlsruhe, 1998.

[117] D. Heck, J. Knapp, J.N. Capdevielle, G. Schatz, and T. Thouw. Corsika: A monte carlo code to simulate extensive air showers. Report FZKA 6019, Karlsruhe, 1998.

[118] Dieter Heck. Air shower simulation with corsika at arbitrary direction of incidence. GAP-2006-084, 2006.

[119] J. Hersil, I. Escobar, D. Scott, G. Clark, and S. Olbert. Observations of extensive air showers near the maximum of their longitudinal development. *Phys. Rev. Lett.*, 6(1):22–23, Jan 1961.

[120] A. M. Hillas. ANGULAR AND ENERGY DISTRIBUTIONS OF CHARGED PARTICLES IN ELECTRON PHOTON CASCADES IN AIR. *J. Phys.*, G8:1461–1473, 1982.

[121] A. M. Hillas. The Origin of Ultrahigh-Energy Cosmic Rays. *Ann. Rev. Astron. Astrophys.*, 22:425–444, 1984.

[122] Anthony M. Hillas. Cosmic rays: Recent progress and some current questions. 2006.

[123] Frederick James. *Statistical Methods in Experimental Physics*. World Scientific Publishing, Singapore, 2nd edition edition, 2006.

[124] Greisen K. *Progress In Cosmic Ray Physics*, volume 3. Amsterdam North-Holland, 1956.

[125] F. Kakimoto et al. A Measurement of the air fluorescence yield. *Nucl. Instrum. Meth.*, A372:527–533, 1996.

[126] N. N. Kalmykov and S.S. Ostapchenko. Yad. Fiz. **56** (1993) 105; Phys. At. Nucl. **56** N3 (1993) 346; N.N. Kalmykov, S.S. Ostapchenko and A.I. Pavlov, Izv. RAN Ser. Fiz. **58** (1994) N12 p.21; N.N. Kalmykov, S.S. Ostapchenko and A.I. Pavlov, Bull. Russ. Acad. Science (Physics) **58** (1994) 1966; N.N. Kalmykov, S.S. Ostapchenko and A.I. Pavlov, Nucl. Phys. B (Proc. Suppl.) **52B** (1997) 17.

[127] Nishimura J. Kamata K. .. *Prog. Theoret. Phys. Suppl.*, 6:93, 1958.

[128] B. Keilhauer et al. Atmospheric profiles at the southern Pierre Auger observatory and their relevance to air shower measurement. 2005.

[129] H. O. Klages. HEAT: Enhancement telescopes for the Pierre Auger Southern Observatory. Prepared for 30th International Cosmic Ray Conference (ICRC 2007), Merida, Yucatan, Mexico, 3-11 Jul 2007.

[130] G. Kulikov and G. Khristiansen. Unknown. *Sov. Phys. JETP*, 35:441.

[131] C. Lachaud and X. Bertou. Local Stations Trigger Monitoring Files. Internal Note of the Pierre Auger Collaboration GAP-2003-046. GAP-2003-046.

[132] R. Lampard, R. W. Clay, and B. R. Dawson. Limits on source distances for the most energetic cosmic rays in intergalactic magnetic fields. *Astropart. Phys.*, 7:213–218, 1997.

[133] M. A. Lawrence, R. J. O. Reid, and A. A. Watson. The cosmic ray energy spectrum above 4*1017 ev as measured by the haverah park array. *J. Phys. G: Nucl. Part. Phys.*, 17(5):733–757, 1991.

[134] A. Letessier-Selvon. The pierre auger project central data acquisition system. Internal Note of the Pierre Auger Collaboration GAP-1999-003, 1999.

[135] I. Lhenry-Yvon and P. Ghia. The communications crisis in 2009: proposal for handling data between june and november. GAP-2010-020, 2010.

[136] A. Lopez-Aguera and G. Rodriguez Fernandez. Signal uncertainty induced by pedestal suppresion procedure. GAP-2003-038, 2006.

[137] M. Ave et al. (AIRFLY Collab.). Measurement of the pressure dependence of air fluorescence emission induced by electrons. *Astropart. Phys.*, 28:41, 2007. arXiv astro-ph/0703132.

[138] M. Ave *et al.* (AIRFLY Collab.). Temperature and Humidity Dependence of Air Fluorescence Yield measured by AIRFLY. *Nucl. Instrum. Meth.*, A597:50–54, 2008. arXiv astro-ph/0711.4583.

[139] S. Maldera. Private communication. Private Communication.

[140] Ioana C. Mariş. *Measurement of the Ultra High Energy Cosmic Ray Flux using Data of the Pierre Auger Observatory*. PhD thesis, Universität Karlsruhe, 2008.

[141] Ioana C. Mariş, J. Blümer, M. Roth, T. Schmidt, and M. Unger. Comparison of Two Methods to Infer the Cosmic Ray Spectrum at Highest Energies. GAP-2007-044, 2007.

[142] Ioana C. Mariş, Johannes Blümer, Markus Roth, Michael Unger, and Darko Veberič. Reducing the influence of the threshold events on the surface detector energy calibration. GAP-2007-116, 2007.

[143] Ioana C. Mariş. *Measurement of the Ultra High Energy Cosmic Ray Flux using Data of the Pierre Auger Observatory*. PhD thesis, Universität Karlsruhe, 2008.

[144] Ioana C. Maris, 2009. private communication.

[145] Ioana C. Mariş, J. Blümer, M. Roth, T. Schmidt, and M. Unger. Comparison of two methods to infer the cosmic ray spectrum at highest energies. GAP-2007-044, 2007.

[146] J. Matthews. A Heitler model of extensive air showers. *Astropart. Phys.*, 22:387–397, 2005.

[147] G. Matthiae and P. Privitera. The schmidt telescope with corrector plate. Internal Note of the Pierre Auger Collaboration GAP-1998-039, 1998.

[148] Gustavo Medina, Gustavo A. Medina Tanco, and Jorge E. Horvath. Deflection of ultra high energy cosmic rays by the galactic magnetic field: From the sources to the detector.

[149] M. Nagano, K. Kobayakawa, Naoto Sakaki, and K. Ando. New measurement on photon yields from air and the application to the energy estimation of primary cosmic rays. *Astropart. Phys.*, 22:235–248, 2004.

[150] R. A. Nam, S. I. Nikolsky, V. P. Pavlyuchenko, A. P. Chubenko, and V. I. Yakovlev. Investigation of Nucleon-Nuclei of Air Cross-Section at Energy Greater Than 10-TeV. In *Muenchen 1975, Fourteenth International Cosmic Ray Conference, Vol.7*, Muenchen 1975, 2258-2262.

[151] Frank Nerling, J. Bluemer, R. Engel, and M. Risse. Description of Cherenkov light production in high-energy air showers. *Astropart. Phys.*, 24:421–437, 2006.

[152] D. Newton, J. Knapp, and A. A. Watson. The optimum ground parameter, s(r opt). Internal Note of the Pierre Auger Observatory GAP-2005-013, 2005.

[153] Victor Olmos-Gilbaja. PhD thesis, Universidade de Santiago de Compostela, 2009.

[154] S.S. Ostapchenko. QGSJET-II: towards reliable description of very high energy hadronic interactions. In *Proc. of the ISVHECRI*, volume 151, page 143 and 147, Pylos, Greece, 2006. NESTOR Institute. arXiv: hep-ph/0412332 (2004) and hep-ph/0501093 (2005).

[155] Alexander D. Panov et al. The results of ATIC-2 experiment for elemental spectra of cosmic rays. 2006.

[156] E. Parizot, I. Lhenry, D. Allard, P. Ghia, and G. Navarra. First steps towards the definition of a quality trigger (t5) for the sd acceptance calculations. GAP-2004-023, 2004.

[157] A. Parra, V.M. Olmos-Gilbaja, J. Alvarez-Muniz, R.A. Pelayo, R. Vazquez, and E. Zas. The trigger efficiency of the surface array of the pierre auger observatory for inclined showers. GAP-2009-135, 2009.

[158] J. Parrisius. Test of the calibration of the auger fluorescence telescopes with an isotropic uv light source. Internal Note of the Pierre Auger Collaboration GAP-2009-045, 2009.

[159] P.Billoir, O.Deligny, and A.Letessier-Selvon. A complete procedure for the reconstruction of inclined air showers. GAP-2003-003, 2003.

[160] T. Pierog, Ralph Engel, D. Heck, S. Ostapchenko, and K. Werner. Latest Results from the Air Shower Simulation Programs CORSIKA and CONEX. 2007.

[161] T. Pierog, Ralph Engel, D. Heck, S. Ostapchenko, and K. Werner. Latest Results from the Air Shower Simulation Programs CORSIKA and CONEX. 2007.

[162] Pierre Auger Collaboration. Auger offline software, 2005. `https://www.auger.unam.mx/AugerWiki/FrontPage`.

[163] Pierre DaSilva Pierre Billior. Towards a parameterization of the lateral distribution function and its asymmetries in the surface detector. GAP-2002-073, 2002.

[164] M. Prouza, J. Ebr, P Travnicek, R. Smida, P. Kubanek, and M. Jelinek. Fram - robotic telescope for monitoring of wavelength dependence of the extinction: description of hardware, data analysis and results. Internal Note of the Pierre Auger Collaboration GAP-2008-176, 1999.

[165] C. L. Pryke and J. Lloyd-Evans. A High performance GPS based autonomous event time tagging system with application in a next generation extensive air shower array. *Nucl. Instrum. Meth.*, A354:560–566, 1995.

[166] J Rautenberg et al. Proc. 30^{th} Int. Cosmic Ray Conf., Merida (Mexico), **1** (2007).

[167] B. Rossi. *High Energy Particles*. Prentice-Hall, Englewood Cliffs, NJ, 1952.

[168] H. Salazar, L. Nellen, and L. Villasenor. Surface detector calibration for the auger observatory. GAP-2001-023, 2001.

[169] A. Schmidt, T. Asch, M. Kleifges, H.-J. Mathes, and H. Gemmeke. New third level trigger for the fluorescence telescopes. Internal Note of the Pierre Auger Collaboration GAP-2004-018, 2007.

[170] T. Schmidt, I.C. Mariş, and M. Roth. Fine tuning of the ldf parameterisation and the influence on s_{1000}, 2007. GAP Note 2007-106.

[171] Talianna Schmidt. Measuring the lateral distribution of extended air showers with data from the surface detector and hybrid data of the Pierre Auger Observatory. (In German). FZKA-7231.

[172] F. Schuessler. *Measurement of the Energy Spectrum of Ultra-High Energy Cosmic Rays using Hybrd Data of the Pierre Auger Observatory*. PhD thesis, Univeristät Karlsruhe, 2007.

[173] F. Schuessler et al. Measurement of the cosmic ray energy spectrum above 1018 ev with the pierre auger observatory. Proc. of the 31th ICRC, 2009.

[174] R. Silberberg, M. M Shapiro, and C. H. Tsao. EXPERIMENTAL TESTS OF COSMIC RAY PROPAGATION AND ORIGIN. (TALK). In *Denver 1973, Cosmic Ray Conference Vol.1*, Denver 1973, 567-572.

[175] CDAS software group. Event reconstruction. v4r4.

[176] P. Sokolsky. INTRODUCTION TO ULTRAHIGH-ENERGY COSMIC RAY PHYSICS. REDWOOD CITY, USA: ADDISON-WESLEY (1989) 208p.

[177] Todor Stanev, Ralph Engel, Anita Mucke, Raymond J. Protheroe, and Jorg P. Rachen. Propagation of ultra-high energy protons in the nearby universe. *Phys. Rev.*, D62:093005, 2000.

[178] P. Summers. First estimate of the primary cosmic ray energy spectrum above 3 eev from the pierre auger observatory. Proc. of the 29th ICRC, 2005. ICRC05.

[179] P. Summers and B. Fick. A numerical recipe for fluorescence detector geometry reconstruction. Internal Note of the Pierre Auger Collaboration GAP-2003-045. GAP-2003-045.

[180] D. Supanitsky and X. Bertou. Semi-analytical model of the three fold charge spectrum in a water cherenkov tank. GAP-2003-113, 2003.

[181] Z. Szadkowski and K. H. Kampert. Sigma-delta compensation of pedestals in the first level sd trigger. GAP-2006-044, 2006.

[182] M. Takeda et al. Extension of the cosmic-ray energy spectrum beyond the predicted Greisen-Zatsepin-Kuzmin cutoff. *Phys. Rev. Lett.*, 81:1163–1166, 1998.

[183] I. E. Tamm and I. M. Frank. *Dokl. Akad. Nauk SSSR*, 14:107, 1937.

[184] The Pierre Auger Collaboration. The aperture of the Pierre Auger Observatory surface detector for extensive air showers below 60°: from the trigger system to exposure calculation. in preprint.

[185] The Pierre Auger Collaboration. Correlation of the Highest-Energy Cosmic Rays with Nearby Extragalactic Objects. *Science*, 318(5852):938–943, 2007.

[186] P. G. Tinyakov and I. I. Tkachev. BL Lacertae are sources of the observed ultra-high energy cosmic rays. *JETP Lett.*, 74:445–448, 2001.

[187] H. Tokuno et al. The Telescope Array experiment: Status and prospects. *J. Phys. Conf. Ser.*, 120:062027, 2008.

[188] H. Ulrich et al. Energy spectra of cosmic rays in the knee region. *Nucl. Phys. Proc. Suppl.*, 122:218–221, 2003.

[189] M. Unger, B. R. Dawson, R. Engel, F. Schussler, and R. Ulrich. Reconstruction of Longitudinal Profiles of Ultra-High Energy Cosmic Ray Showers from Fluorescence and Cherenkov Light Measurements. *Nucl. Instrum. Meth.*, A588:433–441, 2008.

[190] M. Unger, R. Engel, F. Schussler, and R. Ulrich. Longitudinal Shower Profile Reconstruction from Fluorescence and Cherenkov Light. 2007.

[191] M. Unger et al. Measurement of the average Xmax as a function of energy. GAP-2007-005.

[192] Michael Unger. Shower profile reconstruction from fluorescence and cherenkov light. GAP-2006-010, 2006.

[193] Michael Unger and for the Pierre Auger Collaboration. Composition Studies with the Pierre Auger Observatory. *Nucl. Phys. Proc. Suppl.*, 190:240–246, 2009.

[194] M. Unger for the Pierre Auger Collaboration. *Proc. 30^{th} Int. Cosmic Ray Conf., Merida, Mexico*, 2007.

[195] Inés Valiño Rielo. *Detection of horizontal air showers and neutrino induced showers with the Pierre Auger Observatory*. PhD thesis, Universidade de Santiago de Compostela, 2007.

[196] I. Valino, J. Alvarez-Muniz, M. Roth, R. A. Vazquez, and E. Zas. Characterisation of the electromagnetic component in ultra-high energy inclined air showers. *Astropart. Phys.*, 32:304–317, 2010.

[197] R. Vazquez et al. The cosmic ray flux observed at zenith angles larger than 60 degrees with the pierre auger observatory. Proc. of the 31th ICRC, 2009.

[198] Darko Veberič and Markus Roth. Offline reference manual: Sd reconstruction. GAP-2005-035, 2005.

[199] Darko Veberič and Markus Roth. Offline reference manual: Sd reconstruction. GAP-2005-035, 2005.

[200] Tilo Waldenmaier, Johannes Bluemer, and Hans Klages. Spectral resolved Measurement of the Nitrogen Fluorescence Emissions in Air induced by Electrons. *Astropart. Phys.*, 29:205–222, 2008.

[201] Klaus Werner and Tanguy Pierog. Extended air shower simulations based on epos. *AIP Conf. Proc.*, 928:111–117, 2007.

[202] Tadeusz Wibig and Arnold W. Wolfendale. At what particle energy do extragalactic cosmic rays start to predominate? *J. Phys.*, G31:255–264, 2005.

[203] G. T. Zatsepin and V. A. Kuzmin. Upper limit of the spectrum of cosmic rays. *JETP Lett.*, 4:78–80, 1966.

Acknowledgement

This work would not have been possible without the invaluable support of the people that accompanied me. It is both my wish and a great pleasure to express my gratitude to my collaborators, collegues, friends and family.

I want to thank Professor Johannes Blümer for his support as referee and for the possibilities of working in the Institut für Kernphysik and the Pierre Auger Collaboration. Also I am grateful to Professor Günther Quast for being my co-referee.

For valuable discussions and guidance I owe gratitude to my supervisor Doctor Markus Roth. Together with him, Doctor Ioana C. Mariş and Doctor Hans Dembinski have provided support in ideas, analyses and also in reading of this manuscript.

For encouragement, discussions, explanations, inspirations and ideas that went into my work and into this thesis I want to express my gratitude to my colleagues from the KIT and the Auger collaboration. I am especially indebted to Dr. Simone Maldera, Dr. Victor Olmos-Gilbaja, Prof. Jaime Alvarez-Muñiz, Dr. Ralph Engel, Dr. Michael Unger, Dr. Ralf Ulrich, Dr. Fabian Schüssler, Dr. Christine Meurer, Dr. Danays Gonzalez, Dr. Xavier Garrido, Prof. Etienne Parizot, Dr. Carla Bonifazi, Dr. Ricardo Vazquez, Dr. Inés Valiño, Prof. Enrique Zas, Dr. Darko Veberic, Dr. Dariusz Góra, Jan Weseler, Steffen Müller, Karen Caballero Mora and Prof. Lukas Nellen.

With their love and their support my family and my boyfriend encouraged and inspired me. My warmest thanks and thoughts are with them and I wish all of them could have accompanied me to this point.

Appendix A

Monte Carlo set

The showers simulated for the inclined shower library [76] have been used in the context of this work. The detailed binning of the generated showers in zenith and azimuth angles respectively and in the energy are given in table A.1. For each bin showers with random parameters within the borders of the bin have been simulated. In case of the logarithm of the energy $\lg E$ and the azimuth angle ϕ the simulated showers are distributed flatly in the bin. In case of the the zenith angle a distribution corresponding to flatness in solid angle was chosen, the shower zenith angles θ were randomly drawn out of a $\sin\theta\cos\theta$ distribution.

A complete sets was simulated, using the hadronic interaction models `FLUKA` [96,97] for low energies and `QGSJETII` [126, 154] for high energies. Five proton showers and one iron shower per bin were simulated, resulting in 3240 showers in total and 648 per energy bin.

	zenith angle θ								
lower edge θ_{low}	$60°$	$62°$	$64°$	$66°$	$70°$	$74°$	$78°$	$82°$	$86°$
higher edge θ_{high}	$62°$	$64°$	$66°$	$68°$	$72°$	$76°$	$80°$	$84°$	$88°$

	azimuth angle ϕ											
lower edge ϕ_{low}	$0°$	$30°$	$60°$	$90°$	$120°$	$150°$	$180°$	$210°$	$240°$	$270°$	$300°$	$330°$
higher edge ϕ_{high}	$10°$	$40°$	$70°$	$100°$	$130°$	$160°$	$190°$	$220°$	$250°$	$280°$	$310°$	$340°$

	energy $\lg E[eV]$				
lower edge $\lg E_{low}$	18.0	18.5	19.0	19.5	20.0
higher edge $\lg E_{high}$	18.1	18.6	19.1	19.6	20.1

Table A.1: The binning of the Monte Carlo data sets used for cross-checks. For each combination five proton showers and one iron shower with random values of θ, ϕ and E within the respective bin range have been used.

Appendix B

Calibration

Toy Monte Carlo

For the toy Monte Carlo creating fake calibration data sets the distributions and uncertainties of the calibration data were modelled with different functions.

The energy dependent relative uncertainty of the surface detector energy estimator was fitted with a power law in the energy estimator

$$\sigma(S_{SD})/S_{SD} = \exp a \cdot S_{SD}^{b}. \tag{B.0.1}$$

The parameters derived in the fit are shown in table B.1.

For the uncertainty of the fluorescence detector energy estimate a ratio distribution [103]

$$\begin{aligned}
p_Z(z) &= \frac{b(z)\cdot c(z)}{a^3(z)}\frac{1}{\sqrt{2\pi}\sigma_x\sigma_y}\left[2\Phi\left(\frac{b(z)}{a(z)}\right)-1\right] + \frac{1}{a^2(z)\cdot\pi\sigma_x\sigma_y}e^{-\frac{1}{2}\left(\frac{\mu_x^2}{\sigma_x^2}+\frac{\mu_y^2}{\sigma_y^2}\right)} \\
a(z) &= \sqrt{\frac{1}{\sigma_x^2}z^2+\frac{1}{\sigma_y^2}} \\
b(z) &= \frac{\mu_x}{\sigma_x^2}z+\frac{\mu_y}{\sigma_y^2} \\
c(z) &= e^{\frac{1}{2}\frac{b^2(z)}{a^2(z)}-\frac{1}{2}\left(\frac{\mu_x^2}{\sigma_x^2}+\frac{\mu_y^2}{\sigma_y^2}\right)} \\
\Phi(z) &= \int_{-\infty}^{z}\frac{1}{\sqrt{2\pi}}e^{-\frac{1}{2}u^2}
\end{aligned} \tag{B.0.2}$$

was used. This accounts for the fact that the distribution of the ratio of two Gaussian distributed variables is not a Gaussian. The parameters derived for the calibration data sets using the HAS reconstruction and the LDF reconstruction respectively are given in table B.2. The uncertainty of the surface detector energy estimator is distributed around the relation given in equation B.0.1. Also

	a	b
σ_{LDF}	-1.94 ± 0.67	-1.26 ± 1.06
σ_{HAS}	-0.95 ± 1.20	-0.94 ± 1.04

Table B.1: The power law parameters of the parameterisation of the uncertainty of the surface detector energy estimator.

	c	μ_1	σ_1	μ_2	σ_2
$\sigma(E_{FD,LDF})$	41 ± 0.02	-0.259 ± 0.0003	0.064 ± 0.0001	-3.46 ± 0.004	0.696 ± 0.0007
$\sigma(E_{FD,HAS})$	1.63 ± 0.0001	-0.175 ± 0.0003	0.0000181 ± 0.000002	-2.58 ± 0.74	1.09 ± 0.0001

Table B.2: The parameters of the ratio distribution (equation B.0.2) used to model the energy uncertainty of the fluorescence detector for the two calibration data samples.

	c	μ_1	σ_1	μ_2	σ_2
$\sigma(S_{38}) - \sigma_{fit}(S_{38})$	2.65 ± 0.005	-0.014 ± 0.001	0.0003 ± 0.045	-2.54 ± 0.01	0.333 ± 0.001
$\sigma(S_{38}) - \sigma_{fit}(S_{38})$	2.91 ± 0.03	-0.079 ± 0.001	0.066 ± 0.001	-2.50 ± 0.02	0.0002 ± 0.0097

Table B.3: The parameters of the ratio distribution (equation B.0.2) used to model the spread of the surface detector estimator uncertainty around the parameterisation in equation B.0.1.

here a ratio of Gaussian distributed variables is modelled and so again the ratio distribution given in equation B.0.2 is used. The parameters for the spread of the surface detector energy estimator uncertainty around the parameterisation is shown in table B.3.

The energy distribution of the hybrid sample was not fitted. The energies of the events in the fake calibration data sets were drawn from the distribution of the fluorescence detector energy estimate of the real data.